malab
materials analysis lab

IFW
Leibniz-Institut
für Festkörper- und
Werkstoffforschung
Dresden

TECHNISCHE
UNIVERSITÄT
DRESDEN

AMD
SAXONY

Phase formation and size effects in nanoscale silicide layers for the sub-100 nm microprocessor technology

by

Jochen Rinderknecht

Phase formation and size effects in nanoscale silicide layers for the sub-100 nm microprocessor technology

A dissertation submitted to the
Faculty for Mechanical Engineering
of the Technical University of Dresden, Germany,
for the degree of
Doctor of Mechanical Engineering
(Doktoringenieur, Dr.-Ing.)

Dipl.-Min. Jochen Rinderknecht
born 12/04/1968 in Stuttgart

Date of submittal: 10/20/2004
Date of oral examination: 07/13/2005

Advisory Committee
Professor Dr. rer. nat. habil. Dr. h.c. Klaus Wetzig, Chair
Professor Dr. Karen Maex
Dr. rer. nat. habil. Ehrenfried Zschech

Contents

Acronyms

AC	**A**lternating **C**urrent
AES	**A**uger **E**lectron **S**pectroscopy
AFM	**A**tomic **F**orce **M**icroscopy
ASIC	**A**pplication **S**pecific **I**ntegrated **C**ircuit
BEoL	**B**ack-**E**nd **o**f **L**ine
CBED	**C**onvergent **B**eam **E**lectron **D**iffraction
ccp	**c**ubic**c**losed **p**ackage
CH&M	**C**ontiniuos **H**eating and **M**easuring
CMOS	**C**omplementary **M**etal **O**xide **S**emiconductor
CTE	**C**oefficient of **T**hermal **E**xpansion
CVD	**C**hemical **V**apor **D**eposition
DC	**D**irect **C**urrent
DDS	**D**ominant **D**iffusing **S**pecies
DOS	**D**ensity **o**f **S**tate
DRAM	**D**ynamic **R**andom **A**ccess **M**emory
EELS	**E**lectron **E**nergy-**L**oss **S**pectroscopy
EFTEM	**E**nergy **F**iltered **T**ransmission **E**lectron **M**icroscopy
ESD	**E**levated **S**ource/**D**rain
ESRF	**E**uropean **S**ynchrotron **R**adiation **F**acility
fcc	**f**ace **c**entered **c**ubic
FEoL	**F**ront-**E**nd **o**f **L**ine
FWHM	**F**ull-**W**idth at **H**alf-**M**aximum
GIXRD	**G**razing **I**ncidence **X**-**R**ay **D**iffraction
H-M-S	**H**eating-**M**easuring-**S**top
HDC	**H**igh temperature **D**iffraction **C**hamber
IC	**I**ntegrated **C**ircuit
ITRS	**I**nternational **T**echnology **R**oadmap for **S**emiconductors
JCPDS	**J**oint **C**ommittee of **P**owder **D**iffraction **S**tandards
MBE	**M**olecular **B**eam **E**pitaxy
MOSFET	**M**etal **O**xide **S**emiconductor **F**ield **E**ffect **T**ransistor

MPU	**M**icro **P**rocessor **U**nit
OME	**O**xide **M**ediated **E**pitaxy
PAI	**P**re **A**morphization **I**mplant
PVD	**P**hysical **V**apor **D**eposition
RBS	**R**utherford **B**ackscattering **S**pectroscopy
ROBL	**R**ossendorf **B**eam**L**ine
RT	**R**oom-**T**emperature
RTA	**R**apid **T**hermal **A**nnealing
SAD	**S**elective **A**rea **D**iffraction
SALICIDE	**S**elf **A**ligned **S**ILICIDE
SEG	**S**elective **E**pi **G**rowth
SEM	**S**canning **E**lectron **M**icroscopy
SOI	**S**ilicon **O**n **I**nsulator
SR-XRD	**Sy**nchrotron-**R**adiation **X**-**R**ay **D**iffraction
StEM	**St**andard **E**rror of the **M**ean
TEM	**T**ransmission **E**lectron **M**icroscopy
TIME	**Ti**tanium **M**ediated **E**pitaxy
ULSI	**U**ltra **L**arge **S**cale **I**ntegration
VLSI	**V**ery **L**arge **S**cale **I**ntegration
XRD	**X**-**R**ay **D**iffraction
XRR	**X**-**R**ay **R**eflectivity

List of Figures

List of Tables

Used symbols

α	Coefficient of thermal expansion	$[\mathrm{K}^{-1}]$
α_B	Beam-convergence semi-angle	$[^\circ]$
α_c	Critical angle	$[^\circ]$
α_i	Angle of incidence	$[^\circ]$
α_S, β_S	Stoichiometric indices for silicides	
a, b, c	Lattice constants	[Å]
C	Total effective capacitance	$[\mathrm{A\ sec\ V}^{-1}]$
$\mathcal{C}$	Concentration	$[\mathrm{at/cm}^3]$
$\mathcal{C}_{e_{Co}}$	Equilibrium concentration of Co in Si	$[\mathrm{at./cm}^3]$
d	d-space, distance between lattice planes	[Å]
D	Diffusion coefficients	$[\mathrm{cm}^2/\mathrm{sec}]$
$D_{\alpha_S}, D_{\beta_S}$	Chemical inter diffusion coefficients	$[\mathrm{cm}^2/\mathrm{sec}]$
D_{α_i}	Chemical interface diffusion coefficients	$[\mathrm{cm}^2/\mathrm{sec}]$
D_G	Diffusion coefficient for grain boundary diffusion	$[\mathrm{cm}^2/\mathrm{sec}]$
D_S	Diffusion coefficient for surface diffusion	$[\mathrm{cm}^2/\mathrm{sec}]$
D_V	Diffusion coefficient for volume diffusion	$[\mathrm{cm}^2/\mathrm{sec}]$
ΔG	Change of Gibb's free enthalpy	$[\mathrm{kJ\ mol}^{-1}]$
ΔG_{rc}	Recrystallization energy of Si	$[\mathrm{kJ\ mol}^{-1}]$
ΔH	Change of enthalpy	$[\mathrm{kJ\ mol}^{-1}]$
ΔH^0	Interchange energy	$[\mathrm{kJ\ mol}^{-1}]$
ΔH^0_F	Standard enthalpy of formation	$[\mathrm{kJ\ mol}^{-1}]$
ΔS	Change of entropy	$[\mathrm{J\ K}^{-1}\ \mathrm{mol}^{-1}]$
ε	Expansion=$(l - l_0)/l_0$	
e	Euler's number: 2.718	
E	Young's modulus	[Pa]
E_F	Energy at Fermi level	[eV]
F_i	Force per unit length at the interface substrate/silicide $\sigma_t \cdot t_l$	[N/m]
γ	Free surface energy	$[\mathrm{J/m}^2]$

g, q	Geometrical coefficients	
$G_{\alpha_S}, G_{\beta_S}$	Weight coefficients	
h	Contact resistance	[Ω/cm^2]
H	Enthalpy	[kJ mol^{-1}]
h, k, l	Miller indices	
j	Diffusion flux of Si	[kg m^{-2} sec^{-1}]
κ	Dielectric constant	[A sec V^{-1} m^{-1}]
k	Boltzmann's constant: $1.380662 \cdot 10^{-23}$	[J/K]
k^{eff}	Effective diffusion barrier	
K	(Wafer) Curvature	[m]
λ	Wavelength	[Å]
l	Length	[nm]
m^*	Effective mass of tunneling charge carrier	[kg]
M_s	Biaxial Young's modulus ($E/1-\upsilon$)	[Pa]
Me	Metal	
ω	Molecular volume	[liter/mol]
Ω	Electrical resistance	[Ω]
Φ_B	Schottky-barrier height	[eV]
ϖ	Permeance	[A/V]
p	Pressure	[Pa]
Q	Activation energy for diffusion	[J/mol]
ρ	Density	[g/cm^3]
ρ^*	Nucleation rate	
ϱ	Resistivity	[Ω/cm^2]
ϱ_c	Specific contact resistivity	[Ω/cm^2]
r	Radius	[nm]
R	Total resistance	[Ω]
R_g	Universal gas-constant R_g=8.3143	[J K^{-1} mol^{-1}]
R_s	Sheet resistance	[Ω/□]
σ	Stress tensor	
σ_i	Intrinsic film stress	[Pa]
σ_t	Total film stress	[Pa]
σ_T	Thermal film stress	[Pa]
ς	Surface energy	[J/m^2]
S	Entropy	[J K^{-1} mol^{-1}]
S_m	Entropy of mixing	[J K^{-1} mol^{-1}]

S_v	Vibrational entropy	[J/K^{-1}mol^{-1}]
τ	Ratio of the fluxes $j^{Si}_{\alpha_S}/j^{Si}_{\beta_S}$	
$2\,\vartheta$	Bragg angle of constructive interference	[°]
t	Time	[sec]
t_d	Penetration depth	[nm]
t_g	Grooving depth	[nm]
t_i	Max. depth of information	[nm]
t_l	Layer thickness	[nm]
t_m	Metal layer thickness	[nm]
t_{ox}	Gate oxide thickness	[nm]
t_s	Silicide thickness	[nm]
t_{sub}	Substrate thickness	[nm]
T	Absolute temperature	[K]
T_e	Temperature of equilibrium	[K]
T_m	Melting temperature	[K]
U	Ratio of grain diameter to original layer thickness	
U_c	Critical ratio of grain diameter to original layer thickness	
υ	Poisson's ratio	
w	Width	[nm]
z	Coordination number	
Z	Atomic number	

Abstract

Silicides are an essential part of state-of-the-art CMOS devices. They are used as contact material on the active regions as well as on the Si gate of a transistor. In this work, investigations were performed in the systems Co-Si, Co-Ni-Si, and Ni-Si. *In situ* high temperature SR-XRD and CBED techniques were used for phase identification. AES enabled the determination of elemental concentrations in layer stacks. SEM was applied to agglomeration studies. TEM imaging and analytical TEM provided insights into layer structures, grain morphology as well as information about the distribution of chemical elements within silicide layers.

This thesis is divided into two main parts. The first part deals with the phase formation sequences and the phase formation and conversion temperatures in nanoscale thin films on either single crystal or polycrystalline Si substrates. The effect of different types of dopants vs. no doping and the impact of a capping layer on the phase formation and conversion temperatures were studied. In the second part, size effects and agglomeration of thin silicide films were investigated. The effect of different layer thicknesses on the silicidation process was studied. Additionally, the degree of agglomeration of silicide films was calculated.

Furthermore, the ternary CoTiSi phase was found and identified as well as the severely limited miscibility of the monosilicides CoSi and NiSi could be shown. The CTE of NiSi between 400–700 °C and its non-linear behavior was determined.

Kurzfassung

Silizide spielen ein wesentliche Rolle in den technologisch fortschrittlichsten CMOS Bauteilen. Sie finden Verwendung als Kontaktmaterial auf den Aktivgebieten und dem Silizium Gatter von Transistoren. Diese Arbeit beschäftigt sich mit den Systemen: Co-Si, Co-Ni-Si und Ni-Si. Sowohl *in situ* Hochtemperatur-SR-XRD Experimente als auch CBED wurden zur Phasenidentifikation herangezogen. AES erlaubte es, Elementverteilungen in Schichtstapeln zu bestimmen. Für Studien über Agglomerationserscheinnungen wurde REM eingesetzt. TEM und analytisches TEM trugen nicht nur zu Einblicken in Schichtstrukturen und Kornformen bei, sondern lieferten auch Daten zu Elementverteilungen in Silizidschichten.

Diese Dissertation gliedert sich in zwei Hauptteile. Der erste Teil beschäftigt sich mit den Phasenbildungsabfolgen und den Phasenbildungs- und Umwandlungstemperaturen in nanoskaligen dünnen Schichten. Als Trägermaterial wurden einkristalline und polykristalline Siliziumsubstrate verwendet. Der Einfluß verschiedener Dotierungen im Vergleich zu undotierten Substraten sowie die Beeinflussung der Silizidierung durch eine Deckschicht wurden untersucht. Im zweiten Teil waren Größeneffekte verschiedener Schichtdicken und Agglomerationserscheinungen Gegenstand von Untersuchungen. Unterschiede bei der Silizidierung in Zusammenhang mit unterschiedlichen Schichtdicken wurden bestimmt.

Darüberhinaus wurde eine ternäre CoTiSi Phase gefunden und identifiziert. Außerdem konnte die stark eingeschränkte Mischbarkeit der Monosilizide CoSi und NiSi gezeigt werden. Der thermische Ausdehnungskoeffizient von NiSi im Temperaturbereich 400–700 °C und sein nicht-lineares Verhalten wurden bestimmt.

Chapter 1

Introduction

Silicides play a key role in high-performance CMOS (complementary metal oxide semiconductor) devices as a contact material for the polycrystalline Si gate as well as on the active transistor regions. They have been subject of numerous investigations for more than a decade. The development of faster high-performance semiconductor devices and the rapidly increasing integration level of device structures require a deep insight into the related manufacturing processes. Numerous papers and monographs have been published dealing with the properties and applications of silicides [1–5]. Much work and effort has been spent dealing with bulk samples and thin films in the range of tens of nanometers [6–9]. The insights that have been obtained from that work cannot be transferred directly to ultra thin films. In order to achieve high yield and reliable microprocessors at dimensions of $\leq$50 nm gate length, exact knowledge and fundamental understanding of the physical and chemical processes of the silicide formation as well as the material's properties of nanoscale[1] silicide layers is crucial. The application of X-ray diffraction (XRD), especially synchrotron radiation X-ray diffraction (SR-XRD) enables the investigation of thin films in the range of a few nanometers only. The currently deposited metal film-thickness within the manufacturing process of high-performance microprocessor units (MPU) is in the range of $\approx$10–15 nm. The optimization of commonly used materials and the introduction of new materials (see figure 1.1) into the production of modern integrated circuits (IC's), are challenges to technology and to thin film materials analysis.

SR-XRD in combination with other analytical techniques, like transmission electron microscopy (TEM), Auger electron spectroscopy (AES), atomic force

---

[1] Nanoscale meaning significantly below 100 nm.

microscopy (AFM), and scanning electron microscopy (SEM), provide valuable results that help to improve the manufacturing process of semiconductor devices. The investigations performed in this work focus on the silicidation process in several materials systems, two binary and one ternary system, which are currently used or which are candidates for implementation in semiconductor devices: Co-Si, Co-Ni-Si, and Ni-Si. Additionally, the limits for thermal treatments, i. e. the upper and lower temperature limits for rapid thermal annealing (RTA) as well as the limits for further processing, e. g. metallization steps, chemical-mechanical-polishing (CMP), or further thin-film deposition, in the back-end of line (BEoL)[2] were determined.

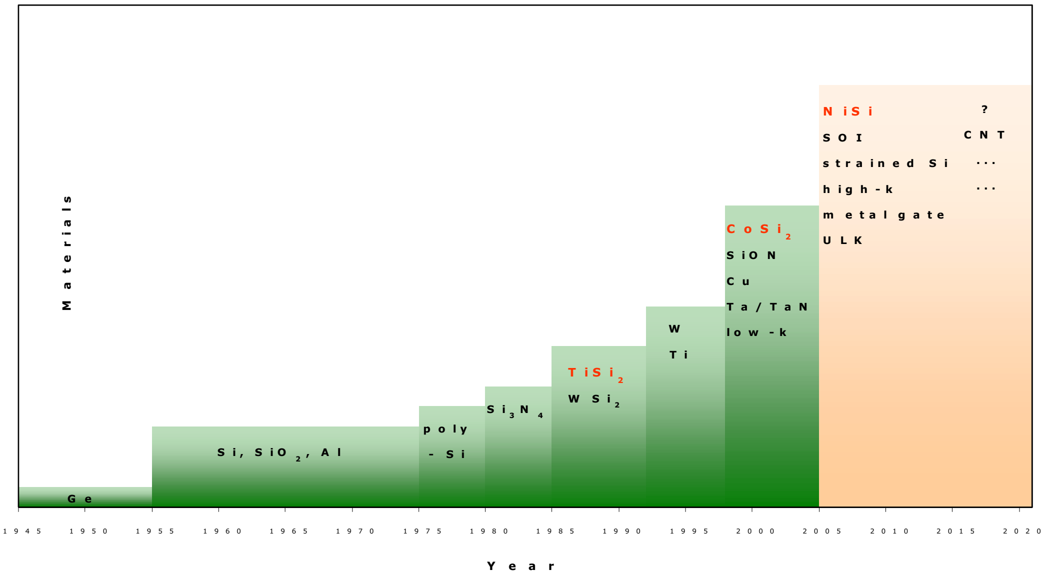

Fig. 1.1: Implementation of new materials into the CMOS process [10].

---

[2] Front-End of Line (FEoL) and Back-End of Line (BEoL) are terms widely used in the semiconductor industry. An arbitrary border was set between all processes dealing with the transistors and the metallic interconnects. Usually all manufacturing steps, including the silicidation steps, prior to the first metal via belong to the FEoL, all subsequent processes are part of the BEoL.

Usage of silicides within advanced microprocessors

Transition metal silicides are commonly used in the microprocessor manufacturing process as contact material for the source and drain regions as well as on the polycrystalline silicon gate of MOSFETs (metal oxide semiconductor field effect transistor) [2, 11]. These silicides exhibit a great potential of manufacturability for the very large and ultra large scale integration (VLSI and ULSI, respectively) due to their thermodynamics and due to their physical properties. In addition, silicides are characterized by a sufficiently high thermal stability to withstand the BEoL processing temperatures. In advanced ICs, nowadays, $CoSi_2$ is widely used due to its low resistivity and high thermal stability [4, 12]. In state-of-the-art manufacturing applications of ICs the SALICIDE (self aligned silicide) process is crucial. After a surface cleaning step, a metal layer is deposited uniformly over the whole wafer. The solid-state silicidation reactions occur only at those regions where the metal is in direct contact with the prepatterned silicon, i. e. at the source/drain as well as the polycrystalline Si gate of the transistors. This is a laterally self-limited process, i. e. on the insulating material, mostly SiO_2 based materials, between the single crystal active regions and the polycrystalline silicon gates no solid-state reaction takes place. Therefore, no further patterning is needed. An annealing step initiates a silicidation, followed by a selective wet-etch step to remove the non-reacted metal on the insulation regions as well as on the silicidized regions. A second high temperature RTA step may be necessary

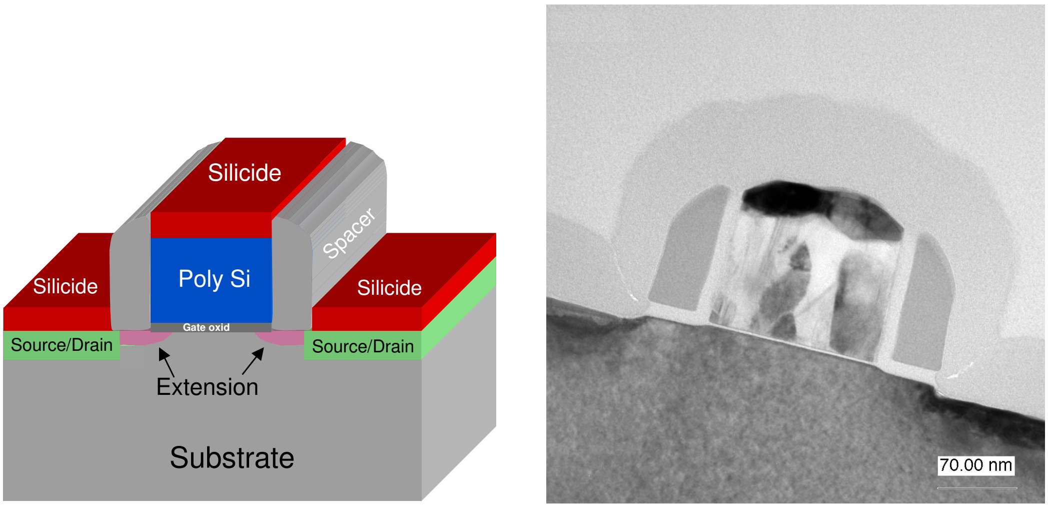

(a) Schematic sketch of a transistor. (b) TEM brightfield image of a transistor.

Fig. 1.2: Cross sections of a MOSFET.

to transfer the intermediate silicide phase(s) into the desired low-resistivity phase. An extended overview about the SALICIDE process was given by Morgan *et al.* [13]. Candidates for potential use in semiconductor industry are $TiSi_2$, $CoSi_2$, NiSi, and $Co_{1-x}Ni_xSi_2$.

History of silicides in CMOS applications

In the early days of microprocessor manufacturing, Al was used as a contact material. It was deposited on to the active regions, i. e. the source and drain regions of the transistor, as well as on the gates. Aluminum adheres well to both Si and SiO_2. Additionally, it forms a self passivating aluminum oxide layer [14]. On the other hand there are some disadvantages, like the risk that aluminum spiking through junctions occurs after thermal processing [15]. This becomes more and more severe with further scaling down of devices. Furthermore, a potential misalignment in metallization, due to the fact that Al is, in contrast to silicides not self-aligning, causes an increase in contact resistance, because the contact area decreases in this case. To overcome these problems, a thin layer of Pt was deposited onto the wafers, subjected to thermal treatment to form PtSi, the first ever used self-aligned silicide, as an underlayer. This layer underneath the Al prevented Si diffusion into the Al layer which was known to cause aluminum spiking. This silicide layer provided a constant contact resistance independently of the alignment of the Al layer. Pt silicide, Cu silicide, and Mo silicide were the first silicides that were used in the production of transistors [16, 17]. Subsequently, Ti silicide was introduced [18, 19]. The metal deposition is followed by two annealing steps. In the first step, the C49 $TiSi_2$ phase is formed which is then patterned in a selective etch process. In a second annealing step C54-$TiSi_2$ is formed [20, 21]. Again, with further shrinking dimensions problems arose that could not be solved with the materials that had been used at that time. It became more and more difficult to form the desired low resistivity phase of $TiSi_2$, the C54 phase. Due to the very small linewidth, i. e. the very small gate length, the transition from C49 to C54 was inhibited [22–24]. Although $TiSi_2$ is no longer in use in high-performance microprocessors, it is still utilized in a great variety of semiconductor devices. Since the transition to the $0.25\,\mu$m CMOS technology, $CoSi_2$ has been the material of choice for manufacturing of microprocessors [12,25]. Currently it is widely used within the semiconductor industry for even the most advanced devices [26, 27]. Recently, NiSi received more and more attention [28–34] and became the focus of studies dealing with it's properties, both chemically and physically, as well as the integration into mass production [35–41]. NiSi does not show the effect of a rapid increase of sheet resistance at very small gate lengths, i. e. below ≈40–45 nm. No increase in sheet resistance can be found using NiSi, even for the most aggressive gate patterning processes leading to gate lengths of≈ 30 nm [30, 31, 33, 40–46]. Additionally, the usage of ternary Co-Ni silicides is subject of various investigations dealing with the phase formation, material's properties, and potential applications [29, 29, 34, 47–55]. Ternary Co-Ni silicides are promising candidates to prolong the "life" of $CoSi_2$ in manufacturing of very small Si gate lengths. In parallel, efforts are made to explore the possibilities of further use of silicides in the manufacturing process of microprocessors, e. g. using silicidized metal gates [56–59]. Figure 1.1 shows a time-line from the past to the mid-range future with respect to the introduction of new materials into the CMOS process, highlighting also the commonly used silicides.

1.1 Motivation

1.1.1 ITRS roadmap requirements

The International Technology Roadmap for Semiconductors (ITRS) [60] predicts the near term future for the manufacturing of high performance semiconductor devices, such as MPUs, application specific integrated circuits (ASIC), and dynamic random access memories (DRAM). The requirements related to silicide structures are given in table 1.1.

1.1.2 Microprocessor performance

In order to further confirm Moore's Law [62], which has been valid for more than 30 years now, an ongoing shrinking of device and interconnect structures is crucial. The introduction of new materials, particulary silicides is needed to match these requirements.

The performance of microprocessors is determined by AC (alternating current) as well as DC (direct current) performance. Frequency = 1/delaytime ≈ $1/RC$ with R the total resistance and C the total effective capacitance at the gate and interconnect level, respectively. The lower the RC value the faster the microprocessor. The integration challenge to achieve this goal is to design the transistors in a way that RC becomes as low as possible. Table 1.2 lists the resistances and capacitances which need to be minimized.

Table 1.1: 2003 ITRS roadmap predicted feature size and parameters related to silicides

Year Feature size	2003	2004	2005	2006	2007	2008	2009
Printed gate length[a] [nm]	65	53	45	40	35	32	28
Physical gate length[a] [nm]	45	37	32	28	25	22	20
Max. Si consumption[b] [nm]	24.8	20.4	17.6	15.4	13.8	13.2	12.0
Silicide thickness[b] [†] [nm]	25	20	21	19	17	16	14
Contact silicide sheet R_s[b] [Ω/□]	6.5	7.9	7.5	8.6	9.6	10.0	11.1
Contact max. resistivity[b] [Ω/cm^2]	1.93^{-07}	1.62^{-07}	1.44^{-07}	1.20^{-07}	1.05^{-07}	0.87^{-07}	0.72^{-07}

a) driven by MPU b) driven by MPU/ASIC

Interims solutions are known

Manufacturable solutions are known

Manufacturable solutions are *NOT* known

[†] Silicide thickness is taken to be 1/2 of the center contact χ_j to avoid consumption-induced increase in contact resistivity. Less than half of the junction can be consumed [61].

Table 1.2: Contributors to the *RC* delay which need to be minimized. See also figure 1.3

Contributors to *RC*
• low parasitic resistances
• low junction capacitance
• low Miller capacitance
• low fringing capacitance

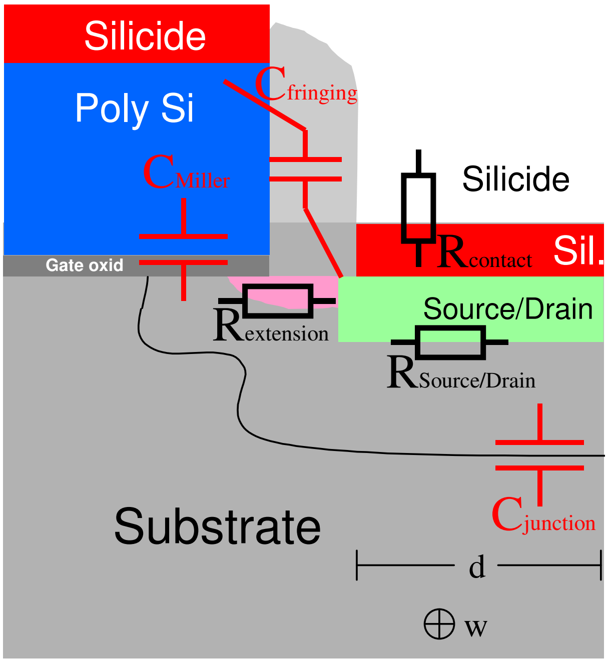

Fig. 1.3: Resistances and capacitances contribution to the RC delay.

The silicidation process affects the first part of RC as $R_{Contact}$, R_{Ext} and $R_{Source/Drain}$ (figure 1.3) all contribute to the total R with

$$R_c = \frac{\sqrt{\varrho_c \cdot R_{Ext}*}}{w} \coth\left(\frac{\sqrt{R_{Ext}*}}{\varrho_c} \cdot l\right) \tag{1.1}$$

and specific contact resistivity can be approximated as

$$\varrho_c \quad \propto \quad exp\left[\frac{4\pi\sqrt{\varpi \cdot m*}}{h} \cdot \frac{\Phi_B}{\sqrt{N_D}}\right] \tag{1.2}$$

with w=width of the active region, l=length of the contact in electron flow direction, ϖ=permeance, $m*$=effective mass of tunneling charge carrier, Φ_B= Schottky-barrier height and N_D=Dopant-concentration at the interface [61]. Additionally, the sheet R_s which is given by

$$R_s = \frac{\varrho}{t_l} \tag{1.3}$$

with ϱ the resistivity of the interconnect layer and t_l being the thickness of the silicide layer. For large linewidths,

$$R = \frac{R_s l}{w} \tag{1.4}$$

and

$$C = lw\frac{\kappa_{ox}}{t_{ox}} \tag{1.5}$$

can be written as

$$RC = R_s l^2 \frac{\kappa_{ox}}{t_{ox}} \tag{1.6}$$

with l=length of the contact in electron flow direction and w being the corresponding width, κ_{ox} the oxide dielectric constant, and t_{ox} the gate oxide thickness [2]. For small linewidths however, the fringing capacitance plays a more and more important role and eventually becomes dominant. Further scaling down of ULSI devices reduces t_l and t_{ox} which increases RC as well as decreases l. Figure 1.4[3] illustrates the trend that with higher integration, i. e. smaller distances between structures, the RC delay becomes greater [63]. The application of low resistivity silicides such as $TiSi_2$ and $CoSi_2$, that are

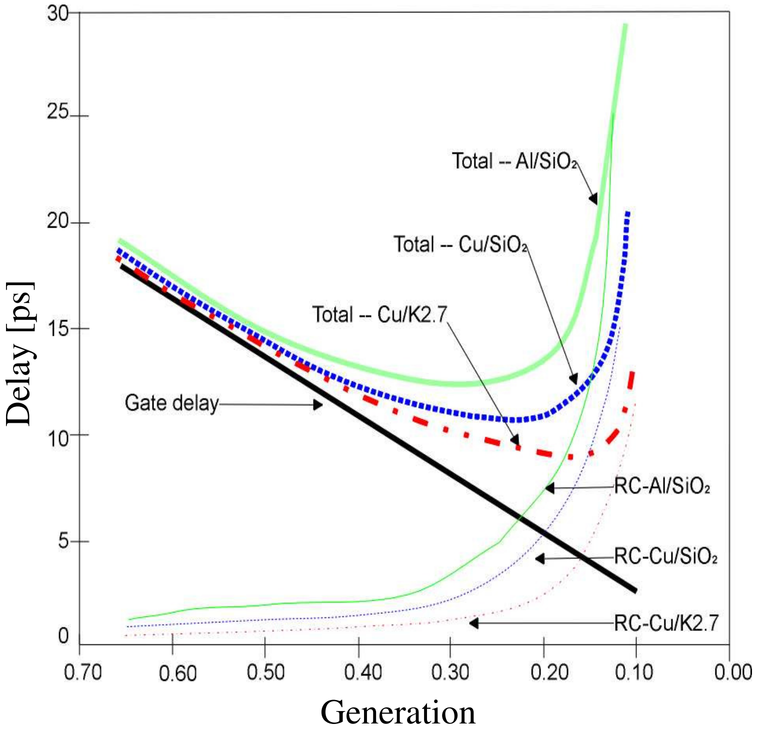

Fig. 1.4: RC delay: speed versus feature size issue [63].

---

[3] Calculations made for the following conditions:
κ=4.0 for SiO_2 and 2.7 for low-κ materials, Al and Cu layer 0.8 μm thick and 43 μm long.

used for mass production of modern IC's, also contributes to a reduced *RC* delay (see equation 1.1). Not only the intrinsic materials properties, e. g. *RC*, influences the performance. There is also an impact of silicide properties like interface roughness of the silicide/Si interfaces, which influence significantly resistance and leakage current [61, 64, 65].

1.1.3 Microprocessor reliability

The determination and understanding of the coefficient of thermal expansion (CTE) can provide useful information about the stress evolution as well as the texturing properties during the thermal treatment, i. e. the silicidation process, and can point to failure mechanism during the manufacturing process. Since the CTE of the silicide layer is in general significantly higher (typically $\approx 10{\cdot}10^{-6}\,K^{-1}$) than the CTE of Si ($2.6{\cdot}10^{-6}\,K^{-1}$), compressive stress arises within the silicide layer while increasing the temperature. This stress can be considered to be biaxial, since the expansion perpendicular to the surface is not constrained. The force that acts at the interface substrate/silicide, which is caused by the stress within the silicide layer, impacts the agglomeration properties of thin layers. Agglomeration phenomena, such as agglomeration of thin films, could lead to discontinuous layers, will become more important as the microprocessor dimensions continue to shrink. Such discontinuous films are likely to cause a microprocessor-device to fail, since conductivity and diffusion barrier properties will change substantially. Especially on small polycrystalline Si gates, agglomeration can lead to interrupted lines that cause an increase in line resistance by several orders of magnitude (see figure 1.5). The transition from the low-resistivity phase NiSi to the high-resistivity (and high temperature) phase $NiSi_2$, will also cause the microprocessor to fail. Usually, agglomeration takes place prior to $NiSi_2$ formation. Furthermore, $NiSi_2$ is likely to form epitaxially. Both mechanisms lead to discontinuous films, and therefore, to non-functional CMOS devices. Consequently, it is important to determine the phase formation and transition temperatures.

Limits of $CoSi_2$ for very small gate lengths

The progress in further scaling down of microprocessor devices leads to smaller and smaller gate lengths. Although it is reported that $CoSi_2$ is stable down to gate lengths of about 40 nm [40,44,45,66,67], severe agglomeration effects take place at geometries between 40–60 nm. Many investigations show a roll-off of

$CoSi_2$ sheet resistance for small gate lengths [30, 31, 35, 40, 44, 45]. Figure 1.5 illustrates a possible failure mechanism. Several missing ($CoSi_2$) grains within the polycrystalline Si line are seen. There are different approaches, mainly by implanting nitrogen, to enhance the thermal stability of $CoSi_2$ at small gate lengths [68–70].

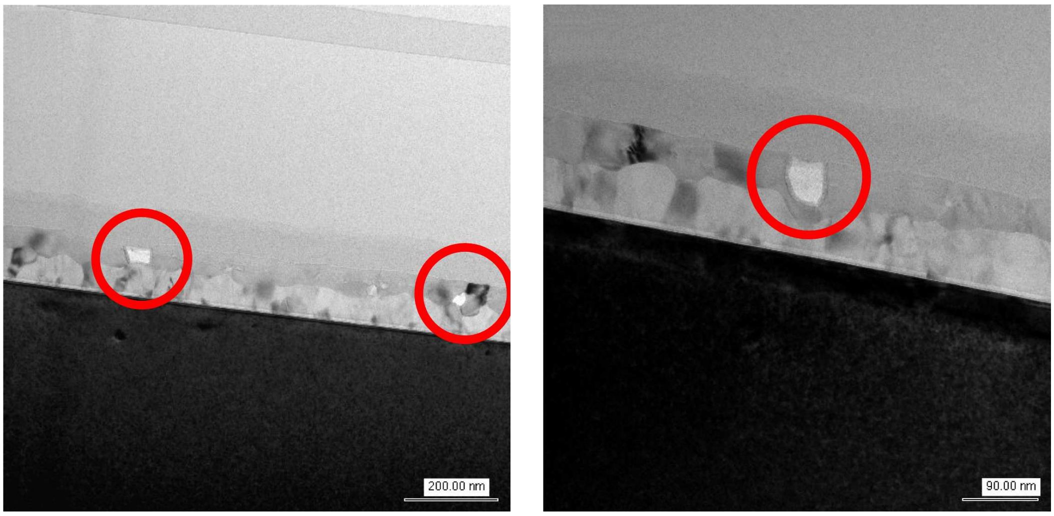

(a) $CoSi_2$ defects: overview.

(b) $CoSi_2$ defects: closeup.

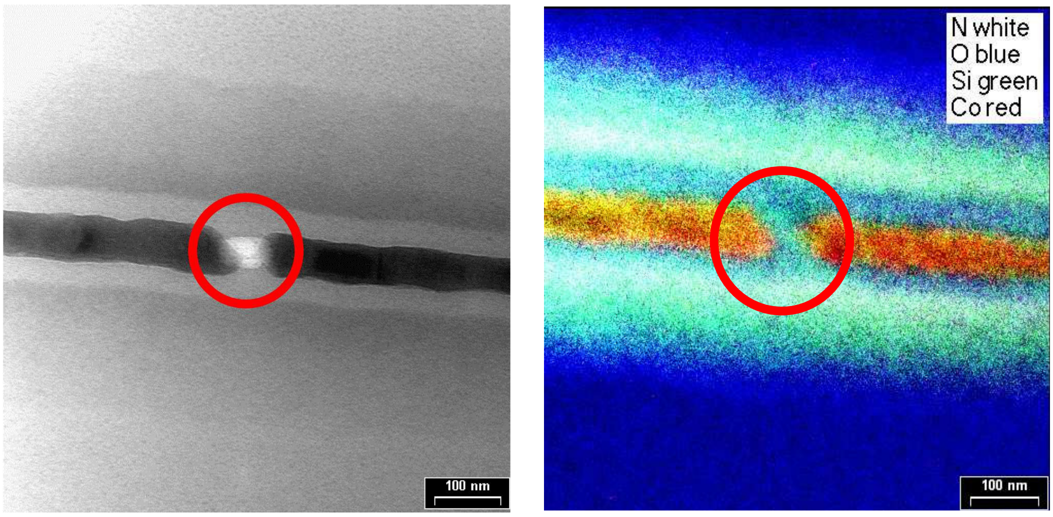

(c) $CoSi_2$ defects: top-down image.

(d) $CoSi_2$ defects: top-down image. False color energy-filtered TEM (EFTEM) image.

Fig. 1.5: $CoSi_2$ defects at a gate length of 60 nm.

1.2 Scope of work

Silicides are used in microprocessor manufacturing as a contact material, which has to be reliable even at small dimensions. To achieve this goal, two main requirements must be fulfilled. The first one is to form, and to maintain, a low-resistivity phase. This means, the formed silicides have to be uniform and continuous. Therefore, this thesis deals with the study of phase formation, i. e. the silicidation process, in nanoscale layers of either Co, Ni or Co-Ni on silicon substrates. These silicides are the presently used and potential future silicides in semiconductor manufacturing. Furthermore, it is necessary to clarify the phase formation sequence, i. e. the successive formation of phases within the binary (Co-Si, Ni-Si) and ternary (Co-Ni-Si) thin films. The impact of dopants, a capping layer, the alloying of Co with 5 at. % Ni, and substrate type on the formation temperatures and the thermal stability of the technologically relevant silicides is subject of this work.

The other requirement that needs to be fulfilled is to ensure that the silicidized areas, i. e. the active regions of the transistor and the polycrystalline Si gates, are uninterrupted. Therefore, agglomeration studies were performed. The impact of a capping layer, doping, and microstructure on the agglomeration of thin silicide films is also part of this work.

To achieve the above mentioned goals and to determine the influence of various parameters, different sets of samples were prepared. These sets exhibited different composition, i. e. Co on Si, Ni on Si, and Co-Ni on Si, different capping layers like Ti and TiN as well as different types of dopants. XRD techniques are applied for the phase analysis in unpatterned thin films. X-ray reflectivity (XRR) was used to characterize the original layer stack with respect to layer thicknesses, surface and interface roughnesses as well as layer densities. AES is utilized to determine spatial distribution of chemical elements in the low concentration range, where analytical TEM (energy-filtered TEM: EFTEM; electron energy-loss spectroscopy: EELS) is no longer applicable. TEM techniques are used to image layer structures as well as grain morphology. EFTEM and EELS are utilized to obtain elemental information of single grains. Additionally, convergent beam electron diffraction (CBED) is used to acquire diffraction patterns of regions in the range of a few nm. AFM and SEM, finally, provide data for the quantification of agglomeration effects.

Chapter 2

Silicide formation and growth: thermodynamics and kinetics

Under equilibrium conditions the stability of a phase at any given temperature, or the reactions of reactants, is defined by the respective thermodynamic properties. In principle it is possible to determine phase diagrams by means of thermodynamic calculations. The considerations described here are limited to conditions of constant pressure for a given temperature. The binary equilibrium phase diagrams of either Co-Si and Ni-Si (figures A.1 and A.2) predict which phase are present in a diffusion couple (supposed infinite supply of both elements) of the respective elements for a given temperature. The thermodynamic equilibrium for constant pressure and a specific temperature is given by the minimized free enthalpy G with

$$G = H - TS \qquad G = G_{min} \qquad (T, p = constant) \tag{2.1}$$

with H=enthaply, T=temperature, S=entropy, and p=pressure. Most important is the contribution of S, since equation 2.1 is dominated at higher temperatures by the term $-TS$. The enthalpy H corresponds to the binding enthalpies between adjacent atoms of the same kind. The following considerations assume a regular solid solution of the respective components. Within systems with more than one elemental component, S is given by the vibrational entropy S_v, which is neglected here[4], and S_m, the entropy of mixing. S_m is determined by the possible atomic arrangements of the different species

---

[4] S_v is in the range of Boltzmann's constant and is independent from the atomic arrangements of the different species of atoms, thus in solid solutions $S \approxeq S_m$.

of atoms present in the system. Analogously, H becomes H_m and G becomes G_m. For N atoms H_m is given by:

$$H_m = N_{AA} \cdot H_{AA} + N_{BB} \cdot H_{BB} + N_{AB} \cdot H_{AB} \tag{2.2}$$

H_m is dependent from the interchange energy[5], H_0, which can be gained ($H_0 > 0$) or is lost ($H_0 < 0$), when two A–B bonds are transferred into an A–A bond and a B–B bond. Since systems with more than one species of atoms are considered in this work, the terms G_m, H_m, and S_m are in general not used, they are referred to as G, H, and S, respectively. During supercooling or superheating (the calculations listed here are totally symmetrical with respect to temperature) the system tries to minimize its free enthalpy G. As is shown in figure 2.1, this can be achieved by compound formation.

However, deposited metal films on silicon are far from equilibrium when they are subjected to RTA conditions. This means, reaction time is short and supply of atoms is limited. Since compound formation is linked to diffusion of atoms as well as to nucleation, there are kinetic constraints, that decrease with increasing temperature. When the temperature is sufficiently high, in other words diffusion of atoms is fast enough, the system starts to lower its free energy by silicide formation. In principle, all phases of the equilibrium phase diagram can be expected. Nucleation problems or kinetic limits might prevent the formation of some phases. The extent to which a phase can grow is determined by the diffusion of atoms needed to form that phase. Therefore, growth of silicides is limited by diffusion. The first step of the silicidation process is the nucleation of a new phase, followed by grain growth. Both phenomena are briefly summarized hereafter.

2.1 Nucleation (basic principles)

The classical theory of nucleation was developed for liquid-to-solid transformations. Under specific conditions it can be applied to solid-phase transform-

---

[5] For N atoms with a coordination number z, and an atomic concentration $\mathcal{C}$ of B-atoms H_m is given by:

$$H_m = 1/2N \cdot z\left[(1-\mathcal{C})H_{AA} + \mathcal{C}H_{BB} + 2\mathcal{C}(1-\mathcal{C})H_0\right] \quad \text{with}$$
$$H_0 = H_{AB} - 1/2(H_{AA} + H_{BB})$$

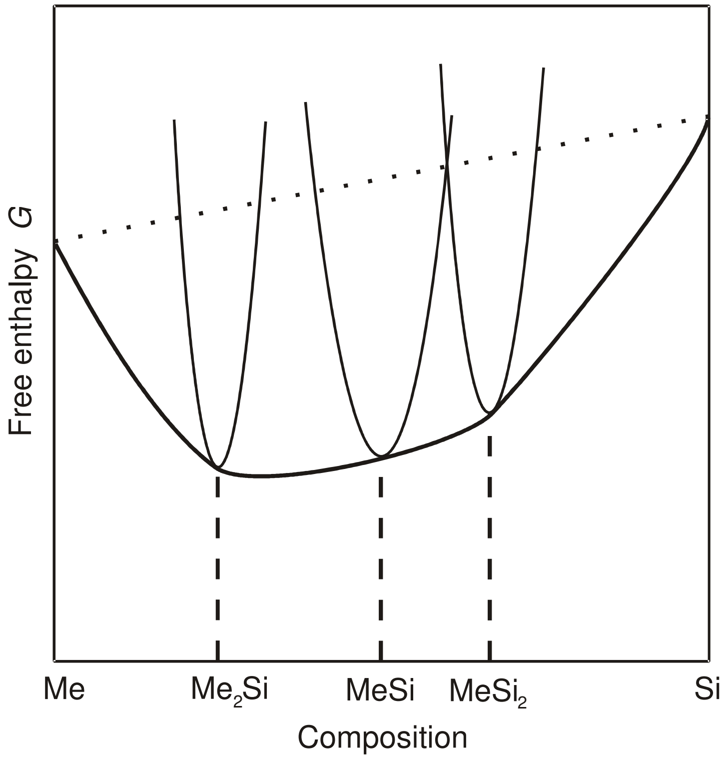

Fig. 2.1: Free enthalpy G (solid line) vs. composition of a diffusion couple. The formation of compounds is energetically favorable compared to a solid solution Me–Si (dotted line).

ations also. Nucleation theory starts at a point where equilibrium is reached, for example the melting point of a substance. The change of Gibb's free enthalpy ΔG is 0 at this equilibrium temperature T_e. Therefore from

$$\Delta G_e = \Delta H - T_e \Delta S \tag{2.3}$$

$$\Delta S = \Delta H / T_e \tag{2.4}$$

ΔS, the change in entropy is obtained, with ΔH, the change in enthalpy of the conversion. At T_e the driving force ΔG is 0 and the equilibrium conditions remain unchanged. At a temperature different from T_e the driving force to lower the free enthalpy, i. e. ΔG leads to nucleation. The higher ΔT, the difference from T_1 to T_e, the higher is the driving force. The formation of a nucleus goes along with an increase of surface/interfacial energy ς for this nucleus and a decrease of "volume" energy.

If ΔG is calculated per unit volume, at a temperature T_1, ΔG becomes

$$\Delta G = qr^2\varsigma - gr^3\Delta G_T \tag{2.5}$$

with q and g being geometrical terms[6], r the radius of the nucleus, and $\Delta G_T = \Delta G_e - \Delta G_{T_1}$. Crystalline nuclei are not spherical and g takes into account that the ratio of surface:volume of such nuclei is greater than that ratio for spheres. The shape of the nuclei is dependent on the surface energy ς also. An averaging factor q compensates for this. Figure 2.2 shows the relation of the free energy of a nucleus with its radius r. As can be seen from figure 2.2,

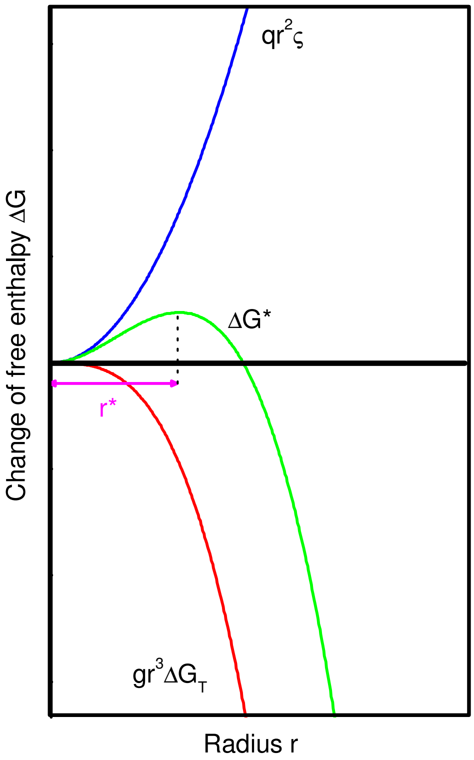

Fig. 2.2: Free energy of a nucleus as a function of it's radius, with r^* being the critical radius and ΔG^* the change in Gibb's free enthalpy of the critical nucleus. Positive surface contribution (blue curve), negative volume contribution (red curve) and their sum (green curve).

ΔG^*, the change on Gibb's free enthalpy of a critical nucleus, passes through

---

[6] For spherical nuclei q would be $4\ \pi$ and g would be $\frac{4}{3}\pi$.

a maximum at a critical radius r^*. Only nuclei with a radius r greater than r^* can grow. This critical radius and the corresponding maximum of ΔG^* indicate the minimal radius of a "stable" nucleus being able to grow any further. By derivation of equation 2.5 one gets

$$\frac{d(\Delta G)}{dr} = 2r\varsigma - 3r^2\Delta G \equiv 0 \tag{2.6}$$

and the critical radius r* is then given by:

$$r^* = \frac{2\varsigma}{3\Delta G_T} \tag{2.7}$$

This means, the higher ΔT is, the higher the driving force ΔG_T is and the smaller becomes r^*.
In a solid-state reaction where a reaction of two adjacent phases (A, B) takes place to form a phase AB there is no longer only one interface A/B. Instead there are two interfaces present: A/AB and AB/B. This leads to an increase of interface energy $\Delta\varsigma$. Two different competing effects must be taken into account. One is the gain of "volume" energy ΔG_V, the other is the loss of surface energy $\Delta\varsigma$ due to a newly formed interface. Since ΔG_V is $\propto r^3\Delta G_T$ and $\Delta\varsigma$ is $\propto r^2\varsigma$ the free energy of the nucleus becomes:

$$\Delta G_N(r) = qr^2\varsigma - gr^3\Delta G_T \tag{2.8}$$

As can also be seen in figure 2.5 ΔG_N exhibits a maximal value of ΔG^* at the critical radius r^*. To illustrate the dependencies of r^* and ΔG^*, the geometrical factors can be neglected[7] so that r^* can be written as:

$$r^* \propto \frac{\varsigma}{\Delta G_T} \tag{2.9}$$

and at a given temperature T, ΔG^* becomes:

$$\Delta G^* \propto \frac{\varsigma^3}{\Delta G_T^2} = \frac{\varsigma^3}{(\Delta H - T\Delta S)^2} \tag{2.10}$$

ΔG^* can be described as the activation energy for the nucleation of AB and from equation 2.10 it can be seen that nucleation is only important when ΔG_V (ΔG) is small compared to ς.

---

[7] Taking into account the geometrical factors g and q equation 2.10 would be:
$\Delta G^* = \frac{4q^3\varsigma^3T_e^2}{27g^2\Delta H^2(T_1-T_e)^2}$.

The rate of nucleation is also important to understand the phase formation processes. The nucleation rate ρ^* is proportional to the concentration of nuclei with r^* and the rate of formation of such nuclei and is given by:

$$\rho^* \propto exp(-\Delta G^*/kT)\ exp(-Q/kT) \tag{2.11}$$

with k Boltzmann's constant and Q, the activation energy for a site change of an atom, standing for the rearrangements of atoms needed to form the nucleus [9]. Using equation 2.10 ($\Delta G^* \propto 1/T^2$) and equation 2.11 ($\Delta G^* \propto 1/T$) it becomes clear that $\rho^* \propto exp(1/T^3)$. This is the reason why nucleation effects are only important in a very tight temperature regime. Below a specific temperature no nucleation takes place and slightly above a critical temperature, reactions are extremely fast. Since $\Delta G^* \propto \varsigma^3/\Delta G_T^2$ small changes in ΔG_T lead to big changes in ΔG^*, and therefore one can expect a nucleation-dominated reaction when the reaction is driven by small changes of free energy and a large increase in surface energy ς.

Nucleation can be divided into two different types. One is homogeneous nucleation, which takes place at perfect interfaces, e. g. at the interface liquid/single-crystal or at the interface of two single crystals. Heterogenous nucleation may take place at other interfaces than the initial interface between two phases. At these sites the initial interface energy $\varsigma_{initial}$ is higher compared with that for homogeneous nucleation and therefore $\Delta\varsigma$, the difference between ς_{final} and $\varsigma_{initial}$ is smaller:

$$\Delta\varsigma_{\ heterogenous\ n.} = \varsigma_{final} - \varsigma_{initial} < \Delta\varsigma_{\ homogeneous\ n.} = \varsigma_{final} - \varsigma_{initial} \tag{2.12}$$

This means that heterogenous nucleation is more likely to take place since the increase in surface energy is smaller when compared to homogeneous nucleation.

2.1.1 Entropy of mixing in the case of Co-Ni silicides

In the previous section the classical theory of nucleation was discussed. There, the influence of ΔS was not discussed in detail. Nucleation controlled reactions are characterized by small thermodynamic driving forces (or small changes in enthalpy ΔH) and therefore other effects might become more important. Recalling equation 2.10

$$\Delta G^* \propto \frac{\varsigma^3}{(\Delta G)_T^2} = \frac{\varsigma^3}{(\Delta H - T\Delta S)^2}$$

it is apparent that nucleation can only effect ΔG^* significantly if the difference of ΔH of the two phases is small as it is the case for the formation of $CoSi_2$ from CoSi (see table 3.3).
The impact of the entropy of mixing on silicide formation was first taken into account by d'Heurle [6], later also by others [49, 55] and recently studied in detail by Detavernier *et al.* [71–74]

The entropy of mixing for an ideal mixing within a solid solution, e. g. $Co_{1-x}Ni_x$, is given by [72, 73] :

$$S_m(x) = -R_g \; [x \; ln(x) + (1-x) \; ln(1-x)]/mol \tag{2.13}$$

with x representing the concentration of Ni in at. %, and R_g being the universal gas-constant $R_g = J/Kmol$. For the case that an element is completely insoluble in CoSi and totally soluble in $CoSi_2$, as is the case for Ni (see section 6.3), the reaction can be written as

$$(1-x) \; CoSi + xB + (1+x) \; Si \rightarrow Co_{1-x}B_xSi_2 \tag{2.14}$$

and $\Delta S = \Delta S_{final} - \Delta S_{initial}$ becomes:

$$\Delta S = \; -R_g \, [x \; ln(x) + (1-x) \; ln(1-x)] > 0 \tag{2.15}$$

Due to this positive change of ΔS, ΔG^* is lowered and thus the nucleation temperature is expected to be lowered, too. A lower nucleation temperature leads to a lower formation temperature for the various silicides.

2.2 Diffusion (basic principles)

The growth of metal-rich Co silicides is diffusion controlled [8]. The dominant diffusing species (DDS), i. e. the species of atoms which predominantly moves within the given material controls the interdiffusion process. In the case of the metal-rich silicides of Co and Ni, Co_2Si and Ni_2Si, respectively, the metal atoms are the DDS. For the CoSi phases the picture changes, here Si is the DDS, whereas for the NiSi, $NiSi_2$, and $CoSi_2$ again the metal atoms are the most mobile ones [4, 44, 75–77]. The diffusion of Si atoms within CoSi can be described by Si vacancy diffusion [76]. This is also important for the device manufacturing. NiSi, where Ni is the DDS, is less prone to be impacted by bridging compared to CoSi. Bridging is the effect that shorts may form between the poly-silicon gate and the active regions via the spacer, due to silicidation of metal deposited on the spacer. If, as it is true for the case of CoSi, Si is the DDS, then there is a Si supply to the spacer which leads to silicidation. In the case of Ni_2Si or NiSi, Si is less mobile, and bridging is less likely.

The transport of matter and vacancies within solids is a thermally induced process. The higher the temperature, the higher the probability for a site change. When the thermally induced vibrational energy is high enough, the atoms are able to leave their equilibrium potential and move to another site. The velocity of diffusion is described by the diffusion coefficient D. In principle diffusion can be formulated as

$$D = D_0 \cdot exp(-Q/kT) \tag{2.16}$$

with D_0 the frequency factor, Q the activation energy for diffusion, k being Boltzmann's constant as well as temperature T. Since diffusion in the solid state is considered here, different types of diffusion need to be treated. These are surface diffusion D_S, grain boundary diffusion D_G, and volume diffusionV_S. Equation 2.16 can therefore be written as:

$$D = D_S \cdot exp(-Q_S/kT) + D_G \cdot exp(-Q_G/kT) + D_V \cdot exp(-Q_V/kT) \tag{2.17}$$

with the indices representing the different types of diffusion. Q is decreasing in the shown order, i. e. $Q_V > Q_G > Q_S$, since the energy needed for surface diffusion is lower than the energy needed for grain boundary and volume diffusion, and volume diffusion is energetically least favorable. The activation energy needed for these types of diffusion was estimated to be [78–80]: $Q_V/Jmol^{-1} \approx 142\,T_m$, $Q_G/Jmol^{-1} \approx 71\,T_m$, $Q_S/Jmol^{-1} \approx 54\,T_m$ for face centered cubic (fcc) metals. For the silicidation process, surface diffusion usually can be neglected because free surfaces normally do not occur within thin films, i. e. unpatterned samples, diffusion relevant for silicidation depends on grain boundary and volume diffusion. With increasing grain size due to grain growth at higher temperatures, the interface fraction decreases, thus leading to a more pronounced bulk diffusion, especially in polycrystalline materials. Therefore, volume diffusion becomes more and more important with increasing temperature.

After nucleation has taken place (see section 2.1), phase growth happens, which in many cases is diffusion-controlled, i. e. determined by the diffusion of the atoms through the reactant to the reaction front which leads to a parabolic growth rate $(\Delta t_l)^2 \propto \mathrm{t}$ [81, 82].

2.3 Growth kinetics

In nanoscale films, the growth kinetics are quite different from bulk samples, where the supply of all reactants is quasi-infinite. In bulk reactions one would expect the formation of all equilibria phases with the metal-rich phases being formed at the metal side and the silicon-rich phases at the Si side under the condition of infinity time and not exceeding the melting- or decomposition temperature of one of the phases. For the case of thin film reactions this is not true, moreover, it is more often the case that only one phase is formed [7]. The formation of the other equilibrium phases is inhibited due to their kinetic instability. Gösele and Tu [7] gave a detailed description of thin film growth and kinetics. They took diffusion aspects into consideration, the existence of a possible reaction barrier as well as the rearrangement of atoms to form new phases. That model, was simplified for the case of silicidation reactions by Maex [9] and is presented hereafter.

For a system of a metal (Me) and Si with two intermediate compounds MeSi$_{\alpha_S}$ and MeSi$_{\beta_S}$ with $\alpha_S < \beta_S$, and α_S as well as β_S being the stoichiometric indices, the change of layer thickness t$_l$ with time (t) is as follows:

$$\frac{dt_{l\alpha_S}}{dt} = G_{\alpha_S} j^{Si}_{\alpha_S} - G_{\alpha_S\beta_S} j^{Si}_{\beta_S} \tag{2.18}$$

$$\frac{dt_{l\beta_S}}{dt} = G_{\beta_S} j^{Si}_{\beta_S} - G_{\beta_S\alpha_S} j^{Si}_{\alpha_S} \tag{2.19}$$

G_{α_S}, G_{β_S}, $G_{\alpha_S\beta_S}$ and $G_{\beta_S\alpha_S}$ are weight coefficients and reflect the change of composition at the interfaces. The diffusion fluxes j of Si within the two compounds MeSi$_{\alpha_S}$ and MeSi$_{\beta_S}$ are independent from each other and can be described as

$$j^{Si}_{\alpha_S} = \frac{\Delta \mathcal{C}^{eq}_{\alpha_S} k^{eff}_{\alpha_S}}{\left(1 + \frac{t_{l\alpha_S} k^{eff}_{\alpha_S}}{D_{\alpha_S}}\right)} \tag{2.20}$$

$$j^{Si}_{\beta_S} = \frac{\Delta \mathcal{C}^{eq}_{\beta_S} k^{eff}_{\beta_S}}{\left(1 + \frac{t_{l\beta_S} k^{eff}_{\beta_S}}{D_{\beta_S}}\right)} \tag{2.21}$$

with $\Delta \mathcal{C}^{eq}$ as the difference between the actual concentration and the equilibrium concentration at the interfaces. D_{α_S} and D_{β_S} are the chemical inter diffusion coefficients and with the use of the elemental diffusion coefficients they are given by:

$$D_{\alpha_S} = \frac{D^{Si}_{\alpha_S}}{\alpha_S + 1} + \frac{\alpha_S D^{Me}_{\alpha_S}}{\alpha_S + 1} \tag{2.22}$$

$$D_{\beta_S} = \frac{D^{Si}_{\beta_S}}{\beta_S + 1} + \frac{\beta_S D^{Me}_{\beta_S}}{\beta_S + 1} \tag{2.23}$$

with Me=Ni or Co in this work. The coefficients k_{α_S}, k_{β_S}, $k_{\alpha_S\beta_S}$ and $k_{\beta_S\alpha_S}$ determine the reaction rates at the interfaces. If supposedly a reaction barrier exists against the growth of layer MeSi$_{\alpha_S}$ on the expense of layer MeSi$_{\beta_S}$ this is described by $k_{\alpha_S\beta_S}$. k^{eff} is the effective barrier at a certain interface:

$$\frac{1}{k^{eff}_{\alpha_S}} = \frac{1}{k_{\alpha_S}} + \frac{1}{k_{\alpha_S\beta_S}} \tag{2.24}$$

$$\frac{1}{k^{eff}_{\beta_S}} = \frac{1}{k_{\beta_S\alpha_S}} + \frac{1}{k_{\beta_S}} \tag{2.25}$$

The growth $dt_{l\alpha_S}/dt > 0$ (or shrinking $dt_{l\alpha_S}/dti < 0$) behavior of a layer depends on the ratio τ between the fluxes $j^{Si}_{\alpha_S}/j^{Si}_{\beta_S}$. τ_1 is the case where no change in thickness of MeSi$_{\alpha_S}$ over time occurs, i. e. $dt_{l\alpha_S}/dt = 0$ and is given by $G_{\alpha_S\beta_S}/G_{\alpha_S}$. For example, if $\tau{>}\tau_1$, then MeSi$_{\alpha_S}$ will grow and if $\tau{<}\tau_1$ the MeSi$_{\alpha_S}$ layer will shrink. Analogously, the growth of MeSi$_{\beta_S}$ can be described by τ_2. τ_1 and τ_2 are determined solely by the composition of the compounds. As long as τ is not between τ_1 and τ_2, one layer will grow while the other layer will shrink.

The most important cases for silicide growth are:

1. The formation of both silicides MeSi$_{\alpha_S}$ and MeSi$_{\beta_S}$ is diffusion-controlled[8] ($k_{\text{coefficient}} \rightarrow \infty$), then τ can be simplified[9] to

   $$\tau = \frac{\Delta\mathcal{C}^{eq}_{\alpha_S} D_{\alpha_S}}{\Delta\mathcal{C}^{eq}_{\beta_S} D_{\beta_S}} \frac{t_{l\beta_S}}{t_{l\alpha_S}} \tag{2.26}$$

   The ratio r depends on $t_{l\alpha_S}$ and $t_{l\beta_S}$ at t=0 and changes over time. With an ongoing reaction τ will always get a value of $\tau_1{>}\tau{>}\tau_2$ and both layers will grow.

---

[8] Meaning the reactions are determined by the supply of atoms to the reaction front, i. e. by the diffusion of the reactants.

[9] τ can be written as $\tau = \frac{\Delta\mathcal{C}^{eq}_{\alpha_S} D_{\alpha_S}(D_{\beta_S}+t_{\beta_S}k^{eff}_{\beta_S})}{(D_{\alpha_S}+t_{l\alpha_S}k^{eff}_{\alpha_S})\Delta\mathcal{C}^{eq}_{\beta_S} D_{\beta_S}} = \frac{\Delta\mathcal{C}^{eq}_{\alpha_S} D_{\alpha_S}}{(D_{\alpha_S}+t_{\alpha_S}k^{eff}_{\alpha_S})\Delta\mathcal{C}^{eq}_{\beta_S}} + \frac{\Delta\mathcal{C}^{eq}_{\alpha_S} D_{\alpha_S} t_{l\beta_S} k^{eff}_{\beta_S}}{(D_{\alpha_S}+t_{l\alpha_S}k^{eff}_{\alpha_S})\Delta\mathcal{C}^{eq}_{\beta_S} D_{\beta_S}}$ and for $k^{eff}_{\alpha_S}, k^{eff}_{\beta_S} \rightarrow \infty$ $\tau = \lim_{k^{eff}_{\alpha_S}, k^{eff}_{\beta_S} \rightarrow \infty} \left(\frac{\Delta\mathcal{C}^{eq}_{\alpha_S} D_{\alpha_S}}{(D_{\alpha_S}+t_{l\alpha_S}k^{eff}_{\alpha_S})\Delta\mathcal{C}^{eq}_{\beta_S}} + \frac{\Delta\mathcal{C}^{eq}_{\alpha_S} D_{\alpha_S} t_{l\beta_S} k^{eff}_{\beta_S}}{(D_{\alpha_S}+t_{l\alpha_S}k^{eff}_{\alpha_S})\Delta\mathcal{C}^{eq}_{\beta_S} D_{\beta_S}} \right) = \frac{\Delta\mathcal{C}^{eq}_{\alpha_S} D_{\alpha_S} t_{l\beta_S}}{t_{l\alpha_S}\Delta\mathcal{C}^{eq}_{\beta_S} D_{\beta_S}}$

2. The formation of both silicides MeSi$_{\alpha_S}$ and MeSi$_{\beta_S}$ is rate-controlled[10] then τ can be written as

$$\tau = \frac{\Delta\mathcal{C}^{eq}_{\alpha_S} k^{eff}_{\alpha_S}}{\Delta\mathcal{C}^{eq}_{\beta_S} k^{eff}_{\beta_S}} \tag{2.27}$$

3. If one of the layers starts to grow, for example MeSi$_{\beta_S}$, then the following case is valid if the formation of MeSi$_{\alpha_S}$ is diffusion controlled and the growth of MeSi$_{\beta_S}$ is rate-controlled and τ becomes:

$$\tau = \frac{\Delta\mathcal{C}^{eq}_{\alpha_S} k^{eff}_{\alpha_S}}{\Delta\mathcal{C}^{eq}_{\beta_S} D_{\beta_S}} t_{l\beta_S} \tag{2.28}$$

In the latter case τ is proportional to $t_{l\beta_S}$, the thickness of the layer MeSi$_{\beta_S}$. If $\tau > \tau_1$ and $\tau > \tau_2$ then both layers will coexist. For small values of τ ($\tau < \tau_1$), MeSi$_{\alpha_S}$ shrinks while MeSi$_{\beta_S}$ grows. In this case MeSi$_{\alpha_S}$ cannot coexist with MeSi$_{\beta_S}$ and MeSi$_{\alpha_S}$ and will vanish. Since τ depends on $t_{l\beta_S}$ and $\tau < \tau_1$ must be maintained, there is a critical thickness of $t_{l\beta_S}$:

$$t_l^{crit}{}_{\beta_S} = \frac{\tau_1 \Delta\mathcal{C}^{eq}_{\beta_S} D_{\beta_S}}{\Delta\mathcal{C}^{eq}_{\alpha_S} k^{eff}_{\alpha_S}} \tag{2.29}$$

When $t_{l\beta_S}$ becomes greater then $t_{l\beta_S}^{crit}$ the MeSi$_{\alpha_S}$ layer can also grow. The critical thickness for a Ni$_2$Si layer was roughly estimated to $t_l{}^{crit} \approx 2\,\mu$m [7]. In this model, the phase which is formed first depends on the material supply and it explains the phase formation sequence by kinetic arguments, such as diffusion- or rate-controlled growth of layers as well as possible reaction barriers due to atomic site changes. Sometimes the nucleation of different phases is possible, but the growth kinetics prevent the formation, i. e. growth of such phases. The first phase that is formed is the phase with the lowest effective reaction barrier at the interfaces and cannot be predicted from the binary equilibria phase diagrams.

---

[10] Meaning the reactions are determined by the reaction rate, i. e. by the velocity of the reactions.

Chapter 3

Silicides - structure and properties

In this work, Co, Ni, and Co-Ni silicides are investigated. The disilicides of Co and Ni, $CoSi_2$ and $NiSi_2$, respectively, are conductors with cubic CaF_2 structure (see figures 3.1 and 3.2). Both exhibit high melting points (see table 3.3) and can be formed by solid-state reactions during RTA processing. Young's moduli of 132 GPa for NiSi [83] and 140–160 GPa for $CoSi_2$ are reported [84, 85]. Table 3.1 lists the properties of the "ideal" silicide.

3.1 Crystal structures

The crystal structures of the metal-rich silicides of Co and especially Ni, show a relatively low crystallographic symmetry compared to the mono- and disilicides. Co_2Si and Ni_2Si crystalize in the same orthorhombic space group. The monosilicides of either Co or Ni exhibit different crystal structures. The CoSi structure is, in general, that of the cubic FeSi prototype. Migli *et al.* predicted a defective CsCl-like structure for CoSi by means of theoretical calculations of electronic properties in conjunction with the crystal structure. CoSi showing this crystal structure is metastable and could be synthesized by von Känel *et al.* [86]. NiSi, in contrast to CoSi, is of the orthorhombic MnP structure type. The disilicides of Co and Ni have in common that they show high crystallographic symmetry, especially the thermodynamically stable di-

Table 3.1: Properties of the ”ideal” silicide

- Low resistivity
- Low silicon consumption
- Low sheet resistance
- Low contact resistance
- Low stress within layer
- Low formation temperature
- Low surface roughness
- Low junction penetration
- Low affinity to bridging[†]

- High chemical stability
- High thermal stability
- High mechanical strength
- High adhesion
- High electromigration resistance

- No contamination of devices, wafers, and tools
- SALICIDE process

[†] Bridging is the effect that shorts are formed between the polycrystalline Si gate and the active regions via the spacer, i. e. a conductive path is formed, for example, through silicidation.

silicides, i. e. CoSi$_2$ and α-NiSi$_2$[11], have a crystal structure which is very close to that of Si. They are related in such a way, that within the silicon structure only half of the tetrahedral sites of the cubic closed package (ccp) are occupied, whereas within the disilicide structure all tetrahedral sites are occupied with Co or Ni, respectively. There is at least one more (metastable) CoSi$_2$ structure [87–89]. Tu proposed a diffusion mechanism of Ni in Si, where Si occupies all of the interstitial positions within the Diamond-type sub-lattice, whereas Ni occupies all the vacant tetrahedral positions [90]. The metal atoms are surrounded by 10 Si atoms which form an Adamantan-like structure type [91]. This kind of structure type for CoSi$_2$, formed as an intermediate phase at temperatures of about 500 °C from metallic double layers, was found by Rangelov *et al.* and Zhang *et al.* [92, 93]. Especially on (111) Si, CoSi$_2$ can be formed with a similar CsCl defective structure as CoSi with this defective CsCl structure [86] by molecular beam epitaxy (MBE). Detailed work on synthesis and properties of this phase was done by Concalves-Conto *et al.* [87–89].

---

[11] The α form is the well known NiSi$_2$ phase. Very few reports name the β-NiSi$_2$ phase which is formed at 983 °C through a polymorphic transition. Hereafter, the usage of NiSi$_2$ refers to the α-NiSi$_2$ phase only. The same is true for the metastable phases β-Co$_2$Si and δ-Ni$_2$Si. They are referred to as Co$_2$Si and Ni$_2$Si, respectively.

Figure 3.1 and 3.2 give visualizations of the technologically most important Co and Ni silicide structures, respectively. The thermodynamical stable high temperature silicide phases, i. e. the disilicides (phase formation sequence see section 6.2), exhibited lattice constants which are very close to that of Si, with a marginal deviation at room temperature (RT) of -1.2 % for $CoSi_2$ and -0.4 % for $NiSi_2$. Table 3.2 lists crystallographic data of Si as well as of Co and Ni silicides.

Table 3.2: Crystallographic data of silicon and silicides

Phase	Space group Prototype	Crystal system	Lattice constants [Å]	Cell volume [Å]^3	Lattice mismatch to Si at RT $\Delta a = \frac{a_{sil.}-a_{Si}}{a_{Si}}$
Si $^{a)}$	227 Diamond	cubic	a = 5.4309	160.18	
α-Co_2Si $^{b)}$	62 Co_2Si	orthorhombic	a = 3.9920 b = 3.6500 c = 6.0910	88.75	
CoSi $^{c)}$	198 FeSi	cubic	a = 4.4463	87.90	
$CoSi_2$ $^{d)}$	225 CaF_2	cubic	a = 5.3640	154.34	-1.2 %
δ-Ni_2Si $^{e)}$	62 Co_2Si	orthorhombic	a = 7.0664 b = 5.0088 c = 3.7321	132.09	
NiSi $^{f)}$	62 MnP	orthorhombic	a = 5.2330 b = 3.2580 c = 5.6590	96.48	
α-$NiSi_2$ $^{g)}$	225 CaF_2	cubic	a = 5.4160	158.87	-0.4 %

Source: JCPDS* numbers [94]: a) 27-1402, c) 50-1337, d) 38-1449, e) 48-1339, f) 38-844, g) 43-989
b) Naval Research Laboratory Center for Computational Materials Science [95]
* Joint Committee of Powder Diffraction Standards

3.2 Physical properties

There are certain demands for materials used in semiconductor manufacturing with respect to manufacturability, reliability, costs as well as environmental, health, and safety aspects. Furthermore the "ideal" silicide should have specific material's properties and should also meet several technological aspects. The most important requirements are summarized in table 3.1. Ti and Co phases match these requirements as to the present knowledge best and, therefore, they are the most commonly used silicides. Ni monosilicide has some

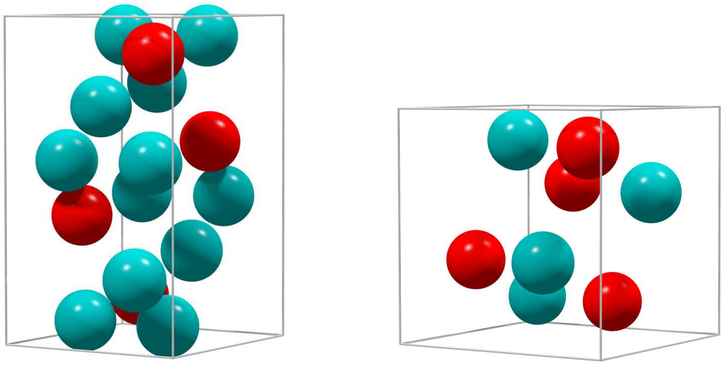

(a) Co_2Si, orthorhombic.

(b) CoSi, cubic.

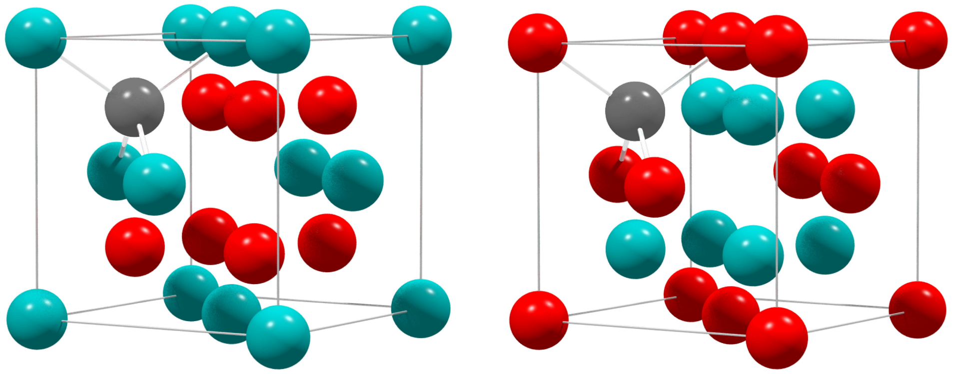

(c) $CoSi_2$, cubic. Tetrahedral site indicated by grey shade.

(d) $CoSi_2$, cubic. Different origin of cell. Tetrahedral site indicated by grey shade.

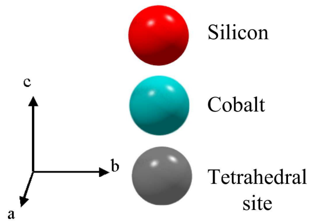

(e) All structures orientated as indicated by the lattice vectors. Tetrahedral site indicated by grey shade.

Fig. 3.1: Crystal structures of Co silicides.

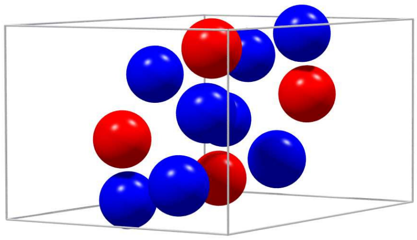

(a) Ni_2Si, orthorhombic.

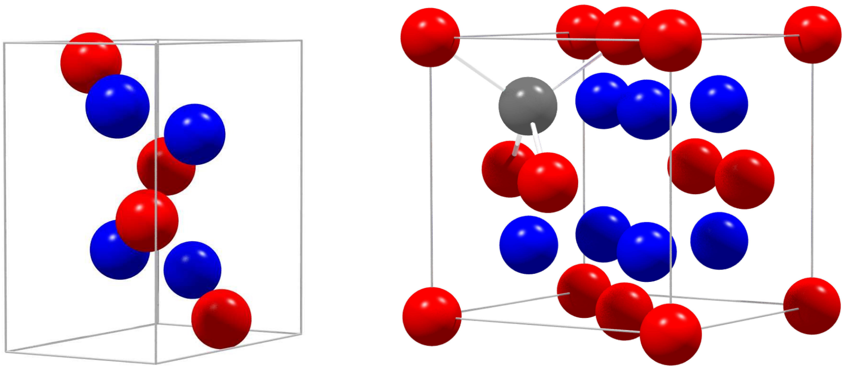

(b) NiSi, orthorhombic.

(c) $NiSi_2$, cubic. Tetrahedral site indicated by grey shade.

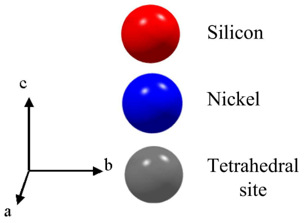

(d) All structures orientated as indicated by the lattice vectors. Tetrahedral site indicated by grey shade.

Fig. 3.2: Crystal structures of Ni silicides.

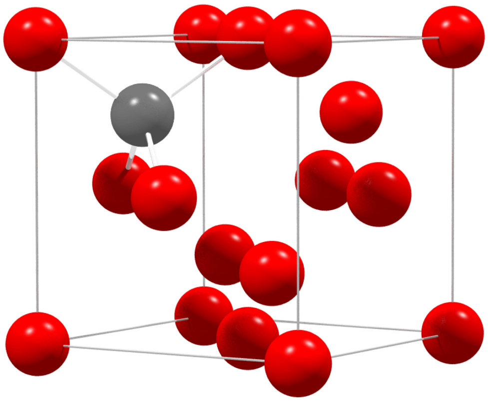

(a) Si, cubic. Tetrahedral site indicated by grey shade.

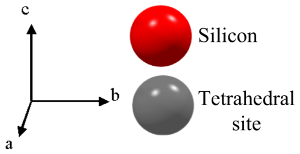

(b) Structure orientated as indicated by the lattice vectors. Tetrahedral site indicated by grey shade.

Fig. 3.3: Crystal structure of Si.

promising material's properties, but due to process integration problems, it was not utilized in mass production until recently. These problems include limited thermal stability, since NiSi is not the thermodynamic stable silicide phase at high temperatures. Furthermore, in the case of a Si excess, which virtually is always the case, NiSi is prone to transform into $NiSi_2$ at higher temperatures. Table 3.3 shows some physical data of Ti, Co, and Ni silicides. Table 3.4 summarizes diffusion data of Co, Ni, and Si as well as the DDS.

Table 3.3: Physical properties of silicides

Silicide	ΔH_F^0 [kJ/mol]	Density ρ [g/cm^3]	Resistivity [$\mu\Omega$cm]	Melting point [°C]
$TiSi_2$ C49†	-134.3	3.85	60–90	1500
$TiSi_2$ C54†		4.07	12–15	1460
α-Co_2Si	-115.5	7.42	110	1320–1334
CoSi	-100.4	6.59	147–180	1460
$CoSi_2$	-102.9	4.95	15	1326
δ-Ni_2Si	-140.6	7.07	18–25	1255–1318
NiSi	-84.83	5.86	8–10.5	992
α-$NiSi_2$	-86.67	4.86	34	981–993
Source:	[71, 96, 97]	[4, 94]	[4, 13, 20, 26, 98]	[99–101]

†: The silicidation of Ti is a two-step process: First a high resistivity C49 phase is formed, which is converted to the C54 phase by means of thermal treatment [20].

Table 3.4: Diffusion data of Co, Ni, and Si in Si and in silicides

Diffusant	Matrix	D_V [cm^2/sec]	E_a [eV]	DDS	Source
Co	Si	$9.2 \cdot 10^{-4}$	2.8	Co	[2]
Ni	Si	$2.0 \cdot 10^{-3}$	0.47	Ni	[2]
Co	Co_2Si		1.5–1.78	Co	[4]
Co	CoSi		1.75–1.9	Co	[4]
Co	$CoSi_2$		2.3	Co	[4]
Ni	Ni_2Si	$2.0\ 10^{-2}$	1.4	-	[102]
Ni	NiSi		1.2–1.8	Ni	[4]
Ni	$NiSi_2$		1.65	Ni	[4]
Si	Ni_2Si	$2.0\ 10^{-2}$	1.4	-	[102]

3.3 Silicon consumption

Silicon consumption is the amount of Si needed to achieve a desired level of sheet or contact resistance on the polycrystalline silicon gate or on the active regions. Since the sheet resistance R_s[12] is dependent on the layer thickness, a desired silicide thickness is needed to obtain suitable resistances. Figure 3.4 illustrates the relationship between sheet resistance and silicide layer thickness.

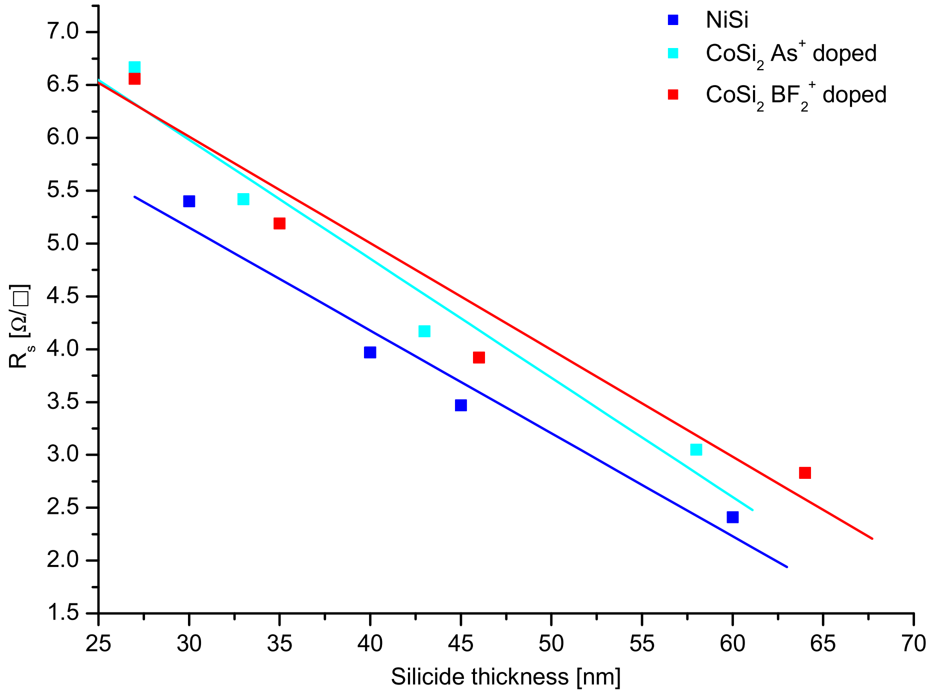

Fig. 3.4: Sheet resistance of NiSi and doped $CoSi_2$ (As^+ and BF_2^+ doped) as a function of silicide thickness. Data taken from literature [103].

---

[12] Sheet Resistance R_s is the resistance of a layer, that is measured by a four point probe. The resistance represents the parallel resistance of an infinite number of infinitely thin parallel sheets. Sheet resistance is expressed as ohms per square (area) and is equal to the average resistivity of a layer multiplied by the thickness of the layer.

Generally, monosilicides with a ratio of Metal (Me):Si=1:1 have an inherent advantage over disilicides with Me:Si=1:2 because the resulting silicide layer thickness is always smaller, i. e. the monosilicides do not grow as deep into the silicon substrate as the disilicides. This is primarily important on the active regions of the transistor, where a deep penetration of the source/drain region alters the transistor properties, i. e. the transistor performance, since the resistivity of the silicides is significantly higher than that of the here heavily doped silicon substrate. A way to overcome these problems is to use elevated source/drains (ESD) [61], and recently the introduction of selective epi growth (SEG) [34, 104, 105].

Table 3.5 summarizes the Si consumption for commonly used silicides. There, the resulting silicide layer thickness is listed in relation to the deposited metal layer thickness t_M, i. e. a metal layer thickness of 100 Å leads to a silicide thickness of 198 Å in the case of CoSi. Besides the overall resulting silicide layer thickness, also the position of the obtained silicide layer relative to the former silicon surface is of importance for the transistor properties. Figure 3.5 compares Co to Ni silicides with respect to the volumetric changes during silicidation as well as the resulting position relative to the original silicon surface.

Table 3.5: Silicon consumption of silicides

Silicide	Normalized Si consumption in terms of $[t_m]^\dagger$	Normalized silicide thickness t_s in terms of $[t_m]^\dagger$
$TiSi_2$ C49	2.22	2.33
$TiSi_2$ C54	2.22	2.44
α-Co_2Si	1.47	1.47
CoSi	1.98	1.98
$CoSi_2$	3.49	3.49
δ-Ni_2Si	0.91	1.49
NiSi	1.83	2.01
α-$NiSi_2$	3.66	3.59
Source:	[4]	[4]

†: Metal thickness t_m is defined to be 1. Thickness in units of t_m.

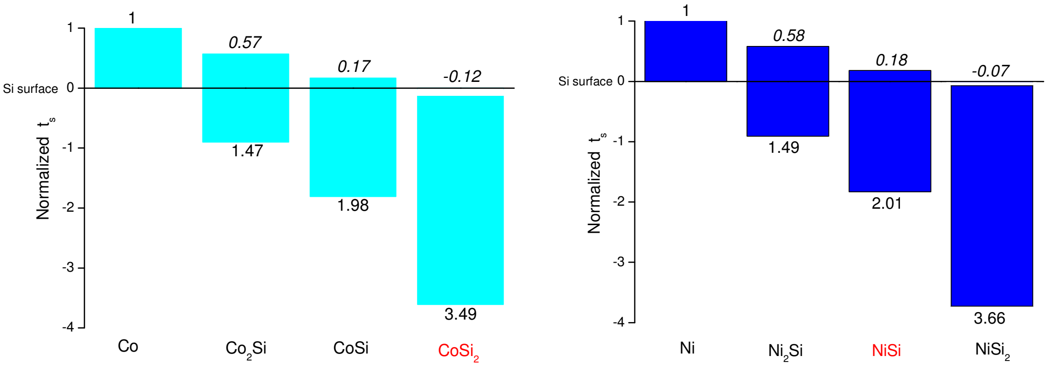

(a) Co: target phase $CoSi_2$. (b) Ni: target phase NiSi.

Fig. 3.5: Volumetric change during silicidation and silicide position after silicidation. Modified after Maex [106].

Chapter 4

Structure analysis of silicides

4.1 X-ray diffraction

XRD is an analytical technique which uses the elastic scattering of X-rays[13] at the inner electron shell of the atoms of condensed matter. It provides the distances between sets of crystallographic lattice planes, the so called *d*-spacing, occupied in regular distances by the atoms, within crystalline materials. It is a nondestructive technique with high accuracy and precision [107]. Usually large areas in the order of several mm^2 are illuminated by the X-rays. Since the number of scattering centers that contribute to the analyzed signal is in the range of 10^{25}, the data statistics is very good. When Bragg's Law is fulfilled, constructive interference happens and intensity maxima in the diffraction pattern occur. Using polychromatic radiation, Laue images can be obtained since many different sets of lattice planes simultaneously contribute to the diffraction pattern [107]. With monochromatic radiation, it is possible to determine the *d*-spacings using equation 4.1 by evaluating the diffraction pattern.

$$n \cdot \lambda = 2d \cdot sin\ \vartheta \tag{4.1}$$

with n=an integer describing the order of diffraction, λ=wavelength of the primary beam, d=the distance between two lattice planes of the same crystallographic orientation, the so-called d-spacing, and ϑ=the Bragg or glancing angle, the angle between the incident (primary) beam and the lattice planes.

---

[13] Wavelength λ between 0.1 Å (10^{-11} m) and 10 Å (10^{-8} m), i. e. 124 keV and 1.24 keV, respectively.

This diffraction pattern is characteristic for all crystalline materials. By means of comparing unknown diffraction patterns with a set of already identified patterns [94] it is possible to identify crystalline fractions within a sample. Having a set of d-values it is possible to calculate the atomic positions within the unit cell of a given substance taking into account the crystallographic symmetry. Other information contained in a diffraction pattern are grain size, mosaicity and lattice distortions as well as strain within samples [108]. The most commonly used geometry to collect diffraction patterns is the Bragg-Brentano geometry [109]. In this focusing geometry, only the lattice planes parallel to the sample surface can be measured. Since the penetration depth is always in the range of several μm this technique is not suitable for ultra-thin film analysis, having to maintain reasonable measuring times. For analysis of thin and ultra-thin[14] layers, a grazing-incidence X-ray diffraction geometry (GIXRD) is used (figure 4.1). In this case, the primary beam is fixed to a low angle of incidence, near the critical angle of total reflection, α_i and only the detector is moving. In polycrystalline, randomly orientated materials, all lattice planes except those being parallel to the sample come into diffraction condition and generate intensity maxima. Highly textured, or even single crystal

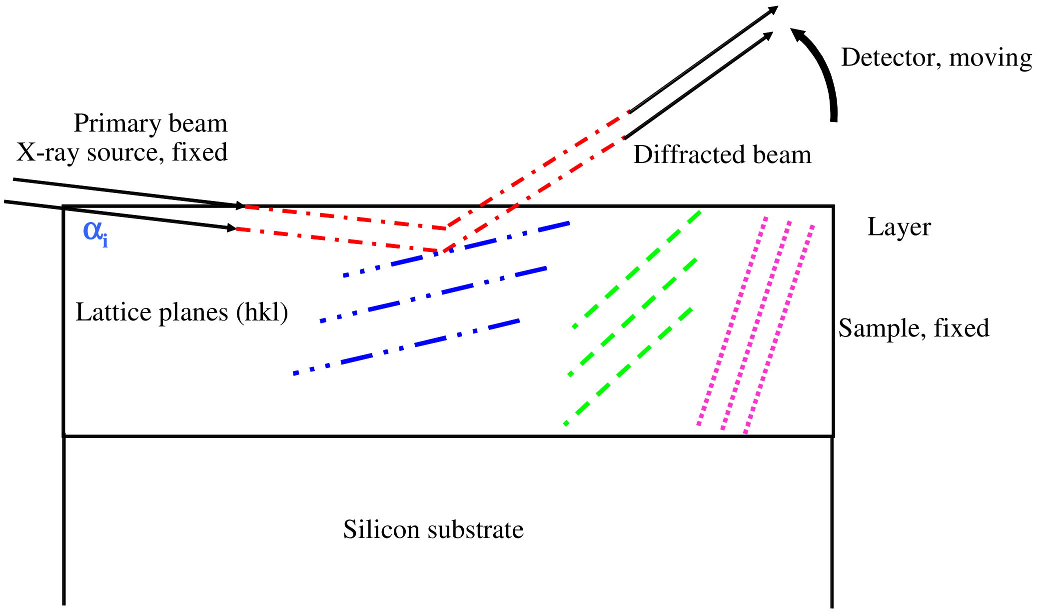

Fig. 4.1: Grazing Incidence XRD set up (schematic view).

---

[14] Layer thickness in the range of 10s–100s of Å.

materials might show a distinct diffraction pattern if the are (by chance) properly aligned. Rotation of the samples would lead to usable diffraction patterns in any way. Figure 4.1 displays this kind of setup.

With this setup, the path of the X-ray beam within the top layer is maximized, and therefore the number of scattering centers of the top layers is maximized, too. This leads to a promotion of the information obtained from the top area of the sample compared to the information acquired from the substrate.
The penetration depth can be calculated using equation 4.2 and depends on the used wavelength, the density ρ of the top layer, and the angle of incidence α_i [110]. Table 4.1 gives an overview about the penetration depth for several top layers under the assumption that a useful signal can only be detected when less than 99 % of the primary beam intensity is absorbed within the sample. The critical angle α_c is determined by the density of the top layer.

Table 4.1: Penetration depth t_d for different top layers

Layer	Critical angle α_c [°]	Penetration depth t_d for $\alpha_i = 0.5°$ [nm]	Max. depth of information t_i for $\alpha_i = 0.5°$ [nm]†
Si	0.237	27.27	22.3
Co	0.443	19.83	8.91
Ni	0.452	17.03	15.34
Co_2Si	0.475	8.29	4.48
CoSi	0.453	8.67	5.28
$CoSi_2$	0.475	9.27	7.51
Ni_2Si	0.482	7.83	4.44
NiSi	0.459	8.23	5.63
$NiSi_2$	0.423	8.86	6.56
TiN	0.289	5.36	5.07
Ti	0.316	4.2	3.74
Values calculated for λ=1.648 Å			
†: t_i calculated for the assumption that a signal can still be detected when 99 % of the primary beam intensity was absorbed within the sample. Azimuthal position of the detector assumed.			

Whenever the angle of incidence α_i is smaller than α_c, than total reflection will occur. The penetration depth t_d is given by

$$t_d \approx \begin{cases} \frac{\lambda}{2\pi(\alpha_c^2-\alpha_i^2)} & \text{for } \alpha_i < \alpha_c \\ \frac{2\alpha_i}{\mu} & \text{for } \alpha_i > \alpha_c \end{cases} \tag{4.2}$$

with t_d being the depth at which the original primary beam intensity was decreased to e^{-1} and μ the absorption coefficient [110][15]. Figure 4.2 and table 4.1 demonstrate the penetration depth t_d for different top layers, calculated for a wavelength of λ=1.648 Å. This wavelength ensures minimal fluorescence radiation (see figure 4.3).

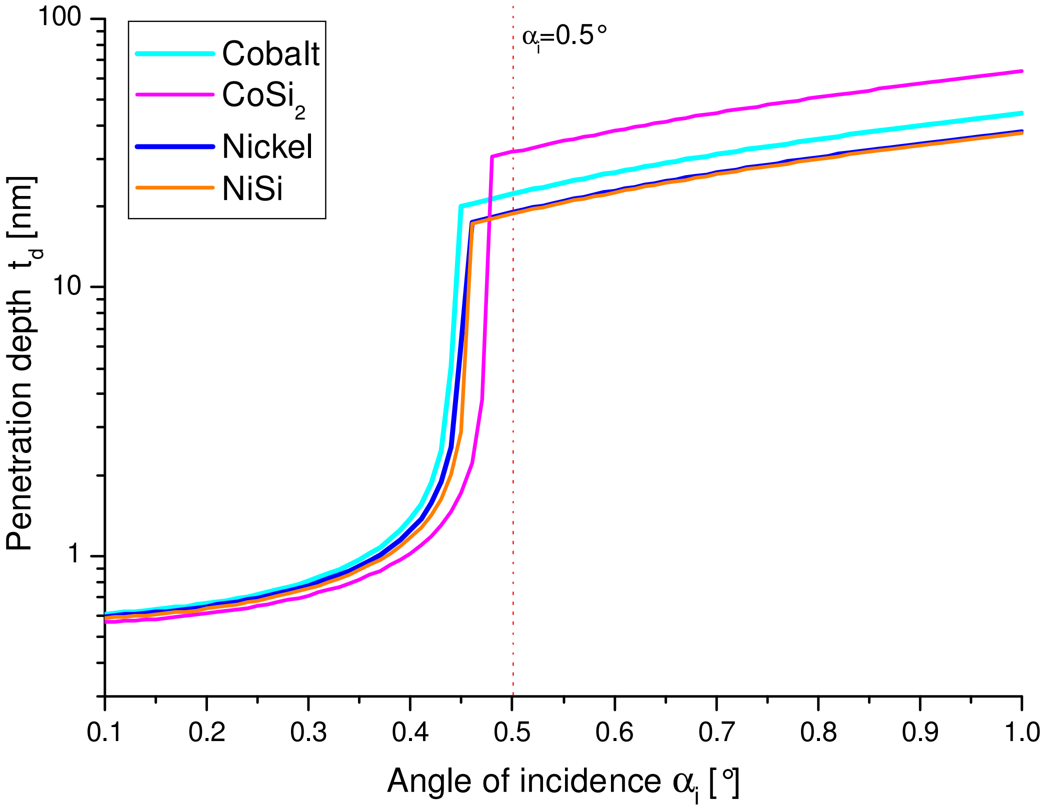

Fig. 4.2: X-ray penetration depth t_d [nm] for Co, Ni, $CoSi_2$, and NiSi vs. angle of incidence α_i for λ=1.648 Å.

---

[15] For synchrotron radiation this is not true, since the primary beam intensity is several orders of magnitude higher compared to conventional X-ray tubes (see section 4.2).

XRD was used for *ex situ* phase identification of samples with Co and Co-Ni layers with and without Ti capping layer that were subjected to thermal treatment (see section F.1 and section F.2). Table 4.2 summarizes the measuring conditions of the *ex situ* laboratory XRD investigation.

Table 4.2: Summary of measuring conditions of the *ex situ* laboratory experiments

Wavelength λ	1.5414 Å (Cu K_α)
Angle of incidence α_i	0.5 °
$2\,\vartheta$ range	10–120 °
Measuring time/step	30 sec
Total measuring time	1100 min. (18.3 h)
Temperature range	*RT*
Illuminated area	≈10 x 10 mm^2
Layer deposition ‡	PVD process

‡ : All layers of Co, Ni, Ti, and TiN were deposited with the physical vapor deposition (PVD) processes that are used for the manufacturing of microprocessor devices, including the respective cleaning steps.

4.2 Synchrotron radiation experiments

There are several main advantages associated with modern synchrotron radiation sources. First of all, its high brilliance[16] of up to $\approx 2 \cdot 10^{20}$ in the energy range of 8 keV [111]. The brilliance is $>10^{12}$ higher than that of conventional X-ray tubes. Furthermore, one of the most prominent features of synchrotron radiation is its high primary beam intensity of about 1000 times higher compared to conventional X-ray tubes which makes it possible to investigate, in general, very small sample volumes, i. e. very few scattering centers as it is the case for ultra-thin layers. Consequently, the measuring time is also significantly lower. Therefore, the usage of synchrotron radiation is the method of choice to investigate nanoscale layers, that are so widely used in microprocessor devices. The emitted radiation is highly collimated which is ideal for XRR measurements. Secondly, it is possible to choose a suitable wavelength for the experiments within a wide range to avoid unwanted fluorescence radiation. For further details and applications of synchrotron radiation scattering techniques, please refer to Jordan-Sweet [112] as well as to Parrish and Hart [113, 114]. More detailed information about synchrotron radiation sources can be found in literature [115, 116].

4.2.1 Experimental setup at the Rossendorf BeamLine

The synchrotron experiments were performed at the Rossendorf BeamLine (ROBL) bending magnet 20 (BM20) at the European Synchrotron Radiation Facility (ESRF). The ESRF storage ring has a diameter of 269 m, and the electrons are accelerated to an energy of up to 6 GeV. A detailed description of ROBL is given by Matz *et al.* [117, 118]. The integrated photon flux was $\approx 3.5 \cdot 10^{11}$ photons/second [119], the energy resolution $1.5–2.5 \cdot 10^{-4}$ $\Delta E/E$ in the energy range 5–12 keV and the resolution in the range of $\Delta d/d = 1.3 \cdot 10^{-4}$. The wavelength was chosen to be 1.648 Å=7.5182 keV for samples containing Co, just below the Co-K absorption edge, and 1.593 Å=8.048 keV, just below the Ni-K absorption edge, for pure Ni samples in order to minimize fluorescence radiation. Figure 4.3 shows the mass absorption coefficients of Co, Ni, Ti, and Si as well as the used wavelengths. The angle of incidence α_i was fixed at 0.5° to enhance the signal arising from the top layer(s) of the sample (see table 4.1 and figure 4.2). For all measurements the conditions were: step

---

[16] Brilliance is defined as the number of photons per second per mm^2 per mrad^2 for an energy bandwidth of 0.1 % of the specific energy.

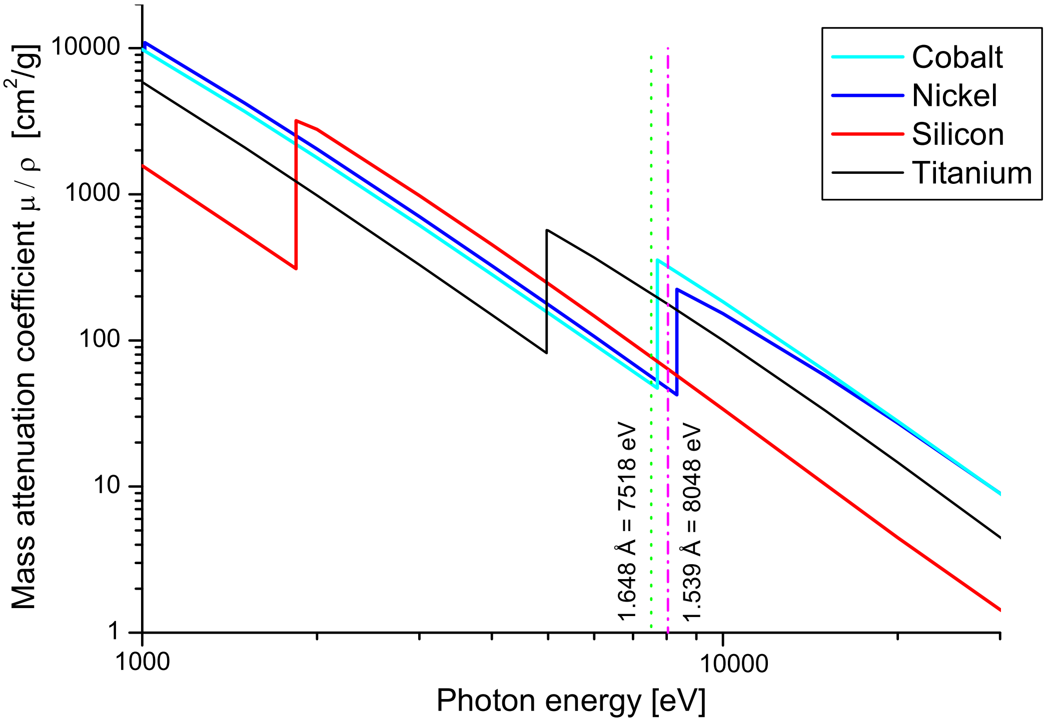

Fig. 4.3: Mass attenuation coefficient of Co, Ni, Si, and Ti.

size 0.1°, vacuum in the range of $4\text{–}9 \cdot 10^{-8}$ Pa, the sample size was $9 \times 9\,\mathrm{mm}^2$ to fit smoothly into a recess of the boron-nitride (BN) sample holder (see figure 4.4) and to be fully illuminated by the primary X-rays. All wafer pieces were cut with a dicing saw to ≈40° rotation angle relative to (100 | 010) silicon substrate orientation to avoid X-ray diffraction peaks origination from the silicon substrate. The measuring time was ≈2.5–4 s per step, being sufficient to collect useful diffraction patterns, resulting in a total measuring time of approximately 22–25 minutes for the whole measured 2ϑ range of ≈20° 2ϑ. To compensate for the decreasing primary beam intensity over time, a monitoring signal, that directly measured the incoming primary beam intensity, was used to adjust the measuring time per step in a way such that the applied X-ray intensity to the sample was kept constant. This monitoring signal arises from a scattering screen being located in the primary beam directly in front of the goniometer. The measurements can be set in a way that only after having reached a specified number of counts, typically 100000–120000 , the next measuring step is started up.
An accurate temperature control was achieved using two independently controlled heating systems, one for the sample holder and one for the environment. Each temperature control system used the signal of its own thermo-

couple to modulate the current through the Ta resistivity heaters to reach and maintain a given temperature. The temperature was stable within the range of ±2.5 K. Ramping rates in the order of several K/sec could be achieved. The sample temperature was measured by a thermocouple in direct contact with the surface of the sample. Figure 4.4 b) shows this NiAl/NiCr[17] thermocouple on the left hand side of the wafer piece, partly covered by the environmental tantalum resistivity heating system. Figure 4.4 a) shows the used high temperature diffraction chamber (HDC) built by Bühler (J. Otto GmbH) and modified by ROBL. Figure 4.5 shows the high temperature diffraction chamber that was used for experiments with Ni samples, different dopants and a TiN capping layer. The diffraction chambers were mounted on a Huber six circle goniometer equipped with stepping motors for all circles. This goniometer with an inner diameter of 400 mm allows a minimum angular step of 0.0001° (0.017 mrad). In front of the scintillation counter, a Soller slit of 15.5 cm was mounted to reduce the divergence of the scattered signal. The distance between the sample and the scintillation counter was 70 cm.

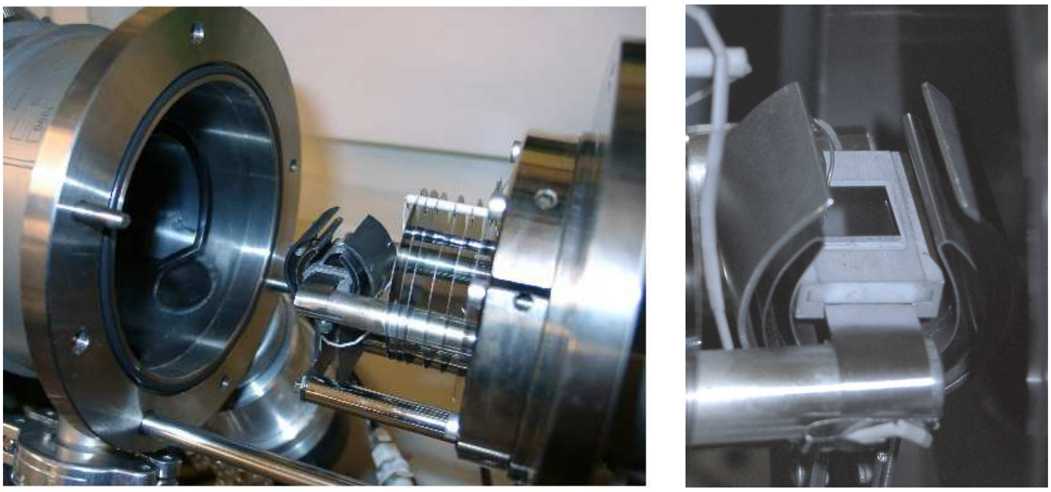

(a) High temperature diffraction chamber.

(b) Sample close up with BN sample holder.

Fig. 4.4: High temperature diffraction chamber that was used for the majority of experiments.

---

[17] In fact, what can be seen is a stainless steal cover with a ceramics inset. Inside this ceramics layer, the actual thermocouple is hidden.

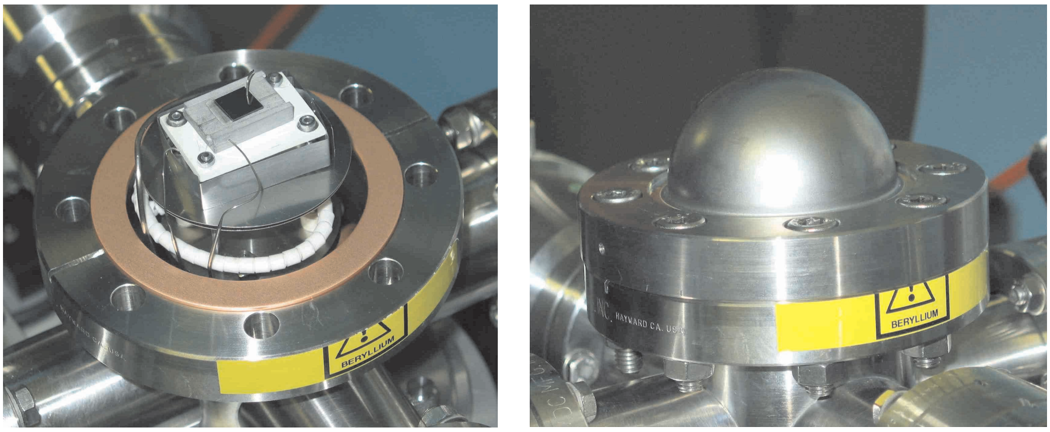

(a) Sample holder with thermocouple.

(b) Beryllium dome.

Fig. 4.5: Oven setup for Ni layer and TiN capping layer experiments.

Table 4.3: Summary of measuring conditions at the ESRF

Wavelength λ	1.648 Å & 1.593 Å[†]
Angle of incidence α_i	0.5 °
$2\,\vartheta$ range	25–62 °
Measuring time/step	2.5–4 sec
Total measuring time	22–25 min.
Temperature range	*RT*–750 °C
Pressure	$4–9 \cdot 10^{-8}$ Pa
Sample size	9 x 9 mm^2
Layer deposition[‡]	PVD process

[†] : All Ni containing samples were measured with that wavelength (see figure 4.3), but the collected diffraction patterns were recalculated with a wavelength of λ=1.648 Å to be able to directly compare peak positions between all investigated samples.

[‡] : All layers of Co, Ni, Ti, and TiN were deposited with the PVD processes that are used for the manufacturing of microprocessor devices, including the respective cleaning steps.

4.3 Transmission electron microscopy

4.3.1 Convergent beam electron diffraction

By means of TEM techniques it is possible to investigate very small areas within samples with resolution down to atomic scale. With the selective area diffraction (SAD) it is possible to investigate an area as small as $0.5\,\mu$m in diameter, but with an error in lateral resolution within the same range. For the examination of very small grains in nanoscale layers it is necessary to reduce this region further. CBED is a TEM technique where a very limited region, in the range of 10 s–100 s of nm, of the specimen contributes to a diffraction pattern. Using CBED it is possible to determine very precisely (with an error in the range of $2 \cdot 10^{-4} \Delta a/a \approx 0.02\,\%$) unit cell and lattice parameters and to determine the crystal system, i. e. the point and space group of crystals with a diameter of ≈10–100 nm. These unique features makes CBED suitable technique to examine very small single grains and second-phase precipitations. In combination with EFTEM, CBED is capable of identifying phases within a sample which cannot be identified by other techniques, e. g. because the volume fraction is too small to be identified by X-ray techniques. Figure 4.6 shows the correlation of the beam-convergence semi-angle α_B and the obtained patterns. Whether Kossel-Möllenstedt or pure Kossel patterns can be collected is primarily a function of α_B [120]. This angle can be adjusted by the so-called C2 aperture [121]. The pattern with small discrete circles is called Kossel-Möllenstedt pattern whereas a pattern with heavily overlapping circles, where no longer single diffraction maxima are visible it is called Kossel[18] pattern. For the identification of single grains with a size in the nm range, the aperture must be set in a way that Kossel-Möllenstedt patterns can be acquired.

By means of computational simulations with software packages like ELDISCA [122] or ACT [123] the measured diffraction pattern is compared to calculated diffraction patterns of known substances acquired from a database [94]. The best match between calculation and measurement, and taking into consideration all other known facts about the sample like chemical composition, history of thermal treatment etc., leads to the identification of a given phase and to the refinement of lattice parameters. If the technical

---

[18] Not to be mixed up with similar looking X-ray patterns also called Kossel patterns, resulting from a similar experimental setup.

conditions of the used TEM are such that tilting of the sample is possible without "loosing" the investigates grain, i. e. the sample is in eucentric position, it is advantageous to tilt the sample and acquire different diffraction patterns under different angles. Especially for high symmetrical substances this is necessary because single pattern might not be unambiguous. For further reference, see the *Practical Introduction into Several TEM Techniques* by Williams [121, 124].

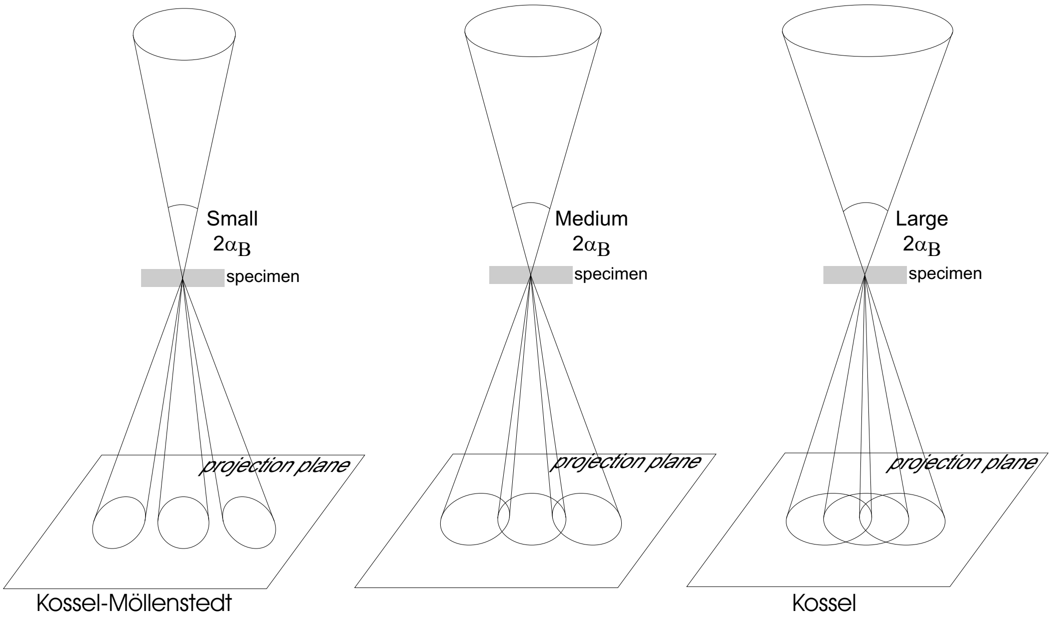

Fig. 4.6: CBED ray diagram: correlation of pattern type with α_B.

In this work, CBED was used to identify single grains of silicides within nanoscale layers, in either patterned structures of actual microprocessor devices as well as on unpatterned wafers, whenever X-ray techniques did not succeed in doing so. Furthermore, this technique was utilized to identify a ternary Co-Ti-Si phase, originating from the interaction of a Ti capping layer with a Co layer on Si substrate (see section 5.2). "Conventional" TEM imaging techniques were applied to image layer structures, interface roughness as well as layer morphology. EFTEM was employed to obtain chemical information such as spatial elemental distribution.

Chapter 5

Results

In situ high-temperature SR-XRD was used to observe the phase formation processes within the metal- and silicide-layers and to determine the phase formation sequences. This could be achieved by identifying the formed phases at different temperatures while thermally treating the samples. With synchrotron radiation it was possible to investigate these processes in layers with a technologically relevant thickness in the range of only a few nm. All the samples investigated with SR-XRD were either heated up, measured and pulled out for further investigations by TEM ("H-M-S" samples), or heated up, measured and subsequently heated up again to the next temperature ("CH & M" samples). Most of the samples were treated like the latter case.

Impact of a capping layer on the silicidation process

Capping layers of either Ti, TiN or SiO_2 are used in the semiconductor manufacturing of processors to protect the deposited metal (Co or Ni) layer from oxidation and to improve degradation due to agglomeration [25,26,41,125–127]. These layers are commonly stripped off after a first RTA together with remaining non-reacted metal. In a second annealing step, the desired silicide is formed out of the previously formed precursor, for instance CoSi is transformed into $CoSi_2$ in the case of Co deposition. Ideally, the capping layer does not interact with the metal layer during the first annealing step and acts as a getter for oxygen and possible contaminants. If the conditions for silicidation are not optimized, or the etch off process does not remove all of the capping layer, formation of unwanted phases might happen (see section 5.2 and [25]). Therefore, samples for *ex situ* and *in situ* experiments were prepared to study the impact of capping layers on the silicidation process itself, the impact on formation and conversion temperatures, as well as possible interaction with the metal or the silicide layer.

5.1 Phase formation sequences

5.1.1 The system Co–Si

Several samples with a deposited metal layer thickness of 10 nm Co, were examined with SR-XRD at the ESRF. The samples were capped with a 10 nm Ti capping layer to investigate the interaction of the capping layer with the silicidation process. During thermal treatment, i. e. after reaching a certain temperature, samples were pulled out to be preserved for further (TEM) analysis.

SR-XRD results of Co|Si samples with Ti capping layer

Samples with a deposited metal layer thickness of 10 nm Co and a capping layer of 10 nm Ti, were investigated. Ti was chosen as a capping layer, since Ti has a higher impact on the Co-Si phase formation compared to a TiN capping layer. In the actual manufacturing process of microprocessors, this Ti capping layer is etched away after the first RTA of the two-step RTA silicide formation process. The films were deposited on a single crystal silicon (001) substrate. Figure 5.1 displays the summary of the results of the samples with Ti capping layer.

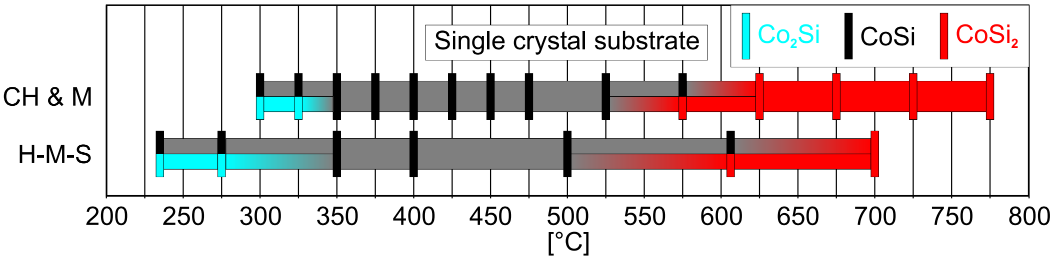

Fig. 5.1: Summary of SR-XRD results of Co|Si samples with Ti capping layer. Vertical boxes represent actual measuring temperatures. All boxes and bars are color coded, i. e. cyan stands for the metal-rich silicide, black for monosilicide, and red for the disilicide phase. Horizontal bars connect measured temperatures. Color gradients indicate that a phase transition started between its lower and upper limit. Monochrome bars show that no new phase was formed between its lower and upper limit. Boxes with two different colors indicate that at this temperature two phases coexist.

Continuous heating and measuring samples

Right from the beginning of the measurements at 300 °C Co_2Si and CoSi were present. Additionally, a weak diffraction maximum at about 53° 2 ϑ (λ=1.648 Å) of metallic Co can also be seen (see figure D.7). The Co_2Si phase was no longer detectable at 350 °C, where only CoSi existed. In the temperature range 350 °C to 525 °C only CoSi could be identified which started to be transformed into $CoSi_2$ between 525 °C and 575 °C, where both the monosilicide and the disilicide can be found. At 625 °C the transformation from CoSi to $CoSi_2$ is finished and no other phases occur up to 775 °C, the highest applied temperature.

Heating-measuring and stop samples

The results of the sample that were heated up to a specific temperature, then measured and pulled out of the HDC were very similar to the CH & M samples. The measurements started at a lower temperature of 230 °C, where Co_2Si and CoSi could be found. At 610 °C still CoSi can be found.

Taking the results of both the CH & M and H-M-S samples the range of existence for Co_2Si can be identified to be between <230 °C and at least 325 °C, succeeded by CoSi which exists from 230 °C to 610 °C which is transformed into $CoSi_2$ at a temperature >525 °C.

Details of the mentioned diffraction patterns can be found in appendix D.2. There, diffraction patterns of various temperatures are presented.

Ex situ XRD measurements

Various samples were investigated using a conventional XRD tool, with a Cu-anode (λ=1.5414 Å) using a GIXRD setup. Samples with a pure Co layer and a Co-Ni (5 at. % Ni)-layer on single crystal, undoped Si substrate were subjected to various RTA conditions, i. e. thermal annealing for 30 sec, and afterwards quenched. The samples were measured after several thermal treatments. The experiments were focussed on the high-temperature regime, since the disilicide formation is technologically more important than the formation of the metal-rich silicides. The impact of the capping layer on the formation temperature of the low-resistivity phases $CoSi_2$ and $Co_{0.95}Ni_{0.05}Si_2$, respectively, is of interest.

Co|Si samples with and without Ti capping layer

The samples with the pure Co layer (15 nm) show after a RTA at 580 °C for 60 seconds diffraction maxima of CoSi and $CoSi_2$, i. e. the conversion to $CoSi_2$ is not completed at this temperature. In the sample subjected to 600 °C for 60 s, only $CoSi_2$ is present, meaning the silicidation process is completed.
The capping layer of 15 nm Ti changes the picture significantly. From 600 °C to 700 °C, there is always CoSi present, indicating that the conversion from CoSi to $CoSi_2$ is not completed. This implies that the RTA temperatures must be significantly higher than 700 °C, or the annealing time needs to be longer. Figure 5.2 summarizes the results of the *ex situ* XRD measurements. For details about the collected diffraction patterns see figure F.1 and figure F.2.

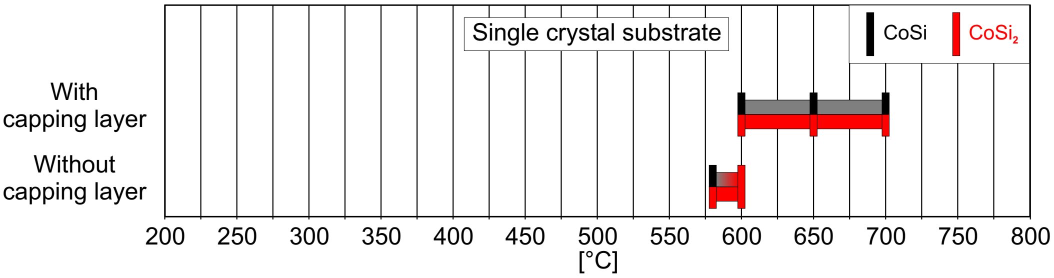

Fig. 5.2: Summary of XRD results of Co|Si samples with and without Ti capping layer. The deposited metal layer thickness was 15 nm for Co as well as 15 nm for the Ti capping layer. Vertical boxes represent actual measuring temperatures. All boxes and bars are color coded, i. e. black stands for monosilicide, and red for the disilicide phase. Horizontal bars connect measured temperatures. Color gradients indicate that a phase transition started between its lower and upper limit. Monochrome bars show that no new phase was formed between its lower and upper limit. Boxes with two different colors indicate that at this temperature two phases coexist.

Summary of analytical results of Co silicides

The samples with a layer stack of 10 nm Co with a 10 nm Ti capping layer on undoped single crystal substrate were investigated with *in situ* SR-XRD to determine the phase formation and conversion temperatures. The formation of Co_2Si takes place below the starting temperature of 230 °C. Co_2Si is stable up to at least 325 °C. The conversion to the monosilicide phase started already at 230 °C and is finished at 350 °C. CoSi is stable up to at least 610 °C and converts to $CoSi_2$ on further heating. The formation of the high temperature phase $CoSi_2$ in the system Co-Si starts at $\leq$575 °C. The phase formation sequence in the case of Co silicides was found to be

$$Co_2Si \rightarrow CoSi \rightarrow CoSi_2$$

within all investigated samples. A capping layer did not have any influence on the phase formation sequence. However, the conversion from CoSi to the $CoSi_2$ is shifted for at least 100 K to higher temperatures when a Ti capping layer was applied.

5.1.2 The system Co–Ni–Si

The widely used $CoSi_2$ has some disadvantages that most likely prevents its usage in future technology nodes of microprocessor manufacturing. Alloying of Co with a low at. % Ni seems to be a promising way to further extend the usage of $CoSi_2$ [31, 34, 48, 52, 53], i. e. to overcome the problems that are associated with $CoSi_2$ (see section 1.1.3). Mainly the reduction of the formation temperature of $CoSi_2$ and therefore lowering the overall thermal budget is of interest in order to reduce agglomeration effects, especially for very small gate lengths below $\lesssim$45 nm. Various samples were investigated with SR-XRD at the ESRF. The deposited metal layer thickness was 10 nm, a value close to that used in manufacturing. Table 5.1 lists the different Co-Ni (5 at. % Ni)|Si samples[19].

---

[19] All Co-Ni|Si samples that were investigated contained 5 at. % Ni and are hereafter referred to as Co-Ni|Si samples. If the Ni content differs from 5 at. %, then this will be noted explicitly.

Table 5.1: Doping species, type, and energy for the Co-Ni|Si samples investigated with SR-XRD

	Substrate	
	(001) Single crystal Si	polycrystalline Si
Implanted dose [at/cm^2], species, and energy	undoped	undoped
	$8 \cdot 10^{15}$ As$^+$ @ 30 keV	$8 \cdot 10^{15}$ As$^+$ @ 30 keV
	$8 \cdot 10^{15}$ P$^+$ @ 15 keV	

SR-XRD results of Co-Ni|Si samples

The silicides are labeled accordingly to a Ni content of 5 at. %, despite the fact that the actual Ni content is smaller than 5 at. % in the formed silicides. Although it became clear that Ni is expelled from CoSi during the monosilicide formation (see section 6.3), CoSi is labeled as $Co_{0.95}Ni_{0.05}Si$ in the current section. This was made for clarification and to distinguish better between pure Ni and pure Co samples. In all cases no separation, i. e. no coexistence of Ni and Co silicides could be observed. These results were expected because the Ni content was too small to form reasonable amounts of Ni silicides that could be detected by means of X-ray techniques. Even the Ni enrichment at the interface to the substrate after thermal treatment (see figures 6.2 and 6.4), was too low to enable the formation of Ni silicides.

Undoped single crystal substrates

The undoped sample shows at 275 °C only $(Co_{0.95}Ni_{0.05})_2Si$, which could be identified by very weak diffraction maxima at $\approx 48.7° \, 2\vartheta$ and $\approx 53.4° \, 2\vartheta$ (λ=1.648 Å). This metal-rich silicide is transformed into the disilicide phase $Co_{0.95}Ni_{0.05}Si$ at temperatures lower than 300 °C, where $Co_{0.95}Ni_{0.05}Si$ is the only phase present. $Co_{0.95}Ni_{0.05}Si$ is stable up to at least 400 °C and is transformed into $Co_{0.95}Ni_{0.05}Si_2$ between 400 °C and 475 °C. Between 475 °C and 650 °C, $Co_{0.95}Ni_{0.05}Si_2$ is the only detectable phase.

As$^+$ and P$^+$ doped samples on single crystal substrates

The As$^+$ doped single crystal sample shows at 275 °C $(Co_{0.95}Ni_{0.05})_2Si$ as well as $Co_{0.95}Ni_{0.05}Si$, whereas in the P$^+$ doped sampled only $(Co_{0.95}Ni_{0.05})_2Si$ is present. At 300 °C, $Co_{0.95}Ni_{0.05}Si$ as well as $(Co_{0.95}Ni_{0.05})_2Si$ can be identified in both doped samples. The conversion to $Co_{0.95}Ni_{0.05}Si$ is continued with further thermal treatment and is completed at 350 °C. The conversion to the disilicide starts at temperatures higher than 450 °C. At 475 °C, both $Co_{0.95}Ni_{0.05}Si$ and $Co_{0.95}Ni_{0.05}Si_2$ can be detected. The conversion to the target phase $Co_{0.95}Ni_{0.05}Si_2$, (see table 3.3), has taken place completely at 550 °C. Figure 5.3 shows the SR-XRD results of a sample on single crystal silicon substrate.

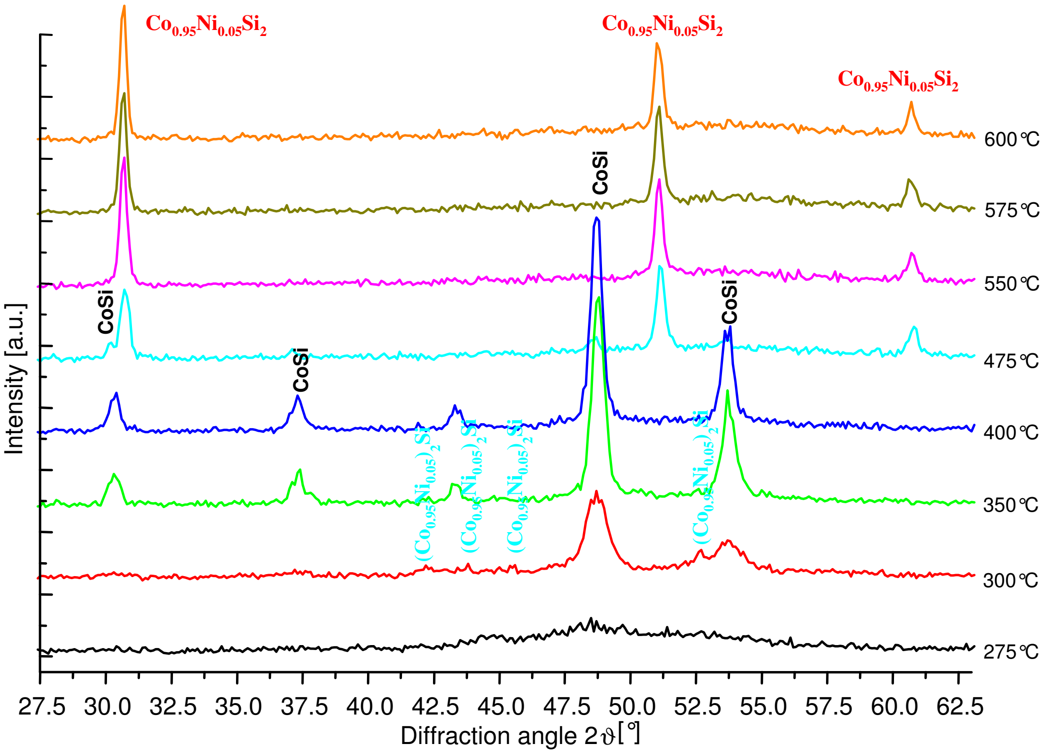

Fig. 5.3: SR-XRD results of Co-Ni|Si sample on P^+ doped single crystal Si substrate in the temperature range 275°C–600°C (λ=1.648 Å). Deposited metal layer thickness was 10 nm. The different intensity maxima are labeled with the corresponding silicide phases. All labels are color coded, i. e. cyan stands for the metal-rich silicide, black for monosilicide, and red for the disilicide phase.

Undoped polycrystalline substrates

At 300 °C, the undoped sample shows the metal-rich silicide $(Co_{0.95}Ni_{0.05})_2Si$ as well as the monosilicide phase $Co_{0.95}Ni_{0.05}Si$. This means, the starting point for the formation of $Co_{0.95}Ni_{0.05}Si$ is lower than 300 °C. The conversion to $Co_{0.95}Ni_{0.05}Si$ is completed at 350 °C. At this temperature, the formation of $Co_{0.95}Ni_{0.05}Si_2$ starts. At 450 °C, and at all investigated higher temperatures, only $Co_{0.95}Ni_{0.05}Si_2$ can be detected, meaning that the conversion to $Co_{0.95}Ni_{0.05}Si_2$ was completed at 450 °C.

As^+ doped samples on polycrystalline substrates

The As^+ doped sample shows at 300 °C only diffraction maxima corresponding to $Co_{0.95}Ni_{0.05}Si$. This indicates that the conversion from $(Co_{0.95}Ni_{0.05})_2Si$, which could be seen at the starting temperature of 275 °C, to $Co_{0.95}Ni_{0.05}Si$ is completed. Similar to the undoped sample, the formation of $Co_{0.95}Ni_{0.05}Si_2$ starts at 350 °C, is still present at 400 °C, and is terminated at 450 °C.

Figure 5.4 summarizes the diffraction results of the Co-Ni (5 at. % Ni) samples. The formation of the (metal-rich) silicides in the lower temperature regime, i. e. temperature lower than ≈400 °C, is very similar for all kinds of substrates and dopants as well as dopant concentrations. On polycrystalline substrates, however, the formation temperature of the disilicide phase is lowered considerably.

Details of the mentioned diffraction patterns can be found in appendix D.3. There, diffraction patterns of various temperatures are presented.

Co-Ni|Si samples with and without Ti capping layer

Figure 5.5 shows a summary of the obtained results for all the investigated samples with a Ti capping layer. In the case of Co-Ni layers without a Ti capping layer, $Co_{0.95}Ni_{0.05}Si$ is present from 450 °C to 550 °C. The formation from $Co_{0.95}Ni_{0.05}Si$ to $Co_{0.95}Ni_{0.05}Si_2$ starts at temperatures below 525 °C. The conversion from monosilicide to disilicide is completed at 600 °C.
At 600 °C, only $Co_{0.95}Ni_{0.05}Si$ can be detected in the sample with the Ti capping layer. Even at 650 °C no traces of $Co_{0.95}Ni_{0.05}Si_2$ can be identified, i. e. the conversion from $Co_{0.95}Ni_{0.05}Si$ to $Co_{0.95}Ni_{0.05}Si_2$ has not been started. The

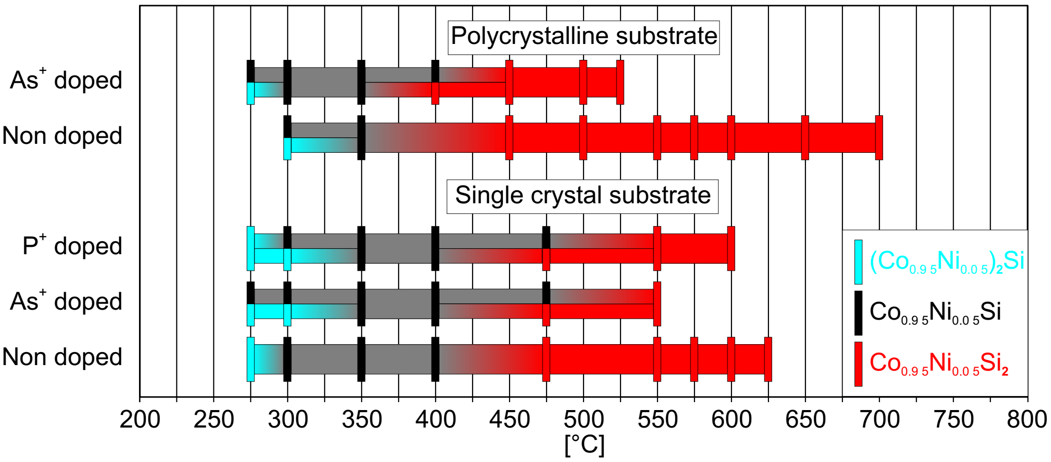

Fig. 5.4: Summary of 38 SR-XRD results of Co-Ni (5 at. % Ni)|Si samples. Deposited metal layer thickness was 10 nm. Vertical boxes represent actual measuring temperatures. All boxes and bars are color coded, i. e. cyan stands for the metal-rich silicide, black for monosilicide, and red for the disilicide phase. Horizontal bars connect measured temperatures. Color gradients indicate that a phase transition started between its lower and upper limit. Monochrome bars show that no new phase was formed between its lower and upper limit. Boxes with two different colors indicate that at this temperature two phases coexist.

Ti capping layer has the effect that still at 700 °C $Co_{0.95}Ni_{0.05}Si$ can be found, whereas the formation of $Co_{0.95}Ni_{0.05}Si_2$ already started.
For details about the collected diffraction patterns see figure F.3 and figure F.4.

Summary of analytical results of ternary Co-Ni silicides

The formation of $(Co_{0.95}Ni_{0.05})_2Si$ starts at a temperature lower than 275 °C in all investigated samples. In general, a lower formation and conversion temperature was observed on polycrystalline substrate samples compared to single crystal substrates. Doping of the substrates leads to a higher thermal stability of $(Co_{0.95}Ni_{0.05})_2Si$ and CoSi in either case. The lowest temperature at which CoSi is formed is 275 °C for As^+ doped samples on single crystal and polycrystalline substrate samples. The formation temperature of CoSi was 300 °C for non-doped and P^+ doped samples. However, doping enhanced the

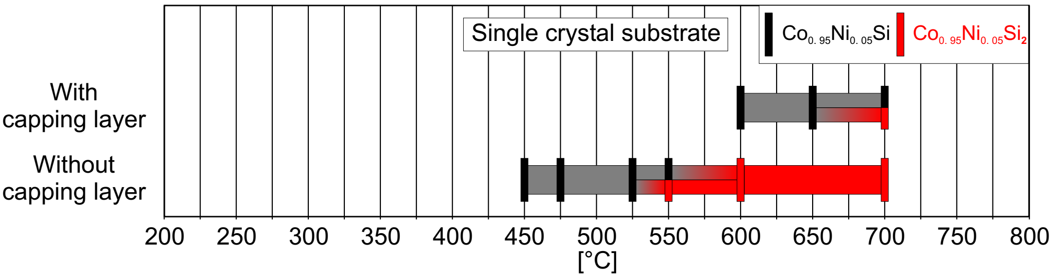

Fig. 5.5: Summary of XRD results of Co-Ni|Si samples with and without Ti capping layer. The deposited metal layer thickness was 15 nm for Co and Co-Ni as well as 15 nm for the Ti capping layer. Vertical boxes represent actual measuring temperatures. All boxes and bars are color coded, i. e. black stands for monosilicide, and red for the disilicide phase. Horizontal bars connect measured temperatures. Color gradients indicate that a phase transition started between its lower and upper limit. Monochrome bars show that no new phase was formed between its lower and upper limit. Boxes with two different colors indicate that at this temperature two phases coexist.

thermal stability of CoSi by at least 75 K on single crystal substrates. The conversion to $Co_{0.95}Ni_{0.05}Si_2$ started on polycrystalline samples at temperatures lower than 400 °C and on single crystal substrates between 400 °C and 475 °C. The phase formation sequence was very similar to the phase formation in the system Co-Si, although, it was shifted to lower temperatures:

$$(Co_{0.95}Ni_{0.05})_2Si \rightarrow CoSi \rightarrow Co_{0.95}Ni_{0.05}Si_2$$

This sequence is valid for all investigated samples. The conversion from the monosilicide to the disilicide phase is shifted for at least 100 K to higher temperatures when a Ti capping layer was used.

5.1.3 The system Ni–Si

Table 5.2 lists the samples with a deposited metal layer thickness of 10 nm, that were investigated with SR-XRD at the ESRF. The deposition temperature of the Ni layers was 150 °C. The dose was set to a level much higher than what usually is used in production to enhance the effect of the doping.

Table 5.2: Doping species, type, and energy for the Ni|Si samples investigated with SR-XRD

	Substrate	
	(001) Single crystal Si	polycrystalline Si
Implanted dose [at/cm^2], species, and energy	undoped	undoped
	$8 \cdot 10^{15}\,\mathrm{B}^+$ @ $5\,\mathrm{keV}$	$8 \cdot 10^{15}\,\mathrm{B}^+$ @ $5\,\mathrm{keV}$
	$8 \cdot 10^{15}\,\mathrm{As}^+$ @ $30\,\mathrm{keV}$	$8 \cdot 10^{15}\,\mathrm{As}^+$ @ $30\,\mathrm{keV}$
	$8 \cdot 10^{15}\,\mathrm{P}^+$ @ $15\,\mathrm{keV}$	

Impact of dopants on the Ni silicidation process

Single crystal substrates

Figure 5.6 is an example of the obtained diffraction patterns and shows the SR-XRD result of the As$^+$ doped single crystal silicon substrate sample. All diffraction maxima could be assigned to Ni silicides and are labeled accordingly. The evolution of the different phases from 200 °C to 750 °C can clearly be retraced. At 700 °C, the intensity of the NiSi diffraction peaks decreases significantly, whereas no indications of NiSi$_2$, the high temperature phase of Ni silicide, could be observed using the grazing incidence geometry. No diffraction peaks are visible at 750 °C. This is due to an epitaxial growth of NiSi$_2$ and the specific diffraction geometry that was used (see figure 4.1 and figure 5.10 as well as section 5.1.3). So, the NiSi$_2$ phase cannot be identified directly, but by the absence of NiSi (see also figure A.2). The silicidation process on single crystal substrates starts at 200 °C. Measurements at *RT* and at 160 °C (not shown here), reveal no clear diffraction maxima which can be attributed to any silicide phases. Ni$_2$Si is detected in all samples at 200 °C, regardless of the doping. Traces of metallic Ni can also be found at 200 °C (see figure D.1). The target phase NiSi (see figure 3.3), starts to form between 250 °C and 275 °C. The conversion to NiSi is completed between 300 °C and 325 °C. NiSi is stable up to 450 °C for undoped samples and at least up to 600 °C for the doped samples. This means, the transition to NiSi$_2$ takes place at significantly higher temperatures for doped samples compared to undoped samples. Further thermal treatment up to 650 °C increases the amount of the NiSi phase. At 700 °C the amount of NiSi seems to decrease, while at 750 °C no more diffraction peaks are visible. There is not such a significant difference between As$^+$ and P$^+$ as dopants compared with B$^+$ doping. In undoped samples the Ni disilicide is formed below 550 °C. The conversion to NiSi$_2$ takes

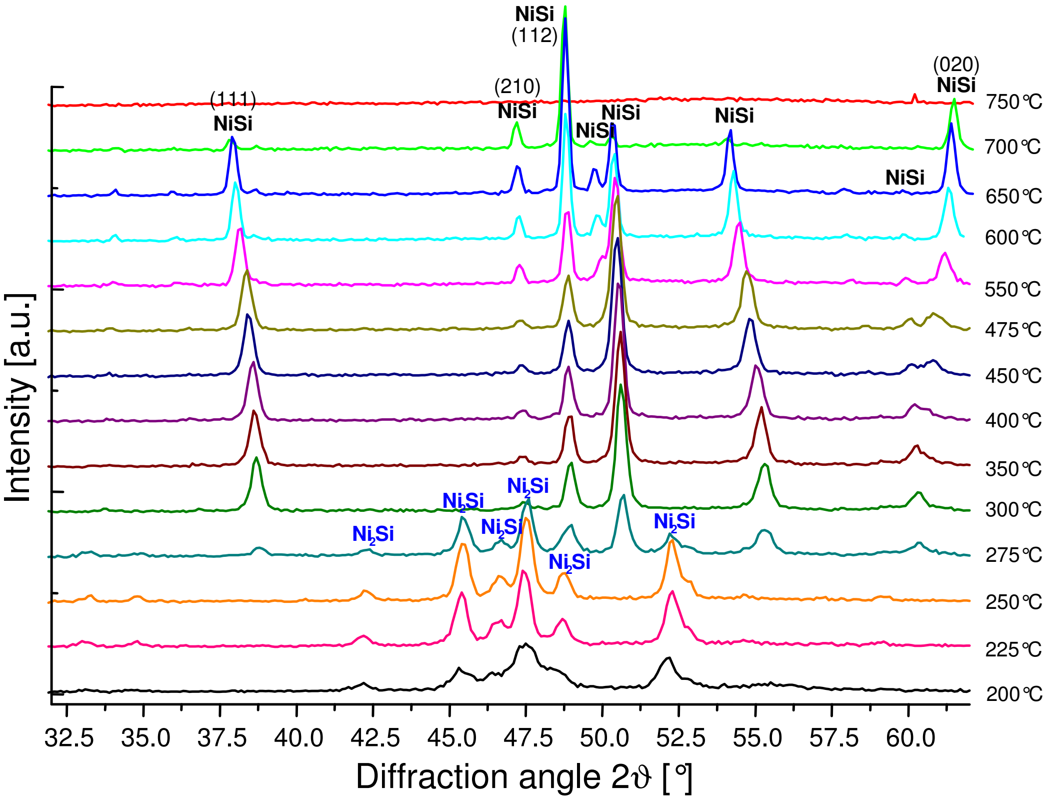

Fig. 5.6: SR-XRD results of Ni|Si sample (λ=1.648 Å). Deposited Ni layer thickness was 10 nm on $8 \cdot 10^{15}$ at/cm^2 As$^+$ doped single crystal substrate. Diffraction patterns between 200 °C and 750 °C with labeled and partly indexed diffraction maxima. All labels are color coded, i. e. blue stands for the metal-rich silicide, black for mono-silicide phase.

place at higher temperatures for doped samples compared to undoped samples (see figure 5.7, lower part).

Polycrystalline substrates

The As$^+$ doped and the undoped samples show NiSi diffraction peaks already at 200 °C. On As$^+$ doped polycrystalline silicon substrate Ni$_2$Si is stable up to at least 275 °C. B$^+$ doping stabilizes the Ni$_2$Si phase compared to undoped and As$^+$ doped samples. The first clear diffraction peaks of NiSi could be observed at 300 °C on B$^+$ doped samples. The conversion of Ni$_2$Si to NiSi is finished at 300 °C. The dopants have a beneficial effect on the thermal stability of NiSi, which is formed on undoped samples below 475 °C. The intensities of the NiSi diffraction maxima rise up to 475 °C. The formation of $NiSi_2$ is retarded for the doped samples, where $NiSi_2$ can be identified at temperatures significantly higher than 525 °C compared to the undoped sample where it is already been formed at 475 °C. Further thermal treatment leads then to further formation of $NiSi_2$ out of NiSi. Figure 5.7 illustrates the formation and transformation temperatures as well as the range of existence for all investigated Ni layer samples.

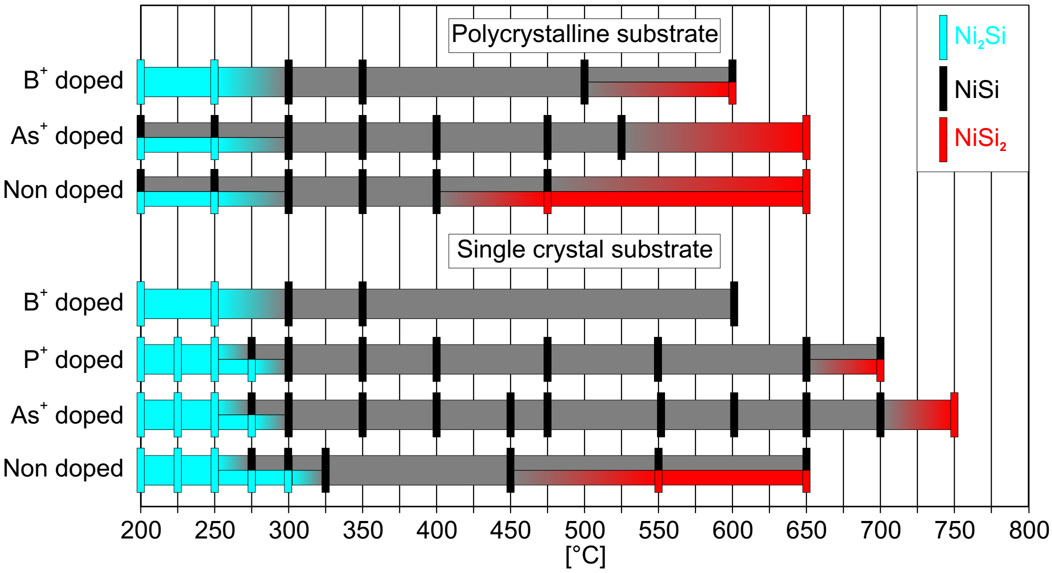

Fig. 5.7: Summary of 60 SR-XRD results of 10 nm Ni|Si samples with various types of dopants. Vertical boxes represent actual measuring temperatures. All boxes and bars are color coded, i. e. cyan stands for the metal-rich silicide, black for monosilicide, and red for the disilicide phase. Horizontal bars connect measured temperatures. Color gradients indicate that a phase transition started between its lower and upper limit. Monochrome bars show that no new phase was formed between its lower and upper limit. Boxes with two different colors indicate that at this temperature two phases coexist.

Details of the mentioned diffraction patterns can be found in appendix D.1. There, diffraction patterns of various temperatures are presented.

In situ SR-XRD measurements of Ni|Si samples

Due to the nature of *in situ* experiments, no etching off of the capping layer can be performed during annealing of the samples. Therefore, the *in situ* experiments do not reflect the conditions of the actual manufacturing process. Nevertheless, they reflect the terms of incomplete etching processes after the first RTA step if parts of the capping layers withstand the etching.

A set of boron doped samples with 10 nm Ni with and without the capping layer were prepared to evaluate the impact of a 15 nm TiN capping layer on the silicidation process under quasi-static conditions. The obtained results can directly be compared to the results presented in figure 5.7. The greater thickness of the capping layer was chosen to compensate for the overall lower Ti content when a TiN capping layer is used rather than a Ti capping layer. Ni is less prone to oxidation than Co, therefor the TiN capping layer is suitable for preventing unwanted oxidation prior to silicidation.

Single crystal substrates

Figure 5.8 shows examples of diffraction patterns obtained at several temperatures for a 15 nm TiN capped, boron doped, 10 nm Ni sample on a single crystal silicon substrate. The diffraction maxima corresponding to TiN at $\approx 45.4^\circ\, 2\vartheta$ (λ=1.648 Å) can clearly be seen in figure 5.8 a) and b).

Figure 5.9 summarizes the SR-XRD results of capped (15 nm TiN) and uncapped, B^+ ($8 \cdot 10^{15}$ at/cm^2 @ 5 keV) doped Ni samples with a layer thickness of 10 nm of Ni. In the case of the uncapped sample Ni_2Si can be observed in the temperature range between 200 °C and 300 °C. At 300 °C only NiSi was detected. That means the conversion from Ni_2Si to NiSi started above 250 °C and was completed at 300 °C. No indication of disilicide formation could be observed up to 600 °C.

Within the capped sample, Ni_2Si can be detected between 200 °C and 300 °C. At 300 °C, NiSi formation already started. At 350 °C, the conversion from Ni_2Si to NiSi was completed, and up to 650 °C no indication of $NiSi_2$ formation could be found.

On a single crystal silicon substrate, a stabilizing effect of the TiN capping layer with respect to the metal-rich phase Ni_2Si could be detected. Ni_2Si was at least stable for a temperature of 50 K higher compared to the uncapped sample. No indications of $NiSi_2$ formation could be observed in both samples, meaning that for the high-temperature regime, no differences between the samples were found.

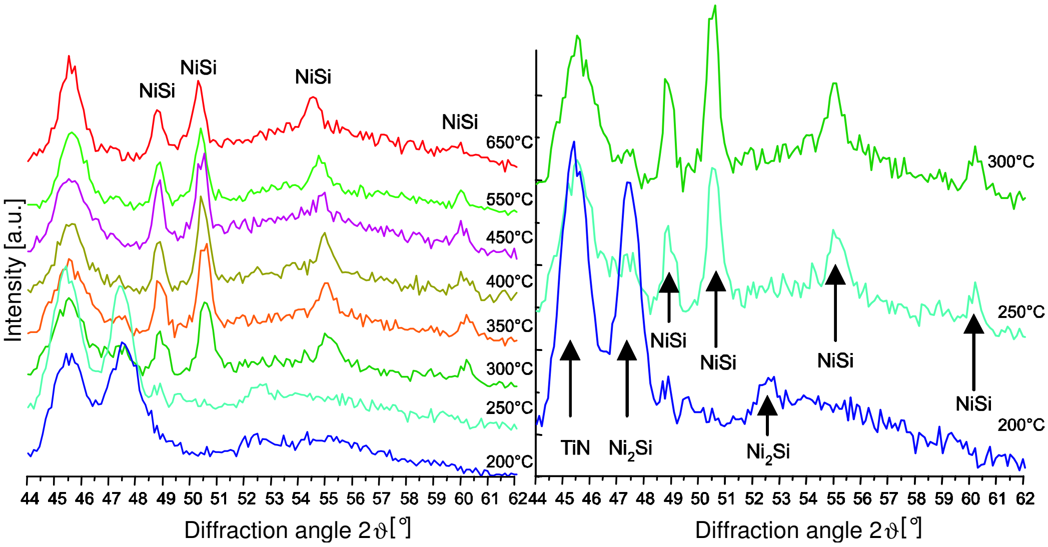

Fig. 5.8: Diffraction patterns of 10 nm Ni|Si sample with a 15 nm TiN capping layer on a B^+ doped single crystal substrate (λ=1.648 Å). On the right hand side, a magnified view of the low temperature regime is shown. The peaks are labeled due to the corresponding phases.

Polycrystalline substrates

The uncapped sample shows evidence for Ni_2Si formation at 200 °C and 250 °C. Below 300 °C, the conversion from Ni_2Si to NiSi started, which was completed at 300 °C. Between 350 °C and 500 °C, only NiSi could be detected. At 600 °C both NiSi and $NiSi_2$ could be observed, meaning that the conversion started between 500 °C and 600 °C, but was not completed yet.
Within the capped layer, diffraction maxima corresponding to Ni_2Si are visible at 250 °C. At 300 °C, the conversion to NiSi was completed. No indications for $NiSi_2$ formation can be found between 350 °C and 655 °C.
In the low temperature regime, no impact of the capping layer was obvious on polycrystalline substrates. Both samples showed diffraction peaks of Ni_2Si at 200 °C and 250 °C. At 300 °C, only NiSi could be found in the capped and in the uncapped sample. The conversion from NiSi to $NiSi_2$ started below 600 °C within the uncapped sample, whereas no proof for $NiSi_2$ formation is detected in the capped sample up to 655 °C.

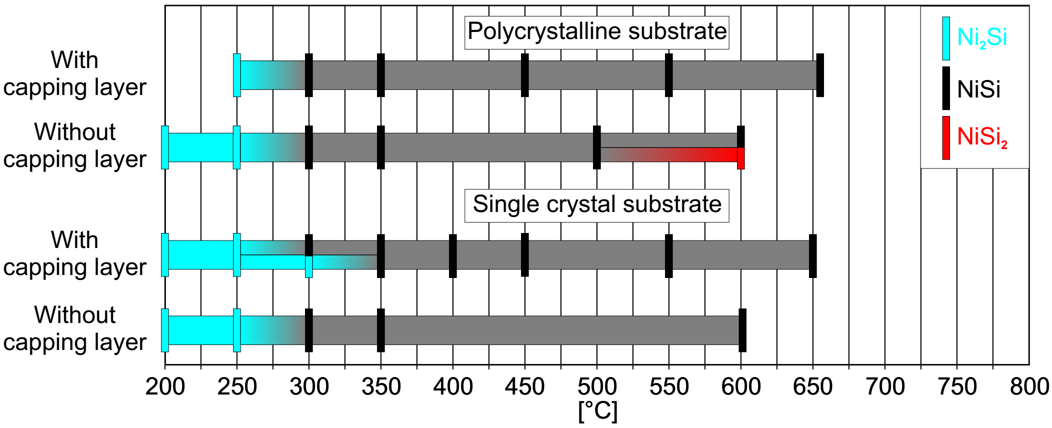

Fig. 5.9: Summary of 31 SR-XRD results of 10 nm Ni|Si samples with and without a 15 nm TiN capping layer on single and polycrystalline silicon substrates. Samples were B^+ ($8 \cdot 10^{15}$ at/cm^2 @ 5 keV) doped. Vertical boxes represent actual measuring temperatures. All boxes and bars are color coded, i. e. cyan stands for the metal-rich silicide, black for monosilicide, and red for the disilicide phase. Horizontal bars connect measured temperatures. Color gradients indicate that a phase transition started between its lower and upper limit. Monochrome bars show that no new phase was formed between its lower and upper limit. Boxes with two different colors indicate that at this temperature two phases coexist.

Epitaxial growth of $NiSi_2$

The vanishing of diffraction peaks in figure 5.6 at 750 °C can be ascribed to the epitaxial growth of $NiSi_2$ along the Si <111> planes. The lattice mismatch Δa of 0.4 % between Si and $NiSi_2$ is extremely small (see table 3.2), and therefore the exact crystallographic orientation of $NiSi_2$ on the silicon substrate is energetically favorable. Figures 5.10 a) and b) show TEM images of the As^+ doped sample after thermal treatment up to 750 °C. The formerly continuous silicide layer of NiSi became discontinuous, i. e. agglomeration occurred, while transforming into $NiSi_2$ at temperatures higher than 650 °C for P^+ doping and higher than 700 °C for As^+ doping (figures 5.6 and D.1). TEM investigations of the P^+ doped samples show NiSi grains next to epitaxially grown $NiSi_2$ islands. Epitaxial growth of $NiSi_2$ at high temperatures was also reported earlier by Lauwers *et al.* [103].

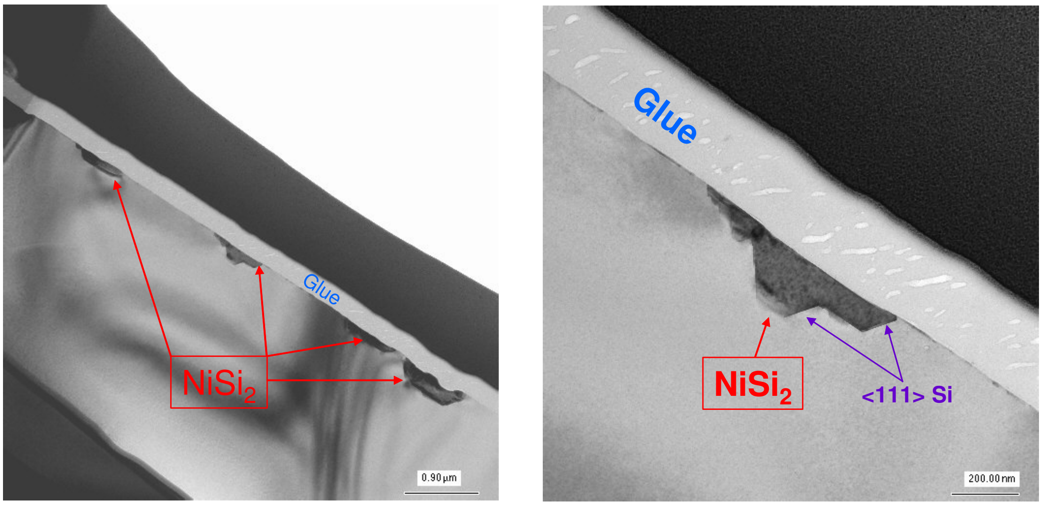

(a) "Islands" of epitaxially grown NiSi$_2$. Discontinuous silicide layer. Brightfield TEM overview image.

(b) TEM closeup image of a). NiSi$_2$ "island".

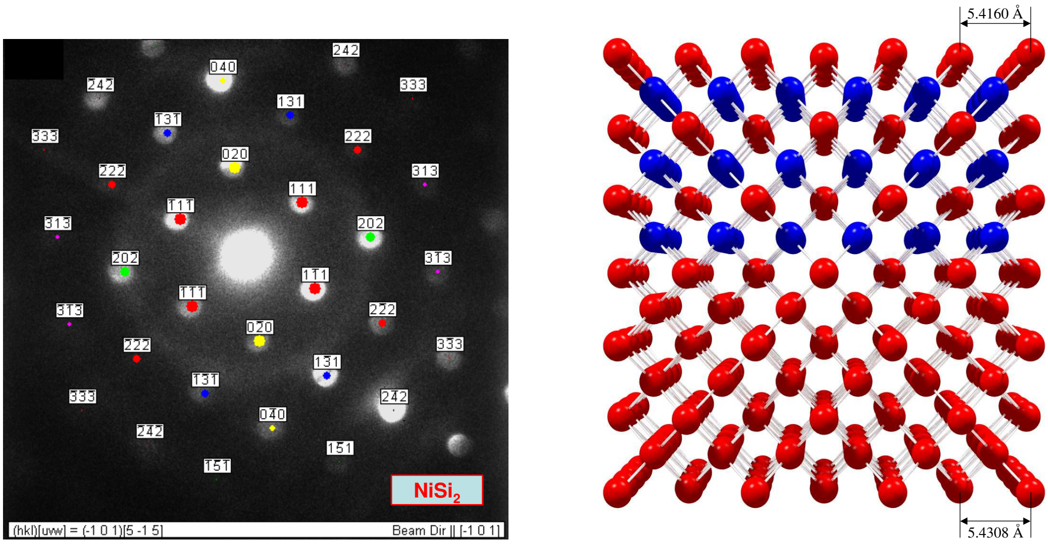

(c) CBED image of NiSi$_2$ "island" with superimposed simulation (colored dots) by ACT [123].

(d) Crystallographic relationship between (001) Si and epitaxially grown NiSi$_2$. Top half: NiSi$_2$ structure, bottom half: silicon structure.

Fig. 5.10: Epitaxial growth of NiSi$_2$ on (001) silicon substrate.

Summary of analytical results of Ni silicides

The formation of Ni_2Si starts below 200 °C in all investigated samples. Doping of the substrates leads to a higher thermal stability of Ni_2Si and NiSi for both types of substrates. The onset temperature at which NiSi is formed was determined to be 275 °C for undoped as well as As^+ and P^+ doped single crystal substrate samples and to be lower than 200 °C for non-doped and As^+ doped polycrystalline samples. Boron however, shifts the formation temperature of NiSi to 300 °C for both types of substrates. The upper limit of thermal stability of NiSi, which is replaced by $NiSi_2$, could be deferred by at least 25 K on polycrystalline substrates and by more than 100 K on single crystal substrates.
The phase formation sequence was found to be

$$Ni_2Si \rightarrow NiSi \rightarrow NiSi_2$$

in all investigated samples. At temperatures higher than ≈700 °C, $NiSi_2$ is formed epitaxially on single crystal substrates.

5.1.4 Summary of impact of capping layer

A capping layer retards the silicidation process due to the interaction of the deposited metal with the capping layer. The deposited capping layer of 15 nm of Ti had a stabilizing effect on the monosilicide phase, CoSi and $Co_{0.95}Ni_{0.05}Si$. This was also reported in literature [53]. The formation temperature of $CoSi_2$ and $Co_{0.95}Ni_{0.05}Si_2$ on undoped single crystal substrate was shifted upwards for at least 100 K when the Ti capping layer was applied.
In the low temperature regime, the TiN capping layer had a stabilizing effect with respect to the thermal stability of Ni_2Si. The thermal stability of Ni_2Si was enhanced on single crystal substrates, i. e. Ni_2Si could still be detected at 300 °C compared to the uncapped samples in which at that temperature only NiSi is present. Especially the conversion from NiSi to $NiSi_2$ is effected at elevated temperatures on polycrystalline samples. This beneficial effect of a TiN capping layer on the thermal stability of NiSi was also observed by Chamirian *et al.* by means of R_s measurements [128]. The formation temperature of $NiSi_2$ on polycrystalline substrates was shifted to higher temperatures by more than 50 K.

5.2 The ternary CoTiSi phase

The Co|Si samples with a Ti capping layer were not subjected to a wet-chemical etching step, as it is the case for the manufacturing process. Since the etching properties of a ternary phase might be different compared to the properties of metallic Co or Co monosilicide, it is of interest not to leave any Ti residuals on top of Co silicide. Any leftovers might have a great impact on further silicidation processes and lead possibly to an increased sheet resistance. Therefore, the investigation of the interaction of the capping layer with the Co layer (possibly also the silicide layer) could reveal insights into phase-formation processes whenever the wet-etch step fails to remove all of the capping layer prior to further processing. No indications of the formation of different phases besides CoSi and $CoSi_2$ could be found using SR-XRD (figure 5.1). Since the detection limit of (SR-)XRD techniques is ≈1–3 vol. % of a phase, TEM analysis were performed. One sample that was heated up to 610 °C out of the sample series "H-M-S" (figure 5.1) was investigated by means of analytical TEM techniques (EFTEM) as well as CBED. The sample was cut and afterwards prepared conventionally for TEM investigations. Figure 5.11 shows two brightfield images of a cross-section of this sample. Figure 5.11 a) shows the sample spot that was used to perform the EFTEM analysis which are presented in figure 5.12. Figure 5.11 b) shows the area of the sample that was investigated by CBED. In figure 5.12, EFTEM maps are presented. Figures 5.12 a)–c) show the elemental maps of Si, Co, and Ti and it becomes clear that several grains consist of all three elements. This can also be seen in figure 5.12 c) which is a false color image derived from a superposition of the three elemental maps. Although it is most likely the case now that there is a ternary phase containing Co, Ti, and Si present, it cannot be determined which phase it is. Since the TEM lamella is considerably thicker than a single grain, it might in principle be possible that the Ti signal (see figure 5.12) c)) within the layer is a signal from a grain/layer underneath the Co-Ti-Si grain.

Hsia *et al.* showed the existence of a Co-Ti-Si layer from silicidation experiments with a Ti underlayer [129]. However, they did not perform any follow-up experiments to characterize that layer. For the identification of the ternary Co-Ti-Si phase, CBED investigations were performed.

Two principle problems arise while analyzing thin layers in the range of a few nm. Sample drift due to a heating up of the sample caused by energy addition by the accelerated electrons and carbon contamination through cracking of hydrocarbon contaminations inside the sample chamber can occur. To minimize these effects, a special proceeding was used to obtain the results

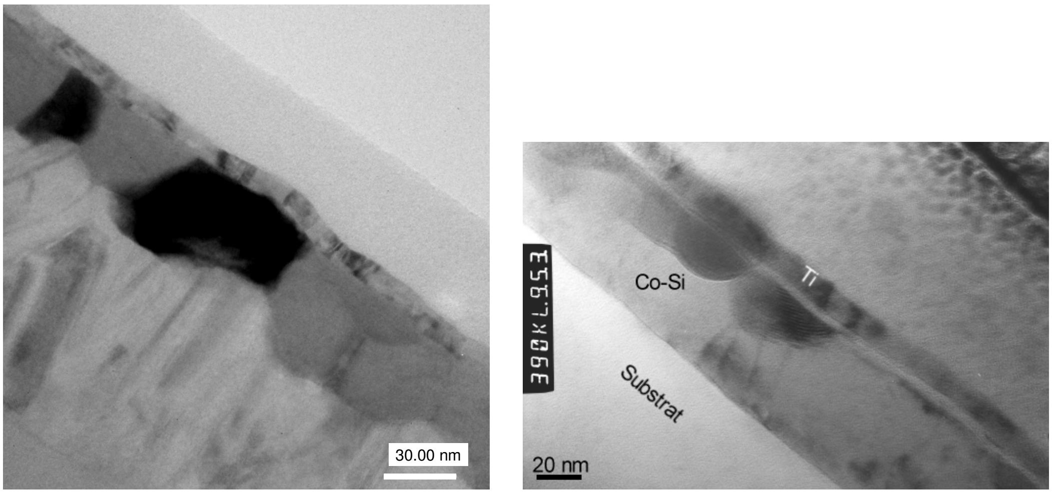

(a) Brightfield TEM image of the region used for EFTEM measurements.

(b) Brightfield TEM image of the region used for CBED investigations.

Fig. 5.11: Brightfield TEM images of sample heated up to 610 °C. Deposited metal layer thickness was 10 nm for Co and also 10 nm for the Ti capping layer.

summarized in figure 5.14. Firstly, the imaging mode of the TEM was used to choose a well suited position of the TEM lamella, and to set up the TEM sample stage to move perpendicular to the layer stack in fine steps. Secondly, the diffraction patterns were collected using solely the CBED mode of the TEM. Diffraction patterns were collected by moving the stage stepwise from the substrate to the sample surface to get distinct diffraction patterns from different spots of the layer stack. Collecting time was approximately 2–3 sec each. The diffraction patterns were taken in the order shown in figure 5.13, starting with point L941. The final step used the imaging mode again to check at which spots the diffraction patterns were taken. The hydrocarbon contamination spots could be used to identify the actual measuring spots. At these contaminated points, diffraction patterns were collected again (this time of lower quality) and compared with the previous pattern to proof that the measured spots were assigned correctly to the points given in figure 5.13.

The evaluation of the CBED patterns could be realized using ELDISCA, a software developed by Thomas [122]. First, on the CBED images the diffraction spots were semiautomatically identified (see figure 5.14, middle column). A set of several possible phases in the system Co–Si–Ti, i. e. Co, α-titanium, Si, Co_2Si, CoSi, $CoSi_2$, CoTiSi, Co_2TiSi, Co_3Ti_2Si [130], were considered to be

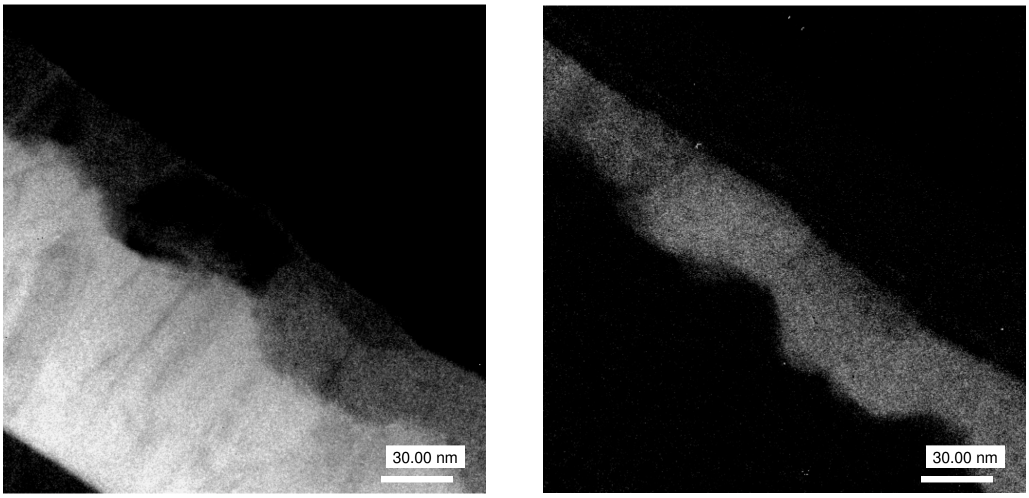

(a) Si EFTEM map. (b) Co EFTEM map.

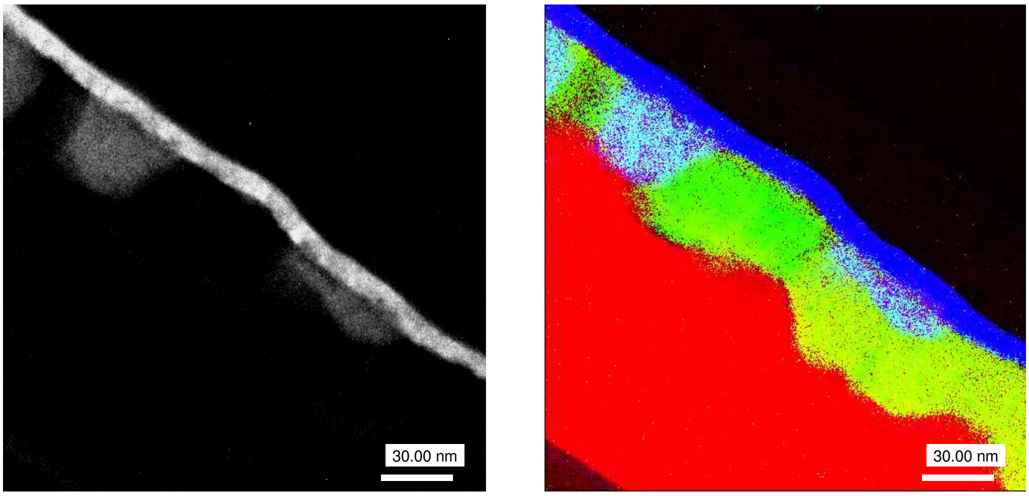

(c) Ti EFTEM map. (d) Superposition of a)–c). False color image: Red = Si, Green = Co, Blue = Ti.

Fig. 5.12: EFTEM images of sample heated up to 610 °C. Deposited metal layer thickness was 10 nm for Co and Ti capping layer [25].

possible solutions for the simulation of the diffraction pattern. This set was chosen because it contains the phases that are stable at room-temperature, crystallographic data was available and it neglects high-pressure phases. The second step is to simulate the CBED patterns with the crystallographic data of the considered phases and to determine the best match of the measured and simulated diffraction patterns. Figure 5.14 shows the results for the spots L945, L946, L947, L949, and L952 where CoTiSi yielded the best possible match. Various other phases could also be identified. The measuring point L948 could be attributed to α-Ti, although no Ti diffraction maxima could be found using SR-XRD. CoSi in L942, L943, and L950 as well and $CoSi_2$ in L944 was also found (see figures C.1 and C.2), which was confirmed by SR-XRD, as was shown in figure 5.1.

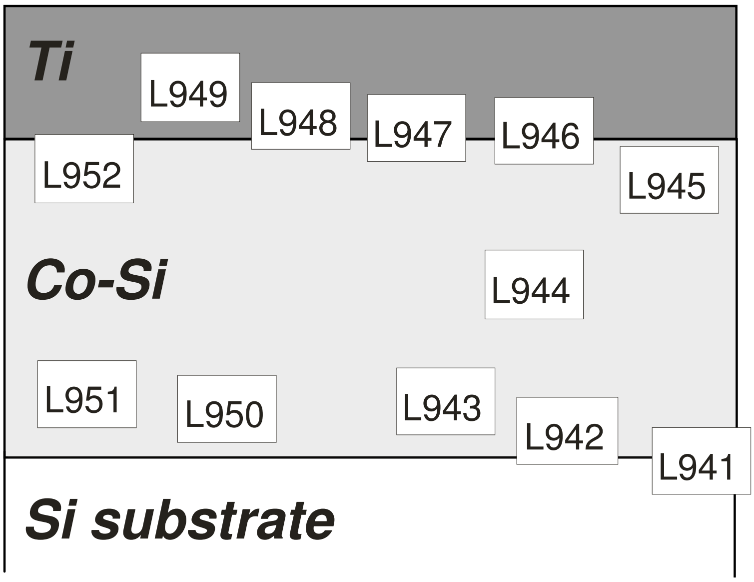

Fig. 5.13: Sketch of analyzed sample positions of CoTiSi CBED investigations.

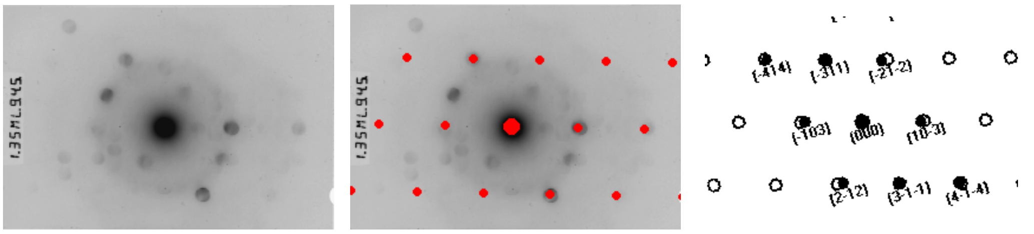

L945: CBED image, ELDISCA recognized diffraction spots, best fit with zone axis [3 8 1].

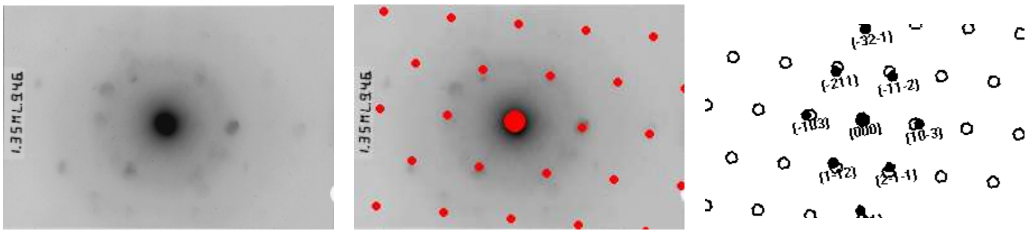

L946: CBED image, ELDISCA recognized diffraction spots, best fit with zone axis [3 5 1].

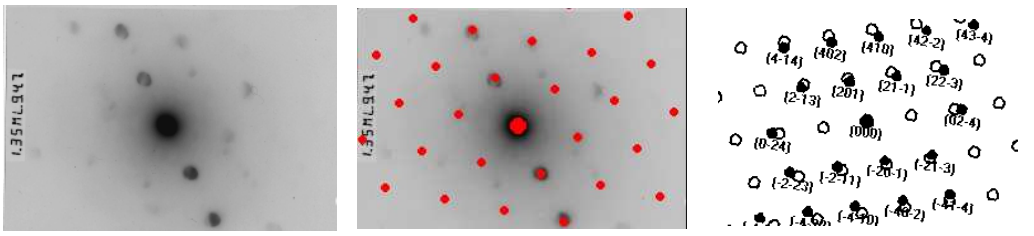

L947: CBED image, ELDISCA recognized diffraction spots, best fit with zone axis $[1\,\bar{4}\,\bar{2}]$.

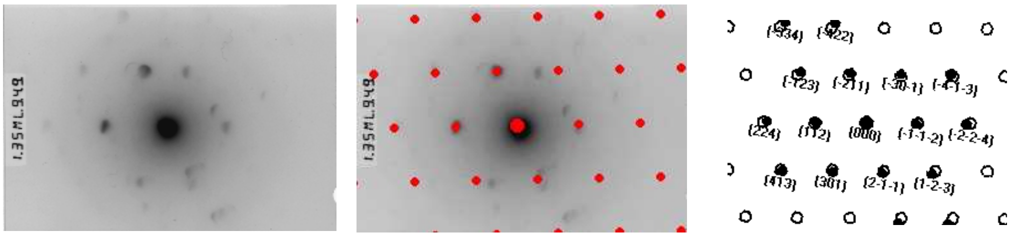

L949: CBED image, ELDISCA recognized diffraction spots, best fit with zone axis $[1\,5\,\bar{3}]$.

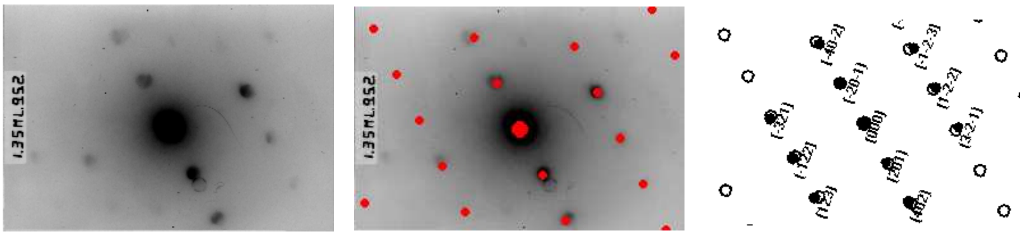

L952: CBED image, ELDISCA recognized diffraction spots, best fit with zone axis $[25\bar{4}]$.

Fig. 5.14: Summary of CBED results that match ternary CoTiSi phase. Left column: CBED pattern. Center column: Superimposed ELDISCA simulation. Right column: best fit with indexed diffraction maxima.

5.3 Size effects

5.3.1 Layer thickness

A set of B^+ doped Ni samples was prepared to investigate the impact of the deposited metal layer thickness. A layer thickness of 8 nm, 10 nm, and 15 nm for the deposited Ni layer was chosen.

Impact of layer thickness on the nickel silicidation process

Single crystal substrates

The onset of Ni_2Si formation could not be determined with starting temperatures of 200 °C. At 200 °C, and up to 250 °C, all samples showed diffraction peaks of Ni_2Si. The starting point of NiSi formation seems to be independent of the deposited Ni layer thickness and is situated at a temperature of about 275 °C for these long time anneals. However, in the 15 nm Ni samples Ni_2Si can still be found at 325 °C, whereas the conversion from Ni_2Si to NiSi is completed at 300 °C for the 8 nm Ni and 10 nm Ni samples. The formation of $NiSi_2$ starts below 550 °C in the 8 nm Ni samples. No indications for $NiSi_2$ formation can be found at 600 °C for the 10 nm Ni sample and 650 °C for the 15 nm Ni sample, respectively. Figure 5.15 summarizes the SR-XRD results.

Polycrystalline substrates

In the temperature range between 200 °C and 250 °C only Ni_2Si could be found within 10 nm Ni and 15 nm Ni samples. At 275 °C the 15 nm Ni sample showed diffraction peaks of NiSi. At 300 °C and 350 °C the conversion from Ni_2Si to NiSi was completed for the 10 nm Ni and 15 nm Ni, respectively. NiSi is stable up to at least 550 °C for the 15 nm Ni sample. In the 10 nm Ni sample $NiSi_2$ could be found at 600 °C. No proof for $NiSi_2$ formation is detected in the capped sample up to 655 °C. Figure 5.15 summarizes the SR-XRD results.

The thinner the deposited metal layer was, the lower the formation and conversion temperatures of the formed Ni silicides were. An increase in layer thickness of 50 %, i. e. from 10 nm to 15 nm, resulted in an increased formation temperature for Ni_2Si of at least 25 K.

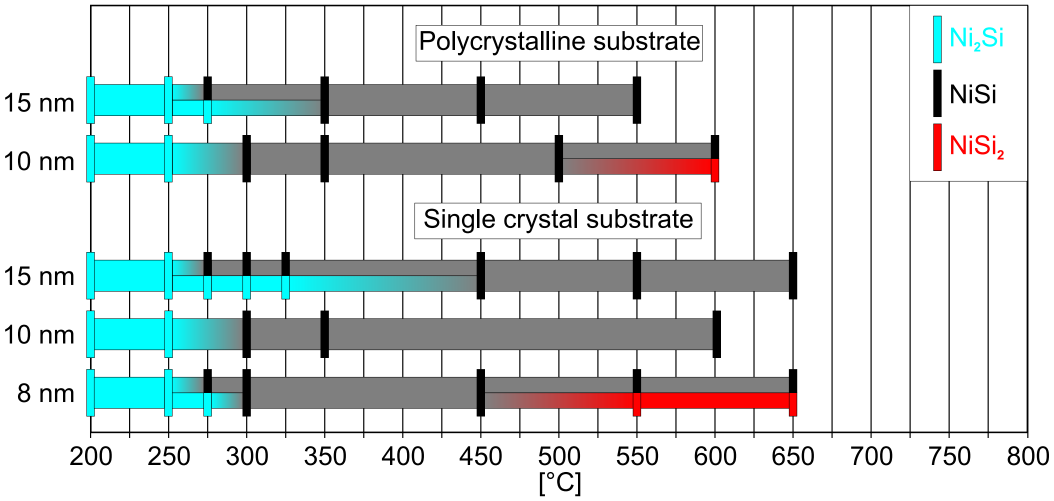

Fig. 5.15: Summary of 32 SR-XRD results of B^+ Ni|Si samples without a capping layer. Vertical boxes represent actual measuring temperatures. All boxes and bars are color coded, i. e. cyan stands for the metal-rich silicide, black for monosilicide, and red for the disilicide phase. Horizontal bars connect measured temperatures. Color gradients indicate that a phase transition started between its lower and upper limit. Monochrome bars show that no new phase was formed between its lower and upper limit. Boxes with two different colors indicate that at this temperature two phases coexist.

Interface roughness of nickel silicide

Figure 5.16 shows TEM images of Ni-silicidized regions as well as the respective EELS spectra of fully processed wafers. In figure 5.16 a), the interface to the polycrystalline silicon substrate is much smoother compared to the interface seen in figure 5.16 b). In addition, EELS spectra were taken from silicidized regions to identify the silicides. The near-edge fine structure of the EELS spectra allowed the silicide phases to be identified.

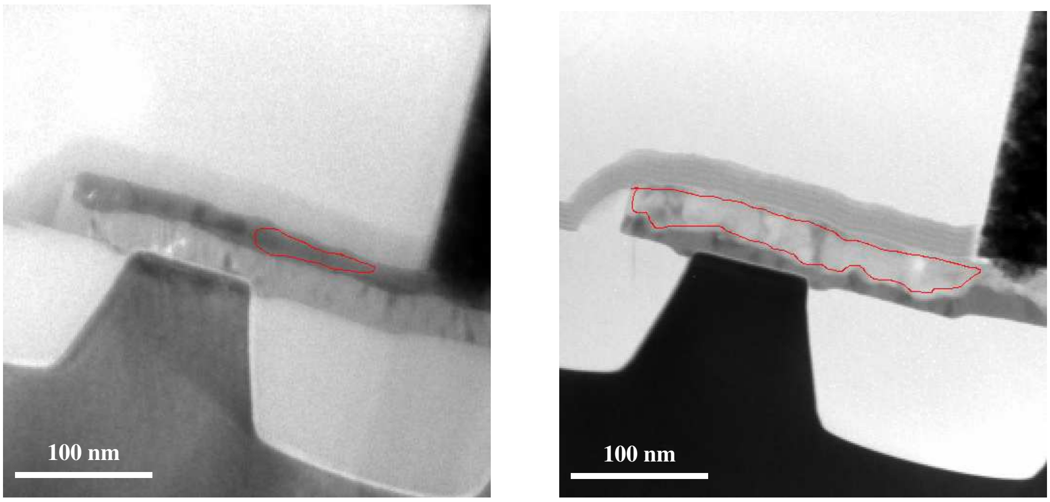

(a) NiSi smooth interface to polycrystalline substrate.

(b) $NiSi_2$ rough interface to polycrystalline substrate.

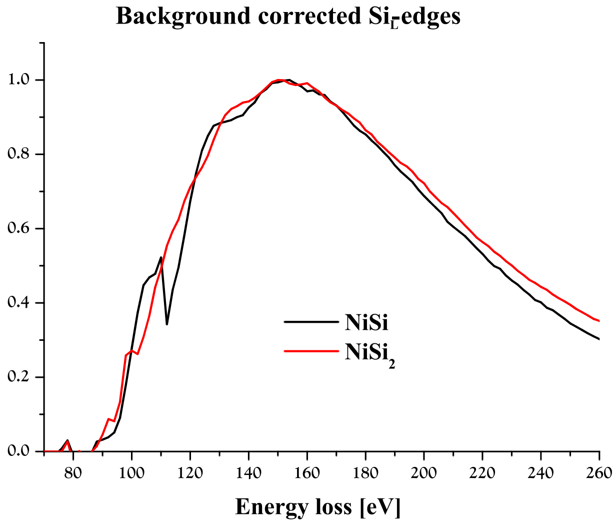

(c) EELS spectra. Fine structure of the Si_L-edge indicates silicide phases.

Fig. 5.16: TEM images of NiSi and $NiSi_2$: diffusion-controlled (NiSi: upper part) vs. nucleation-controlled ($NiSi_2$: lower part) formation. Red regions indicate area analyzed by EELS.

5.3.2 Agglomeration of silicide layers

Agglomeration of $Co_{0.95}Ni_{0.05}Si_2$ layers

An example of partial agglomeration, a term introduced by Pramanick [131], is demonstrated in figure 5.17. The sample, with a original layer stack of 15 nm Co-Ni (5 at. % Ni) on single crystal silicon substrate, that is shown in figure 5.17 was subjected to an annealing temperature of 650 °C. The overall annealing time was more than 2 hours since it was also investigated by means of SR-XRD at the ESRF. It is clearly seen that the layer is no longer continuous after the thermal treatment. The difference in contrast in the Co map (figure 5.17 c)) between the trapezoid-shaped $Co_{0.95}Ni_{0.05}Si_2$ grains and the disilicide layer is due to a different orientation of the respective grains. Furthermore, agglomeration is a process taking place in two dimension of the layer (neglecting the dimension perpendicular to the layer surface), therefore the trapezoid-shaped grains form islands on the $Co_{0.95}Ni_{0.05}Si_2$ layer that also contribute to the higher contrast of these grains in (figure 5.17 c)). This can also be seen in the brightfield image, where the low indexed $Co_{0.95}Ni_{0.05}Si_2$ grains on top of the continuous layer, appear darker (figure 5.17 a)–b)). The Ni content, although near the detection limit, was distributed throughout the $Co_{0.95}Ni_{0.05}Si_2$ layer. The corresponding SR-XRD patterns, that indicate that only $Co_{0.95}Ni_{0.05}Si_2$ is present, are shown in figure D.16. This figure exhibits several diffraction maxima corresponding to $Co_{0.95}Ni_{0.05}Si_2$, indicating that $Co_{0.95}Ni_{0.05}Si_2$ does not grow epitaxially in these samples.

For the case of Co-Ni (5 at. % Ni)|Si samples, partial agglomeration, which already lead to a discontinuous silicide layer, occurs at temperatures as low as 650 °C, where the conversion to the disilicide phase $Co_{0.95}Ni_{0.05}Si_2$ is completed.

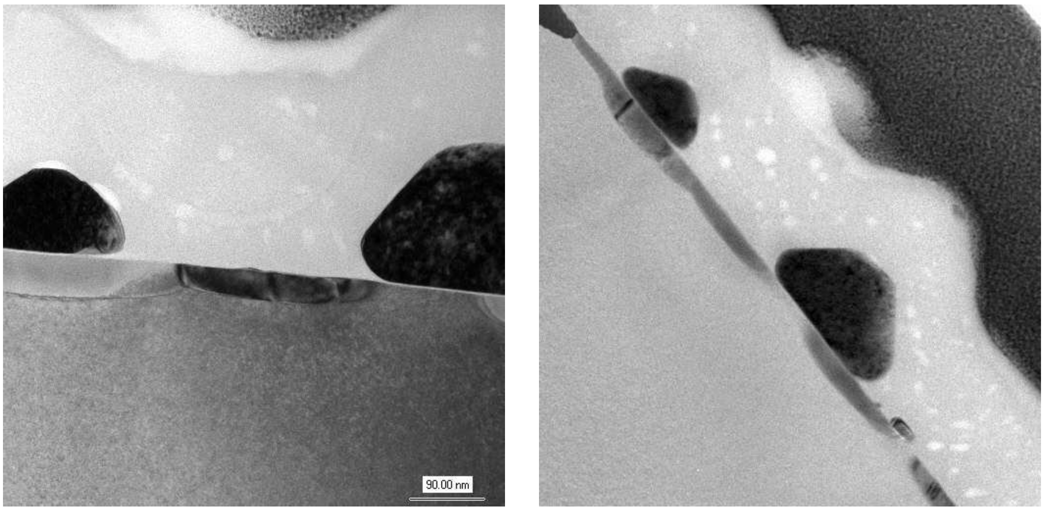

(a) TEM brightfield image. (b) TEM brightfield image.

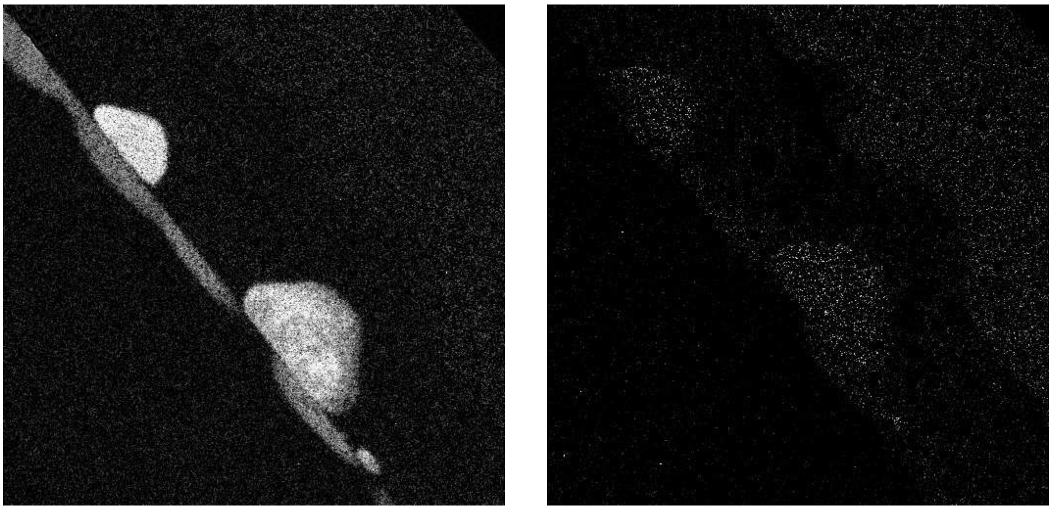

(c) EFTEM Co map. (d) EFTEM Ni map.

Fig. 5.17: TEM images of partial agglomeration of a Co-Ni(5 at. % Ni)|Si sample annealed at 650 °C. Images b)–d), i. e. the EFTEM elemental maps and the corresponding brightfield image, show the same spot. The bright layer on top of the silicide, visible in the brightfield images, is residing epoxy glue due to the TEM sample preparation. The deposited metal layer thickness was 15 nm.

Agglomeration of NiSi layers

Figure 5.18 a) shows a top-down-view SEM image of an initially deposited 12.5 nm Ni layer that was annealed to 700 °C for 30 sec. The contrast in the SEM image corresponds to different materials on the surface. The elemental maps (figures 5.18 b)–c)) show the rather inhomogeneous distribution of Ni and Si, respectively. In the Ni map, dark spots are visible, indicating areas with a depletion in Ni. In the Si map, exactly the same spots show an enrichment of Si, meaning the formation of silicon "islands" surrounded by NiSi. Figure 5.20 AFM images of NiSi layers. The mapped areas were 1 x 1 μm^2 and 10 x 10 μm^2, respectively. Again, the agglomeration effect can clearly be seen from the images. Especially the comparison with the sample heated up to 450 °C (figure 5.19) reveals a larger mean grain size as well as a much more inhomogeneous surface of the NiSi sample subjected to 700 °C for 30 sec (figure 5.20). As can be seen from the AES and AFM investigations, the agglomeration of Ni silicide films starts before the conversion to NiSi$_2$ proceeds to a significant extent, i. e. NiSi$_2$ content of $\gtrsim$3–5 vol. %, since XRD and resistivity measurements revealed that the films consisted of NiSi.

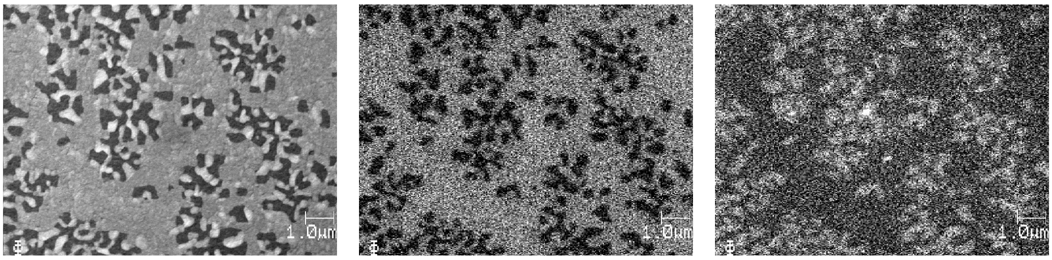

(a) SEM top-down view of an agglomerated NiSi layer.

(b) AES elemental map of Ni surface distribution.

(c) AES elemental map of Si surface distribution.

Fig. 5.18: AES data of agglomerated NiSi layer. Sample annealed at 700 °C for 30 sec. SEM top-down view (a). Elemental maps (b)–c)) to show Ni and Si surface distribution. Deposited Ni layer thickness was 12.5 nm.

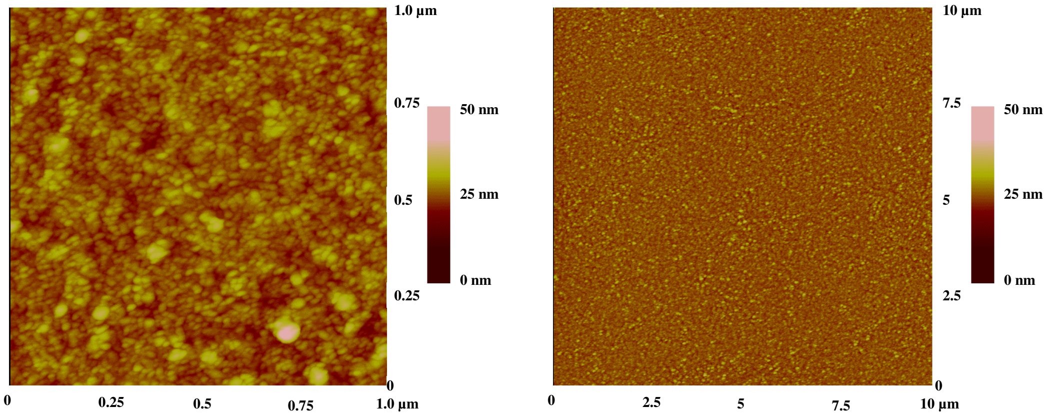

(a) AFM image of an 1 x 1 μm^2 area of NiSi layer.

(b) AFM image of a 10 x 10 μm^2 area of NiSi layer.

Fig. 5.19: AFM maps of NiSi layer. The sample was annealed at 450 °C for 30 sec. Height scale (0–50 nm) on the right hand side of the images. Deposited Ni layer thickness was 12.5 nm.

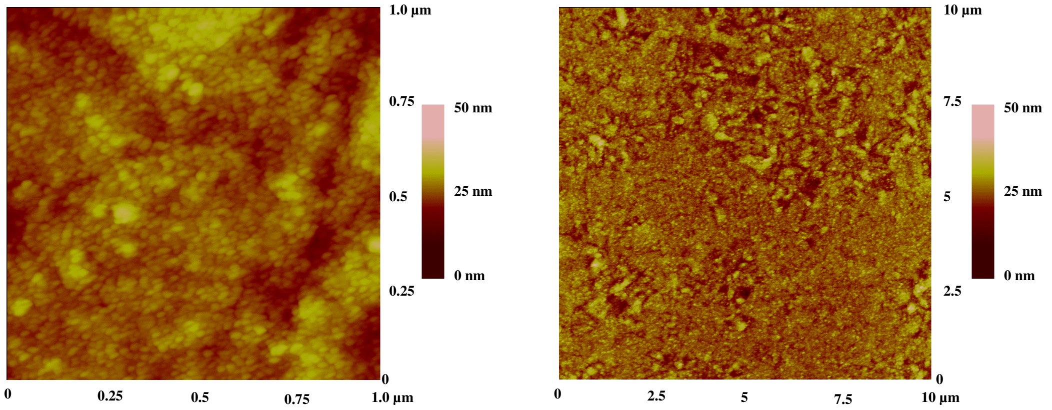

(a) AFM image of an 1 x 1 μm^2 area of NiSi layer.

(b) AFM image of a 10 x 10 μm^2 area of NiSi layer.

Fig. 5.20: AFM maps of NiSi layer. The sample was annealed at 700 °C for 30 sec. Height scale (0–50 nm) on the right hand side of the images. Deposited Ni layer thickness was 12.5 nm.

Degree of agglomeration

In order to estimate the degree of agglomeration of silicide layers, top-down SEM images were taken. In these images, Si appears dark, while NiSi appears bright. By means of digital image processing, and setting an appropriate contrast threshold, the separation of the two phases is possible. This enables the calculation of the surface area fraction of each phase. The area fraction of Si on the surface is no direct measure of agglomeration. However, the higher the fraction of Si of the surface is (in area %), the further the agglomeration process has proceeded, obviously never reaching 100 %. The morphology of the NiSi layers is shown using TEM cross-section images. All samples had an initially deposited Ni layer of 12.5 nm and were subjected to an annealing temperature of 650 °C for 30 sec to form the silicide layer. After the silicidation step, remaining Ni or metal-rich Ni silicides were etched off. By means of X-ray diffraction and electrical resistivity measurements, it was confirmed that the formed silicide layer consisted of NiSi. As agglomeration effects lead to a degradation of sheet resistance R_s, experiments were carried out to evaluate the impact of doping or pre-amorphization implantation (PAI) prior to silicidation. The samples of figure 5.21 were doped with $2.5 \cdot 10^{15}$ at/cm^2 and got no post-pre-amorphization annealing. They showed a Si surface area fraction of 5 area %. The TEM image shows a continuous NiSi layer.

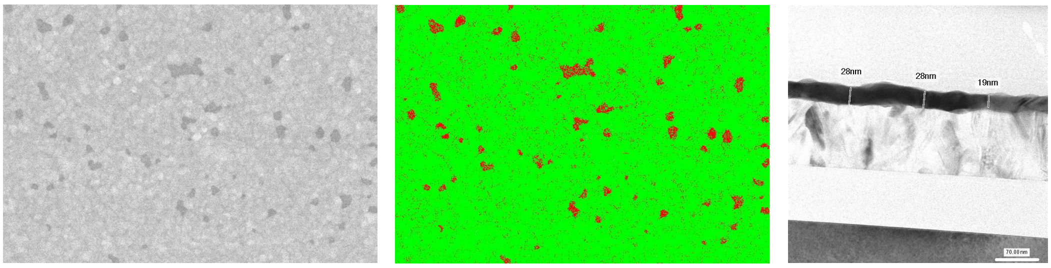

Fig. 5.21: Left: SEM top-down view of NiSi layer.
Middle: Area fraction analysis for several crystalline phases of NiSi layers, Si red, NiSi green.
Right: TEM cross-section image of NiSi layer.
Whole width of SEM images is 295 μm, TEM image is 440 nm wide.
Area fraction analysis: 5 area % Si on surface. Sample doped with $2.5 \cdot 10^{15}$ at/cm^2 B$^+$. Initially deposited layer thickness of Ni was 12.5 nm. For an enlarged view of TEM images see figure E.1 a).

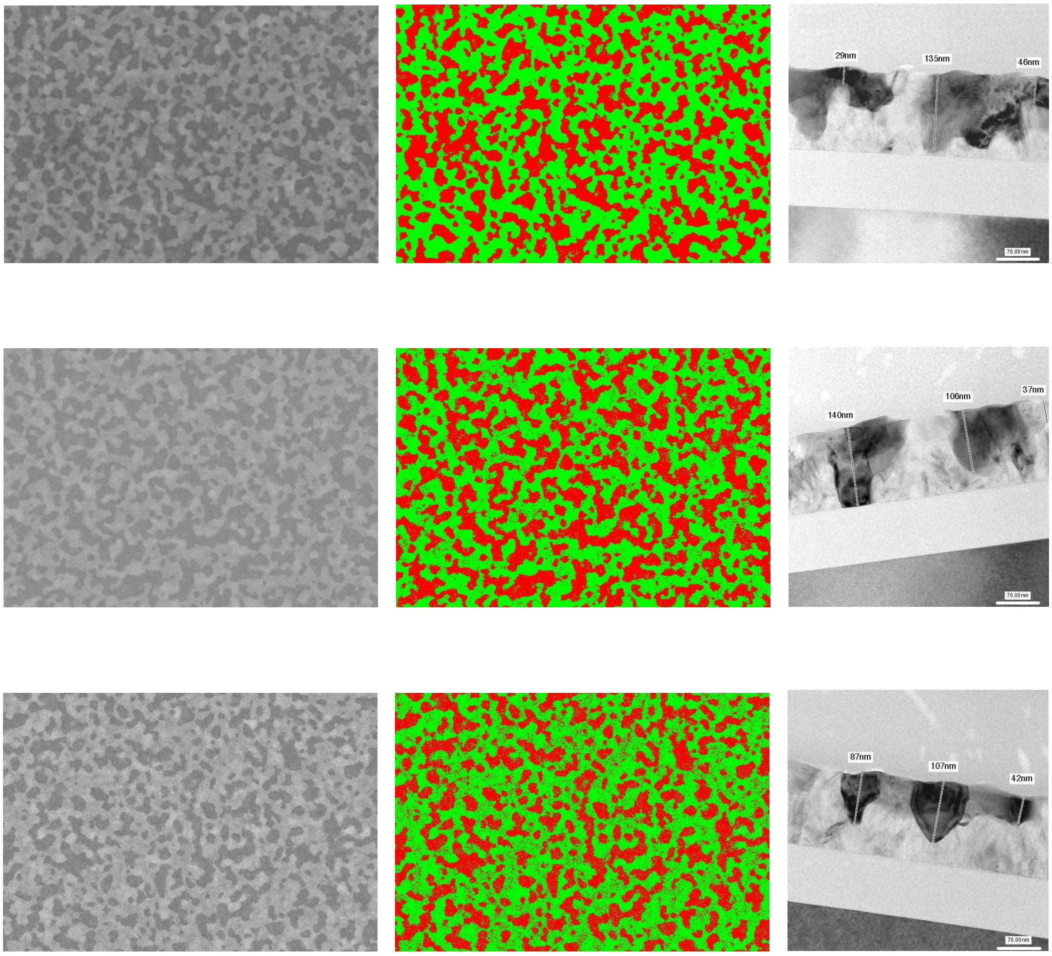

Fig. 5.22: First column: SEM top-down view of agglomerated NiSi layers.
Second column: Area fraction analysis for several crystalline phases of agglomerated NiSi layers, Si red, NiSi green.
Third column: TEM cross-section images of NiSi layers.
All samples subjected to Xe^+ pre-amorphization implant with a dose of $2{\cdot}10^{14}\,\mathrm{at/cm^2}$ with subsequent post-PAI annealing of 0 sec, 30 sec, and 300 sec (1^{st}, 2^{nd}, 3^{rd} row) and a RTA step of 650 °C for 30 sec. Initially deposited layer thickness of Ni was 12.5 nm.
Whole width of SEM images is 295 μm, TEM images are 440 nm wide.
Area fraction analysis: 42 area % Si on surface, regardless of PAI annealing time. For an enlarged view of TEM images see figure E.1b)–d).

The samples of figure 5.22 were subjected to a PAI step through implantation of 2·10^{14} at/cm^2 Xe$^+$. After silicidation, they got post-PAI anneals at 600 °C for 0 sec, 30 sec, and 300 sec, respectively. They showed a Si surface area fraction of 42 area %, regardless of the additional annealing time. All of the samples were affected by severe agglomeration such that the NiSi layer is fairly discontinuous. The PAI step failed in reducing the degree of agglomeration for these Ni silicide films. The angularity of the NiSi grains increased with post-PAI annealing time heading towards their equilibrium shape (see section 6.5).

The comparison of figure 5.21 and figure E.1 b)) reveals that the doping is much more efficient in retarding agglomeration. Both samples were treated equally with respect to thermal treatment, the only difference was on the one hand the B$^+$ doping and on the other hand Xe$^+$ pre-amorphization.

Summary of agglomeration results

Agglomeration of NiSi layers could be investigated directly by means of AES elemental mapping as well as SEM imaging. Samples that were subjected to a thermal treatment of 700 °C for 30 sec suffered from severe agglomeration. The agglomeration of the layer started prior to the formation of NiSi$_2$, which could be also be proven. The average NiSi grain size increased significantly by increasing the annealing temperature from 450 °C to 700 °C for 30 sec each.
Partial agglomeration of a Co$_{0.95}$Ni$_{0.05}$Si$_2$ layer could be observed for a sample subjected to 650 °C for ≈3–4 hours. The evolution of the agglomeration process proceeded until islanding occurred and the grains almost developed their equilibrium shape (see figure 6.12).
Estimates about a degree of agglomeration could be made by means of calculation the surface area fraction of Si of a NiSi layer. Experiments with Ni layer subjected to RTA conditions of 650 °C for 30 sec and a pre-amorphization step showed that the degree of agglomeration is independent of a post-PAI annealing time, i. e. post-PAI had no impact on the degree of agglomeration. Boron doping, however, leads to a significant reduction of agglomeration effects. The samples with B$^+$ doping exhibited a continuous NiSi layer in contrast to the PAI samples that showed discontinuous NiSi layers.

Chapter 6

Discussion of results

6.1 Temperature limits for low-resistivity phases

6.1.1 Capping layer

Capping layers can play an important role for the silicidation process. The most commonly used capping layers Ti and TiN were examined in this work. They are able to improve the thermal stability of the silicide layers, i. e. they are capable of retarding agglomeration of thin silicide layers [41, 125].
A Ti capping layer has the effect of shifting formation temperatures to higher values for the formation of Co and Co-Ni silicides. This impact on $CoSi_2$ or $Co_{0.95}Ni_{0.05}Si_2$ formation from Co or Co-Ni layers, as can be seen from figures 5.2 and 5.5, was also reported in literature [26, 53]. The XRD results showed, that the conversion from the respective monosilicides to $CoSi_2$ and $Co_{0.95}Ni_{0.05}Si_2$ was retarded for more than 100 K. This stabilizing effect of a Ti capping layer on silicide formation for Co and Co-Ni silicides (with various Ni contents) was also confirmed by Chamirian *et al.* [53], and recently by Kittl *et al.* for Ni silicides [31] by R_S measurements and *ex situ* XRD investigations.
Figure 5.9 shows that the formation temperature of $NiSi_2$ was increased by at least 55 K, when a TiN capping layer was applied. Only a very minor impact on the conversion temperature from Ni_2Si to NiSi could be observed, and only on single crystal silicon substrates. The TiN capping layer leads to a reduction of heterogeneous nucleation of $NiSi_2$. Therefore, mainly the conversion from NiSi to $NiSi_2$ is affected. The impact of a TiN capping layer on the thermal

stability of NiSi was also reported by Chamirian *et al.* [128]. In literature, the effect of a lowered onset temperature for Ni silicidation using a Ti capping layer was reported [126]. This was explained by the reduction of interfacial oxide at the Si/Ni interface by Ti. These findings were not confirmed by any other authors, nor by the results presented in this work. This might be due to the sample preparation process using state-of-the-art manufacturing tools and a metal deposition after a pre-clean of the silicon surface, thus no oxide diffusion barrier was present in the investigated samples. Nevertheless, a Ti or TiN capping layer is used to getter oxygen contaminations and other impurities which might affect the silicidation process. Therefore, a reduction of SiO_2 is quite possible, since the free energy change ΔG is negative for this reaction [126]:

$$\Delta G_{750\,^\circ C} \text{ for } Ti + SiO_2 \rightarrow TiO_2 + Si = -34\,kJ/mol \tag{6.1}$$

It is energetically more favorable to form Ni_2Si rather than $TiSi_2$, since the heat of formation for Ni_2Si (-140.6 kJ/mol) is higher compared to that of $TiSi_2$ (-134.3 kJ/mol).
A Ti or TiN capping layer retards the silicidation process due to the interaction of the deposited metal with the capping layer, since it reduces the mobility of Co and Ni during silicidation [2]. Ti atoms segregate at the interface metal/Si [126, 131]. This leads to a reduced mobility of the metal atoms, since the main diffusion-controlled mass transport takes place along grain boundaries.

The fact that the Ti capping layer had a higher impact on the formation temperatures of the respective disilicides can be explained by the higher mobility and higher reactivity of the Ti atoms originating from a pure Ti layer rather than from Ti-nitride phases, since the bonding energy for a Ti-Ti bond in Ti is significantly lower than for a Ti-N bond in TiN[20].

No agglomeration was found in Ni|Si samples subjected to an annealing temperature of 650 °C with a 15 nm TiN capping layer, whereas samples with epitaxially grown $NiSi_2$ (and no capping layer) showed clear island formation (see figure 5.10). This effect of decreased agglomeration is due to a pinning of grain boundaries at the interface silicide/capping layer, thus leading to less severe grain boundary grooving [125–127].

---

[20] 141.4 ±21 kJ/mol for Ti-Ti in Ti compared to 476.1 ±33.1 kJ/mol for a Ti-N bond in TiN [132].

The usage of a Ti(N) capping layer can even lead to the formation of ternary Co-Ti silicides, especially when the capping layer is not, or only partially, removed after the initial step of silicidation [25]. In section 5.2, the ternary phase CoTiSi was identified by means of CBED. In literature, several ternary Co-Ti-Si phases are reported, amongst them CoTiSi, $Ti_2Co_3Si_3$, and $Ti_4Co_4Si_7$ as possible phases [133, 134]. The phase identification was sometimes rather uncertain due to the small sample volume and the analytical techniques used [127].

However, the capping layer usually is stripped off after a first RTA step, so the capping layer effect might be reduced on CMOS devices with respect to the formation of $CoSi_2$.

6.1.2 Dopants

Silicon as a semiconducting material needs to be doped to adjust its properties to a desired level of conductivity. The resistivity of Si can be altered in the order of several magnitudes by ion implantation of either acceptor atoms (e. g. B, In) or donor atoms (e. g. As, P). After implantation, a high-temperature step ($T \geq 1000\,°C$) follows in order to activate the implanted species, i. e. to incorporate the implanted atoms into the silicon lattice. These implants have an impact on the silicidation process, particularly formation and transition temperatures are generally higher in doped samples compared to undoped samples (see figure 5.7 and figure 5.4). This was also confirmed by several authors [44, 45, 69].

The SR-XRD results of the Co-Ni|Si samples showed, that doping of the substrate leads to a higher thermal stability of $(Co_{0.95}Ni_{0.05})_2Si$, the metal-rich phase, of at least 25 K on single crystal substrates. CoSi ($Co_{0.95}Ni_{0.05}Si$) was stabilized to ≥75 K on As^+ and P^+ doped single crystal substrates. However, the formation temperature of CoSi ($Co_{0.95}Ni_{0.05}Si$) was lowered by at least 25 K on As^+ doped single crystal substrates. On polycrystalline substrates, the thermal stability of $(Co_{0.95}Ni_{0.05})_2Si$ was decreased by 25 K.

As^+ doping stabilizes NiSi, i. e. NiSi is stable for at least 50 K higher temperatures, compared to P^+ doping, which might be due to a somewhat higher binding energy to Si of 0.054 eV compared to 0.045 eV for P, since the bonding between Si and the implanted species must be destroyed to form a silicide. For Ni silicides, boron seems to stabilize the metal-rich phase (Ni_2Si) on polycrystalline Si substrates slightly (see figure 5.7) in contrast to what is reported by Lavoie *et al.* [44]). There, p-type doping decreases the formation temperatures of metal-rich Ni silicides by more than 50 K. However, these experiments were conducted on silicon-on-insulator (SOI) substrates, which behave differently compared to bulk silicon substrates [135]. When high doses of implants are applied, and when not all implanted atoms are incorporated into the Si lattice, which is very likely in that case, then the effect of grain boundary stuffing can occur [131]. This phenomenon leads to reduced mobility of metal atoms, especially on polycrystalline substrates, which in turn leads to higher formation temperatures and therefore to less severe agglomeration effects. During silicidation, the dopants are likely to be expelled to a certain extent from the formed silicides, and therefore, are prone to segregate at grain boundaries. Although this local enrichment of dopants changes the local concentration of implanted atoms significantly, no formation of Co_xAs_y or Co_xB_y phases could be proven [136].

6.2 Mechanisms for phase formation and growth in silicides: nucleation and diffusion

Heterogenic nucleation is the predominant nucleation process in thin film layers. Since lattice defects, e. g. grain boundaries, impurities, interfaces, unsaturated bonds, etc. are regions of lower bonding energies, at these sites the activation energy for site changes is also lowered. Those regions act as nucleation centers, i. e. sites where nucleation is most likely to happen. As the energy needed for the formation of nuclei is therefore lower in polycrystalline materials compared to single crystals, the overall lower formation and transformation temperatures on polycrystalline substrates (see figures 5.7 and 5.4) can be explained. This was also confirmed in literature [31,69,137], where the formation temperature of $CoSi_2$ and $NiSi_2$ was up to 75 K lower on polycrystalline substrates compared to single crystal substrates.
Whenever nucleation plays the dominant role in the formation of a phase, usually the resulting layers are quite rough. Since (heterogenous) nucleation does not take place uniformly within thin films, the grain growth is therefore nonuniform too. Interfaces tend to be much rougher than it is the case for the formation of diffusion-controlled phases. This effect is damped in thick layers, since the resulting surface/interface is "far away" from the original interface and the intergrowth of many grains lowers the roughness. Therefore, this effect is pronounced in very thin layers, because the phase formation is finished before a smoothing can occur. This confirms results published in literature that show that the formation of $NiSi_2$ and $CoSi_2$ is known to be nucleation controlled [6, 8, 44, 138]. Figure 5.16 shows a comparison of NiSi and $NiSi_2$ on fully processed production wafers. The interface roughness to the polycrystalline silicon substrate is significantly higher for the $NiSi_2$ sample. On the one hand, this indicates that nucleation processes have a strong impact on $NiSi_2$ formation, also under RTA conditions. On the other hand, this result also shows that the formation of NiSi is diffusion controlled rather than nucleation controlled.

Since the difference of ΔH of these phases is small (see table 3.3), the entropy of mixing ΔS can influence ΔG^*. ΔS^* is increased by the alloying and thus ΔG^* and the nucleation temperatures are reduced. The alloying effect of lowering the formation and conversion/transition temperatures for the $(Co_{1-x}Ni_x)_2Si$, $Co_{1-x}Ni_xSi$, and $Co_{1-x}Ni_xSi_2$ phases compared to pure Co silicides that was observed in this work (see figure 5.4) can be explained by the contribution of the entropy of mixing. This alloying effect was also confirmed by various other authors [34,47,48,50,51,53,55,71,72,74]. The higher the Ni content, the lower the formation temperatures of the silicides [45]. The more Ni is present in the system, the more likely it is, that sufficient Ni is available to form a Ni_xSi_y nucleus.

The SR-XRD experiments, that were conducted under quasi-static conditions with annealing times of ≈15–20 min., showed clear evidence for the coexistence of two phases (see figures 5.7 and 5.4). In the investigated nanoscale layers, the supply of the metal stops before the critical thickness $t_{l\beta_S}$ is reached. In that case, one of the fluxes, e. g. $D^{Me}_{\alpha_S}$, becomes 0 and the second phase starts to grow. Due to its diffusion-controlled nature, the phase formation processes tend to follow a parabolic growth rate (growth $\propto t^{\frac{1}{2}}$) for the case of the metal-rich phases up to the monosilicides CoSi and NiSi [6,7,9,139]. Knowing that the investigated nanoscale layers are well below the critical layer thickness t_l, it is obvious that the reactions within these films that lead to the formation of the second formed phase are supply-controlled. That means, the second phase is formed at lower temperatures (for the same annealing times) in thin films compared to bulk samples, since the second phase formation starts when the supply of Me atoms ceases. Furthermore, another deliberation must also be taken into account. The average grain size within nanoscale layers is significantly smaller than for bulk samples. It is in the range of 1–10 nm (the layer thickness itself) for nanoscale layers and about 1 μm for bulk samples [73]. This leads to a much more pronounced grain boundary diffusion and thus to a considerably higher effective diffusion coefficient, thus accounting also for the lowering of the formation and conversion temperatures.

Phase formation sequence in the system Co–Si

The phase formation sequence in the case of Co silicides was found to be for all varied parameters:

$$Co_2Si \rightarrow CoSi \rightarrow CoSi_2$$

This can be seen in figure 5.1. Although at the starting temperature Co_2Si and CoSi are present, it is clear that Co_2Si is the first phase that is formed, since it has the lowest heat of formation ΔH^0_F, the ratio of Me:Si is highest for Co_2Si reflecting the conditions at the interface Me:substrate and from other SR-XRD experiments. This cannot be directly expected from the equilibrium phase-diagram, figure A.1, although only three phases are known to exist below 400 °C (compare section 2.3). From that result it can be concluded that Co_2Si is the phase with the lowest effective reaction barrier at the interface. Since the supply of Si could be considered to be infinite, no diffusion barrier existed, and the experiments were carried out under quasi-static conditions, the shown order of subsequent silicide formation was the same as reported in literature [6, 8, 75, 139, 140].

Phase formation sequence in the system Co–Ni–Si

The phase formation sequence in the system Co-Ni(5 at. % Ni)-Si could be determined also. It was very similar to the phase formation in the system Co-Si for all varied parameters:

$$(Co_{0.95}Ni_{0.05})_2Si \rightarrow CoSi \rightarrow Co_{0.95}Ni_{0.05}Si_2$$

As is shown and discussed in further detail in chapter 6.3, CoSi and NiSi are almost immiscible. Therefore, in the phase formation sequence only CoSi is listed. The AES results showed that the Ni content was enriched at the interface silicide/Si substrate. It can be assumed that Ni is incorporated into Co_2Si and into the disilicide after complete silicidation, since Co_2Si and Ni_2Si as well as $CoSi_2$ and $NiSi_2$ form an uninterrupted solid solution series [48, 51, 55, 72]. The alloying of Co with 5 at. % Ni did not change the phase sequence, (see section 5.1.2, and especially figure 5.4), however, the formation temperature was reduced. This finding was also confirmed in literature ny RBS, R_S measurements, *ex situ* XRD, and AES [34, 51–53].

The phase formation sequence in the system Co-Ni-Si could also be confirmed with AES. Figure 6.2 shows depth profiles of Co-Ni|Si samples after various RTA treatments. This figure shows the phase formation sequence of $(Co_{0.95}Ni_{0.05})_2Si \rightarrow CoSi \rightarrow Co_{0.95}Ni_{0.05}Si_2$ which can be concluded from evaluating the ratio of Co:Si. Starting with a mixture of Co_2Si and CoSi, figures 6.2 a), followed by CoSi, 6.2 b)–d), and completed by $CoSi_2$, 6.2 e).

In most cases, two phases coexisted over a certain temperature range. Since the thickness of the silicide layer is far below the critical thickness (see equation 2.29), this is an indication that the phase growth is supply-limited (see chapter 2.3). A capping layer did not have any influence on the phase formation sequence. The type of dopant (n- or p-type) and the used dose also had no impact on it. The same is true for the type of substrate, i. e. polycrystalline substrate or single crystal substrate. The temperatures for phase formation and conversions/transitions were changed significantly in some cases. For example, the temperatures were shifted by 50 K using n-type or p-type dopants, maintaining the same phase sequence [44]. On polycrystalline substrates, the formation and conversion/transition temperatures were decreased significantly compared with the single crystal substrates.

The determined phase formation sequences are in agreement with the subsequent growth of silicides described by Vankar [141], as well as by Gösele and Tu [7] and is also typical for interdiffusion controlled growth processes of welded samples or layer stacks.

Phase formation sequence in the system Ni–Si

In literature several approaches for the determination of the phase formation sequence in the system Ni-Si were pursued. Canali *et al.* [142] examined the case that Ni is in excess, i. e. they deposited ≈280 nm of Ni on top of a ≈90 nm Si film, and found the phase formation sequence to be for all varied parameters:

$$\mathrm{Ni_2Si} \rightarrow \mathrm{Ni_5Si_2} \rightarrow \mathrm{Ni_3Si}$$

This phase formation sequence was explained by the growth of the respective silicide layer until all Si was consumed by this phase and was then succeeded by more and more metal-richer phases.

For thin films however, not all phases can be expected, and usually not all phases occur that are present in the binary phase diagram of Ni-Si (see figure A.2). In the case of a thin Ni film and now assuming that Si is in excess, as it is always the case for a thin Ni film on Si substrate, a different phase formation sequence was presented in literature recently by Lavoie *et al.* [44]:

$$\mathrm{Ni_3Si} \rightarrow \mathrm{Ni_{31}Si_{12}} \rightarrow \mathrm{Ni_2Si} \rightarrow \mathrm{NiSi} \rightarrow \mathrm{NiSi_2}$$

In this work, dealing with thin films of Ni on various Si substrates, the phase formation sequence was determined to be:

$$\mathrm{Ni_2Si} \rightarrow \mathrm{NiSi} \rightarrow \mathrm{NiSi_2}$$

This phase formation sequence, from the metal-rich silicide Ni_2Si to the monosilicide NiSi and finally to the disilicide $NiSi_2$ was found to be valid for all investigated Ni|Si samples and the given experimental conditions (see chapter 5, especially figure 5.7). The SR-XRD experiments showed that neither at *RT* nor at 160 °C silicidation processes occurred that could be detected with the given measuring setup. The metal-rich silicides Ni_3Si and $Ni_{31}Si_{12}$ were not observed. Obviously, the starting temperatures were higher than the thermal stability ranges of these phases. Furthermore, the annealing times of 15–20 min. were such, that the conversion of the metal-rich silicides Ni_3Si and $Ni_{31}Si_{12}$ to Ni_2Si was obviously already completed. Lavoie *et al.* [44] heated up with a ramping rate of $3\,K\cdot sec^{-1}$ and took at least every 100 ms a diffraction pattern. Using this technique, they were able to determine the metal-rich silicides that are stable in a temperature range of only a few K. These low symmetry phases, that are very difficult to identify due to peak overlap, have been missed due to the reasons mentioned above.

Nevertheless, the determination of the onset temperatures of phase formation of Ni_2Si and NiSi is crucial with respect to the manufacturing process of CMOS devices, because Ni_2Si could be target phase prior to the etching off of non-reacted metal and contaminants developing a two-step manufacturing process. The temperature at which $NiSi_2$ starts to form is also of great importance, since no further process steps must exceed this temperature to avoid the formation of this high-resistivity phase. The annealing times of several minutes, and cumulated in the range of a few hours, reflect the conditions of the BEoL processing in semiconductor manufacturing. Different approaches can be taken into account in the development of a process order suitable for mass production. One could be the (direct) formation of NiSi prior to etching off non-reacted metal as well as contaminations. For this approach it is important to know the temperatures at which the formation of NiSi is completed and at which temperatures $NiSi_2$ is formed. Another approach could be to choose the manufacturing conditions in such a way that a mixture of Ni_2Si and NiSi is present prior to the wet-etch process and to fully convert these silicides to NiSi within the BEoL process.

However, the phase formation can be changed significantly using diffusion barriers. Especially when epitaxial films of either $CoSi_2$ or $NiSi_2$ are of interest, it is common to use a diffusion barrier, e. g. a layer of C, Cr, Mo, Hf, Ta, W, Zr, SiN, SiO_2 (OME: oxide mediated epitaxy) or Ti (TIME: titanium mediated epitaxy), to limit the supply of metal atoms [4, 127, 143–147]. In these cases,

the first silicide-phase that is formed is either CoSi [143, 144] or the silicon-rich phases, i. e. $CoSi_2$ or $NiSi_2$ [145–147]. It seems that the efficiency of the diffusion barrier determines whether an "intermediate" monosilicide phase is formed or not. Suggesting, the more impermeable the barrier for the metal atoms is, the more likely direct formation of epitaxial disilicides happens. By means of reactive-CVD (chemical vapor deposition) or MBE, epitaxial $CoSi_2$ can be formed, too [11, 148].
Falke, for example, demonstrated, when a Ti underlayer underneath the Co film is deposited, it is possible to obtain the following phase formation sequence [149]:

$$CoSi_2 \rightarrow CoSi \rightarrow CoSi_2$$

6.3 Limited miscibility of CoSi and NiSi

Since the XRD investigations revealed no clear indication of a formation of ternary Co-Ni silicides, AES experiments were conducted on various Co-Ni|Si samples. The AES conditions for all measurements were:

- Sputtering with: 1 keV Ar^+ ions
- Sputter area: 2.25 mm^2
- Sputtering energy: 20 keV, 20 nA
- Analyzed area: 50 x 60 μm^2

Figure 6.1 shows AES depth profiles[21] of two samples with a 15 nm Co layer with 9 at. % and 5 at. % Ni sputtered from alloy targets of the according composition on an undoped single crystal silicon substrate.

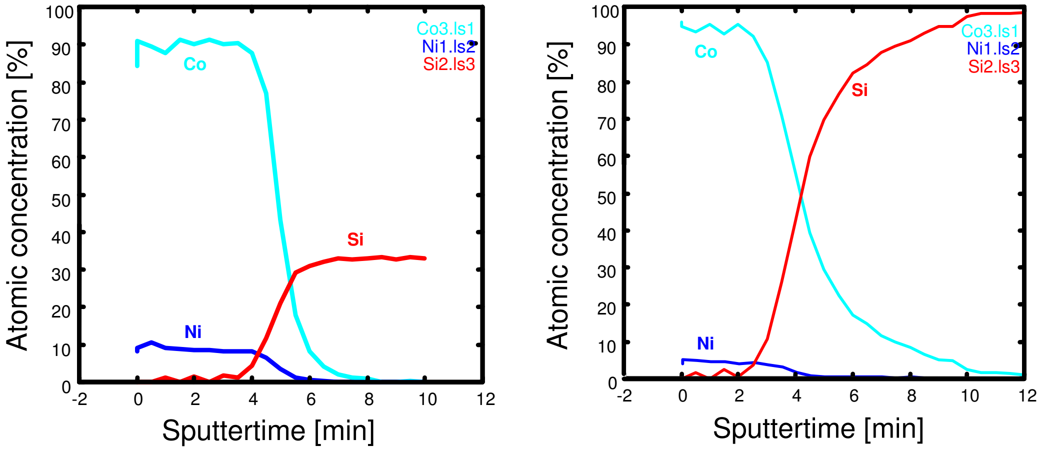

(a) Co-Ni|Si sample with 9 at. % Ni.

(b) Co-Ni|Si sample with 5 at. % Ni.

Fig. 6.1: AES depth profiles of Co-Ni|Si samples after deposition.

The Ni distribution right after deposition of the metal layer is homogenous while sputtering through the metal layer towards the substrate (see figure 6.1).

---

[21] The calculation of the atomic concentration profiles is based on sensitivity factors which were determined by two reference samples, NiSi and $CoSi_2$, respectively. Both were characterized for their stoichiometry, i. e. the ratio of Ni:Si and Co:Si by Rutherford backscattering spectroscopy (RBS). The so calculated atomic concentration values are valid for the components with compositions close to these standards.

After thermal treatment, however, this behavior changes dramatically. An enrichment of Ni can always be found at the interface silicide/silicon as figure 6.2 shows. The AES spectra of figure 6.2 a) shows that for the applied RTA conditions (30 sec @ 450 °C) the ratio of Co:Si is ≈2:1 (and a few at. % Ni, see figure 6.3), indicating that $(Co_{0.95}Ni_{0.05})_2Si$ is present at this temperature within the upper part of the layer stack. Towards the substrate the ratio changes to ≈1:1, i. e. CoSi is present. At this temperature, already an enrichment of Ni at the interface silicide/substrate can be observed. At 475 °C, the ratio of Co:Si is ≈1:1 showing that only CoSi is present. SR-XRD, however, revealed that the conversion to $Co_{0.95}Ni_{0.05}Si_2$ is completed at 475 °C, at least for an annealing time of 2 h. The element ratio of Co:Si of ≈1:1can also be detected at 525 °C. At 550 °C the ratio of Co:Si is 1:1 for short sputtering times, i. e. in the upper part of the layer stack, and slightly >1:1 in the lower part. This observation indicates a bilayer structure with CoSi on top of $CoSi_2$, showing also the point where the formation of $Co_{0.95}Ni_{0.05}Si_2$ already started. At this temperature the element ratio of Co:Si is 1:2, meaning the conversion to $Co_{0.95}Ni_{0.05}Si_2$ is completed at 600 °C.

Figure 6.3 summarizes the Ni concentration vs. sputter time for all samples shown in figure 6.2. Note the slight enrichment of Ni at a sputter time of ≈3 min. This corresponds to the presence of $(Co_{0.95}Ni_{0.05})_2Si$ on top of CoSi. Due to their identical crystal structure (see table 3.2), it can be assumed that Co_2Si and Ni_2Si form a solid solution. Therefore, Ni remains within the crystal lattice of the Co_2Si phase. At 450 °C and 525 °C, the highest concentration of Ni can be found at the interface silicide/substrate, corresponding to a sputter time of ≈8 min. The sample subjected to 475 °C exhibited a slightly thicker deposited metal layer than the other samples. The metal layer thickness was ≈2 nm thicker. Therefore, the highest Ni concentration can be found after a sputter time of ≈13 min. With higher RTA temperatures, the silicidation process further proceeds compared to lower RTA temperatures, i. e. more silicide is formed and thus the silicide thickness t_s increases (see table 3.5 and figure 3.5). With increasing t_s, the distance between the surface of the sample and the interface silicide/substrate is increased, too. This can be seen for RTA temperatures of 550 °C–700 °C, where the highest Ni concentrations can be observed for sputter times of ≈10–12 min. For these RTA temperatures the maxima in the Ni concentration vs. sputter time exhibit a higher full-width half-maximum (FWHM) compared with the lower RTA temperatures, indication an increased t_s. This means the Ni is distributed within a thicker (di)silicide. Therefore, the absolute concentration of Ni in % is reduced for higher RTA temperatures. There is still an enrichment of

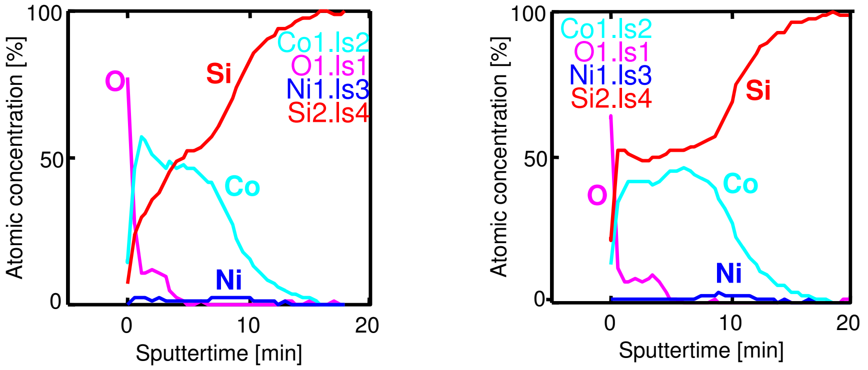

(a) Anneal temperature 450 °C. $(Co_{0.95}Ni_{0.05})_2Si$ on top of CoSi.

(b) Anneal temperature 475 °C. Only CoSi is present.

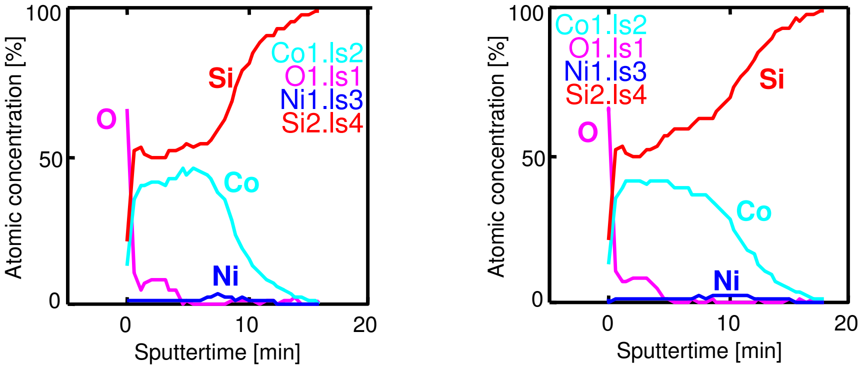

(c) Anneal temperature 525 °C. Only CoSi is present.

(d) Anneal temperature 550 °C. CoSi on top of $CoSi_2$.

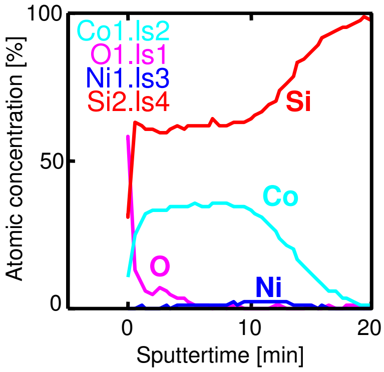

(e) Anneal temperature 600 °C. $CoSi_2$.

Fig. 6.2: AES depth profiles of Co-Ni (5 at. %)|Si samples of different anneal temperatures. Annealing time was 30 sec. Atomic concentration of Co, Ni, O, and Si vs. sputter time is shown.

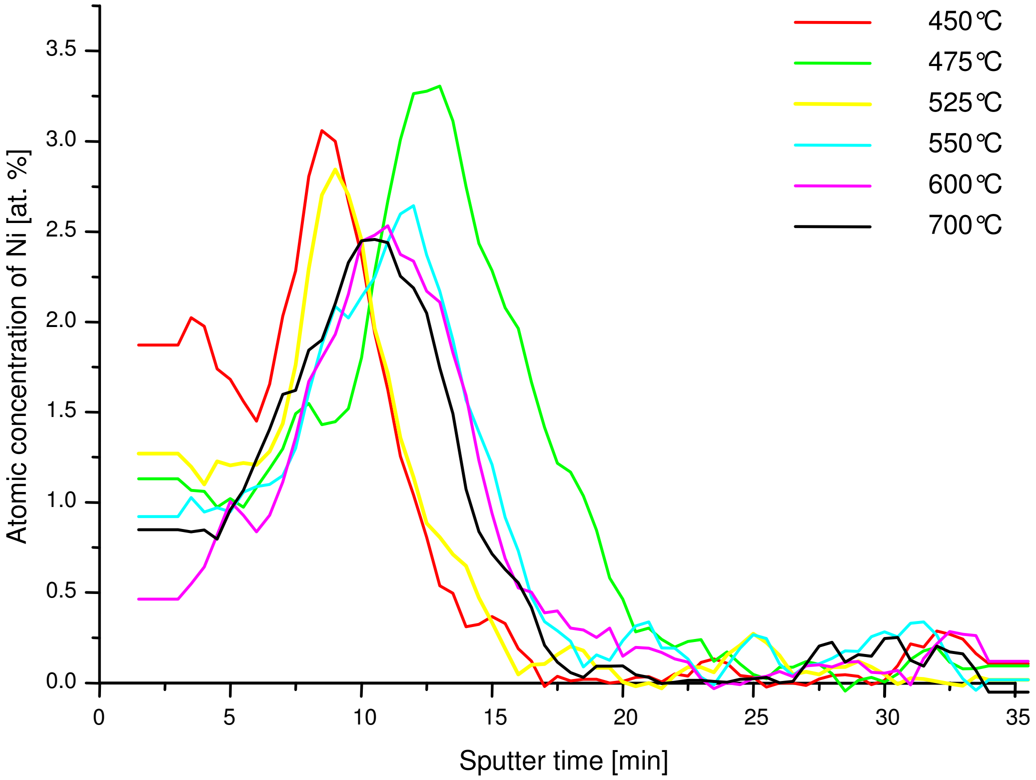

Fig. 6.3: Ni concentration versus sputter time for different annealing temperatures. Co-Ni (5 at. %)|Si samples annealed for 30 sec. Curves smoothed for clarity. Sputter time ∝ sputtering depth. Note the relative enrichment of Ni in the upper part of the layer stack for the sample subjected to 450 °C. The peak maxima correspond to the interface silicide/Si substrate. The sample subjected to 475 °C (green line) exhibited a slightly higher metal thickness of ≈2 nm thicker compared to the other samples. Complete spectra are presented in figure 6.2.

Ni at the interface silicide/substrate, although $Co_{0.95}Ni_{0.05}Si_2$ is formed. The RTA time was too short to rehomogenize the sample completely with respect to the Ni concentration. To prove if an enrichment of Ni at the interface silicide/substrate as discussed above, is also valid for layer stacks, samples with different layer stacks and various relative layer thicknesses have been prepared. Initially, a layer stack of 12.5 nm Ni on top of 14 nm Co on silicon substrate was deposited (figure 6.4 a)). At 350 °C (figure 6.4 b), the Ni silicide formation already started at the interface metal layer/substrate, whereas most of the Ni is still on top of the layer stack. Thermal treatment at higher tem-

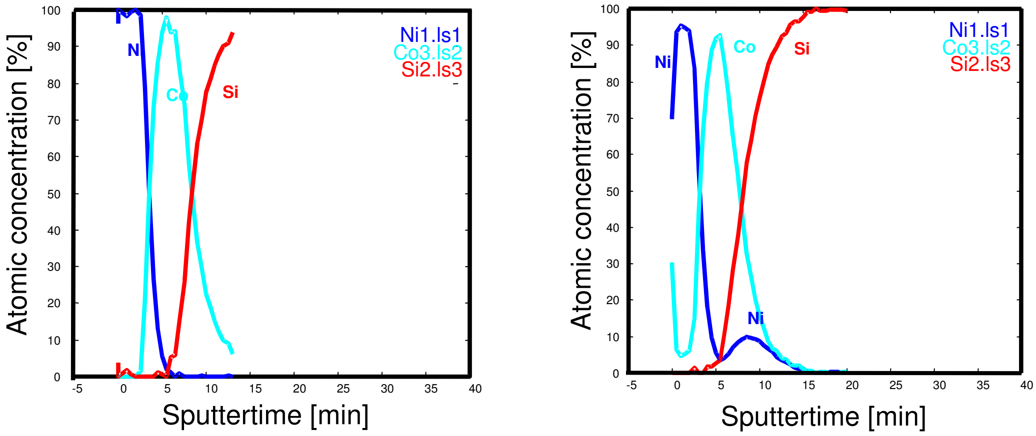

(a) Layer as deposited.

(b) Anneal temperature 350 °C. Ni silicide formation already started at the interface to the Si substrate.

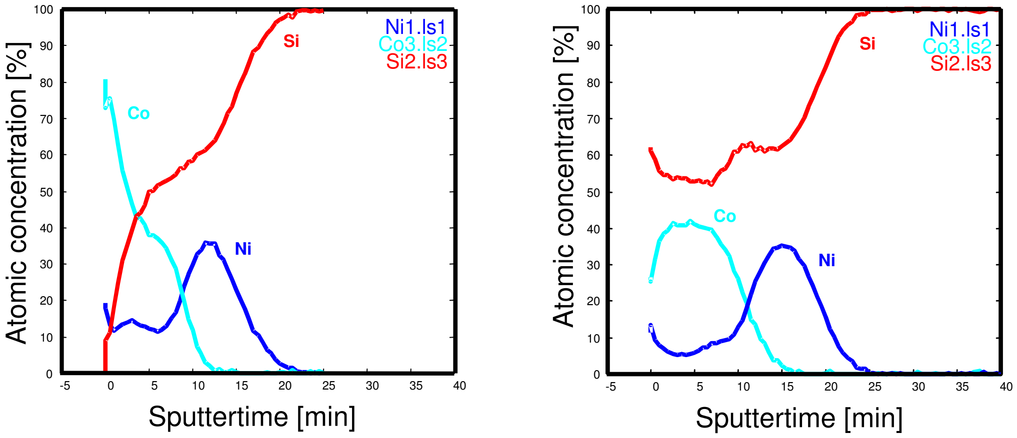

(c) Anneal temperature 400 °C. Co-Ni-Si on top of $NiSi_2$.

(d) Anneal temperature 470 °C. Co-Ni-Si on top of $NiSi_2$.

Fig. 6.4: Layer inversion of Ni | Co | Si layer stack. Initially deposited layer thickness: 12.5 nm Ni | 14 nm Co | silicon substrate. Annealing time was 30 sec.

peratures (figures 6.4 c)–d)) leads to the formation of $NiSi_2$ at the "bottom" of the layer stack while in the upper part Co, Ni, and Si can be found. The same findings were also verified for layer stacks of 5 nm Ni | 15 nm Co | Si substrate, 10 nm Ni | 10 nm Co | Si substrate, and 1 nm Ni | 19 nm Co | Si substrate. For details see figure B.1. Finstad *et al.* also reported that this behavior of Ni can lead to an inversion of an initially deposited order of metal layers [55].

EFTEM investigations were performed on a 10 nm Ni | 10 nm Co | Si substrate sample. Figure 6.5 shows a TEM brightfield image and several elemental mappings. The existence of two different layers, i. e. the layer inversion, can clearly be seen. The lower layer is enriched with Ni, whereas the upper layer is enriched with Co.

The fact that CoSi and NiSi are almost immiscible was proven by AES depth profiling. Whenever Co-Ni or layer stacks of Co and Ni are investigated by means of AES, an enrichment of Ni at the interface to the silicon substrate is detected (see section 6.3 et seq. and figure 6.2). The shown AES profiles state evidently that there is only a very small miscibility in the range of $\lesssim$5 at. % of Ni and Co in the monosilicide of the other metal. This was found to be true for Co with 5 at. % and 9 at. % Ni as well as for a layer stack of Ni on top of Co. This phenomenon can even lead to an inversion of an initially deposited sequence of metal layers [6, 55]. This was also proven by AES depth profiles as it can be seen in figure 6.4. EFTEM examinations, also confirmed these results (see figure 6.5).

Ni and Co posses very similar physical and chemical properties. As neighbors in the periodic system of elements, the difference in radius and atomic mass is only 0.6 % and 0.38 %, respectively [96]. Both crystallize in a fcc lattice and possess similar melting points. They are totally soluble in each other in liquid and form a continuous mixed crystal series, which can be seen in the corresponding phase diagram (see figure A.3) [150]. In table 6.1 some basic properties of Co and Ni are summarized. They also show very similar chemistry and the main silicides that are formed are similar, too, e. g. with respect to crystal structure and heat of formation ΔH_F^0. The metal-rich silicides Me_2Si as well as the disilicides $MeSi_2$ are completely soluble in each other [48, 51, 55, 72] due to isomorphism and similar lattice parameters.

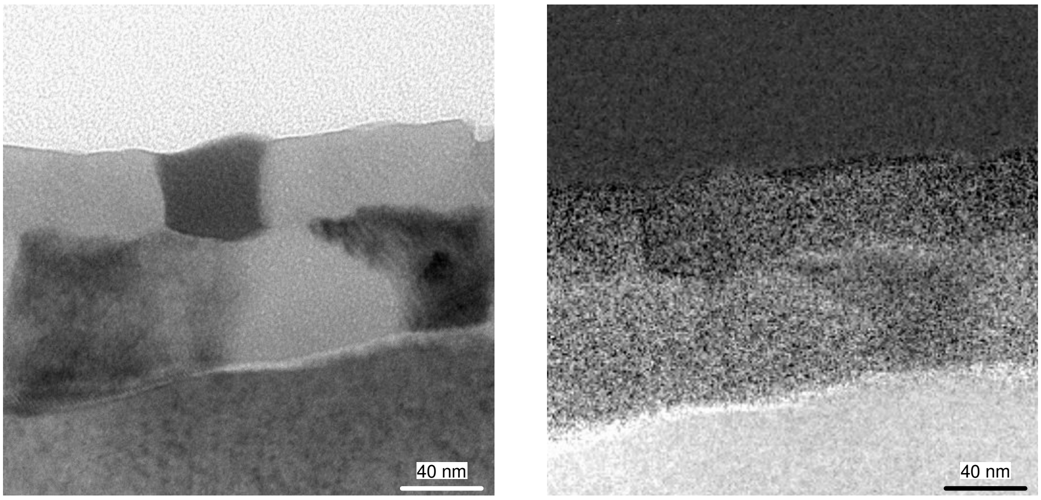

(a) TEM brightfield image. (b) EFTEM Si map.

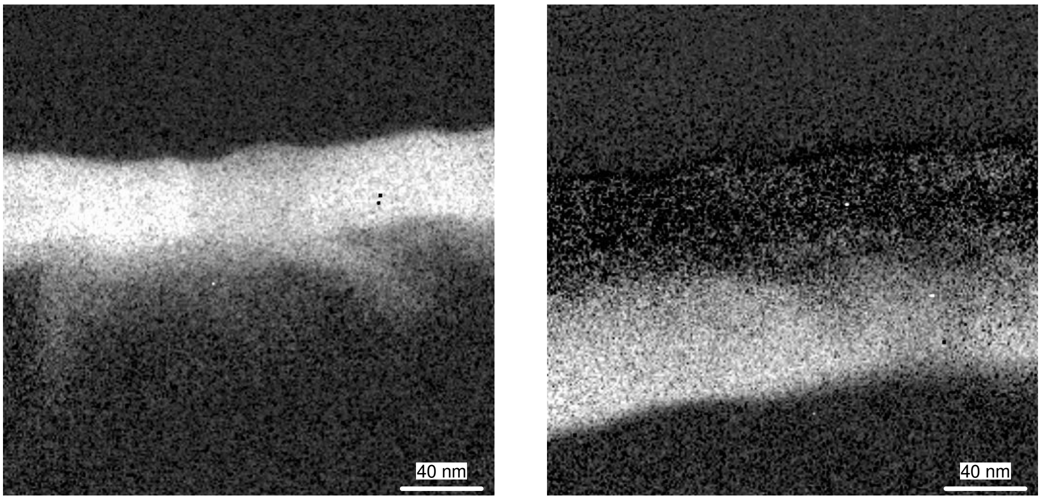

(c) EFTEM Co map. (d) EFTEM Ni map.

Fig. 6.5: Layer inversion of 10 nm Ni | 10 nm Co | Si layer stack after anneal at 450 °C for 30 sec. For more brightfield images of that sample, see figure B.1 e). The bilayer structure of a) can also be seen in the elemental maps b)–d) (The brighter the signal, the higher the atomic concentration). Evidence for the layer inversion is best seen in c) and d) with the enrichment of Co on top, and Ni at the bottom.

This can be expected by the Hume-Rothery rules[22], here applied to silicides, saying that metals show a great extent of solubility in each other when their lattice parameters do not differ by more than 15 %. Table 3.2 and table 3.3 give an overview about the crystallographic data and physical properties of the silicides of Co and Ni.

CoSi with the cubic FeSi structure-type and the orthorhombic NiSi with MnP structure-type have different crystal structures (table 3.2). Therefore, it is expected that they are not soluble in each other for a wide range of concentrations. A very early work from the beginning of the 1960s dealing with the system CoSi-NiSi specifies a solubility of NiSi in CoSi of 50 at. % and a solubility of CoSi in NiSi of 20.1 at. % [151] which could not be proven by other authors. The solubility of CoSi in NiSi and vice versa was estimated by Finstad *et al.* to be 0–5 % [55]. For the Ni rich side, Panday and Schubert [152] found a solubility of at least 7 at. % Co in NiSi for powder samples annealed at 900 °C for 10 days.

The formation of Me_2Si (*Me* being Co **and** Ni) starts at the interface to the silicon substrate. It can be assumed that the solid solution $Co(Ni)_2Si$ is formed. Nevertheless, it is also possible that Ni_2Si and Co_2Si form almost simultaneously with a trend of lower formation temperatures for Ni_2Si since its heat of formation is ≈40 % higher than that of Co_2Si, although no proof of Ni_2Si could be found with XRD techniques. This is due to the fact that the detection limit for XRD is in the range of 3–5 vol. %. When the monosilicide phase is formed, Ni is expelled from the solid solution leading to ”pure”,

---

[22] William Hume-Rothery formulated 4 rules dealing with the solubility of metals.

1. Extensive substitutional solid solution occurs only if the relative difference between the atomic diameters (radii) of the two species is less than 15 %. If the difference >15 %, the solubility is limited.
2. For appreciable solid solubility, the crystal structures of the two elements must be identical.
3. A metal will dissolve a metal of higher valency to a greater extent than one of lower valency. The solute and solvent atoms should typically have the same valence in order to achieve maximum solubility.
4. Electronegativity difference close to 0 gives maximum solubility. The more electropositive one element and the more electronegative the other, the greater is the likelihood that they will form an intermetallic compound instead of a substitutional solid solution. The solute and the solvent should lie relatively close in the electrochemical series.

i. e. Ni-free, CoSi. Once the Ni is expelled from the CoSi, it remains at the interface to the silicon substrate, at least under RTA conditions. Further supply of Si leads to the formation of the respective Me-monosilicides and Me-disilicides.

Table 6.1: Physical and chemical properties of Ni and Co

Property	Co	Ni
Atomic number (Z)	27	28
Atom radius in element [Å]	2.506	2.492
Atomic weight	58.933	58.693
Molar volume [cm^3/mol]	6.67	6.59
Density [$\mathrm{g/cm}^3$]	8.900	8.908
CTE [$\mathrm{K}^{-1} \cdot 10^6$]	13.0	13.4
Melting point [°C]	1495	1455
Boiling point [°C]	2927	2913
Electronegativities (Pauling)	1.88	1.91
Enthalpy of vaporization [kJ/mol]	375	378
Enthalpy of atomization [kJ/mol]	426	431
ΔH_f^0 [kJ/mol]	425	430
Diatomic Me-Si bond enthalpies [kJ/mol] @ RT	276 ±17	318 ±17
Electrical resistivity [mΩcm]	6	7
Young's modulus [GPa]	209	200
Source: http://www.webelements.com [132]		

Fermi level (basic principles)

As it was shown in the previous section, CoSi and NiSi possess only a very limited miscibility in each other. Imai *et al.* performed density of state (DOS) calculations for a variety of transition metal silicides [153, 154]. They used the band calculation program CASTEP[23] that is based on a first-principle

---

[23] CAmbridge Serial Total Energy Package [155].

pseudopotential method. This method is based on a plane-wave basis and determines the electron–electron interaction and a pseudopotential description of the electron–core interaction. The calculated DOS values are compared to the Fermi level of the respective structure. A (hypothetical) isolated, i. e. a molecule with no interaction to other molecules, with a molecular configuration where the bonding hybrid states are occupied and the anti-bonding states are left empty, is stable. The Fermi energy E_F is located in the gap between bonding and anti-bonding states. In solid states these bonding states are broadened to bands, but the trend that configurations with the E_F at small DOS values are stable still remains [156]. From DOS calculations and from the comparison with E_F it can be predicted which structures are stable and which are not. The principle, formulated by Imai *et al.*, of *"the DOS at the Fermi level would be, hopefully, smaller in an energetically-favored structure"* [153] is valid for the most transition metal silicides, especially for the silicides of Co and Ni. Figure 6.6 shows the calculated DOS for CoSi and NiSi for different crystal structures.

If a solid solution of CoSi and NiSi shall exist, then both silicides must have the same crystal structure. For the case of the FeSi structure type, the crystal structure of CoSi exhibits (see figure 3.1 c) and table 3.2), the energy at E_F for NiSi (figure 6.6 c)) would be at a higher DOS value than for the MnP structure type (figure 6.6 d)). This means, it is energetically more favorable for NiSi to crystallize in the MnP structure type rather than in the FeSi (that of CoSi) structure type. If the solid solution would exhibit the MnP structure type (figure 3.2 b) and table 3.2) than the E_F of CoSi would be in a region of very high DOS values (figure 6.6 a)) and, therefore, it would be unstable. Due to these DOS calculations it is evident that a solid solution of CoSi and NiSi in either one of the two crystal structure types FeSi or MnP would be energetically less favorable than the coexistence of two separate phases. Thus, the crystal structures that are formed in the investigated samples originate from the DOS of the different phases. Since the deviation of additional energy that would have been needed to form a solid solution between CoSi and NiSi in the case of the FeSi structure is smaller than it would be for the MnP structure type, one can expect a higher solubility of NiSi in CoSi rather than a higher solubility of CoSi in NiSi. This "asymmetric" solubility was qualitatively also found by Wittman *et al.* [151]. This approach explains the severely limited miscibility of CoSi and NiSi in the solid state by means of first-principle calculations. In literature, usually a more qualitatively discussion dealing with the different crystal structures of CoSi and NiSi can be found.

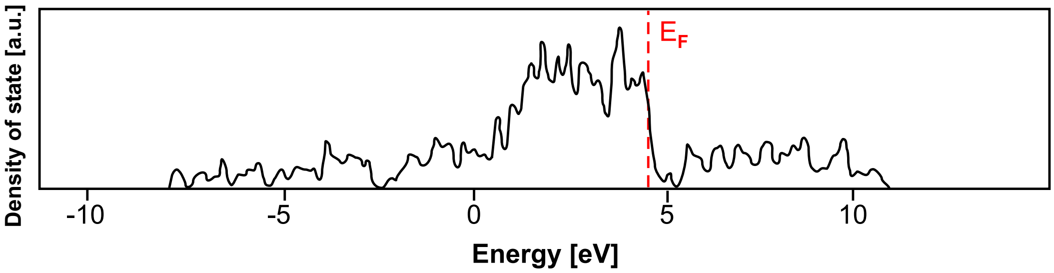

(a) Calculated DOS of CoSi in structure type MnP. E_F: energy of Fermi level. DOS at E_F is high ⇒ unstable structure.

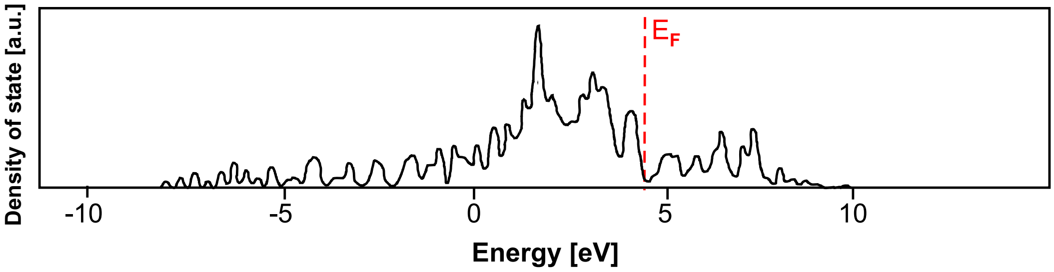

(b) Calculated DOS of CoSi in structure type FeSi. E_F: energy of Fermi level. DOS at E_F is low ⇒ stable structure.

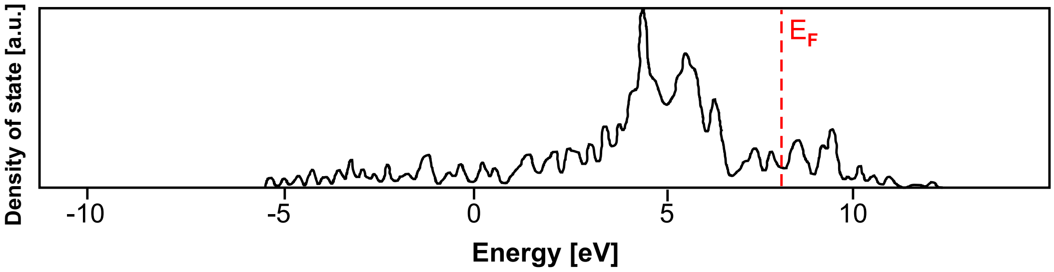

(c) Calculated DOS of NiSi in structure type FeSi. E_F: energy of Fermi level. DOS at E_F is high ⇒ unstable structure.

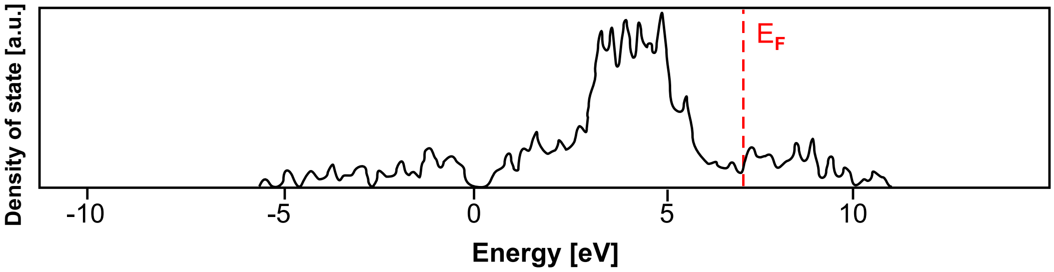

(d) Calculated DOS of NiSi in structure type MnP. E_F: energy of Fermi level. DOS at E_F is low ⇒ stable structure.

Fig. 6.6: DOS of CoSi for structure type FeSi and DOS of NiSi for structure type MnP. Modified after Imai *et al.* [154]. The DOS value at E_F is very high in figure a) compared to figure b) and therefore CoSi in structure MnP is unstable. The DOS value at E_F is higher in figure c) compared to figure d) and therefore NiSi in structure FeSi is unstable.

6.4 CTE of $CoSi_2$ and NiSi and the impact on stress/agglomeration

The CTE α of the silicides affects the stress that is present during formation of the layer, and it also affects the stress in the manufactured device. High stress can lead to adhesion problems as well as to agglomeration of layers. The linear CTE $\alpha\,[\mathrm{K}^{-1}]$ is given by

$$\alpha = \frac{\Delta l}{l_0 \cdot \Delta T} \tag{6.2}$$

with Δl the change in length, l_0 the initial length and ΔT the temperature difference. In order to be able to calculate Δl it is necessary to determine the change of interatomic distances with temperature.

6.4.1 Stress evolution of $CoSi_2$ during thermal treatment

During thermal treatment of metal layers deposited on substrates several processes take place which affect the stress within these layers. First of all, the linear CTE of the substrate, i. e. the silicon substrate, effects the stress within the silicide layers. The CTE of the silicon substrate, is significantly smaller than the CTE of the used silicides. Neglecting phase formation processes and phase transformations during heating, thermal treatment will lead to compressive stress within the silicide layers and tensile stress within the silicon substrate as long as the adhesion between layer(s) and substrate is given. Secondly, phase formation processes can lead to stress relaxation during thermal treatment due to atomic rearrangement of the compounds within the layer stack and to a change of layer thicknesses. Lattice mismatch between components, i. e. silicide and substrate, also contributes to the total stress, except for $CoSi_2$ and $NiSi_2$ (see table 3.2). In nanoscale films usually biaxial stress within the layer, with low or no stress component perpendicular to the substrate surface, occurs.

Two techniques can be utilized to determine the stress. One, indirect, method is the wafer curvature technique, an interferometric method where the curvature of the wafer is measured and subsequently the stress of the layer is calculated.

Equation 6.3 (Stoney equation) gives the correlation between the wafer curvature and the stress within the layer.

$$Curvature\ K = \frac{1}{r} = \frac{1}{M_s}\frac{6\,\sigma_t\,t_f}{{t_{sub}}^2} \tag{6.3}$$

with r=measured "radius" of the wafer, σ_t total film stress, t_f=film thickness, M_s=biaxial modulus=E/(1−υ), E=Young's modulus with υ=Poisson's ratio, and t_{sub}=substrate thickness. Solving equation 6.3 for σ_t leads to

$$\sigma_t = M_s\frac{{t_{sub}}^2}{6\,r\,t_f} \tag{6.4}$$

which makes clear that the layer stress is inverse proportional to the film thickness. Tensile stress within the layer leads to a convex substrate, compressive stress causes a concave substrate. In principle, thicker films possess lower stress. Since t_f is orders of magnitude smaller than t_{sub}, the stress within the silicide film can be considered to be independent of silicide thickness. One difficulty for *in situ* measurements is the determination of the layer thickness during heating. The layer thickness (and also to a negligible amount the substrate thickness due to thermal expansion) changes during thermal treatment due to phase formation processes.

Another, direct, method is to use XRD to determine the interatomic distances within crystalline material. By means of XRD techniques, diffraction patterns are collected and intensity maxima can be determined using peak fitting algorithms. The peaks correspond to specific Bragg angles (see section 4.1). The universal equation describing the relation between the interatomic distances, i. e. the d-spacing, and the crystal symmetry is:

$$\frac{1}{d^2} = \left(\frac{\left(\begin{array}{c}\frac{h^2}{a^2}sin^2\alpha + \frac{k^2}{b^2}sin^2\beta + \frac{l^2}{c^2}sin^2\gamma + \frac{2kl}{bc}(cos\,\beta\,cos\,\gamma - cos\,\alpha) + \\ \frac{2hl}{ac}(cos\,\alpha\,cos\,\gamma - cos\,\beta) + \frac{2hk}{ab}(cos\,\alpha\,cos\,\beta - cos\,\gamma)\end{array}\right)}{\begin{array}{c}1 - cos^2\alpha - cos^2\beta - cos^2\gamma + \\ 2\,cos\,\alpha\,cos\,\beta\,cos\,\gamma\end{array}}\right) \tag{6.5}$$

with h, k, l being the Miller indices of the lattice planes and α, β, γ being the angles between the lattice vectors. For cubic system such as CoSi or CoSi$_2$ is simplified to:

$$\frac{1}{d^2} = \frac{h^2 + k^2 + l^2}{a^2} \tag{6.6}$$

Stress causes shifts of the positions of the intensity maxima of diffraction patterns. Compressive stress leads to peak shifts towards higher Bragg angles $2\,\vartheta$, i. e. towards smaller d-spaces. Tensile stress leads to larger d-spaces and, therefore, it causes peak shifts towards smaller Bragg angles. These are opposite trends which interfere with each other. For cubic polycrystalline materials biaxial compressive stress would lead to smaller average lattice constants, assuming random orientation of the grains. The peak shift can easily be attributed to the altered lattice constant a. Using a GIXRD setup, no lattice planes parallel to the substrate surface contribute to the collected diffraction patterns. This means, another difficulty exists for highly orientated crystal grains. All diffraction maxima monitored by the detector scan arise from lattice planes that are all differently tilted to the substrate surface (see figure 4.1). When biaxial stress is present in the layer, one has to take into account the orientation of the different lattice planes contributing to the diffraction patterns. Therefore, lattice constants determined by analyzing different lattice planes are affected differently by the biaxial stress within the layer depending on the tilt angle of the lattice planes relative to the sample surface.

Several diffraction maxima (indexed (110), (220), and (311) for $CoSi_2$, see figure 6.7), were used to determine the lattice constant a for this phase. Figure 6.7 shows the diffraction patterns of the investigated samples in the temperature range 300 °C to 775 °C. Since equation 6.6 is valid for the cubic phase $CoSi_2$, each peak can be used to determine the lattice constant a. The mean value of a was used for further calculations[24]. The CTE of $CoSi_2$ α=$10.1 \cdot 10^{-6}$ [K^{-1}] [85] was used to determine the overall stress in the $CoSi_2$ layer. It was assumed that a biaxial stress was present due to the nature of the unpatterned thin film of the sample. The change of slope of the dotted line and the cyan line at temperatures above 625 °C is assumed to result from the conversion of CoSi to $CoSi_2$ which was completed between 575 °C and 625 °C. The rearrangement of atoms to form $CoSi_2$ out of CoSi and the herewith related grain growth with the associated reduction of free interface energy account for the observed stress relaxation. Lower compressive stress leads to smaller changes of a with increasing temperature. This data was visualized in figure 6.8. Volumetric changes (see figure 3.5) due to phase formation processes lead to an intrinsic stress σ_i in the silicide layer during silicidation. However, there is no more intrinsic stress after cooling down the films after the silicidation process is completed, since no more phase formation processes take place.

---

[24] The precision of the determination of a was $\leq \pm 0.005$ Å.

The total stress σ_t during thermal treatment is given by:

$$\sigma_t = \sigma_i + \sigma_T \tag{6.7}$$

with σ_i=intrinsic stress and σ_T=thermal stress due to the different CTEs of Si and the silicide. The thermal stress σ_T within a $CoSi_2$ layer is given by [157]:

$$\sigma_T = -(\alpha_{CoSi_2} - \alpha_{Si}) \cdot \left(\frac{E}{1-v}\right)_{CoSi_2} \cdot (T - T_0) \tag{6.8}$$

with α_{CoSi_2} and α_{Si} the linear CTEs of $CoSi_2$ and Si, respectively. T is the current temperature and T_0 is the temperature at which the film is in stress free state. From equation 6.8 it can be seen that σ_T is $\propto T$. Figure 6.8 shows the stress within the 35 nm $CoSi_2$ vs. temperature. The stress is increasing linearly with temperature (see figure 6.8, black line). When the silicidation process is completed entirely, the intrinsic compressive stress σ_i becomes zero due to atomic rearrangement and dislocation gliding [158]. This temperature of stress relaxation can be estimated to be ≈600 °C (see figures 5.1 and 6.7). At higher temperatures, thermal stress accounts for the obtained stress values listed in table 6.2. After cooling down to RT, however, there is tensile stress in the silicide layer of ≈1 GPa (see table 6.2). Stress values in that range for nanoscale $CoSi_2$ films at RT were confirmed also by other authors [85,158,159].

The total stress within the $CoSi_2$ layer σ_t can be calculated using the SR-XRD results with equations 6.9 and 6.10

$$\varepsilon = \frac{a - a_{CTE}}{a_{CTE}} \tag{6.9}$$

and

$$\sigma_t = \varepsilon \left(\frac{E}{1-v}\right)_{CoSi_2} \tag{6.10}$$

with a=experimentally determined lattice constant a of $CoSi_2$ and a_{CTE} the calculated value of a using the CTE of $CoSi_2$ [85]. $E/(1-v)$=the biaxial modulus of $CoSi_2$ with a value of -140 GPa [85].

The force per unit lengths that acts on the silicide film at the interface substrate/silicide F_i is given by the product of total stress and film thickness [157]:

$$F_i = \sigma_t \cdot t_l \tag{6.11}$$

with σ_t the total stress within the film and t_l the (silicide) layer thickness. Since the thermal stress increases with increasing temperature, one way to reduce stress within the silicide layers is to optimize the RTA steps with respect

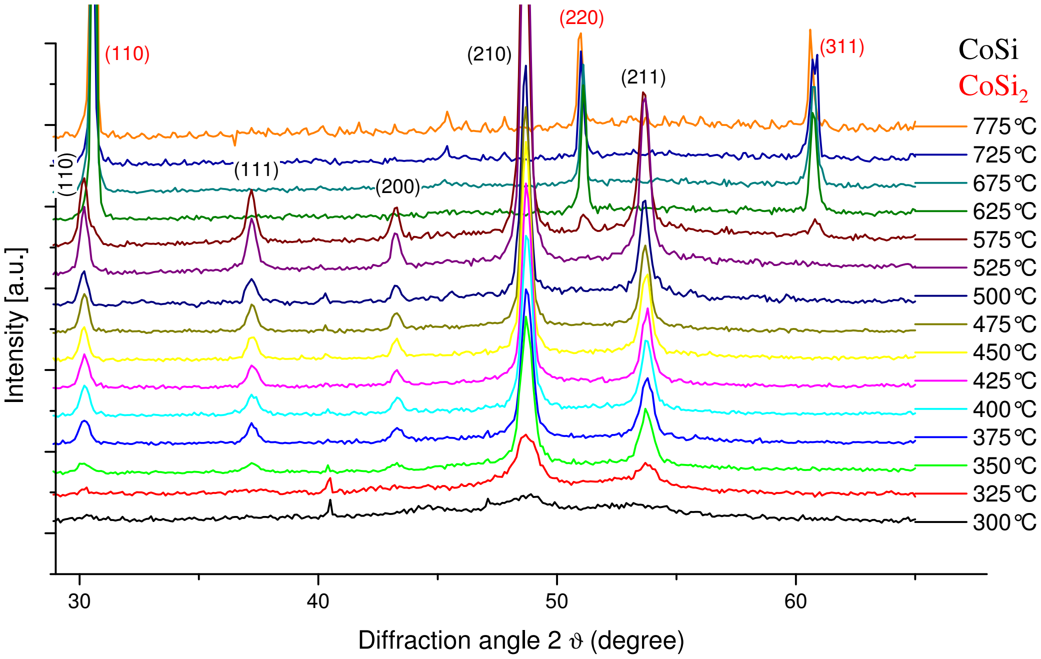

Fig. 6.7: SR-XRD results of Co|Si sample with Ti capping layer on single crystal Si substrate in the temperature range 300°C–775°C (λ=1.648 Å). Deposited metal layer thickness was 10 nm for Co and Ti capping layer, leading to a CoSi$_2$ layer thickness of 35 nm. The intensity maxima are indexed due to their corresponding lattice planes. These indices were used to calculate stress within the silicide layers. Black indices mark diffraction maxima belonging to CoSi, red ones belong to CoSi$_2$.

Table 6.2: Stress in 35 nm CoSi$_2$ layer. Numerical data, calculated using equations 6.9 and 6.10

Temperature [°C]	σ_t [MPa]
575	-109±10
625	-288±49
675	-360±88
725	-457±122
775	-591±32
RT after cooling down from 775	+1141±119

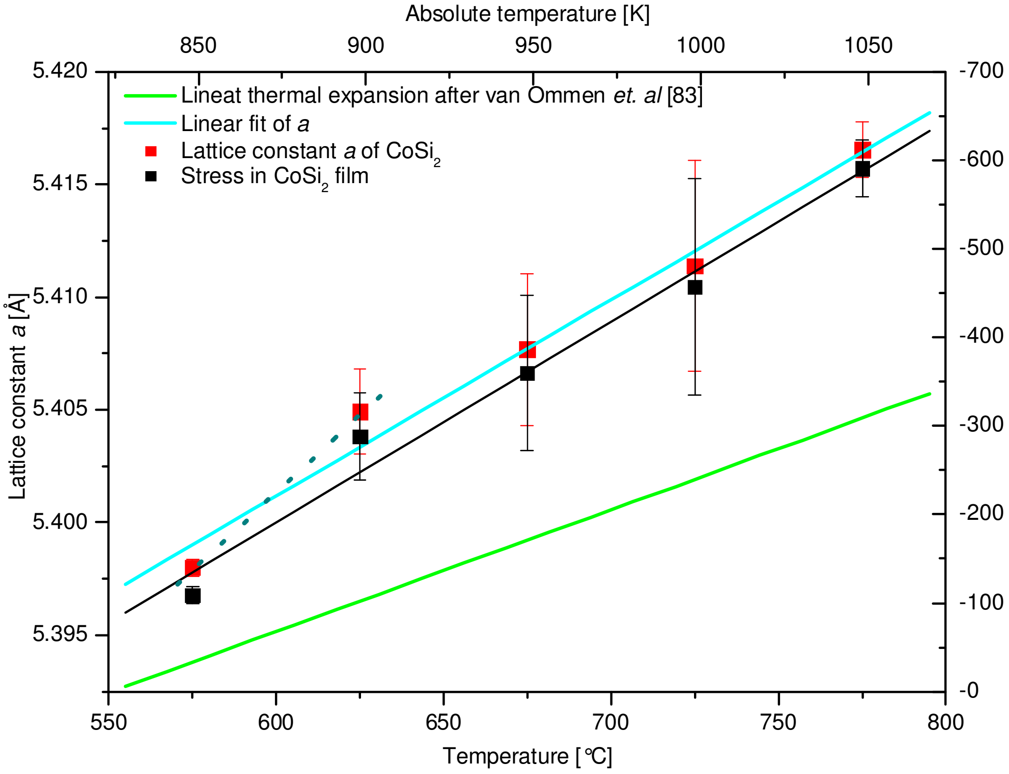

Fig. 6.8: Lattice constant a of CoSi$_2$ vs. temperature. Linear fit of a (cyan line for T between 575 °C–775 °C; and dotted line for T<625 °C), and a calculated with a CTE from literature [85] (green line). Layer stack was 10 nm Co with a 10 nm Ti capping layer on single crystal substrate, leading to a CoSi$_2$ layer thickness of ≈35 nm. The corresponding diffraction patterns can be seen in figure 6.7.

to lowering the applied temperatures. Another way is to reduce silicide thickness, although this is limited, for instance, because of thickness depending agglomeration effects (see section 6.5).

6.4.2 Coefficients of thermal expansion of NiSi

Only very few data can be found in literature regarding the CTE of NiSi, dealing mostly with single crystals [160,161], except for one study of polycrystalline NiSi films [39]. Detavernier *et al.* determined a linear CTE of NiSi for the temperature range 100 °C–725 °C of α_a=42·$10^{-6}\,K^{-1}$, α_b=-43·$10^{-6}\,K^{-1}$, and α_c=34·$10^{-6}\,K^{-1}$. In this work, the CTE was determined too, and the non-linear CTE terms were determined in addition to the linear one. The CTE depends on temperature and is strongly anisotropic.

In the case of orthorhombic substances, for instance NiSi, suitable diffraction maxima with appropriate Miller indices have to be chosen to be able to determine the lattice constants. The equation for an orthorhombic system like NiSi, can be simplified to

$$\frac{1}{d^2} = \frac{h^2}{a^2} + \frac{k^2}{b^2} + \frac{l^2}{c^2} \tag{6.12}$$

using the universal equation 6.5.

The diffraction patterns of the As^+ doped single crystal sample was evaluated to determine the CTE of NiSi. Despite this wide range of existence of Ni monosilicide between 275 °C and 700 °C, only the data between 400 °C and 700 °C was used. Below 400 °C, the (020) and (210) peaks of NiSi could not be fitted with reasonable precision. Since the FWHM was too high and the peak intensity too low, the peak positions could not be determined with sufficient accuracy. At temperatures >700 °C, $NiSi_2$ was formed. All diffraction maxima were fitted using a Voigt function to determine the exact position. Figure 6.9 shows the trends of the lattice constants of NiSi in the range of 400 °C to 700 °C and the resulting cell volume. Superimposed are the corresponding nonlinear fits. The error bars are the standard error of the mean (StEM). Having determined the d-spacing corresponding to a specific set of indexed diffraction maxima for at least three different peaks, a set of equations can be formulated. For example, the triple of peaks (210), (112), and (211) with Bragg angles that were determined for a wavelength of λ=1.648 Å at 400°C of 47.385° 2ϑ, 48.895° 2ϑ, and 50.539° 2ϑ, respectively lead to a set of three equations with three unknown variables[25]. Such a set of equations is solvable. Since more

---

[25] Additional peaks (103) 55.32° 2ϑ and (020) 60.77° 2ϑ were used (λ=1.648 Å).

than three diffraction maxima can be indexed, the system of equations is over-determined, and a fit of the obtained values becomes possible. Table 6.3 shows the peak triples that were used to determine the lattice constants of NiSi in the temperature range between 400 °C and 700 °C. These sets were chosen out of 19 sets because the yielded the most consistent values.

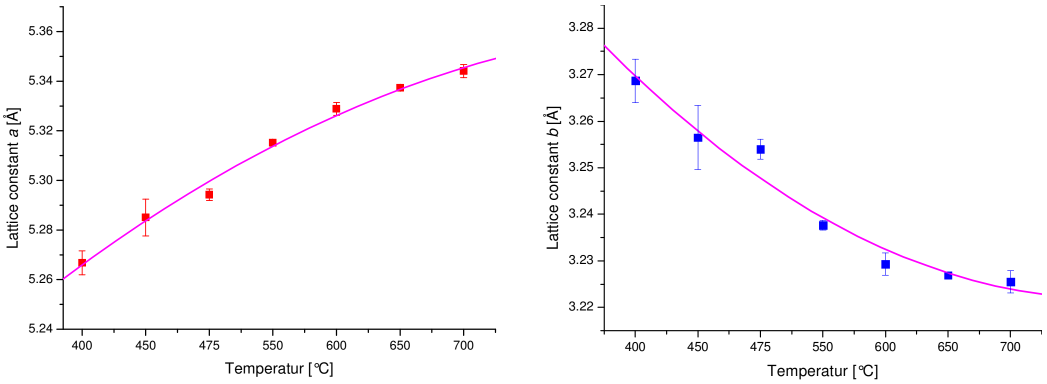

(a) Lattice constant a vs. temperature.
(b) Lattice constant b vs. temperature.

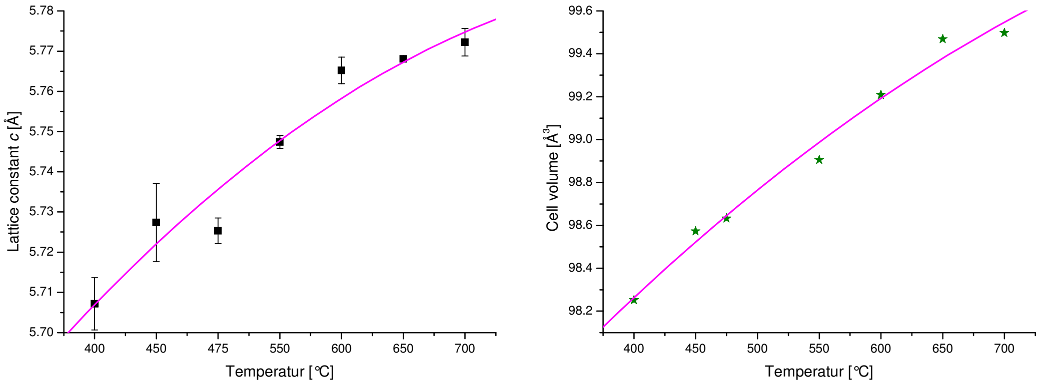

(c) Lattice constant c vs. temperature.
(d) Cell volume vs. temperature.

Fig. 6.9: Lattice constants of NiSi vs. temperature with superimposed polynomial fits in the temperature range 400 °C–700 °C.

Figure 6.9 shows the changes of the lattice constants a, b, and c with temperature and the high degree of anisotropy for the changes of the lattice constants with changing temperature. Noticeable is the negative change of b which becomes smaller with increasing temperature. Although all bond lengths increase with temperature, bond angles perpendicular to the b-axes are also increased causing the compression of b [160]. Engström and Lönnberg also have found such anisotropies in disilicides [162]. This anisotropy can also be

Table 6.3: Peak triples used to determine the lattice constants of NiSi

Sets of peak triples used to calculate the lattice constants
(112) (211) (210)
(112) (211) (020)
(112) (103) (210)
(112) (210) (020)
(211) (210) (020)
(103) (210) (020)

seen in figure 5.6, where the diffraction maxima of (020) are shifted towards higher values of 2ϑ against the overall trend of all other diffraction peaks.

Figure 6.10 shows the nonlinear fits according to the equations given in table 6.4. The best fit of the temperature-dependent changes could be achieved using a second order polynomial fit. For all fitting calculations, absolute temperature [K] was used. From figure 6.10 one would expect that the Δ*Lattice constant/lattice constant at RT* is zero. However, this is not the case, which can be seen best for the case of the blue line representing the change of lattice constant b with temperature. Two independent effects can explain the observed behavior. Firstly, the NiSi layer is subjected to intrinsic stress σ_i caused by the volumetric changes during silicidation and thermal stress σ_T due to the different CTEs of NiSi and Si. The lattice constants for *RT* that were used for the calculation (see table 3.3) are based on stress free powder samples [94]. However, after the silicidation process is completed and the sample is cooled down to *RT*, the sample exhibits tensile stress (see section 6.4.1). This leads to lattice constants other than the used. Secondly, the change of lattice constant b with temperature follows a sigmoidal curve[26] for polycrystalline NiSi [39] as well as for NiSi single crystals [161]. Since the lattice constants were determined in the temperature range 400 °C–700 °C, i. e. the temperature range with decreasing b, only that part of the curve could be calculated. Table 6.4 shows the polynomial equations used to fit the changes of the lattice constants with temperature. The fit equations are only valid

---

[26] Lattice constant b increases for low temperatures of ≈350 °C–400 °C and decreases for T>400 °C.

in the temperature interval 400 °C to 700 °C. Barmin and Frolov investigated NiSi single crystals and found a similar anisotropic behavior of the CTE of NiSi [161].

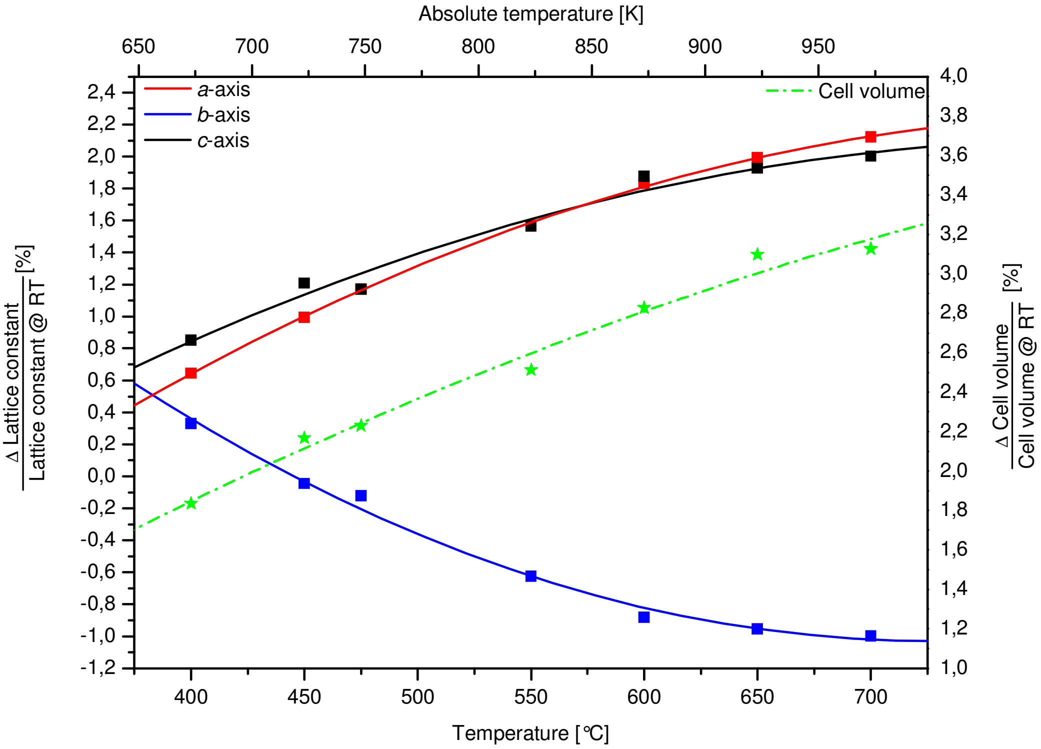

Fig. 6.10: Fit of nonlinear changes of NiSi lattice constants in the temperature range 400 °C–700 °C. Relative changes [%] of a, b, c and the cell volume are shown.

Since the CTE was determined for the temperature range 400 °C–700 °C and α is temperature dependent, l_0 is $\mathrm{l}_{400\,°\mathrm{C}}=\mathrm{l}_{673.15\,\mathrm{K}} \cdot \alpha_a$, the CTE for the lattice constant a, becomes $\alpha_a(T)$. The coefficients of thermal expansion α_a, α_b, and α_c can then be derived from equation 6.2 by partial differentiation after T:

$$\alpha(T)_{laticce\ const.} = \begin{cases} \frac{1}{l_0} \cdot \frac{\partial\, a(T)}{\partial T} \\ \frac{1}{l_0} \cdot \frac{\partial\, b(T)}{\partial T} \\ \frac{1}{l_0} \cdot \frac{\partial\, c(T)}{\partial T} \end{cases} \tag{6.13}$$

Table 6.4 shows the calculated fit equations describing the non-linear coefficients of thermal expansion for NiSi. In table 6.5, the determined anisotropic coefficients of thermal expansion of NiSi are listed.

Table 6.4: Fit equations of NiSi lattice constant changes with temperature in the temperature range 400 °C–700 °C

Lattice constant [Å]	Second order polynomial fit equations. T [K]
a	$a = 4.783\,\text{Å} + 10.373 \cdot 10^{-4}\text{Å} \cdot \mathrm{K}^{-1} \cdot \mathrm{T} - 4.726 \cdot 10^{-7}\,\text{Å} \cdot \mathrm{K}^{-2} \cdot T^2$
b	$b = 3.649\,\text{Å} - \ 8.494 \cdot 10^{-4}\text{Å} \cdot \mathrm{K}^{-1} \cdot \mathrm{T} + 4.249 \cdot 10^{-7}\,\text{Å} \cdot \mathrm{K}^{-2} \cdot T^2$
c	$c = 5.268\,\text{Å} + \ 9.441 \cdot 10^{-4}\text{Å} \cdot \mathrm{K}^{-1} \cdot T - 4.380 \cdot 10^{-7}\,\text{Å} \cdot \mathrm{K}^{-2} \cdot T^2$

Table 6.5: Coefficient of thermal expansion for NiSi in the temperature range from 400 °C to 700 °C

$\alpha(T)$ for NiSi $[\mathrm{K}^{-1}] \cdot T$ [K]
$\alpha(T)_a = \ \ 19.70 \cdot 10^{-5} - 17.95 \cdot 10^{-8} \cdot \mathrm{T}$
$\alpha(T)_b = -25.98 \cdot 10^{-5} + 25.99 \cdot 10^{-8} \cdot \mathrm{T}$
$\alpha(T)_c = \ \ 16.54 \cdot 10^{-5} - 15.35 \cdot 10^{-8} \cdot \mathrm{T}$

As was shown above, the lattice constants could be determined as a function of temperature. The results were fitted using polynomial equations following an approach of Engström and Lönnberg [162]. The polynomial fit (see figure 6.10) was chosen to determine the CTE of NiSi which shows an anisotropic behavior of this phase. The lattice constant b decreases with increasing temperature whereas a and c increase with increasing temperature. The overall cell volume however increases with temperature. The structural reasons for this uncommon behavior were presented by Rabadanov and Ataev [160] showing that bond angles decrease while bond lengths increase leading to a contraction of the b-axes.

The observed strong anisotropic thermal expansion leads to a texturing of the NiSi layer, which can be seen by the splitting of diffraction peaks at ≈50° $2\,\vartheta$ and ≈ 62° $2\,\vartheta$ (λ=1.648 Å) as is displayed in figure 5.6. The anisotropic nature of the CTE of NiSi accounts for an anisotropic stress field within the silicide layer. This stress field leads to different growth conditions that could result in preferred growth of NiSi into one direction, which in turn might cause shorts beneath polycrystalline silicon transistor gates with sub-100 nm gate lengths.

To compare the values of the CTE of NiSi with values from Detavernier *et al.* a linear fit was performed, although the goodness-of-fit of the polynomial fit is better, leading to the following results (in brackets values from Detavernier *et al.* [39]):

$$\begin{aligned}\alpha_a &= \ 49.21\pm0.01\,(42)\ \cdot 10^{-6}\,K^{-1}\\ \alpha_b &= \text{-}45.97\pm0.13\,(\text{-}43)\cdot 10^{-6}\,K^{-1}\\ \alpha_c &= \ 39.09\pm0.08\,(34)\ \cdot 10^{-6}\,K^{-1}\end{aligned}$$

Taking into account the experimental setup of both studies, not being optimized for highly accurate determination of lattice constants, the agreement of the obtained values is reasonable.

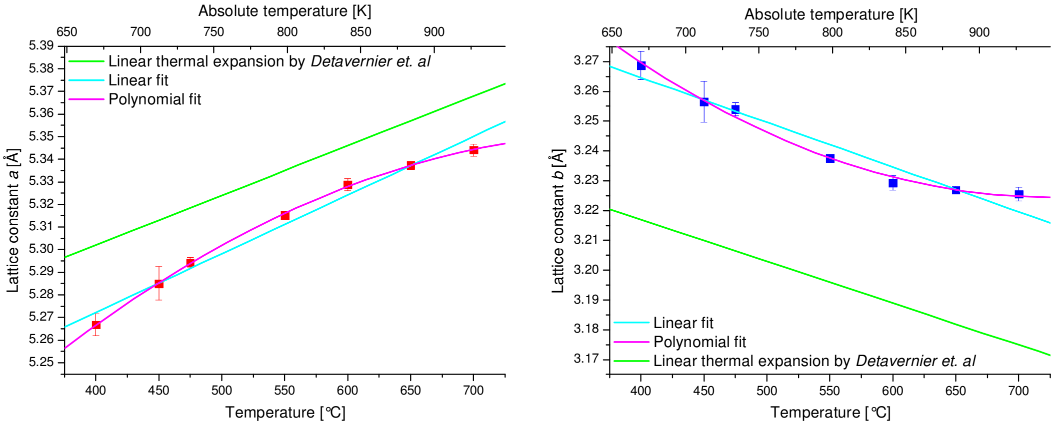

(a) Lattice constant a vs. temperature with various fits. Linear fit: α_a=49.21±0.01 and 42 (Detavernier *et al.*, green line).

(b) Lattice constant b vs. temperature with various fits. Linear fit: $\alpha_b = -45.97 \pm 0.13$ and 43 (Detavernier *et al.*, green line).

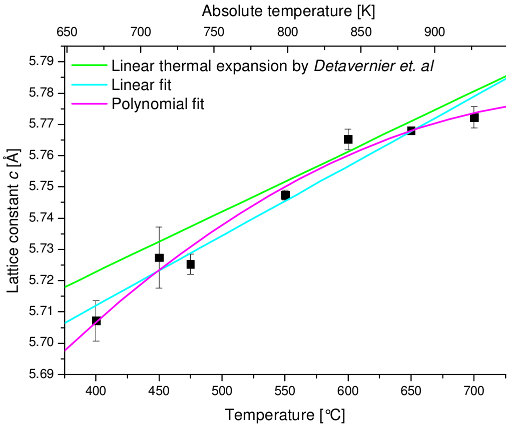

(c) Lattice constant c vs. temperature with various fits. Linear fit: α_b=39.09±0.08 and 34 (Detavernier *et al.*, green line).

Fig. 6.11: Lattice constant changes vs. temperature of NiSi between 400 °C–700 °C. Resulting CTE (polynomial fit: magenta curve; linear fit: cyan line) and comparison with literature (green line) [39] is shown.

6.5 Agglomeration and size effect

As was shown in chapter 5.3.2, NiSi films suffered from severe agglomeration (see for example also figure 5.17). These agglomeration effects could lead to discontinuous films, i. e. electric "opens". In such a case, the microprocessor fails inevitably. Agglomeration is the end stadium of a three-step degradation process as shown schematically in figure 6.12. The first step during thermal treatment is grain boundary grooving, followed by a pinch-off step and finished by agglomeration or island formation. During grain boundary grooving, the shape of the grains is only slightly altered. Mainly the corners and edges are rounded and the grooving depth t_g (see figure 6.12 b) for definition) increases. When the grains are rounded to an extent that the single grains only make contact at a small region, the second step is reached. The maximum value of t_g is reached. Beyond this point, further agglomeration leads to a islanding of the film and a meaningful value of t_g can no longer be formulated.

Upon further thermal treatment, the grains tend to reach their equilibrium shape[27], which is usually a polyhedron with sharp edges and corners in solids. The main driving force for these processes is the lowering of grain boundary energy, i. e. the interface energy, to minimize the overall energy of the system. The transport of atoms is due to a gradient in chemical potential caused by the sharp ridges at the grain boundaries [163]. Pramanick developed a semi-empirical model for grain boundary grooving and agglomeration based on kinetic and energetic considering empirical findings obtained from the system Si-Co [131]. One of the key values is the grooving depth t_g, meaning the distance between the maxima surface and the adjacent grain boundary. It is dependent on the diffusion type (surface/interface or bulk diffusion). Another key parameter is U, the ratio between the grain diameter and the original layer thickness, i. e. the layer thickness prior to the agglomeration process. There is a critical ratio U_c for which a layer starts to break into separated islands, i. e. agglomeration starts. Taking into account the loss of volume during grain boundary grooving with respect to the original shape, U_c is lowered significantly. This mass loss to the substrate or to other grains is

---

[27] For an isotropic free surface energy ς this would be a sphere, since the ratio between surface and volume is smallest for a sphere. In crystalline matter however, a strong anisotropy of ς is given, depending on the crystallographic orientation of the surfaces. Therefore the sphere-shape can not be maintained while minimizing the free surface/interface energy of the system.

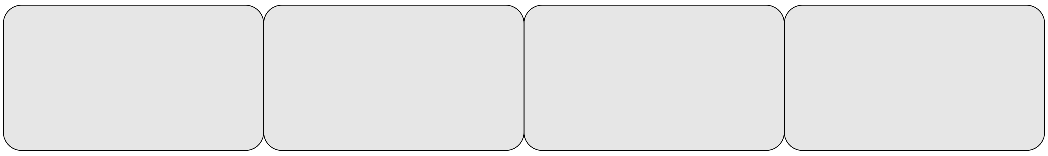

(a) First step: Grain boundary grooving.

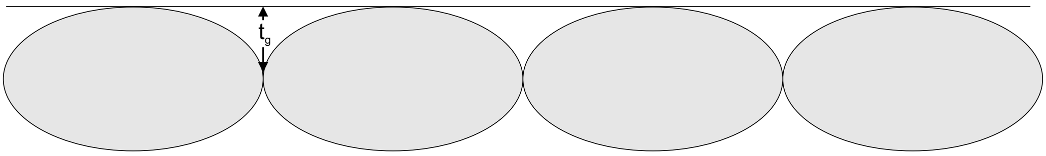

(b) Second step: Pinch-off.

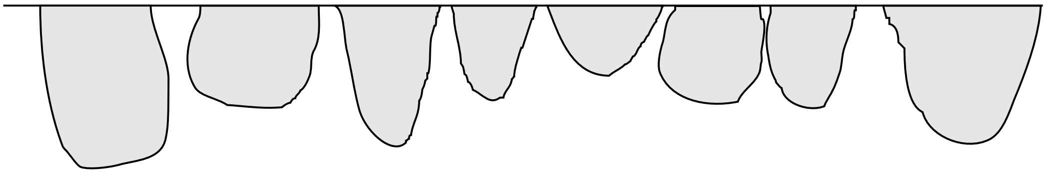

(c) Third step: Island formation/Agglomeration of film.

Fig. 6.12: Scheme demonstration the agglomeration process in thin films. Sketch modified after [131].

quite common. Following Pramanick, the grooving depth can be expressed as:

$$t_g \propto (A \cdot t)^n (U)^x \tag{6.14}$$

and

$$A = D_{\alpha_S} \gamma \mathcal{C}_{e_{Co}} \omega^2 / kT \tag{6.15}$$

with n=exponent for time (t) dependence (n=1/2, 1/3 or 1/4)[28], U, the ratio of grain diameter to original layer thickness, $x \approx 2.84$[29], D_{α_S}=interdiffusion coefficient, γ=CoSi$_2$/Si interface energy, $\mathcal{C}_{e_{Co}}$=equilibrium concentration of Co in Si ($\approx 10^{17}$ cm^{-3}), ω=molecular volume, k=Boltzmann's constant, and

---

[28] 1/2 for the case that the sample is annealed near its melting point and evaporation and condensation becomes important; 1/3, when inter diffusion is the dominant diffusion mode; 1/4, when surface diffusion dominates.

[29] Empirical value obtained by Pramanick [131].

absolute temperature T. It is apparent from these equations that agglomeration depends not only on U, it is time dependent, too. That means, virtually any silicide layer will start to agglomerate, given sufficient time. Pramanick determined from his experiments the relevant values for $CoSi_2$ layers on either single crystal and polycrystalline silicon substrates for samples annealed at 700 °C for $t = 10$'s of seconds, to be:

$$t_g \approx \begin{cases} 220.0\,(t)^{1/3}\,(U)^{2.84}\,[\text{Å}] & \text{for polycrystalline Si substrates} \\ 5.022\,(t)^{1/4}\,(U)^{2.84}\,[\text{Å}] & \text{for single crystal Si substrates} \end{cases} \tag{6.16}$$

It can be seen that the proportionality factor A is 40 times higher for polycrystalline substrates compared to single crystal substrates. This is mainly caused by the much higher diffusivity of Co atoms along the polycrystalline silicon grain boundaries, i. e. due to increased interface/grain boundary diffusion. As the formation of islands starts when t_g reaches the layer thickness, it can be seen that agglomeration is to start much sooner on polycrystalline substrates. Pramanick estimated the critical $CoSi_2$ layer thickness to be ≈30 nm [131]. This silicide layer thickness of ≈30 nm corresponds to a deposited layer thickness of <8.6 nm (see table 3.5). Kittl *et al.* found that NiSi films thinner than $\lesssim 22$ nm rather tend to agglomerate than to form $NiSi_2$ [31]. This could be confirmed for the samples 12.5 nm Ni samples annealed to 650 °C for 30 sec. A more general dependency for the grooving depth considering the temperature effect is

$$t_g \approx \begin{cases} I\,(D_{\alpha_S}/kT)^{1/3}\,(t)^{1/3}\,(U)^{2.84}\,[\text{Å}] & \text{for polycrystalline Si substrates} \\ I\,(D_{\alpha_i}/kT)^{1/4}\,(t)^{1/4}\,(U)^{2.84}\,[\text{Å}] & \text{for single crystal Si substrates} \end{cases} \tag{6.17}$$

with I=system-specific constant, D_{α_S}=interdiffusion coefficient, k=Boltzmann's constant, T=absolute temperature, D_{α_i}= Interface diffusion coefficient, and all other terms with their meaning described earlier. The silicide layer in figure 5.17 that showed the partial agglomeration of $Co_{0.95}Ni_{0.05}Si_2$ grains originates from a 15 nm Co-Ni (5 at. % Ni) layer and was heated up to 650 °C. The agglomeration can be explained by the much longer annealing time compared to the RTA samples examined by Pramanick.

As can be seen from equation 6.17, there is a kinetic part ($(A \cdot t)^n$) and a energetic (grain-size dependent) part (U^x). This gives rise to different approaches to enhance the thermal stability of $CoSi_2$ or NiSi films. Since the obvious ways to improve thermal stability, i. e. to increase the silicide layer thickness and/or gate lengths, are not applicable due to scaling requirements, other ways, like alloying, implantation with nitrogen etc. need to be pursued [31, 68–70, 131, 164, 165].

Doping of the substrate, and therefore, the presence of dopants within the silicide layer increases thermal stability (see figure 5.7), because the dopants segregate within the grain boundaries and thus reduce the mobility of Co or Ni atoms needed for grain boundary grooving (D_{α_S} and D_{α_i} are lowered). Another way of reducing metal mobility would be the formation of cavities at the silicide grain boundaries by implantation of nitrogen or argon [70]. A different approach would be the transition from RTA conditions to even shorter annealing times, i. e. spike annealing[30], thus reducing t. It might also be possible to reduce annealing temperatures within narrow ranges. However, the latter two approaches suffer from narrow process windows, since the silicidation process itself must be maintained.

Pursuing the energetic way, it is clear, that U needs to be changed. Since, the silicide layer cannot be increased in thickness, the grain size must be reduced. This can be achieved by a pre-amorphization step prior to metal deposition. The amorphization of the substrate can be achieved by implantation high doses of Si^+, Ge^+, N^+, Xe^+ etc., resulting in a highly distorted Si lattice without long range order. The recrystallization energy ΔG_{rc} can be regained during the thermally induced recrystallization process of the substrate. By using equation 2.11, it is clear that ΔG_{rc} adds up to ΔG and the critical size of a nucleus is reduced (see also figure 2.2). Furthermore, the nucleation rate ρ^* (see equation 2.11) is increased. All in all, the pre-amorphization leads to smaller and more silicide grains, and therefore, to a reduction of U, the ratio of grain size to layer thickness. As can be seen from figure 5.22, the PAI of $2{\cdot}10^{14}$ at/cm^2 of Xe^+ did not lead to the desired effect of suppressing agglomeration. Furthermore, the uniformity of the NiSi layer increased with increasing post-PAI time (see also figure E.1 b)–d)). The PAI leads to a partial destruction of the Si lattice, and therefore to a much higher degree of anisotropy of the substrate. Due to this anisotropy, there is no driving force for the grain to grow into a direction of energetically favorable lattice planes. From these considerations one would expect the highest non-uniformity for the samples without PAI-anneal, as it is the case for the investigated samples with PAI. On the other hand, if the kinetic rate of the recrystallization of the amorphous silicon is greater than the silicidation rate, large non-uniformities may arise [131], which could be caused by the Xe^+ implantation. Moreover, the angularity of the NiSi grains is increasing with PAI annealing time, i. e. the grains are further ahead in the process of reaching their equilibrium shape. Similar effects could be proven for $CoSi_2$ [166]. This can be explained with

---

[30] Annealing times in the range of 0–3 sec at considerably higher temperatures ($\Delta T \approx$+200 K) used for "conventional" RTAs.

the higher diffusivity of Ni in the already partially recrystallized silicon substrate. The fact that more grain boundaries are present, and therefore, grain boundary diffusion dominates volume diffusion, leads to this effect. From the comparison of figure E.1 a) and b) it is apparent, that doping (in this case $2.5 \cdot 10^{15}$ at/cm^2 B^+) is much more efficient in suppressing agglomeration. The NiSi layer is continuous for the case of the doped samples, whereas severe agglomeration took place in the sample that was subjected to a preamorphization step.

Additionally, a capping layer, mandatory for $CoSi_2$ process integration, reduces agglomeration effects, since grain boundaries get pinned at the interface to the capping layer [41, 125–127]. However, this approach might not be production worthy for the case of Ni silicide, since it is not conform to less processing steps, and lower cycle times.

On thin polycrystalline lines, the problem of agglomeration is even worse, since the contribution of grain boundary diffusion to the total effective diffusion is much higher compared to that of thin films on single crystal substrates, i. e. the active regions of a transistor. Therefore, the mobility of metal atoms is higher leading to an increased affinity towards agglomeration. Severe agglomeration is known to occur in thicker silicide films on polycrystalline Si substrates (see figure 1.5) compared with single crystal Si substrates.

Impact of layer thickness

The experiments with different layer thicknesses (section 5.3.1) showed an influence of the deposited metal layer thickness on the silicidation processes. A decreased metal layer thickness reduced the phase formation and conversion temperatures. In literature, on the one hand, it is suggested that agglomeration (see section 6.5) of the NiSi film is a prerequisite for the transformation of NiSi to $NiSi_2$ due to the higher energy needed to form $NiSi_2$ out of NiSi than for agglomeration [128]. Agglomeration is known to be dependent on the layer thickness, so the observed thickness effect can be explained. This observation was also reported by Besser *et al.* [45]. On the other hand, the considerations of the previous paragraph are also valid and contribute to the lowering of the formation and conversion/transition temperatures. When the maximum possible grain size within nanoscale layers is further reduced, which is obvious for the case of a reduction of the deposited layer thickness, the interface fraction increases. Therefore, the fraction of grain boundary diffusion is increased leading to a considerably higher effective diffusion coefficient. Due to this reasoning, the effect that in thinner layers the transformation is finished earlier than in thicker films can be explained, since the diffusion lengths are shorter, grain boundary diffusion and agglomeration are pronounced.

Chapter 7

Summary and outlook

Ti and Co silicides, $TiSi_2$ and $CoSi_2$, respectively, have been widely used in the semiconductor industry. Today and for the near-term future, i. e. the next technology nodes, $CoSi_2$, NiSi as well as possibly ternary silicides like $Co_{(1-x)}Ni_xSi$, have already been implemented, or are most likely to be implemented into manufacturing of microprocessor devices. These silicides are used as contact materials due to their advantageous physical properties. Further scaling down of device structures, and the herewith associated reduction of transistor gate lengths and layer thicknesses are the driving forces for the introduction of new materials, e. g. the used silicides. This thesis deals with the phase formation of Co silicides and the herewith connected problems using $CoSi_2$ as contact material for the most advanced microprocessor units, as well as the impact of a Ti capping layer onto the silicidation. Additionally, the silicidation process within a ternary system Co-Ni-Si (5 at. % Ni) was examined. Most of the studies are related to Ni silicides, their properties and the formation as well as conversion temperatures of the various Ni silicides. The impact of different substrates, either polycrystalline or single crystalline, miscellaneous dopants, a TiN capping layer and several deposited layer thicknesses were subject of analytical investigations.

In situ SR-XRD experiments were conducted using annealing parameters that reflect the conditions of the BEoL process, with its typical long annealing times. Using a combination of techniques it was possible to determine formation and conversion temperatures of the silicidation processes as well as limits for thermal treatment. The experimental data can be considered for the implementation of NiSi into mass production of microprocessors.

Phase formation sequences

In situ SR-XRD experiments at elevated temperatures were conducted to monitor the phase formation sequence within the investigated samples. SR-XRD in conjunction with a grazing-incidence set-up is capable of examining nanoscale layers in the range of ≈10–15 nm and to determine the formation and conversion temperatures of the investigated samples.

The phase formation sequences were found to be:

$$\mathrm{Co_2Si} \rightarrow \mathrm{CoSi} \rightarrow \mathrm{CoSi_2} \text{ (System Co-Si)}$$

$$\mathrm{(Co_{0.95}Ni_{0.05})_2Si} \rightarrow \mathrm{CoSi} \rightarrow \mathrm{C_{0.95}Ni_{0.05}Si_2} \text{ (System Co-Ni-Si)}$$

$$\mathrm{Ni_2Si} \rightarrow \mathrm{NiSi} \rightarrow \mathrm{NiSi_2} \text{ (System Ni-Si)}$$

The respective formation and conversation temperatures can be found in section 5.1.1 for the case of Co silicdes, in section 5.1.2 for the system Co-Ni-Si, and in section 5.1.3 for the investigated Ni silicides.

The alloying of Co with 5 at. % reduced the formation and conversion temperatures of the respective silicides slightly. This effect could be explained taking into account the entropy of mixing which usually is neglected for silicidation processes [72, 73]. For $\mathrm{CoSi_2}$ formation out of CoSi, ΔS should be considered, since the $\Delta \mathrm{H}_F^0$ for CoSi and $\mathrm{CoSi_2}$ are very similar (-100.4 kJ/mol for CoSi compared to -102.9 kJ/mol for $\mathrm{CoSi_2}$). The phase formation sequence remained the same as for the system Co-Si. The formation of NiSi requires a lower thermal budget than that needed to form $\mathrm{CoSi_2}$ which could be shown by the SR-XRD experiments. The formation temperatures for the low resistivity target phase NiSi are significantly lower than for $\mathrm{CoSi_2}$ in the Co-Si and Co-Ni-Si systems.

TEM provided valuable insights into the formation of NiSi and $\mathrm{NiSi_2}$. These phases are formed by either a diffusion-controlled (NiSi) mechanism or a nucleation-controlled ($\mathrm{NiSi_2}$) mechanism resulting in different interface roughnesses. Particularly, a higher interface roughness of the nucleation-controlled phase $\mathrm{NiSi_2}$ was observed. The layer thickness effect, i. e. the effect that the formation temperatures are reduced on thinner metal layers, could be explained with the growth kinetics of the silicide phases.

Impact of the capping layer

The capping layer of either Ti or TiN had the effect that the formation temperatures of the observed metal-rich silicides, i. e. Co_2Si, $(Co_{0.95}Ni_{0.05})_2Si$ as well as Ni_2Si were shifted to higher temperatures. The thermal stability of the monosilicides was increased by +50 K (TiN capping on Ni layer) and +100 K (Ti capping layer on Co layer). For the formation of $CoSi_2$ a capping layer is mandatory, since Co is known to be prone to oxidize. The used capping layer however interacts with the Co and Si to form a ternary Co-Ti-Si compound. Using EFTEM and CBED in conjunction with the software package ELDISCA [122] it was possible to identify the formed phase to be CoTiSi. The formation of $CoSi_2$ is known to be nucleation-controlled leading to a relatively rough silicide/silicon interface [6,8,73]. Since NiSi is less prone to oxidation, it can be processed without a capping layer. Figure 7.1 summarizes the impact of the used capping layers.

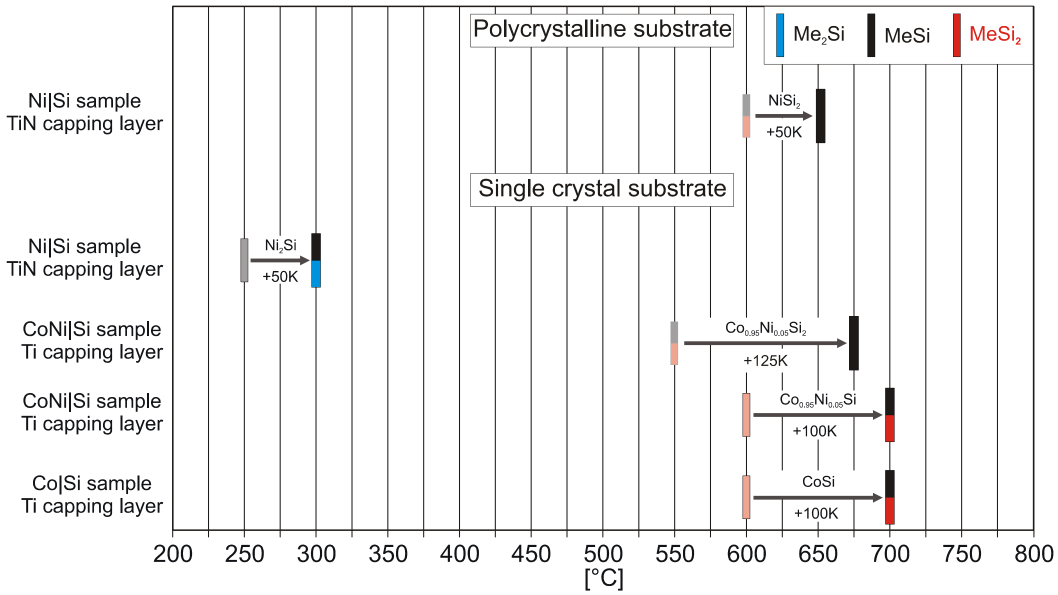

Fig. 7.1: Impact of capping layer on phase formation temperatures. Faint colors represent temperatures without capping layer. Bigger boxes represent samples with capping layer. Arrows indicate shifts of formation temperatures. Vertical boxes represent the lowest temperature where a specific phase was detected while increasing temperature. All boxes and bars are color coded, i. e. cyan stands for the metal-rich silicide, black for monosilicide, and red for the disilicide phase. Monochrome bars show that only one phase is present. Boxes with two different colors indicate that at this temperature two phases coexist.

Impact of dopants

Doping the silicon substrate with As^+ or P^+ prior to silicidation for Co-Ni|Si and pure Ni|Si samples stabilized the metal-rich phases. The $(Co_{0.95}Ni_{0.05})_2Si$ formation temperature was increased by +25 K on single crystal and polycrystalline substrates. On B^+ doped samples, Ni_2Si was stabilized only on single crystal substrates. On p-type polycrystalline Ni|Si samples, however, the formation of NiSi was inhibited for -100 K compared to n-type or non-doped substrates. On single crystal substrates, the effect of monosilicide formation shifted to lower temperatures was less pronounced. It could only be observed for Co-Ni|Si samples, there the shift was -25 K. The formation of $Co_{0.95}Ni_{0.05}Si_2$ and $NiSi_2$ was generally shifted to higher temperatures on doped substrates. This effect was independent of the substrate type. For Co-Ni|Si samples, the shift was +75 K and for Ni|Si samples +150 K on single crystal substrates. On polycrystalline substrates, the shift was +50 K for As^+ doped and +25 K for B^+ doped substrates, respectively. Figure 7.2 summarizes the impact of the used dopants.

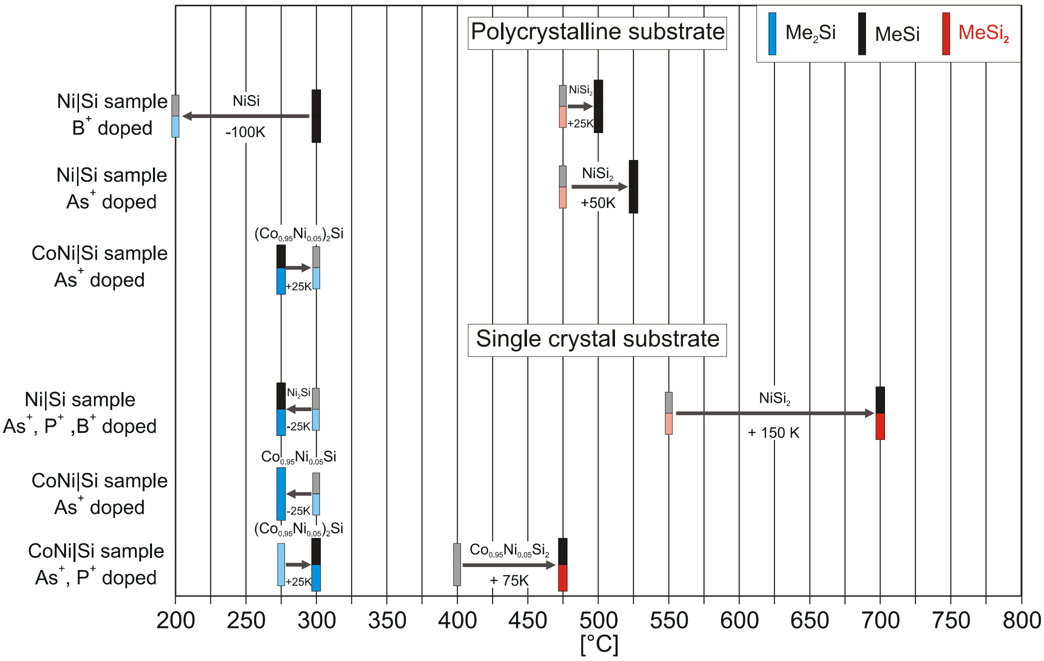

Fig. 7.2: Impact of doping on phase formation temperatures. Faint colors represent temperature without doping. Bigger boxes represent doped samples. Arrows indicate shifts of formation temperatures. Vertical boxes represent the lowest temperature where a specific phase was detected while increasing temperature. All boxes and bars are color coded, i. e. cyan stands for the metal-rich silicide, black for monosilicide, and red for the disilicide phase. Monochrome bars show that only one phase is present. Boxes with two different colors indicate that at this temperature two phases coexist.

Agglomeration effects

A capping layer has a positive effect on the sensitivity to agglomeration of the investigated nanoscale layers. Anyhow, agglomeration took place on non-capped Ni|Si samples prior to the formation of $NiSi_2$. This is in agreement with what was reported by Chamirian *et al.* [128]. Using AES, AFM, and SEM in combination with digital image processing, it was possible to determine the degree of agglomeration of different silicide layers. The impact of a special thermal treatment, i. e. a post PAI annealing step, could be determined to be negligible, whereas a doping with B^+ leads to a significant reduction of agglomeration effects. The agglomeration effects could be explained was based on the theory of grain boundary grooving formulated by Mullins [163,167] and refined by Pramanick [131]. It could be shown that agglomeration consists of an energetic part and a kinetic part, and that it depends on layer thickness, the ratio of grain diameter to layer thickness, temperature, and time. Since diffusion effects agglomeration, the impact of dopants and a possibly deposited capping layer can be interpreted as a result of decreases mobility of Co and Ni within these layers. In contrast to polycrystalline substrates, grain boundary diffusion does not take place within single crystal substrates. Therefore, agglomeration is less severe on single crystal substrates. The agglomeration of thin $CoSi_2$ layers on the narrow polycrystalline silicon gates, is most likely the limiting factor for further use of $CoSi_2$ within the manufacturing process. Due to this fact, NiSi will replace $CoSi_2$ as contact material, since the thermal budget for forming NiSi is lower than that needed for $CoSi_2$.

Limited miscibility of CoSi and NiSi

During annealing, Ni is always enriched at the silicide/substrate interface which could be proven by AES and EFTEM. This effect can even lead to a layer inversion of an originally deposited layer stack. This severely limited miscibility of CoSi and NiSi in the solid state accounts for the Ni enrichment at the interface, although the disilicides are totally soluble in each other. DOS calculations by Imai *et al.* [153,154] computing the structure of CoSi with the structural parameters of NiSi and vice versa and evaluating the energetic position of Fermi level E_F with the DOS, showed that it is energetically more favorable to expel the Ni from the CoSi rather than to incorporate it into the energetically unfavorable crystal structure. After full conversion to the disilicide phase $Co_{0.95}Ni_{0.05}Si_2$ there is no longer an enrichment of Ni at the bottom of the layer stack detectable, which is a further proving of the total solubility of $CoSi_2$ and $NiSi_2$, first described by Wittmann *et al.* [151].

CTE of NiSi

The coefficients of thermal expansion of polycrystalline NiSi were determined in the range of 400° C–700° C. From temperature-dependent diffraction patterns obtained with SR-XRD, the anisotropic, non-linear coefficients of thermal expansion of NiSi were calculated. The rare case of a negative CTE for the *b*-axis of NiSi could be proven. This behavior was explained with the fact that during thermal treatment of the sample, the bond-angles within the NiSi structure decreased while bond lengths increased leading to the contraction of the *b*-axes. Nevertheless, the cell volume increases with temperature. Using a linear approach[31] of computing the CTE of NiSi to compare the obtained values with data in literature, an agreement with literature data could be demonstrated. The formation of $NiSi_2$ might take place in an epitaxial manner. This could be confirmed with SR-XRD investigation of a Ni layer on single crystal substrate at 750° C. The formerly typical diffraction pattern changed to a diffraction pattern without noticeable intensity maxima. Based on GIXRD and TEM imaging, the growth of $NiSi_2$ grains along the <111> planes of the silicon lattice could be proven. This epitaxial growth is possible due to the very small lattice mismatch of only 0.4 %, thus resulting in the energetically favored epitaxial growth driven by the minimizing of the interface energy. This effect leads to discontinuous $NiSi_2$ films.
The obtained results provide material-specific data for the usage of current and future silicides within the manufacturing of even the most advanced microprocessors.

Conclusions

The study of the silicidation process in the system Co-Si leads to the following conclusions: The low resistivity target phase $CoSi_2$ needs to be replaced in future technology nodes. It's high formation temperature of at least 625 °C, when subjected to long time anneals, and >700° C for RTA treatments, leads to a high sensitivity for agglomeration effects. In conjunction with decreasing layer thicknesses and smaller gate lengths it is more and more likely that $CoSi_2$ will fail for polycrystalline silicon gates lengths considerably smaller than $\leq$40–45 nm. The reduction of available Si limits the use of $CoSi_2$, especially on thin SOI substrates since the disilicide phase has to be formed. Furthermore, the nucleation-controlled formation of $CoSi_2$ results in a relatively high interface roughness, causing problems for very thin silicide layers.

---

[31] Although knowing that a second-order polynomial yields better results.

A capping layer is beneficial with respect to oxidation of the deposited metal layer and tendency to agglomeration of the silicide layers.

The alloying of Co with 5 at. % Ni yielded lower formation and conversion temperatures, thus extending the usability of $Co_{0.95}Ni_{0.05}Si_2$ ($CoSi_2$), although the problem with the interface roughness is not addressed with that approach. Agglomeration effects are expected to be reduced also, which give rise to the assumption that using a ternary silicide is a promising way to extend the deployment of a Co-based silicide for the near-term future.

One promising candidate for the next technology nodes will be NiSi. NiSi shows some beneficial properties like its lower resistivity and fewer Si consumption compared to $CoSi_2$ and $(Co,Ni)Si_2$. The Si consumption is 35 % less of that for $CoSi_2$ maintaining the same level of sheet resistance R_s. The penetration depth of the silicide into the active region of the transistor is therefore lower too, which makes NiSi more suitable for usage on thin SOI substrates. Additionally, the surface of the resulting silicide is at a point more distant from the source/drain region compared to $CoSi_2$ (see figure 3.5). NiSi showed no break up at small linewidths, i. e. no roll-off of sheet resistance at small gate lengths, at least not for gate lengths as small as 30 nm [30, 67]. Since agglomeration is dependent on temperature, time and layer thickness, the overall significantly lower thermal budget needed to form NiSi, leads to less severe agglomeration effects. Additionally, NiSi can be formed in a one step process, which is advantageous for the manufacturing of semiconductor devices. If to a certain extent metal-rich silicides remained after the first silicide formation step, the conversion to NiSi can be accomplished within the further BEoL processing. NiSi processing can take place without a capping layer, although a capping layer is known to retard agglomeration. There are a lot of advantages linked to the usage of NiSi, there are also some disadvantages, or at least some aspects which should be considered. The thermal conditions of the BEoL processing need to be taken into account, since the thermal treatment must not exceed the formation temperatures of $NiSi_2$. To mitigate agglomeration of NiSi prior to the formation of $NiSi_2$, a capping layer should be deposited. The coefficients of thermal expansion of NiSi should be considered for future development. The negative CTE of the *b*-axis might lead to an anisotropic growth of NiSi within the silicide layer, due to the fact that such a behavior leads to anisotropic strain fields within this layer. This might cause growth "paths" and a preferential texture of NiSi, which in turn might have an impact on the channel of the transistor, e. g. shorts may be formed between the active area and the transistor gate.

Outlook

This thesis is focused on the optimization of the manufacturing process of microprocessors. Prior to the transition from $CoSi_2$ to NiSi within the semiconductor industry the usage of $CoSi_2$ can be further extended. The alloying of Co with Ni seems to be a promising way to mitigate some issues related with $CoSi_2$. Work is being done dealing with the influence of alloying elements on the nucleation and formation of Co silicides [50, 51, 74]. Additionally, the formation temperatures can be lowered by optimizing the manufacturing process. Nevertheless, the trend to higher concentrations of dopants and the possible introduction of SiGe substrates counteracts the extendibility of $CoSi_2$, since formation temperatures are shifted to higher values and the formation of Co-Ge silicides is highly problematic [168, 169], whereas the formation of Ni-Ge silicides is possible [170]. It is very likely that for the next technology nodes, SOI substrates will be used and NiSi will replace $CoSi_2$ because of its superior device properties [33]. Some aspects of the Ni silicidation process need to be explored in detail. One aspect is the texture of NiSi in thin films, i. e. investigations are going on currently dealing with a special off-axis fiber-texture of NiSi called axiotaxy [171–173]. Investigations of the CTE of NiSi and its implications for the silicidation process and device properties have only just begun besides this work [39, 160, 161]. The extension of the thermal stability range of NiSi is crucial for the implementation of NiSi into production. Several approaches by alloying small quantities of Re, Pt, and W to tailor the formation properties of NiSi are currently being under investigation within the semiconductor industry [137, 174, 175]. The feasibility of a one-step process needs to be demonstrated as well as a process window has to be specified in which metal-rich Ni silicides are converted into NiSi during BEoL processing. Some work in the field of process optimization needs to be done to reduce agglomeration of NiSi layers, since even thinner silicide layers are required for future technology nodes. Some other considerations should also be taken into account like the usage of a dual-silicide approach, for instance $CoSi_2$ on the active regions, where the lateral extent is larger than on the gates, and NiSi on the very narrow polycrystalline silicon gates. Another approach is the utilization of raised soure/drain regions, i. e. the SEG approach [104], to overcome the problems related with the penetration of the active regions by the silicide. Finally, the introduction of metal-gates possibly is an option for the 45 nm technology and beyond [56, 57, 57, 59], which would finalize the era of silicides as contact materials on transistor gates.

Chapter 8

Publications related to this work

Publications related to the current work in chronological order:

- **EFTEM study of Ti/TiN and Co-silicide thin films at cross-sections of device structures**
  W. Blum, H.-J. Engelmann, J. Rinderknecht, E. Zschech in
  Proceedings of 11th International Conference on Microscopy of Semiconducting Materials, 537–540, 1999 [25]

- **Determination of phase formation processes in nanoscale Co-Ti layers using synchrotron radiation in conjunction with a high temperature chamber**
  J. Rinderknecht, F. Berberich, W. Matz, E. Zschech in
  Bi-annual report 1999/2000 Forschungszentrum Rossendorf, Germany, FZR-322, 2001 [176]

- ***In situ* high temperature synchrotron-radiation diffraction studies of Ni and Co-Ni silicidation processes**
  J. Rinderknecht, oral presentation at the
  European Workshop on Materials for Advanced Metallization 2002, Vaals, The Netherlands, March 3–6, 2002 and published in
  Microelectronic Engineering 64, 143–149, 2002 [29]

- **Phase formation processes in nanoscale nickel layers during heat treatment on different silicon substrates**
  J. Rinderknecht, H. Prinz, T. Kammler, F. Berberich, E. Zschech in
  Bi-annual report 2001/2002 Forschungszentrum Rossendorf, Germany, FZR-364, 2003 [177]

- ***In situ* high temperature synchrotron-radiation diffraction studies of silicidation processes in nanoscale Ni layers**
  J. Rinderknecht, H. Prinz, T. Kammler, N. Schell, E. Zschech, K. Wetzig, T. Gessner, poster presentation at the
  European Workshop on Materials for Advanced Metallization 2003, La Londe Les Maures, France, March 9–12, 2003 and published
  in Microelectronic Engineering 70, 226–232, 2003 [178]

- **Silicides in the system Co-Ni-Si and Ni-Si - Phase formation and Raman spectroscopy**
  J. Rinderknecht, invited talk at the
  Symposium on phase formation in thin silicide systems, Instituut voor Kern- en Stralingsfysica, KU Leuven, October 22^{nd}, 2004

- **NiSi Challenges in High-Performance Logic CMOS for 65 nm and beyond**
  T. Kammler, P. Press, J. Rinderknecht, S. Waidmann, C. Lavoie, oral presentation at the
  European Workshop on Materials for Advanced Metallization 2005, Dresden, Germany, March 6–9

Acknowledgements

First of all, I would like to thank Prof. Dr. Dr. h.c. Klaus Wetzig, director of the Leibniz Institute of Solid State Analysis and Structural Research, IFS, Dresden for providing the opportunity to prepare this thesis and being the doctoral thesis supervisor. I also want to express deep gratitude to Prof. Dr. Karen Maex for all the fundamental studies and excellent contributions to the field of silicides and materials science as well as her willingness to be one of the evaluators. I feel deeply indebted to Dr. Ehrenfried Zschech, manager Materials Analysis Laboratory (MALab), for all his support throughout the years in all possible ways at AMD, his critical comments, encouraging discussions, the careful reading of the manuscript, and for pointing into the right direction during my work at AMD. He gave me the freedom to be able to conduct all the work that is presented here. I also want to thank Dr. Norbert Mattern, head of the department of X-Ray Structural Research, IFS, Dresden for useful discussions and valuable hints regarding X-ray techniques. Dr. Hartmut Prinz, MALab, was so kind as to read all parts of the manuscript during all stages over and over again, thus improving the overall quality tremendously. Additionally, he assisted in most of the mathematical parts. For all the useful discussion about silicides, their usage within microprocessors, aid in experimental design, as well as for unrelentingly pointing out weak spots, I want to express thanks to Dr. Thorsten Kammler, Integration engineer AMD.

All the work that was done by the MALab staff can not be overestimated. All people within this extraordinary team are creating a very inspiring and fruitful working environment. To name a few, the work of the TEM staff, Dr. Hans-Jürgen Engelmann, Holger Saage[32], Dr. Heiko Stegmann, Beate Volkmann, and Yvonne Ritz providing excellent TEM results must be acknowledged.

---

[32] Now at the Institut für Werkstofftechnik und Werkstoffprüfung, University of Magdeburg.

Furthermore, I would like to show appreciation to Inka Zienert for preparing the excellent XRR measurements and simulations. Kornela Dittmar and Diethelm Heiler did a great job with respect to the AES profiles. Constanze Korn also contributed to this work with administrative support.
Some more people at AMD are to be mentioned. Dr. Volker Kahlert and Austin Frenkel were responsible for the metal layer deposition, the implants were performed by Dr. Marc Herden. Michaela Jacob was of great help in all aspects of literature research. Thanks to all of them.
Furthermore, I would like to thank Dr. Jürgen Thomas, IFS for the wonderful CBED studies which enabled the identification of the ternary CoTiSi phase. The work of Rainer Kaltofen with preparing additional samples, that unfortunately led into a dead-end street, also needs to be acknowledged.
I also want to show gratitude to Dr. Wolfgang Matz and Dr. Johannes von Borany for administrative support providing the possibility to use the ROBL beamline at the ESRF, thus enabling the SR-XRD studies. I feel indebted to Dr. Norbert Schell, Dr. Florian Berberich, and Udo Strauch due to their excellent support during the synchrotron radiation experiments.
Special thanks to Dr. Julia Meinershagen for being a "language advisor" and also special thanks to Prof. Dr. Paul Keller, Institut für Mineralogie und Kristallchemie, Universität Stuttgart, for having laid the foundation of scientific work for me.
Last, but not least I want to thank my parents Helga Rinderknecht and Rolf Rinderknecht for supporting me. Finally, I would like to thank my family Anke and Teresa Ruhland for all that they are and their continuous aid and motivation they provide.

References

[1] N. G. Einspruch, G. B. Larrabee, editor. *VLSI Electronics Microstructure Science.* Academic press, New York, 1983.

[2] S. P. Muraka. *Silicides for VLSI Applications.* Academic press, 1983.

[3] F. M. d'Heurle. *Solid State Devices 1985.* Elsevier Science Publishers B.V., 1986.

[4] K. Maex, M. van Rossum. *Properties of Metal Silicides.* INSPEC, London, 1995.

[5] R. T. Tung, K. Maex, P. W. Pellegrini, L. H. Allen, editor. *Silicide Thin Films - Fabrication, Properties, and Applications*, volume 402, Pittsburgh, Pennsylvania, 1996. Materials Research Society, MRS Materials Research Society.

[6] F. M. d'Heurle. Nucleation of a new phase from the interaction of two adjacent phases: Some silicides. *Journal of Materials Research*, 3(1):167–195, 1998.

[7] U. Gösele, K. N. Tu. Growth kinetics of planar binary diffusion couples: "Thin-film case" versus "Bulk cases". *Journal of Applied Physics*, 53:3252–3260, 1982.

[8] F. M. d'Heurle, C. S. Petersson. Formation of thin films of $CoSi_2$: Nucleation and diffusion mechanism. *Thin Solid Films*, 128:283–297, 1985.

[9] K. Maex. Silicides for integrated circuits: $TiSi_2$ and $CoSi_2$. *Materials Science and Engineering*, 80:53–153, 1993.

[10] E. Zschech. Challenges on the path to high-performance microprocessors: Scaling-down and new materials. *VDI Berichte*, 1803:3–6, 2003.

[11] H. S. Rhee, H. S. Lee, J. H. Park, B. T. Ahn. *In-situ* growth and growth kinetics of epitaxial (100) $CoSi_2$ layer on (100) Si by reactive chemical vapor deposition. *Materials Reseach Society Symposium*, 611:C10.3.1–C10.3.1, 2000.

[12] K. Wieczorek, M. Horstmann, H.-J. Engelmann, K. Dittmar, W. Blum, A. Sultan, P. Besser, A. Frenkel. Integration challenges for advanced salicide processes and their impact on CMOS device performance. *Materials Research Society Symposium*, 611:C5.1.1–C5.1.11, 2000.

[13] A. E. Morgan, E. K. Broadbent, M. Delfino, B. Coulman, D. K. Sadana. Characterization of a self-aligned cobalt silicide process. *Journal of the Electrochemical Society: Solid State Science and Technology*, 134(4):925–935, 1986.

[14] J. M. Andrews. The role of the metal-semiconductor interface in silicon integrated circuit technology. *Journal of Vacuum Science Technology*, 11(6):972–984, 1974.

[15] F. M. d'Heurle. Silicide interfaces in silicon technology. *Journal of Electronic Materials*, 27(11):1138–1147, 1998.

[16] J. M. Anderson. The role of the metal-semiconductor interface in silicon integrated circuit technology. *Journal of Vacuum Science Technology*, 11:972–984, 1974.

[17] D. Kahng, M. P. Lepselter. Planar epitaxial silicon Schottky barrier diodes. *The Bell system technical journal*, pages 1525–1528, 1965.

[18] S. P. Muraka, D. B. Fraser. Thin film interaction between titanium and polycrystalline silicon. *Journal of Applied Physics*, 51:342–349, 1980.

[19] D. B. Scott, R. A. Chapman, C.-C. Wei, S. S. Mahanti-Shetti, R. A. Haken, T. C. Holloway. Titanium disilicide contact resistivity and its impact on $1\,\mu$m CMOS circuit performance. *IEEE Transactions on Electron Devices*, 34:562–574, 1987.

[20] R. A. Roy, L. A. Clevenger, C. Cabral jr., K. L. Saenger, S. Brauer, J. L. Jordan-Sweet, J. Bucchignano, G. B. Stephenson, G. Morales, K. F. Ludwig jr. *In-situ* diffraction analysis of the C49-C54 titanium silicide phase transformation in narrow lines. *Applied Physics Letters*, 66(14):1732–1734, 1995.

[21] R. W. Mann, L. A. Clevenger, P. D. Agnello, F. R. White. Silicides and local interconnections for high-performance VLSI applications. *IBM Journal of Research Development*, 39(4):403–417, 1995.

[22] T. C. Hsiao, P. Liu, J. C. S. Woo. An advanced Ge pre-amorphization salicicde technology for sub-quarter-micrometer SOI CMOS devices. *Symposium on VLSI Technology Digest of Technical Papers*, pages 95–96, 1997.

[23] J. A. Kittl, Q. Z. Hong. Materials aspects of Ti and Co silicidation of narrow polysilicon lines. *Thin Solid Films*, 290–291:473–476, 1996.

[24] D.-X. Xu, S. R. Das, J. P. McCaffrey, C. J. Peters, L. E. Erickson. Process window of nickel and platinum silicides in deep sub-micron regime. *Materials Research Society Symposium Proceedings*, 402:59–64, 1996.

[25] W. Blum, H.-J. Engelmann, J. Rinderknecht, E. Zschech. EFTEM study of Ti/TiN and Co-silicide thin films at cross-sections of device structures. *Proceedings of 11th International Conference on Microscopy of Semiconducting Materials*, 164:537–540, 1999.

[26] A. Lauwers, P. Besser, M. de Potter, E. Kondoh, N. Roelandts, A. Steegen, M. Stucchi, K. Maex. Performance and manufacturability of the Co/Ti (cap) silicidation process for 0.25 μm MOS-technologies. *IITC*, pages 98–101, 1998.

[27] K. Maex, A. Lauwers, P. Besser, E. Kondoh, M. de Potter, A. Steegen. Self-aligned $CoSi_2$ for 0.18 μm and below. *IEEE Transactions on Electron Devices*, 46(7):1545–1550, 1999.

[28] Q. Xiang, B. Yu, H. Wang, M.-R. Lin. High performance sub-50 nm CMOS with advanced gate stack. *Symposium On VLSI Technology Digest of Technical Papers*, 2001.

[29] J. Rinderknecht, H. Prinz, T. Kammler, F. Berberich, E. Zschech. *In situ high-temperature synchrotron-radiation diffraction studies of Ni and Co-Ni silicidation processes. Microelectronic Engineering*, 64:143–149, 2002.

[30] J. A. Kittl, A. Lauwers, O. Chamirian, M. J. H. van Dal, A. Akheyar, M. de Potter, R. Lindsay, K. Maex. Ni and Co based silicides for advanced CMOS applications. *Microelectronic Engineering*, 70:158–165, 2003.

[31] J. A. Kittl, A. Lauwers, O. Chamirian, M. J. H. van Dal, A. Akheyar, O. Richard, J. G. Lisoni, M. de Potter, R. Lindsay, K. Maex. Silicides for 65 nm CMOS and beyond. *Materials Research Society Symposium Proceedings*, 765:D7.5.1–D7.5.12, 2003.

[32] E. A. Guliants, W. A. Anderson. Thin Ni-silicides for low resistance contacts and growth of thin crystalline Si layers. *Materials Research Society Symposium*, 611:C7.14.1–C7.14.6, 2000.

[33] Q. Xiang, C. Woo, E. Paton, J. Foster, B. Yu, M.-R. Lin. Deep sub-100 nm CMOS with ultra low gate sheet resistance by NiSi. *Symposium On VLSI Technology Digest of Technical Papers*, pages 76–77, 2000.

[34] A. Lauwers, M. de Potter, O. Chamirian, R. Lindsay, C. Demeurisse, C. Vrancken, K. Maex. Silicides for the 100 nm node and beyond: Co-silicide, Co(Ni)-silicide and Ni-silicide. *Microelectronic Engineering*, 64:131–142, 2002.

[35] H. Iwai, T. Ohguro, S.-I. Ohmi. NiSi salicide technology for scaled CMOS. *Microelectronic Engineering*, 60:157–169, 2002.

[36] F. Deng, R. A. Anderson, P. M. Asbeck, S. S. Lau. Salicidation process using NiSi and its device applications. *Journal of Applied Physics*, 81(12):8047–8051, 1997.

[37] K. P. Liew, Y. Li, M. Yeadon, R. Bernstein, C. V. Thompson. Characterization and modeling of stress evolution during nickel silicides formation. *Symposium on Advanced Materials for Micro- and Nano- Systems Proceedings*, 2003.

[38] C. Lavoie, R. Putrell, C. Coïa, C. Detavernier, P. Desjardins, C. Cabral jr., J. L. Jordan-Sweet, F. M. d'Heurle, J. M. E. Harper. *In situ* monitoring of thin film reactions during rapid thermal annealing: nickel silicide formation. *Electrochemical Society Proceedings*, 11:455–467, 2002.

[39] C. Detavernier, C. Lavoie, F. M. d'Heurle. Thermal expansion of the isostructural PtSi and NiSi: negative expansion coefficient in NiSi and stress effects in thin films. *Journal of Applied Physics*, 93(5):2510–2515, 2003.

[40] J. P. Lu, D. Miles, J. Zhao, A. Gurba, Y. Xu, C. Lin, M. Hewson, J. Ruan, L. Tsung, R. Kuan, T. Grider, D. Mercer, C. Montgomery. A novel SALICIDE process technology for CMOS devices with sub-40 nm physical gate length. *Technical Digest of IEEE IEDM*, pages 14.5.1–14.5.4, 2002.

[41] B. Froment, M. Müller, H. Brut, R. Pantel, V. Carron, H. Achard, A. Halimaoui, F. Boeuf, F. Wacquant, C. Regnier, D. Ceccarelli, R. Palla, A. Beverina, V. DeJonghe, P. Spinelli, O. Leborgne, K. Bard, S. Lis, V. Tirard, P. Morin, F. Trentesaux, V. Gravey, T. Mandrekar, D. Rabilloud, S. Van, E. Olson, J. Diedrick. Nickel vs. cobalt silicide integration for sub-50 nm CMOS. *Presented at the ESSDERC 2003, Estoril, Portugal, 16–18, 2003*, 2003.

[42] T. Moimoto, T. Ohguro, H. S. Momose, T. Iinuma, I. Kunishima, K. Suguro, I. Katakabe, H. Nakajima, M. Tsuchiaki, M. Ono, Y. Katsumata, H. Iwai. Self-aligned nickel-mono-silicide technology for high-speed deep submicrometer logic CMOS ULSI. *IEEE Transactions on Electron Devices*, 42(5):915–922, 1995.

[43] R. Chau, J. Kavalieros, B. Roberts, R. Schenker, D. Lionberger, D. Barlage, B. Doyle, R. Arghavani, A. Murthy, G. Dewey. 30 nm physical gate length CMOS transistor witp 1 ps n-MOS and 1.7 ps p-MOS gate delays. *IEDM*, pages 3.1.1–3.1.4, 2000.

[44] C. Lavoie, F. M. d'Heurle, C. Detavernier, C. Cabral jr. Towards implementation of a nickel silicide process for CMOS technologies. *Microelectronic Engineering*, 70:144–157, 2003.

[45] P. Besser, S. Chan, E. Paton, T. Kammler, D. Brown, P. King, L. Pressley. Silicides for the 65 nm technology node. *Materials Research Society Symposium Proceedings*, 766:59–70, 2003.

[46] Q. Xiang. NiSi Salicide for sub-10 nm CMOS. *Electrochemical Society Proceedings*, 2002-2:354–361, 2002.

[47] M. F. Wu, J. De Wachter, A.-M. Van Bavel, H. Pattyn, G. Langouche, J. Vanhellemont, H. Bender, K. Temst, B. Wuyts, Y. Bruynseraede. Growth and properties of ion beam synthesized $Si/Co_xNi_{1-x}Si_2/Si(111)$ structures. *Journal of Applied Physics*, 75(2):1201–1203, 1993.

[48] F. M. d'Heurle, D. D. Anfiteatro, V. R. Deline. Reaction of silicon with films of Co-Ni alloys: Phase separation of the monosilicides and nucleation of the disilicides. *Thin Solid Films*, 128:107–124, 1985.

[49] S. J. Park, J. H. Huh, H. Jeon. A study on the $CoSi_2$ formation by using Ni interposed layer on Si substrate. *Presented at MRS Spring Meeting, San Francisco, CA*, 2000.

[50] C. Lavoie, C. Cabral jr., F. M. d'Heurle, J. L. Jordan-Sweet, J. M. E. Harper. Effects of alloying elements on cobalt silicide formation. *NSLS Activity Report*, pages 2–16 – 2–20, 2001.

[51] O. Chamirian, A. Steegen, H. Bendler, A. Lauwers, M. de Potter, F. Marabelli, K. Maex. Study of $CoSi_2$ formation from Co-Ni-alloy. *Microelectronic Engineering*, 60:221–230, 2002.

[52] H.-X. Mo, X.-P. Qu, J.-H. Liu, G.-P. Ru, B.-Z. Li. Formation and properties of ternary silicide $(Co_xNi_{1-x})Si_2$ thin films. In M. Zhang, K. N. Tu, editor, *1998 5th international conference on solid-state and integrated circuit technology proceedings*, pages 271–274, Wanshou Road, Beijing, China, 1998. Chinese institute of electronics, Institute of electrical and electronics engineers, publishing house of electronics industry.

[53] O. Chamirian, A. Lauwers, C. Demeurisse, H. Guérault, A. Vantomme, K. Maex. $CoSi_2$ formation from Co_xNi_{1-x}/Ti system. *Microelectronic Engineering*, 64:173–180, 2002.

[54] N. E. Christensen J. Kudrnovský. Electronic structure and properties of transitional-metal disilicides $CoSi_2$, $NiSi_2$ and their alloys $Co_xNi_{1-x}Si_2$. *Solid State Communications*, 78(2):153–157, 1991.

[55] T. G. Finstad, D. D. Anfiteatro, V. R. Deline, F. M. d'Heurle, P. Gas, V. L. Moruzzi, K. Schwarz, J. Tersoff. The formation of disilicide from bilayers of Ni/Co and Co/Ni on silicon: Phase separation and solid solution. *Thin Solid Films*, 135:229–243, 1986.

[56] Z. Krivokapič, V. Moroz, W. Maszara, M.-R. Lin. Locally strained ultra-thin channel 25 nm narrow FDSOI devices with metal gate and mesa isolation. *IEEE International Electron Devices Technical Digest*, pages 18.5.1–18.5.4, December 2003.

[57] Z. Krivokapič, C. Tabery, W. Maszara, Q. Xiang, M.-R. Lin. High performance 45 nm CMOS technology with 20 nm multi-gate devices. *presented at SSDM 2003*, 2003.

[58] J. Kedzierski, E. Nowak, T. Kanarsky, Y. Zhang, D. Boyd, R. Carruthers, C. Cabral jr., R. Amos, C. Lavoie, R. Roy, J. Newbury, E. Sullivan, J. Benedict, P. Saunders, K. Wong, D. Canaperi, M. Krishnan, K. L. Lee, B. A. Rainey, D. Fried, P. Cottrell, H. S. P. Wong, M. Ieong, W. Haensch. Metal-gate FinFET and fully-depleted SOI devices using total gate silicidation. *IEDM 2002*, pages 247–250, 2002.

[59] Z. Krivokapič, W. Maszara, K. Achutan, P. King, J. Gray, M. Sidorow, E. Zhao, J. Zhang, J. Chan, A. Marathe, M. R. Lin. Nickel silicide metal gate FDSOI devices with improved gate oxide leakage. *IEDM 2002*, pages 271–274, 2002.

[60] Semiconductor International Association (SIA). *International Technology Roadmap for Semiconductors (ITRS).* Semiconductor International Association (SIA), 2003.

[61] C. M. Osburn, J. Y. Tsai, J. Sun. Metal Silicides: Active elements of ULSI contacts. *Journal of Electronic Materials*, 25(11):1725–1739, 1996.

[62] G. Moore. Moore's law for semiconductor devices. *www.webopedia.com*, 1965.

[63] M. T. Bohr. Interconnect scaling the real limiter to high performance ULSI. *Proceedings IEEE UEDM*, pages 241–244, 1995.

[64] G. Palasantzas. Roughness effects on the thermal stability of thin films. *Journal of Applied Physics*, 81(1):246–250, 1997.

[65] F. La Vie, E. Rimini. Electrical characterization of ultra-shallow junctions formed by diffusion from a CoSi layer. *IEEE Transactions on Electron Devices*, 44:526–534, 1997.

[66] C. Lavoie, C. Cabral jr., C. Detavernier, J. L. Jordan-Sweet, F. M. d'Heurle. Toward implementation of NiSi: Advantages and limitations over $TiSi_2$ and $CoSi_2$. *Oral presentation at the European Workshop on Materials for Advanced Metallization 2003, La Londe Les Maures, France, March 9–12*, 2003.

[67] J. A. Kittl, A. Lauwers, O. Chamirian, M. J. H. van Dal, A. Akheyar, M. de Potter, R. Lindsay, K. Maex. Ni- and Co-based silicides for advanced CMOS applications. *Microelectronic Engineering*, 70:158–165, 2003.

[68] W.-T. Sun, M.-C. Liaw, C. C.-H. Hsu. Suppressing of cobalt silicide agglomeration using nitrogen (N_2^+) implantation. *IEEE Electron Device Letters*, 37:196–800, 1998.

[69] C. Cabral jr., L. A. Clevenger, R. A. Roy, G. B. Stephenson, C. Lavoie, K. L. Saenger, J. L. Jordan-Sweet, R. Viswanathan, G. Morales, K. F. Ludwig jr. *In-situ* X-ray diffraction analysis of $CoSi_2$ formation on single and polycrystalline silicon as a function of linewidth and dopant

at rapid thermal annealing rates. *Conference Proceedings ULSI XI*, pages 436–445, 1996.

[70] A. Alberti, F. La Via, S. Ravesi, E. Rimini. Improvement of $CoSi_2$ thermal stability by cavity formation. *Applied Physics Letters*, 79(21):3419–3421, 2001.

[71] C. Detavernier, R. L. van Meirhaeghe, F. Cardon, K. Maex. Controlling $CoSi_2$ nucleation: the effect of entropy of mixing. *Materials Reseach Society Symposium*, 611:C7.9.1–C7.9.6, 2000.

[72] C. Detavernier, R. L. Van Meirhaeghe, F. Cardon, K. Maex. Influence of mixing entropy on the nucleation of $CoSi_2$. *Physical Review B*, 62(18):12045–12051, 2000.

[73] C. Detavernier. *Fundamental study of nucleation and epitaxial growth of* $CoSi_2$. PhD thesis, University of Gent, 2001.

[74] C. Detavernier, R. L. van Meirhaeghe, K. Maex, F. Cardon. Silicide engineering: influence of alloying elements on $CoSi_2$ nucleation. *Materials Research Society Symposium Proceedings*, 611:C8.4.1–C8.4.6, 2001.

[75] G. van Gurp, W. van der Weg, D. Sigurd. Interactions in the Co/Si thin film system. II. Diffusion marker experiments. *Journal of Applied Physics*, 49:4011–4020, 1978.

[76] C. M. Comrie, J. E. McLeod. Diffusion in cobalt silicide during silicide formation. *Crucial Issues in Semiconductor Materials and Technology*, pages 369–374, 1992.

[77] C. M. Comrie, J. E. McLeod. *Crucial Issues in Semiconductor Materials and Processing Technologies*, volume 222 of *NATO ASI Series*. Kluwer Academic, Applied Sciences edition, 1992.

[78] T. Spann. *Ein Beitrag zur Beschreibung von Diffusionsprozessen in den Dünnschichtsystemen Cu/Ni/Au und* $CuSn_6$*/Ni/Au*. PhD thesis, Bergakademie Freiberg, Freiberg, 1996.

[79] D. Gupta, P. S. Ho. Diffusion process thin-films. *Thin solid films*, (72):399–416, 1980.

[80] N. A. Gjostein. *Diffusion*, chapter 9: Short circuit diffusion, pages 241–274. American Society for Metals, Metals Park, Ohio, 1973.

[81] S. R. Elliot. *The Physics and Chemistry of Solids*. John Wiley & Sons Ltd., Baffins Lane, Chichester, West Sussex, England, 1998.

[82] H. Eyring, S. H. Lin, S. M. Lin. *Basic Chemical Kinetics.* John Wiley & Sons Ltd., Baffins Lane, Chichester, West Sussex, England, 1980.

[83] M. Qin, V. M. C. Poon. Young's modulus measurement on nickel silicide film on crystal silicon by a surface profiler. *Journal of Materials Science Letters*, 19:2243–2245, 2000.

[84] A. G. Alekseev, A. S. Bolgar, A. L. Borisova, G. A. Bovkum, I. T. Brakhnova, L. A. Dvorina, S. V. Drozdova, V. S. Fomenko, S. P. Gordienko, Y. M. Goryachev, M. S. Koval'chenko, Ta. Y. Kosolapova, O. P. Kulik, V. A. Obolonchik, Yu. B. Paderno, A. D. Panasyuk, O. I. Popova, B. M. Rud', T. I. Serebryakova, I. I. Timofeeva, I. M. Vinitskii. *Handbook of high temperature compounds: Properties, Production, Applications.* Hemisphere Publishing Corporation, New York, 1990.

[85] A. H. van Ommen, C. W. T. Bulle-Lieuwma, C. Langereis. Properties of $CoSi_2$ on (001) Si. *Journal of Applied Physics*, 64:2706–2716, 1988.

[86] H. von Känel, C. Schwarz, S. Goncalvens-Conto, E. Müller, L. Miglio, F. Tavazza, G. Malegori . New epitaxially stabilized CoSi phase with the CsCl structure. *Pysical Review Letters*, 74(7):1163–1166, 1995.

[87] S. Goncalvens-Conto, U. Schärer, E. Müller, H. von Känel. Competitive metastable phase in low-temperature epitaxy of $CoSi_2$/Si(111). *Physical Review B*, 55(1):7213–7221, 1997.

[88] S. Goncalvens-Conto, E. Müller, K. Schmidt, H. von Känel. New epitaxially stabilized silicide phases. *Materials Research Society Symposium Proceedings*, 402:493–498, 1996.

[89] H. von Känel, E. Müller, S. Goncalvens-Conto, C. Schwarz, N. Onda. Structural properties of epitaxial silicide layers on Si. *Applied Surface Science*, 104/105:204–212, 1996.

[90] K. N. Tu. Selective growth of metal-rich silicide of near-noble metals. *Pysical Review Letters*, 27(4):221–224, 1975.

[91] N. W. Cheung, J. W. Mayer. Lattice-location experiments of the Ni-Si interface by thin-crystal channelling of helium atoms. *Physical Review Letters*, 46(10):671–674, 1981.

[92] G. Rangelov, T. Fauster. Thermally induced evolution of codeposited Co-Si layers on Si(100) surfaces. *Surface Science*, 365:403–410, 1996.

[93] S.-Z. Zhang, J. Cardenas, F. M. d'Heurle, B. G. Svensson, C. S. Petersson. On the formation of epitaxial $CoSi_2$ from the reaction of Si with a Co/Ti bilayer. *Pysical Review Letters*, 66:58–60, 1995.

[94] International Center for Diffraction Data. JCPDS-ICDD. CD-ROM, 2003.

[95] Naval Research Laboratory Center for Computational Materials Science. The Co_2Si (C37) Structure. http://cst-www.nrl.navy.mil/lattice/struk/c37.html, 2003.

[96] D. Wagman, W. Evans, V. Parker, R. Schumm, I. Halow, S. Bailey, K. Churney, R. Nuttall. *The NBS tables of chemical thermodynamic properties*. Number Supplement no. 2 in Journal of Physical and Chemical reference data. American Institute of Physics, New York, 1982.

[97] R. Blachnik, S. Koritnig, D. Steinmeier, A. Wilke, A. Feltz, H. Reuter, E. Stieber. *Taschenbuch für Chemiker und Physiker*, volume 3. D'Ans, Lax, Berlin, Heidelberg, 4^{th} edition, 1998.

[98] R. S. Howell, G. Sarcona, S. K. Saha, M. K. Hatalis. Preparation and stability of low temperature cobalt and nickel silicides on thin polysilicon films. *Journal of Vacuum Science and Technology A*, 18(1):87–93, 2000.

[99] T. B. Massalski, H. Okamoto, P. R. Subramanian, L. Kacprzak, editor. *Binary Alloy Phase Diagrams*, volume 2. W. Scott jr., ASM International, Materials Park, OH, 2^{nd} edition, 1990.

[100] T. B. Massalski, H. Okamoto, P. R. Subramanian, L. Kacprzak, editor. *Binary Alloy Phase Diagrams*, volume 2. W. Scott jr., ASM International, Materials Park, OH, 2^{nd} edition, 1990.

[101] G. V. Samsonov, I. M. Vinitskii. *Handbook of Refractory Compounds*. IFI/Plenum Data Company, New York, 1980.

[102] L. R. Zheng, L. S. Hung, J. W. Mayer, G. Majni, G. Ottaviani. Lateral diffusion of Ni and Si through Ni_2Si in Ni/Si couples. *Applied Physics Letters*, 41(7):646–649, 1982.

[103] A. Lauwers, P. Besser, T. Gutt, A. Satta, M. de Potter, R. Lindsay, N. Roelandts, F. Loosen, S. Jin, H. Bender, M. Stucchi, C. Vrancken, B. Deweerdt, K. Maex. Comparative study of nickel silicide and cobalt silicide for sub 0.25 μm technologies. *Microelectronic Engineering*, 50:103–116, 2000.

[104] K. Derbyshire. Thermal processing - Struggle to achieve ideal devices. *Semiconductor Magazine*, pages 16–21, February 2003.

[105] H. van Meer, K. de Meyer. 70 nm fully-depleted SOI CMOS using a new fabrication scheme: the spacer/replacer scheme. *Symposium On VLSI Technology Digest of Technical Papers*, pages 170–171, 2002.

[106] M. van Rossum K. Maex, editor. *Properties of Metal Silicides*, chapter 1.2, pages 15–30. INSPEC, London, 1995.

[107] I. Kleber, H.-J. Bautsch, J. Bohm, editor. *Einführung in die Kristallographie.* Verlag Technik GmbH, Berlin, 17^{th} edition, 1990.

[108] I. C. Noyan, J. B. Cohen. *Residual stress.* Materials Research and Engineering. Springer verlag, New York, Berlin, Heidelberg, 1987.

[109] H. Krischner. *Einführung in die Röntgenfeinstrukturanalyse.* Vieweg & Sohn Verlagsgesellschaft mbH, Braunschweig, 1990.

[110] G. H. Vineyard. Grazing-incidence diffraction and the distorted-wave approximation for the study of surfaces. *Pysical Review B*, 26(8):4146–4159, 1982.

[111] ESRF. Brilliance at the ESRF. http://www.esrf.fr/Accelerators/Performance/Brilliance, 2003.

[112] J. L. Jordan-Sweet. Synchrotron X-ray scattering techniques for microelectronics-related materials. *IBM Journal of Research Development*, 44(4):457–476, 2000.

[113] W. Parrish, M. Hart. Advantages of synchrotron radiation for polycrystalline diffractometry. *Zeitschrift für Kristallographie*, (179):161–173, 1987.

[114] A. L. Robinson. Third-generation synchrotron light sources. *Standford Linear Acceleration Center Beam Line*, 24(1):17–27, 1994.

[115] A. S. Schlachter, A. L. Robinson. *Third-generation synchrotron sources: X-rays of unprecedented brightness for scientific and industrial applications.* McGraw-Hill Yearbook of Science and Technology. New York, 1996.

[116] A. S. Schlachter. Third-generation synchrotron light sources. In A. S. Schlachter, F. J. Wuilleumier, editor, *New directions in research with third-generation soft X-ray synchrotron radiation sources.* NATO Advanced Study Institute, 1992.

[117] W. Matz, N. Schell, G. Bernhard, F. Prokert, T. Reich, J. Claußner, W. Oehme, R. Schlenk, S. Dienel, H. Funke, F. Eichhorn, M. Betzl, D. Pröhl, U. Strauch, G. Hüttig, H. Krug, W. Neumann, V. Brendler, P. Reichel, M. A. Denecke, N. Nitsche. ROBL - a CRG beamline for radiochemistry and materials research at the ESRF. *Journal Synchrotron Radiation*, 6:1076–1085, 1999.

[118] FZR Rossendorf. X-ray optics. http://www.fz-rossendorf.de/pls/robis/-info?id=697, 2003.

[119] W. Matz, F. Prokert, R. Schlenk, J. Claußner, N. Schell, F. Eichhorn, G. Bernhard. The Rossendorf Beamline at the ESRF (Project ROBL). Wissenschaftlich technische Berichte FZR-158, Research Center Rossendorf, Forschungszentrum Rossendorf, Postfach 510919, D-01314 Dresden, Germany, 1996.

[120] W. Kossel, G. Möllenstedt. Elektroneninterferenzen im konvergenten Bündel. *Annalen der Physik*, 36(113):113–140, 1936.

[121] D. B. Williams. *Practical Analytical Electron Microscopy in Materials Science.* Philips Electron Optics Publishing Group Plenum press, Mahway, New Jersey, 2nd edition, 1987.

[122] J. Thomas. Software ELDISCA. *Leibniz Institute for Solid State and Materials Research Dresden.*

[123] TSL. Software ACT, Automated Crystallography for the TEM.

[124] D. B. Williams, C. B. Carter. *Transmission Electron Microscopy: A Textbook for Materials Science.* Plenum Press, New York, 1996.

[125] C.-J. Choi, Y.-W. Ok, T.-Y. Seong, H.-D. Lee,. Effect of a SiO_2 capping layer on the electrical properties and morphology of nickel silicides. *Japanese Journal of Applied Physics*, 1(41):1969–1973, 2002.

[126] W. L. Tan, K. L. Pey, S. Y. M. Chooi, J. H. Ye, T. Osipowicz. Effect of titanium cap in reducing interfacial oxides in the formation of nickel silicide. *Journal of Applied Physics*, 91(5):2901–2909, 2002.

[127] R. T. Tung, F. Schrey. Increased uniformity and thernal stability of $CoSi_2$ thin films by Ti capping. *Applied Physics Letters*, 67(15):2164–2166, 1995.

[128] O. Chamirian, J. A. Kittl, A. Lauwers, O. Richard, M. J. H. van Dal, K. Maex. Thickness scaling issues of Ni silicide. *Microelectronic Engineering*, 70:201–208, 2003.

[129] S. L. Hsia, T. Y. Tan, P. L. Smith, G. E. McGuire. Cosi and $CoSi_2$ phase formation on bulk and SOI Si substrates. *Materials Research Society Symposium Proceedings*, 320:373–378, 1994.

[130] P. Villars, L. D. Calvert. *Pearson's handbook of crystallographic data for intermetallic phases.* ASM International, Materials Park, Ohio, 2^{nd} edition, 1991.

[131] S. Pramanick. *Capillarity, agglomeration and diffusion phenomena in nanoscale cobalt silicide films.* PhD thesis, North Caroline State University, Department of Materials Science and Engineering, 1994.

[132] WebElements^{TM} Periodic table. Chemistry: WebElements Periodic Table: Professional Edition. http://www.webelements.com, 2003.

[133] T. S. Kang, J. H. Je. Real-time X-ray scattering study on the thermal evolution of interface roughness in $CoSi_2$ formation. *Applied Physics Letters*, 80(8):1361–1363, 2002.

[134] W.-J. Wu, B.-Z. Li, K. Shao, Z. Sun, Z.-G. Gu, W.-N. Huang, G.-B. Jiang. Epitaxial $CoSi_2$ film grown on Si substrate by solid interaction of Co/Ti/Si and TiN/Co/Ti/Si multilayer. *SPIE*, 2364:494–498, 1994.

[135] T. Kammler. personel communication, 2003.

[136] K. Maex, R. F. de Keersmaecker, G. Gosh, L. Deleay, V. Probst. Degradation of doped Si regions contacted with transition-metal silicides due to metal-dopant compound formation. *Journal of Applied Physics*, 66:5327–5334, 1989.

[137] P. S. Lee, D. Mangelinck, K. L. Pey, J. Ding, D. Z. Chi, T. Osipowicz, J. Y. Dai, A. See. Enhanced stability on Ni monosilicide on MOSFETs poly-Si gate stack. *Microelectronic Engineering*, 60:171–181, 2002.

[138] C. Lavoie, C. Cabral jr., F. M. d'Heurle, J. M. E. Harper. Exploring thin-film reactions by means of simultaneous surface roughness and resistance measurements. *Defect and Diffusion Forum*, 194–199:1477–1490, 2001.

[139] S. S. Lau, J. W. Mayer, K. N. Tu. Interactions in the Co/Si thin-film system. I. Kinetics. *Journal of Applied Physics*, 49:4005–4010, 1978.

[140] H. Miura, E. Ma, V. Thompson. Initial sequence and kinetics of silicide formation in cobalt/amorphous-silicon multilayer thin films. *Journal of Applied Physics*, 70(8):4287–4294, 1991.

[141] V. D. Vankar. Kinetics of growth or refractory metal/near noble metal silicides. *Proceedings of the Indian Academy of Sciences*, 57(2):195–203, 1991.

[142] C. Canali, G. Majni, G. Ottaviani, G. Celotti. Phase diagrams and metal-rich silicide formation. *Journal of Applied Physics*, 50(1):255–258, 1979.

[143] J. S. Byun, D.-H. Kim, W. S. Kim. Epitaxial growth of $CoSi_2$ layer on (100)Si and facet formation at the $CoSi_2$/Si interface. *Journal of Applied Physics*, 78(3):1725–1730, 1995.

[144] C. Detavernier, R. L. van Meirhaeghe, F. Cardon, K. Maex, B. Brijs, W. Vandervorst. Epitaxial $CoSi_2$ formation by Cr or Mo interlayer. *Materials Research Society Symposium Proceedings*, 611:C10.2.1–C10.2.6, 2001.

[145] R. K. K. Chong, M. Yeardon, W. K. Choi, E. A. Stach, C. B. Boothroyd. Nitride mediated epitaxy of $CoSi_2$ on Si (001). *Applied Physics Letters*, 82(12):1833–1835, 2003.

[146] R. T. Tung. Oxide mediated epitaxy of $cosi_2$ on silicon. *Applied Physics Letters*, 68(24):3461–3463, 1996.

[147] R. Pretorius, J. W. Mayer. Silicide formation by concentration controlled phase selection. *Journal of Applied Physics*, 81(5):2448–2450, 1997.

[148] S. Mantl, L. Kappius, A. Antons, M. Löeken, F. Klinkhammer, M. Dolle, Q. T. Zhao, S. Mesters, C. Buchal, H. L. Bay, H. Trinkaus, K.-H. Heinig. Growth, patterning and microelectronic applications of epitaxial cobaltdisilicide. *MRS Symposium Proceedings*, 514:145–155, 1998.

[149] M. Falke. *Elektronenmikroskopische Untersuchung der Bildung von $CoSi_2$-Schichten auf Si(001).* PhD thesis, Technical University of Chemnitz, Chemnitz, Germany, 1999.

[150] T. B. Massalski, H. Okamoto, P. R. Subramanian, L. Kacprzak, editor. *Binary Alloy Phase Diagrams*, volume 2. W. Scott jr., ASM International, Materials Park, OH, 2^{nd} edition, 1990.

[151] A. Wittmann, K. O. Burger, H. Nowotny. Mono- und Disilizidsysteme der Eisengruppe. *Monatshefte für Chemie*, 92:961–966, 1961.

[152] P. K. Panday, K. Schubert. Strukturuntersuchungen in einigen Mischungen T-B^3-B^4 (T=Mn, Fe, Co, Ir, Ni, Pd B^3=Al, Ga, Tl; B^4=Si, Ge). *Journal of Less-Common Metals*, 18:175–202, 1969.

[153] Y. Imai, M. Mukaida, T. Tsunoda. Calculation of the density of states of transition disilicides and their related compounds systematically calculated by a first-principle pseudopotential method using plane-wave basis. *Intermetallics*, 8:381–390, 2000.

[154] Y. Imai, M. Mukaida, K. Kobayashi, T. Tsunoda. Calculation of the density of states of transition metal monosilicides by a first-principle pseudopotential method using plane-wave basis. *Intermetallics*, 9:261–268, 2001.

[155] M. C. Payne, M. P. Teter, D. C. Allan, T. A. Arias, J. D. Joannopoulus. Iterative minimization techniques for *ab initio total-energy calculations: molecular dynamics and conjugate gradients. Reviews of Modern Physics*, 64:1045–10970, 1992.

[156] V. L. Moruzzi, P. Oelhafen, A. R. Williams. Stability in ordered and amorphous transition-metal compounds. *Physical Review B*, 27(12):7194–7198, 1983.

[157] W. D. Nix. Mechnical properties of thin films. *Metallurgical transactions A*, 20A:2217–2245, 1989.

[158] A. Steegen, K. Maex. Silicide induced stress in Si: Origin and consequences for MOS technologies. unpublished, 2002.

[159] G. Lucadamo, C. Lavoie, C. Cabral jr., R. A. Carruthers, J. M. E. Harper. *In-situ* and *ex-situ* measurement of stress evolution in the cobalt-silicon system. *Materials Research Society Symposium*, 611:C6.3.1–C6.3.6, 2000.

[160] M. Kh. Rabadanov, M. B. Ataev. Atomic structure and high anisotropy of thermal expansion in NiSi single crystals. II Temperature-induced structural changes. *Crystallography Reports*, 47(3):379–382, 2002.

[161] S. M. Barmin, A. A. Frolov. Giant anisotropy of the thermal expansion of NiSi single crystals. *Soviet Physics Solid State*, 32(5):897–898, 1990.

[162] I. Engström, B. Lönnberg. Thermal expansion studies of the group IV-VII transition-metal disilicides. *Journal of Applied Physics*, 63:4476–4484, 1988.

[163] W. W. Mulins. Theory of thermal grooving. *Journal of Applied Physics*, 28(3):333–339, 1957.

[164] A. Alberti, F. La Via, M. G. Grimaldi, S. Ravesi. Effect of lateral dimensional scaling on the thermal stability of thin $CoSi_2$ layers reacted on polycrystalline silicon. *Journal of Vacuum Science and Technology B*, 18(2):717–720, 2000.

[165] A. Alberti, F. La Via, E. Rimini. Reaction and thermal stability of cobalt disilicide on polysilicon resulting from Si/Ti/Co multilayer system. *Journal of Vacuum Science and Technology B.*, 17(4):1448–1455, 1999.

[166] D. P. Adams, S. M. Yalisove, D. J. Eaglesham. Interfacial and surface energetics of $CoSi_2$. *Journal of Applied Physics*, 76(9):5190–5194, 1994.

[167] W. W. Mulins. Magnetically induced grain-boundary motion in bismuth. *Acta Metallurgica*, 4:421–432, 1956.

[168] S.-L. Zhang. Phase and morphology stabilities of Ni-germanosiliicdes formed on single-crystal and polycrystalline SiGe. *Oral presentation at the European Workshop on Materials for Advanced Metallization 2003, La Londe Les Maures, France, March 9–12*, 2003.

[169] S.-L. Zhang. Nickel-based contact metallization for SiGe MOSFETs: progress and challenges. *Microelectronic Engineering*, 70:174–185, 2003.

[170] L. J. Jin, K. L. Pey, W. K. Choi, E. A. Fitzgerald, D. A. Antoniadis, A. J. Pitera, M. L. Lee, D. Z. Chi. The interfacial reaction of Ni on (100) $Si_{1-x}Ge_x$ ($x = 0, 0.25$) and (111) Ge. *Symposium on Advanced Materials for Micro- and Nano- Systems Proceedings*, 2003.

[171] C. Detavernier, A. S. Özcan, J. L. Jordan-Sweet, F. M. Ross, J. Tersoff, C. Lavoie. An off-normal fiber-like texture in thin films on single crystalline substrates. *in press*, page in press, 2004.

[172] C. Detavernier, C. Lavoie. Texture of NiSi films on Si(100) and (110) substrates. *in press*, page in press, 2004.

[173] C. Detavernier, A. S. Özcan, J. L. Jordan-Sweet, C. Lavoie. Axiotaxy: A new type of texture in thin films. *Oral presentation at the Denver X-ray conference 2003, Denver, Colorado, USA, August 4–8*, 2003.

[174] C. Lavoie. personel communication, 2003.

[175] M. Oztürk. personel communication, 2003.

[176] J. Rinderknecht, F. Berberich, W. Matz, E. Zschech. Determination of phase formation processes in nanoscale Co-Ti layers using synchrotron radiation in conjunction with a high temperature chamber. Bi-annual report 1999/2000 FZR-322, Forschungszentrum Rossendorf, Germany, 2001.

[177] J. Rinderknecht, H. Prinz, T. Kammler, F. Berberich, E. Zschech. Phase formation processes in nanoscale nickel layers during heat treatment on different silicon substrates. Bi-annual report 2001/2002 FZR-364, Forschungszentrum Rossendorf, Germany, 2003.

[178] J. Rinderknecht, H. Prinz, T. Kammler, N. Schell, E. Zschech, K. Wetzig, T. Gessner. *In situ* high temperature synchrotron-radiation diffraction studies of silicidation processes in nanoscale Ni layers. *Microelectronic Engineering*, 70/2–4:226–232, 2003.

[179] J. A. van Beek, P. J. T. L. Oberndorff, A. A. Kodentsov, F. J. J. van Loo. Interactions in the Co-Ni-Si system at 800 °C. *Journal of Alloys and Compounds*, 297:137–143, 2000.

Thesen zur Dissertation

1. Silizide spielen eine wichtige Rolle in den technologisch fortschrittlichsten CMOS Bauteilen. Sie finden Verwendung als Kontaktmaterial auf den Aktivgebieten und dem Silizium Gatter von Transistoren. Kobaltdisilizid ($CoSi_2$) findet in der Fertigung aktueller Mikroprozessoren Verwendung. Mit fortschreitender Technologieentwicklung und damit verbundener Verkleinerung der Strukturen ergeben sich Probleme beim Einsatz von $CoSi_2$.
2. Aufgrund von Agglomerationserscheinungen bei sehr dünnen und schmalen ($\leq$60 nm) polykristallinen Silizidschichten kommt es zu Unterbrechungen der $CoSi_2$ Schichten. Diese führen zu erhöhten elektrischen Widerständen und können auch den Ausfall des Bauteils bewirken.
3. Durch *in situ* Hochtemperatur-Synchrotronstrahlung-Röntgenbeugungsexperimente (SR-XRD) an nanoskaligen Schichten, d. h. Schichtdicken im Bereich 10er nm, konnte die Phasenbildungsabfolge zu
   $Co_2Si \rightarrow CoSi \rightarrow CoSi_2$ bestimmt werden.
4. Um die temperaturabhängigen Agglomerationserscheinungen bei der Verwendung von $CoSi_2$ zu reduzieren, wurden 5 at. % Ni zu Co hinzulegiert. Die Zugabe von Ni sollte die Phasenbildungs- und Umwandlungstemperaturen erniedrigen. *In situ* SR-XRD-Experimente mit 5 at. % Ni als Legierungselement zeigten nur leicht herabgesetzte Temperaturen im Vergleich zu reinen Co Proben.
5. Auger Elektronenspektroskopie (AES) zeigte in jedem Fall eine Anreicherung von Ni an der Grenzfläche zum Silizium-Substrat nach thermischer Behandlung der Probe.
6. Dieser Effekt konnte auch bei Schichtstapeln Ni auf Co auf Si beobachtet werden und führte zu einer Umkehrung der ursprünglich abgeschiedenen Schichtfolge.

7. Die Silizide Co_2Si und Ni_2Si sowie $CoSi_2$ und $NiSi_2$ sind vollständig miteinander mischbar. Die Monosilizide der jeweiligen Elemente sind nur sehr eingeschränkt miteinander mischbar, was zu den beobachteten Effekten führt.

8. Aufgrund der Oxidationsneigung von Co wird beim zweistufigen thermischen Silizidierungsprozess eine Ti Deckschicht verwendet. Diese Deckschicht dient dazu die Oxidation von Co zu verhindern sowie Verunreinigungen aufzunehmen. Wird diese Deckschicht vor dem zweiten Temperschritt nicht, oder nicht vollständig entfernt, so kann es zur Bildung einer ternären Co-Ti-Si Phase kommen. Durch den Einsatz von Elektronenbeugung mit konvergentem Strahl im TEM (CBED) und energiegefilterter TEM (EFTEM) konnte die ternäre Phase CoTiSi identifiziert werden.

9. NiSi wird höchstwahrscheinlich in absehbarer Zeit $CoSi_2$ als Werkstoff in der Mikroprozessorfertigung ersetzen. NiSi bietet eine Reihe von Vorteilen gegenüber $CoSi_2$: Die Bildungstemperatur von NiSi ist deutlich geringer. Es kommt nicht zu unterbrochenen Silizidschichten, auch bei extrem schmalen Linienbreiten. Verglichen mit $CoSi_2$ ist der Siliziumverbauch von NiSi für einen gegebenen Schichtwiderstand $\approx 35\,\%$ geringer. Nachteilig an NiSi ist, daß es nicht die thermodynamisch stabile Hochtemperaturform darstellt. NiSi wandelt sich bei hohen Temperaturen zu $NiSi_2$ um.

10. Die Bildung von NiSi erfolgt diffusionsgesteuert. Dies führt zu glatteren, und damit besseren Grenzschichten im Vergleich zu $CoSi_2$- oder $NiSi_2$-Schichten. Die Bildung der Disilizide erfolgt nukleationsgesteuert.

11. Auf einkristallinem Silizium-Substrat erfolgt die $NiSi_2$-Bildung epitaktisch. Dies konnte durch SR-XRD sowie durch TEM-Aufnahmen und Mikrobeugung im TEM gezeigt werden.

12. NiSi weist einen negativen thermischen Ausdehnungskoeffizienten (CTE) auf. Die b-Achse der NiSi-Elementarzelle verkleinert sich mit steigender Temperatur. Der negative thermische Ausdehnungskoeffizient von NiSi und sein nicht-lineares Verhalten konnte für den Temperaturbereich 400 °C – 700 °C durch *in situ* Hochtemperatur-SR-XRD Experimente bestimmt werden.

13. Bei der thermischen Behandlung von Ni-Silizidschichten erfolgt vor der $NiSi_2$-Bildung eine Agglomeration der Silizidschicht. Der Agglomerationsgrad von NiSi-Schichten konnte für verschiedene Herstellungsparameter mittels Rasterelektronenmikroskopie (REM/SEM) bestimmt werden.
14. Mittels der durchgeführten quasi-statischen SR-XRD Untersuchungen konnte die Phasenbildungsabfolge zu $Ni_2Si \rightarrow NiSi \rightarrow NiSi_2$ bestimmt werden.

15. Im Vergleich zu einkristallinen Substraten sind die Bildungs- und Umwandlungstemperaturen der Silizide auf polykristallinen Substraten erheblich niedriger. Dies wird durch die größere Anzahl an Diffusionswegen und Keimbildungszentren erklärt.
16. Deckschichten aus Ti oder TiN erhöhen die Phasenbildungs- und Umwandlungstemperaturen. Im Falle von Ti auf Co wird die thermische Stabilität um +100 K, bei TiN auf Ni um +50 K erhöht.
17. Dotierungselemente führen im Allgemeinen ebenfalls zu einer Erhöhung der Phasenbildungs- und Umwandlungstemperaturen. Dieser Effekt kann im Falle von NiSi auf einkristallinem Si-Substrat zu einer Erhöhung der thermischen Stabilität um bis zu +150 K beitragen.
18. Deckschichten aus Ti oder TiN reduzieren die Neigung zur Agglomeration dünner Silizidschichten, erhöhen also die thermische Stabilität dieser Schichten. Die Elemente der Deckschichten behindern die Diffusion der silizidbildenden Elemente. Agglomeration ist abhängig von der Temperatur, Zeit, Verhältnis von Korndurchmesser zu Schichtdicke und der Schichtdicke.
19. Die abgeschiedene Schichtdicke der Metallschichten hat einen Einfluß auf die Phasenbildungs- und Umwandlungstemperaturen der Silizide. Je dünner die (Silizid-)Schichten, desto kürzer sind die Diffusionspfade. Außerdem verringert sich die durchschnittliche Korngröße und somit wird die Korngrenzendiffusion stärker betont. Dies bedingt einen deutlich größeren effektiven Diffusionskoeffizienten, welcher die beobachteten niedrigeren Phasenbildungs- und Umwandlungstemperaturen hervorruft.

Lebenslauf

Persönliche Angaben	
Name, Vorname	Rinderknecht, Jochen
geboren	4. Dezember 1968 in Stuttgart
Nationalität	deutsch
Wohnort	Dresden
Schulbildung	Sept. 1975 - Juli 1979 Grundschule in Pleidelsheim
	Aug. 1979 - Mai 1988 Gymnasium in Pforzheim, Baden-Württemberg Abschluß: Allgemeine Hochschulreife
Studium	Okt. 1990 - Aug. 1997 Studium der Mineralogie an der Universität Stuttgart
	Abschluß: Diplom-Mineraloge, mit Auszeichnung Studienschwerpunkt: Kristallographie
	Thema der Diplomarbeit: Mineralogische Untersuchungen an Ettringit-Thaumasit-Mischkristallen aus Sohlhebungen in sulfathaltigen Auffüllungen
Beruflicher Werdegang	seit Sept. 1997 AMD Saxony LLC & Co. KG Materials Analyst, Materials Analysis Department

Appendix A

Phase diagrams

A.1 The systems Co–Si

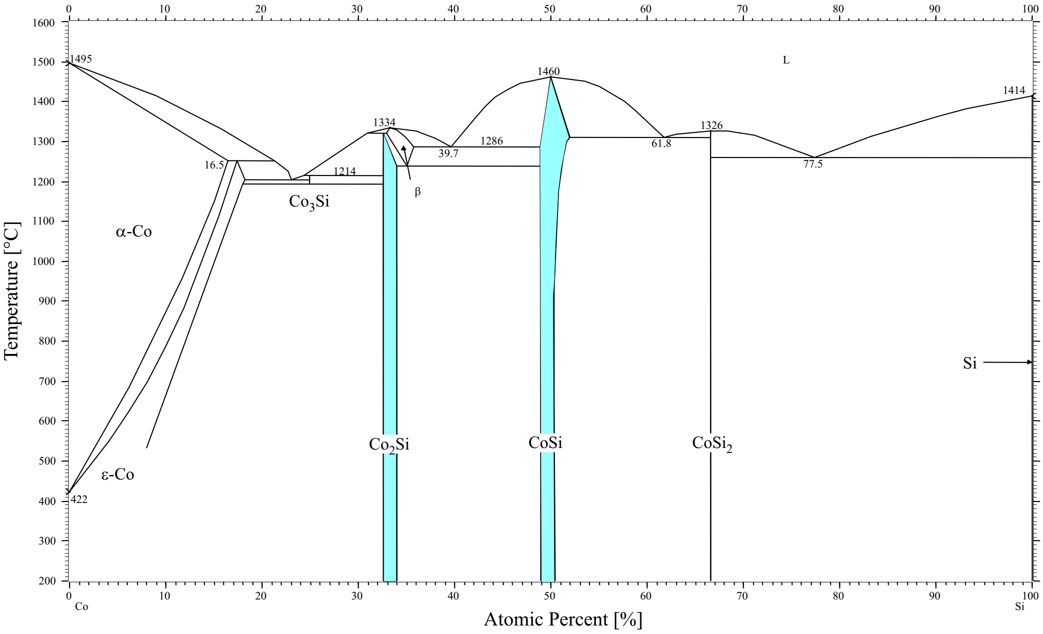

Fig. A.1: Phase diagram Co–Si [99].

A.2 The system Ni–Si

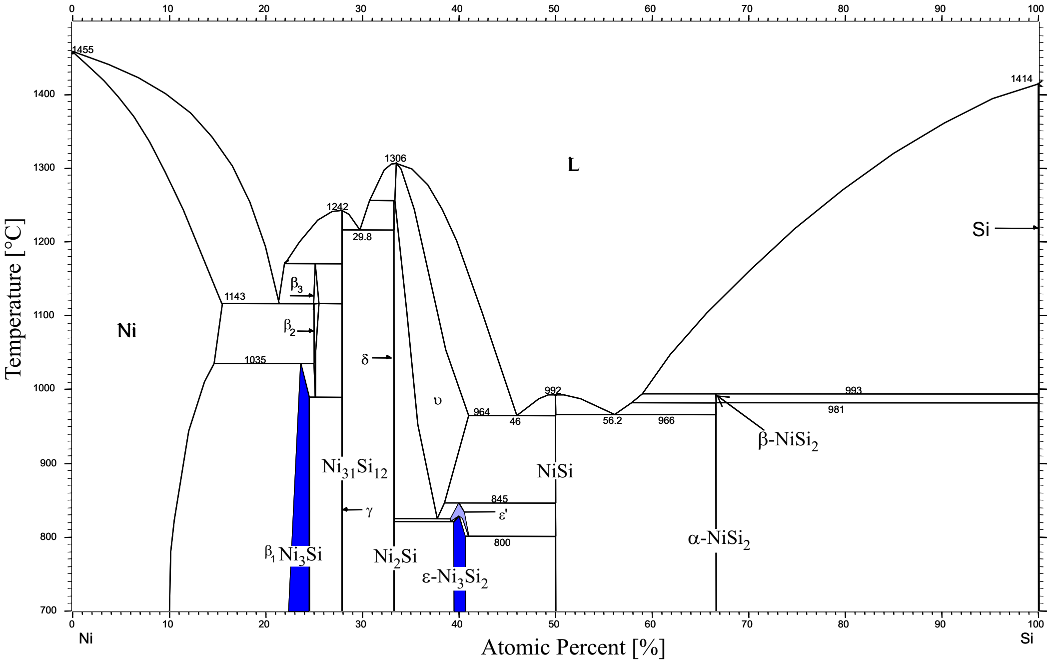

Fig. A.2: Phase diagram Ni–Si [100].

A.3 The system Co–Ni

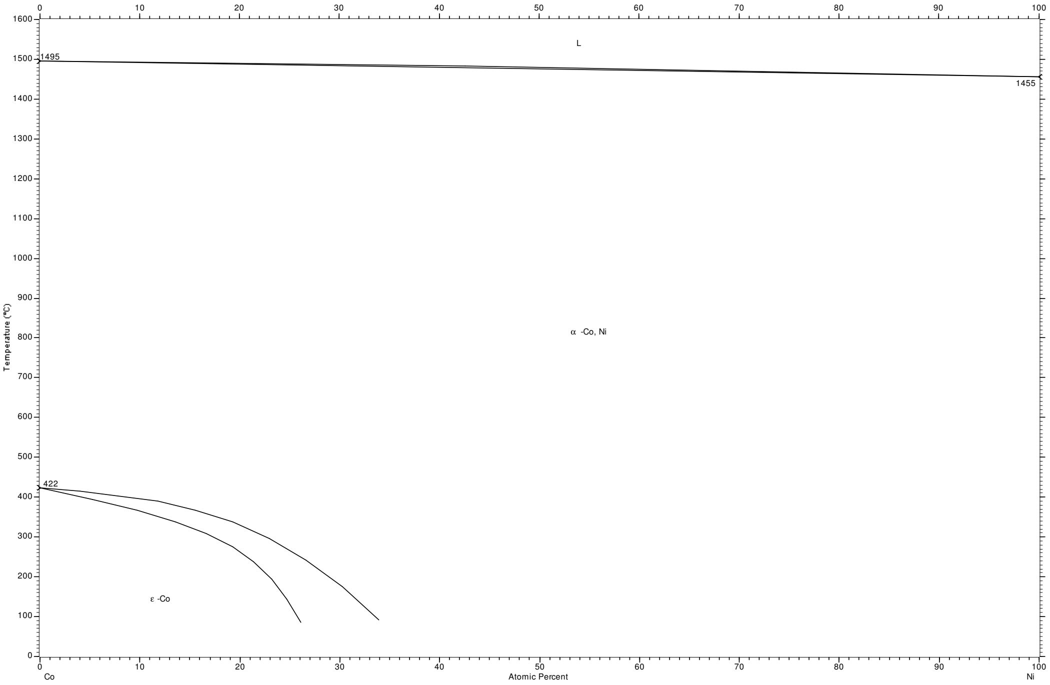

Fig. A.3: Phase diagram Co–Ni [150].

A.4 The system Co–Ni–Si

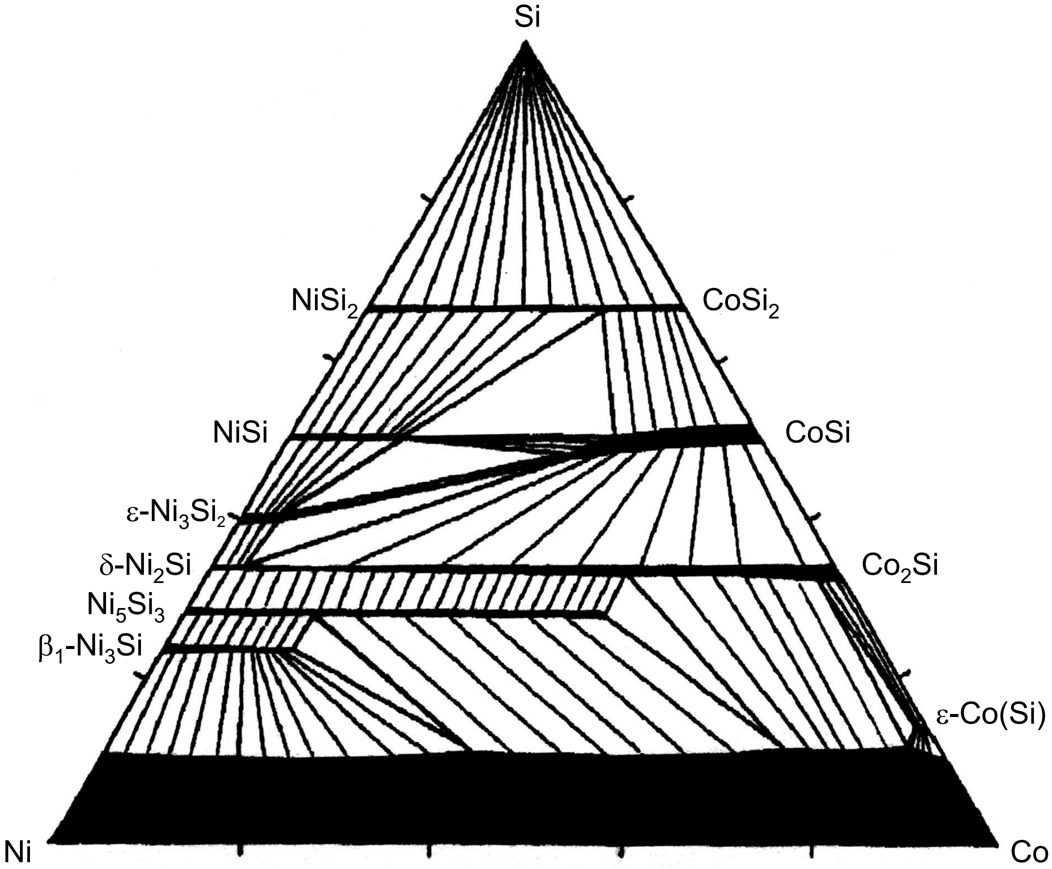

Fig. A.4: Phase diagram Co–Ni–Si. Isothermal section at 800 °C [179].

Appendix B

AES results

B.1 AES depth profiles of Co-Ni|Si samples

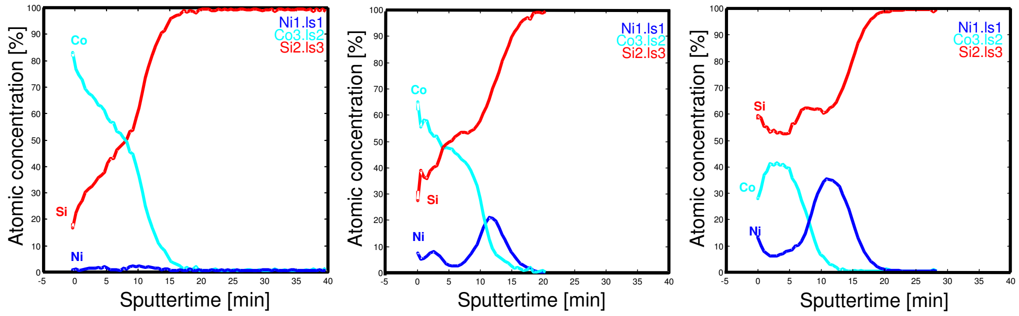

(a) 1 nm Ni | 19 nm Co | Si. (b) 5 nm Ni | 15 nm Co | Si. (c) 10 nm Ni | 10 nm Co | Si.

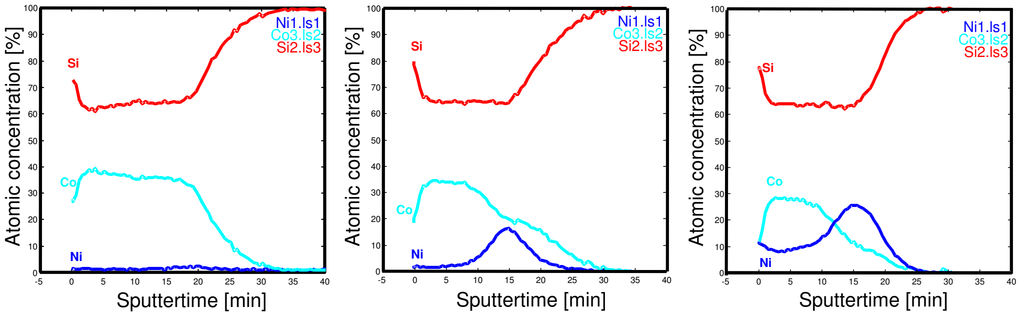

(d) 1 nm Ni | 19 nm Co | Si. (e) 5 nm Ni | 15 nm Co | Si. (f) 10 nm Ni | 10 nm Co | Si.

Fig. B.1: AES depth profiles of Ni | Co | Si samples (5 at.%, 25 at.%, 50 at.% Ni) annealed at 450 °C (top row) and 600 °C (bottom row).

Appendix C

CBED results

In figure C.1 are the results of the CBED investigations shown that belong to CoSi.

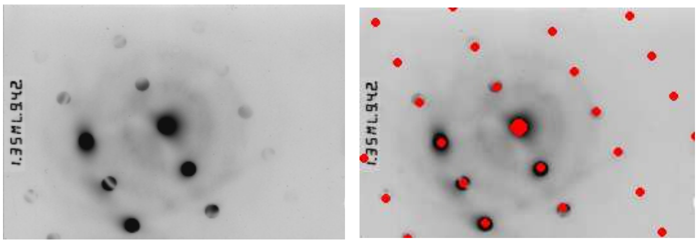

L942 CBED image, ELDISCA recognized diffraction spots, best fit with zone axis [1 3 1].

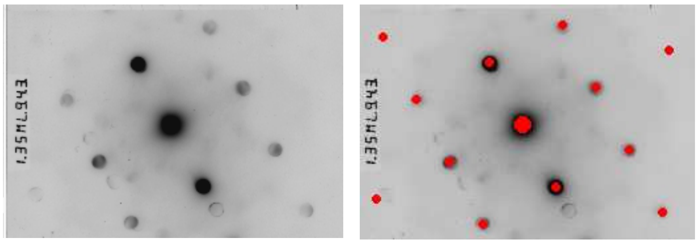

L943 CBED image, ELDISCA recognized diffraction spots, best fit with zone axis [5 2 1].

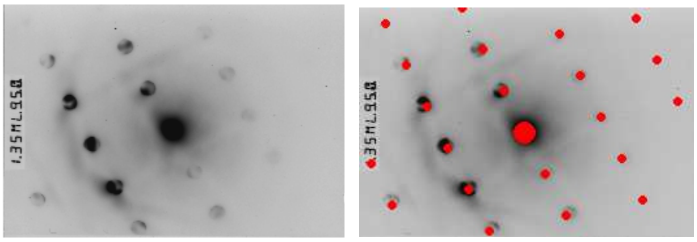

L950 CBED image, ELDISCA recognized diffraction spots, best fit with zone axis [1 1 3].

Fig. C.1: Summary of CBED results of sample heated up to 610 °C for CoSi.

In figure C.2 are the results of the CBED investigations shown that belong to $CoSi_2$ and α-Ti.

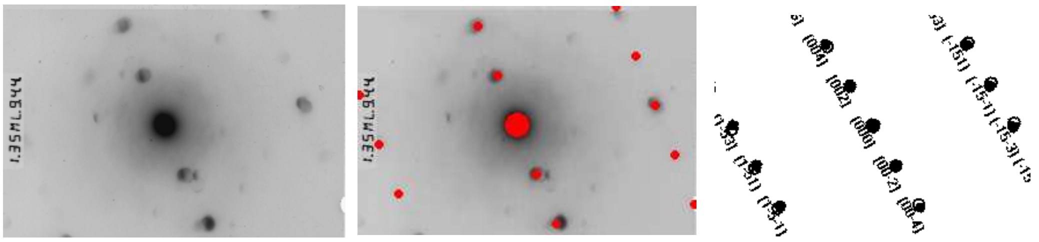

(a) $CoSi_2$

L944 CBED image, ELDISCA recognized diffraction spots, best fit with zone axis [5 1 0].

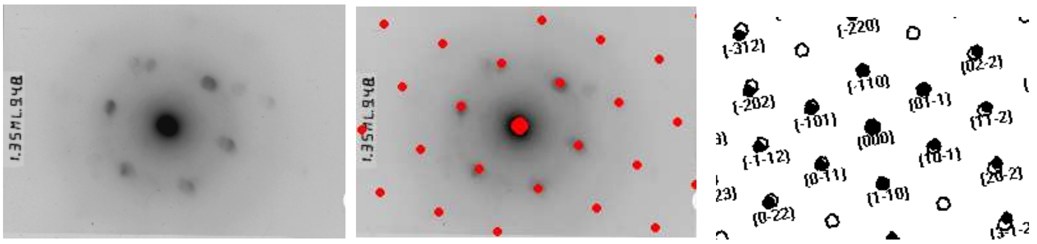

(b) α-Ti

L948 CBED image, ELDISCA recognized diffraction spots, best fit with zone axis [1 1 1].

Fig. C.2: Summary of CBED results of sample heated up to 610 °C for $CoSi_2$ a) and α-Ti b).

Appendix D

SR-XRD results

D.1 SR-XRD results of Ni|Si samples

The following figures are closeups of specific key temperatures, where phase conversions could be observed, of figure 5.6 to illustrate the phase identification. The colors match those used in figure 5.6 in chapter 5.

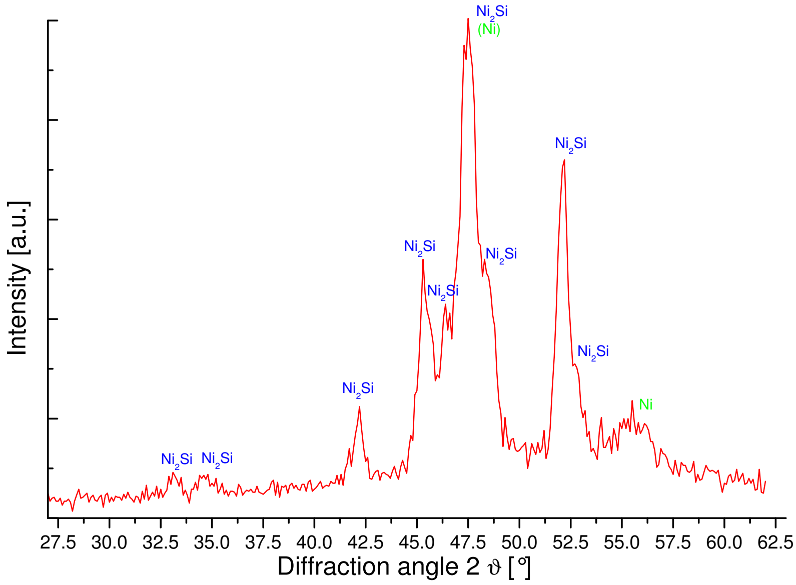

Fig. D.1: SR-XRD result of Ni|Si sample at 200 °C (λ=1.648 Å).

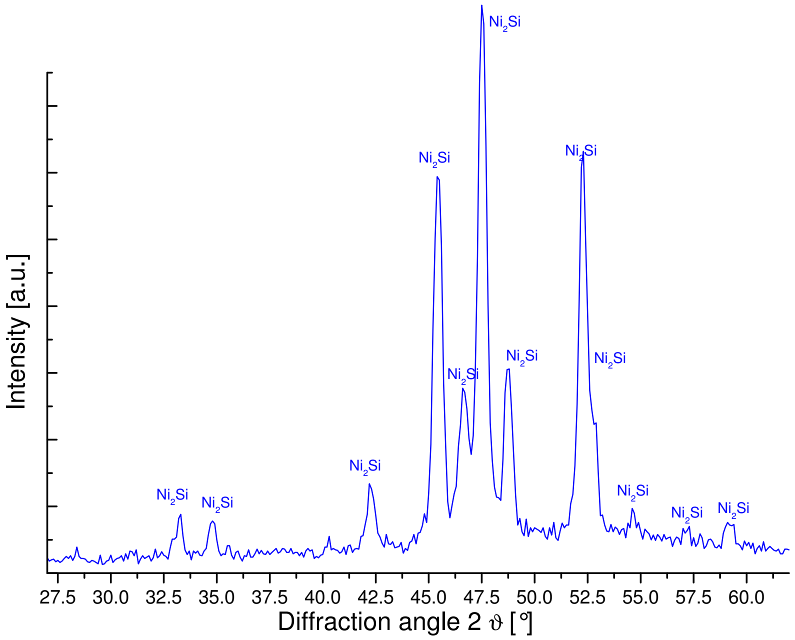

Fig. D.2: SR-XRD result of Ni|Si sample at 250 °C (λ=1.648 Å).

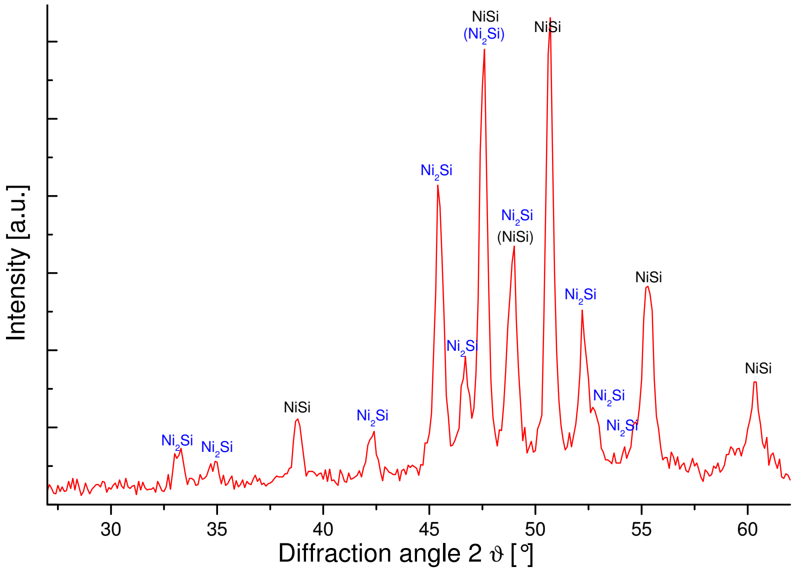

Fig. D.3: SR-XRD result of Ni|Si sample at 275 °C (λ=1.648 Å).

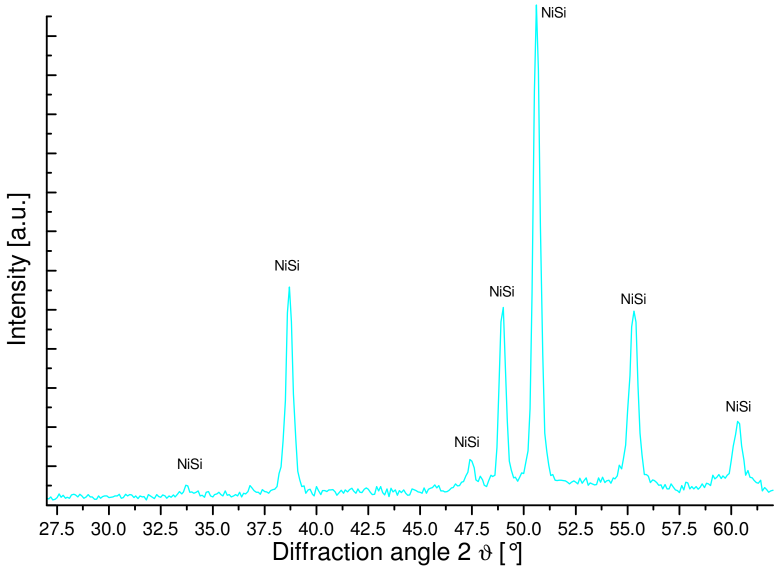

Fig. D.4: SR-XRD result of Ni|Si sample at 300 °C (λ=1.648 Å).

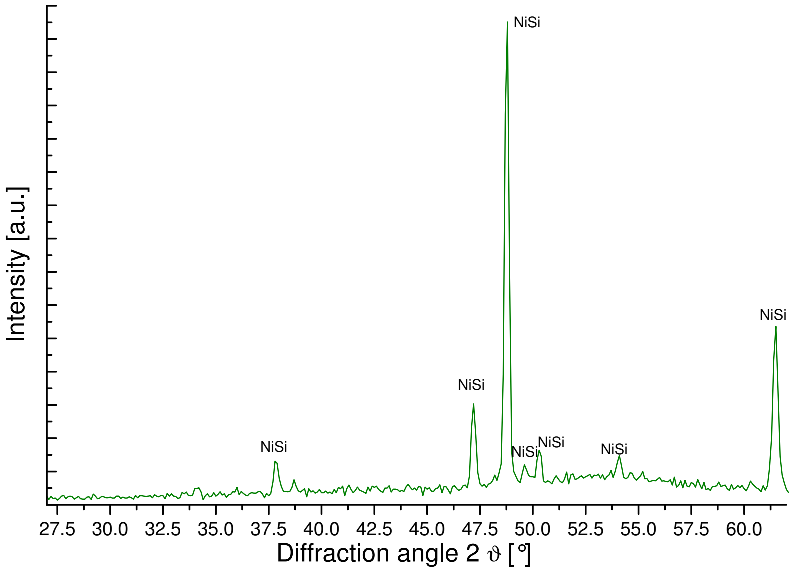

Fig. D.5: SR-XRD result of Ni|Si sample at 700 °C (λ=1.648 Å).

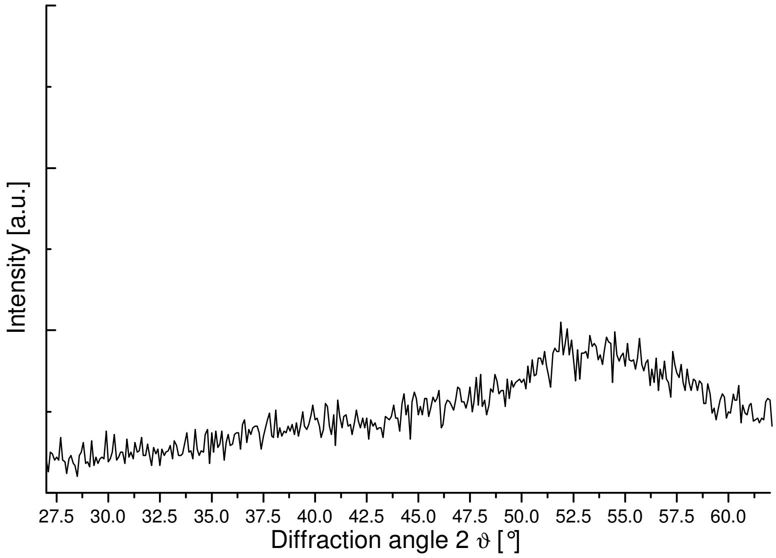

Fig. D.6: SR-XRD result of Ni|Si sample at 750 °C (λ=1.648 Å).

D.2 SR-XRD results of Co|Si samples

The following figures are closeups of specific key temperatures, where phase conversions could be observed, of figure 6.7 to illustrate the phase identification. The colors match those used in figure 6.7 in section 5.1.1.

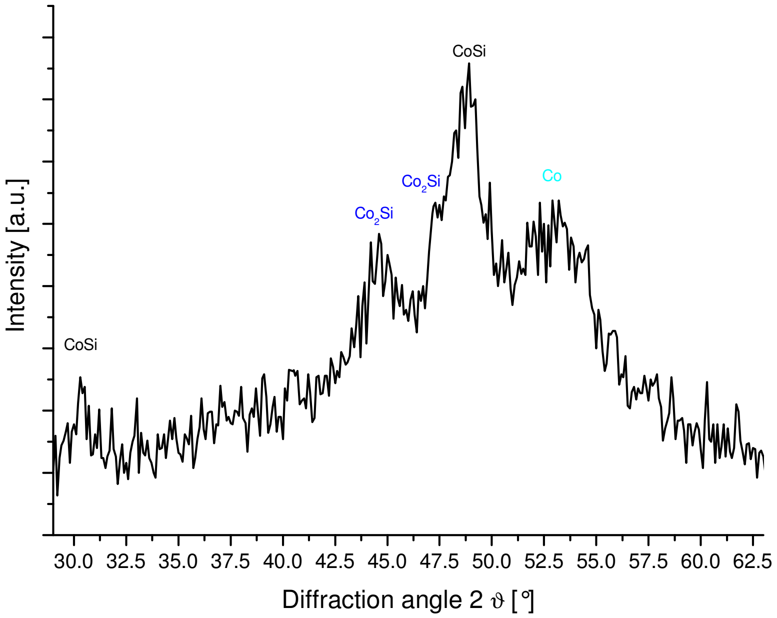

Fig. D.7: SR-XRD results of Co|Si sample with Ti capping layer at 300 °C (λ=1.648 Å).

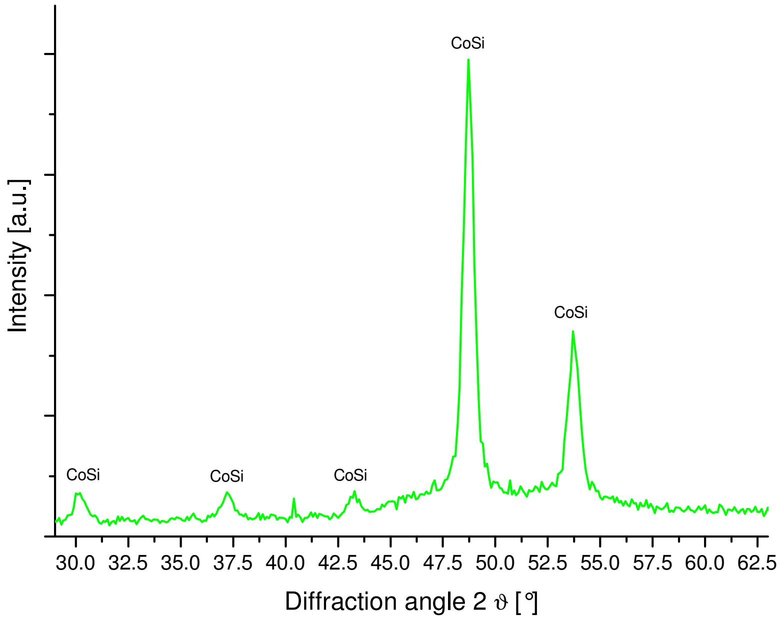

Fig. D.8: SR-XRD results of Co|Si sample with Ti capping layer at 350 °C (λ=1.648 Å).

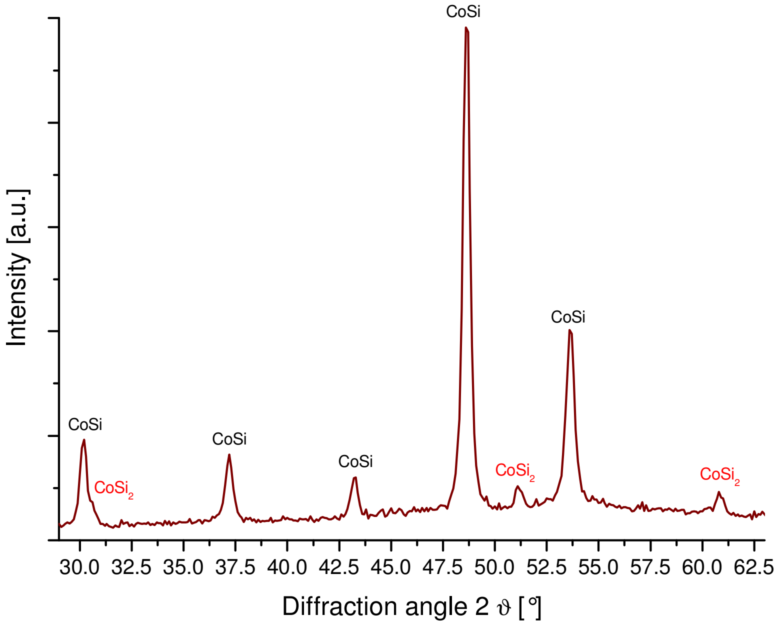

Fig. D.9: SR-XRD results of Co|Si sample with Ti capping layer at 575 °C (λ=1.648 Å).

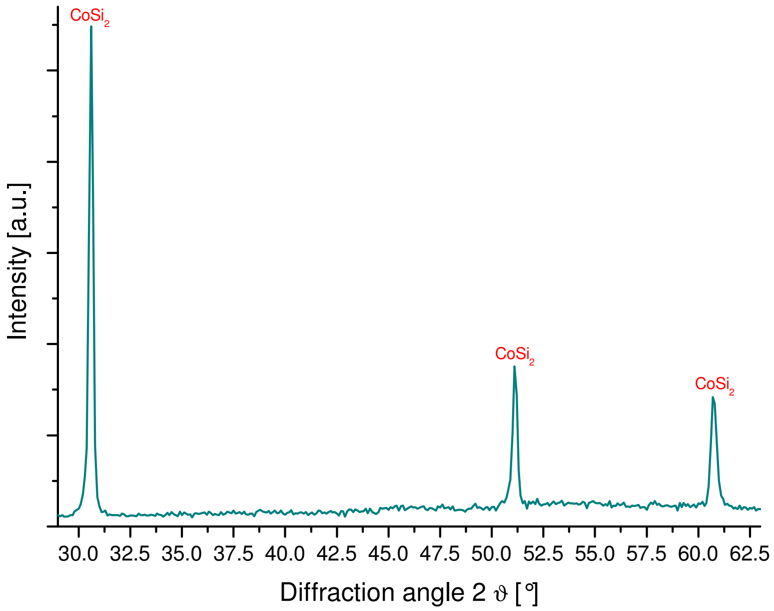

Fig. D.10: SR-XRD results of Co|Si sample with Ti capping layer at 625 °C (λ=1.648 Å).

D.3 SR-XRD results of Co-Ni|Si samples

The following figures are closeups of specific key temperatures, where phase conversions could be observed, of figure 5.4 to illustrate the phase identification. The colors match those used in figure 6.7 in section 5.1.2.

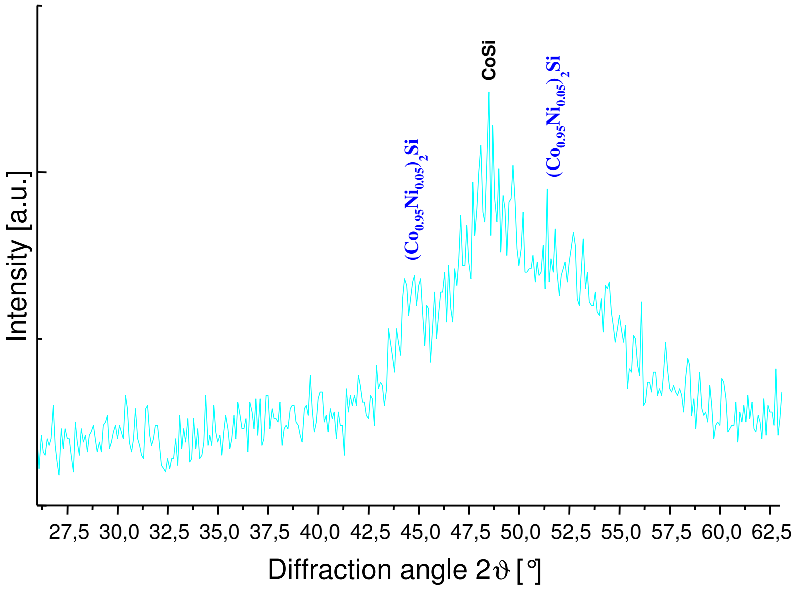

Fig. D.11: SR-XRD results of Co-Ni|Si sample at 275 °C (λ=1.648 Å).

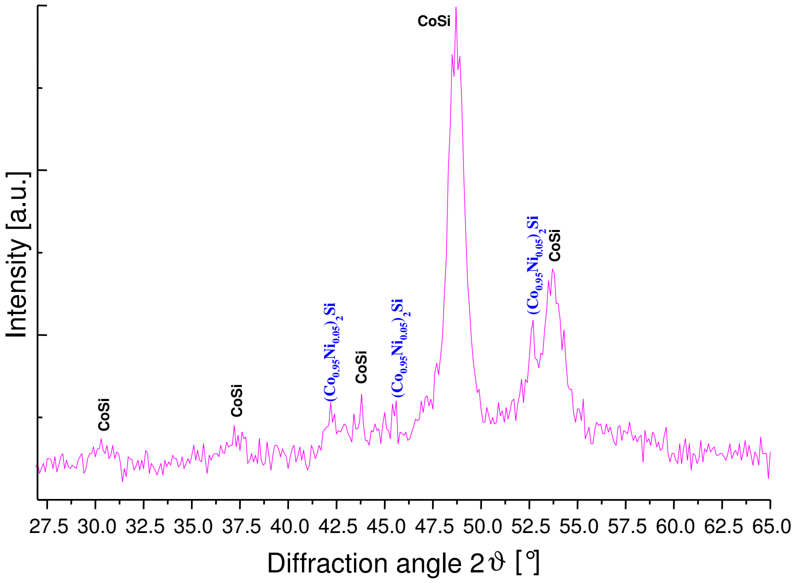

Fig. D.12: SR-XRD results of Co-Ni|Si sample at 300 °C (λ=1.648 Å).

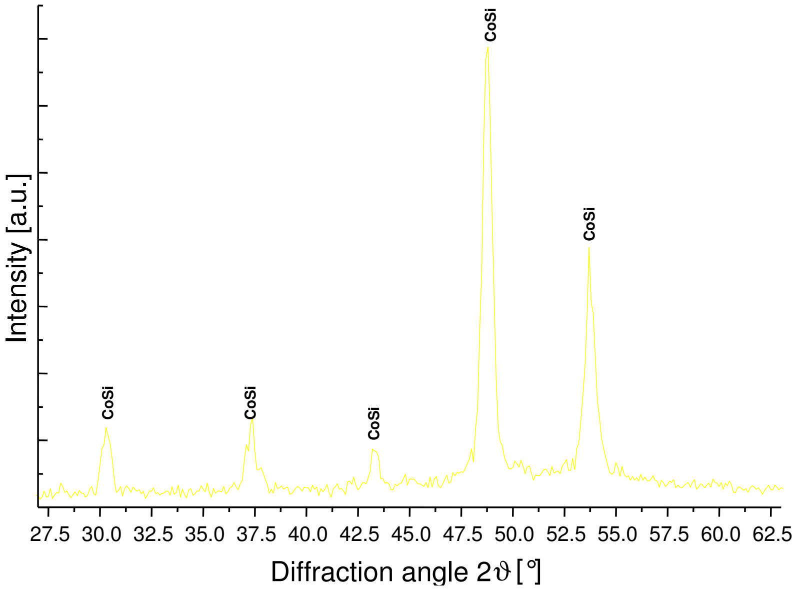

Fig. D.13: SR-XRD results of Co-Ni|Si sample at 350 °C (λ=1.648 Å).

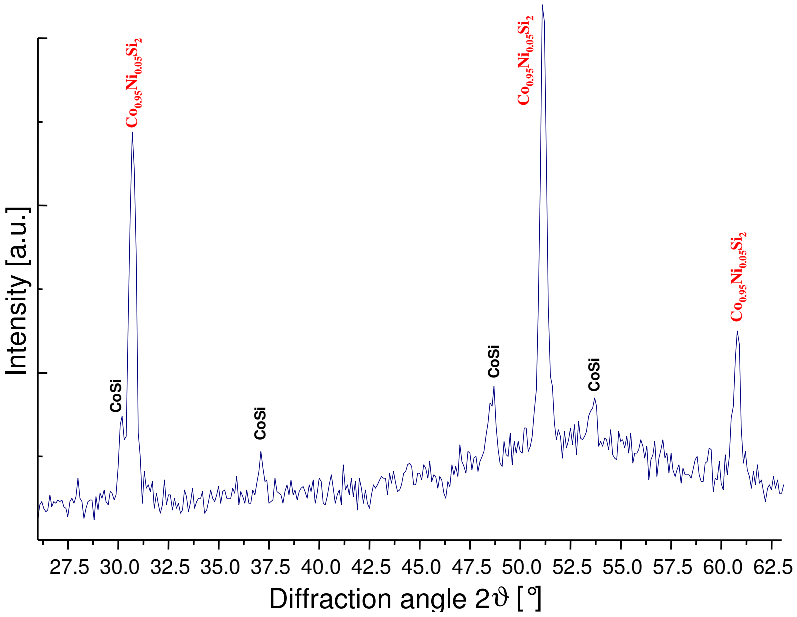

Fig. D.14: SR-XRD results of Co-Ni|Si sample at 475 °C (λ=1.648 Å).

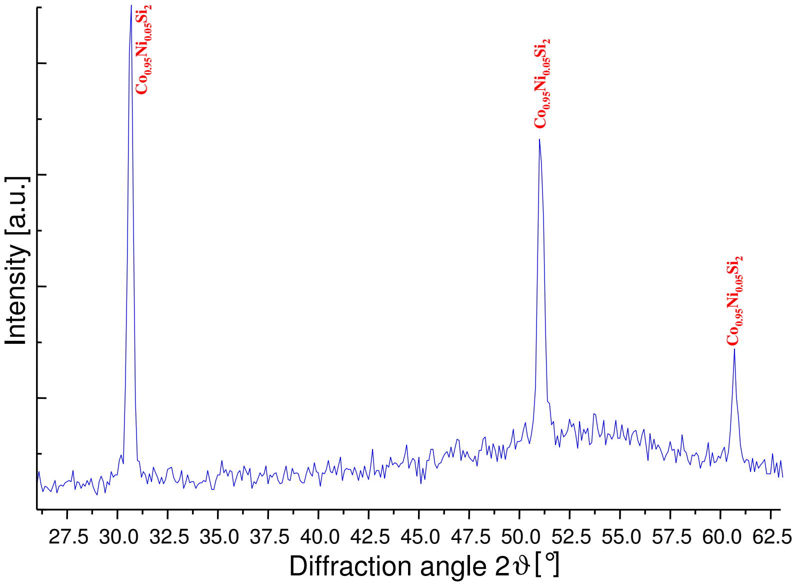

Fig. D.15: SR-XRD results of Co-Ni|Si sample at 600 °C (λ=1.648 Å).

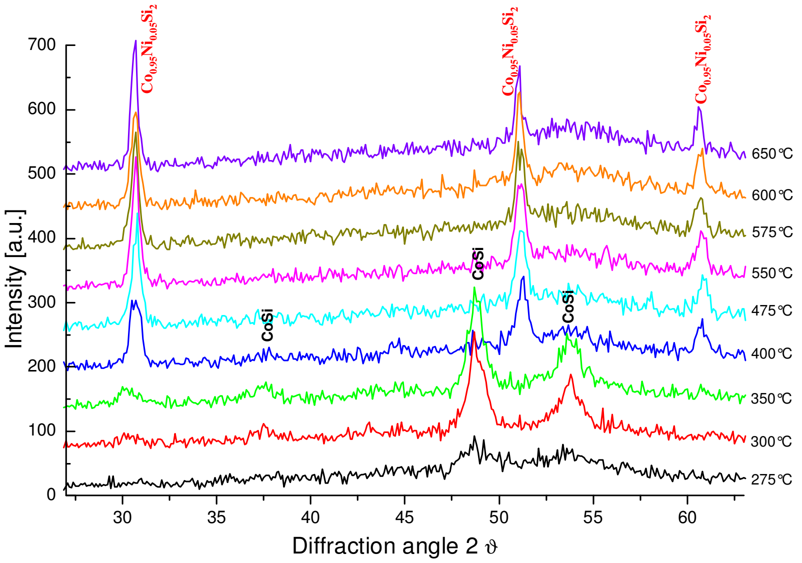

Fig. D.16: SR-XRD results of Co-Ni|Si sample annealed up to 650 °C (λ=1.648 Å). Sample showed partial agglomeration.

Appendix E

TEM results

E.1 TEM results of Ni|Si samples: interface roughness

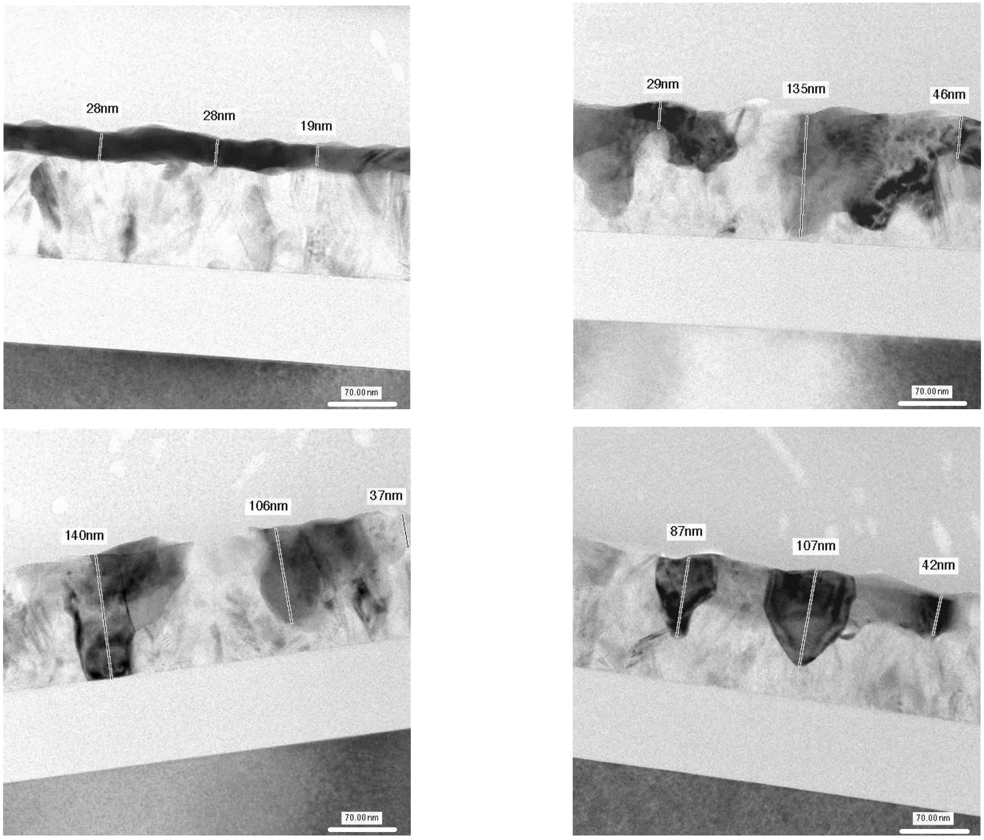

Fig. E.1: TEM cross-section images of NiSi layers. All samples annealed at 650 °C for 30 sec. Sample a) doped with $2.5 \cdot 10^{15}$ at/cm^2, no PAI. Samples b)–d) with PAI annealing time of 0 sec, 30 sec, and 300 sec, respectively. Xe$^+$ preamorphization with dose of $2 \cdot 10^{14}$ at/cm^2.

Appendix F

XRD results

Different samples have been investigated using conventional XRD equipment. The capping layer that was used consisted of 15 nm Ti.

F.1 Co|Si samples with and without Ti capping layer

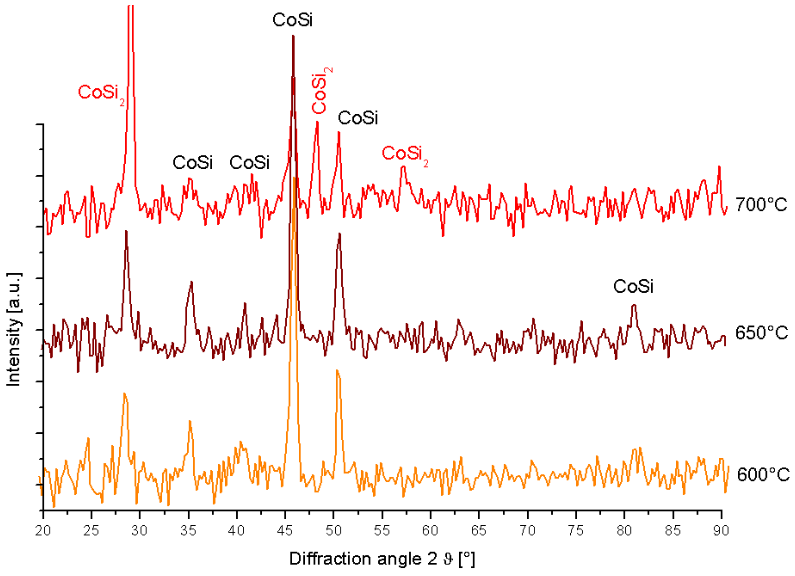

Fig. F.1: XRD results of Co|Si sample with Ti capping layer in the temperature range 600 °C–700 °C (λ=1.5414 Å).

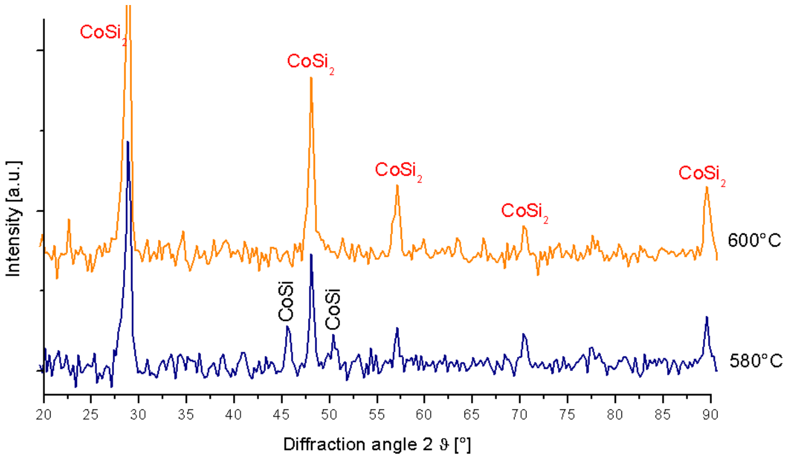

Fig. F.2: XRD results of Co|Si sample without Ti capping layer in the temperature range 580 °C–600 °C (λ=1.5414 Å).

F.2 Co-Ni|Si samples with and without Ti capping layer

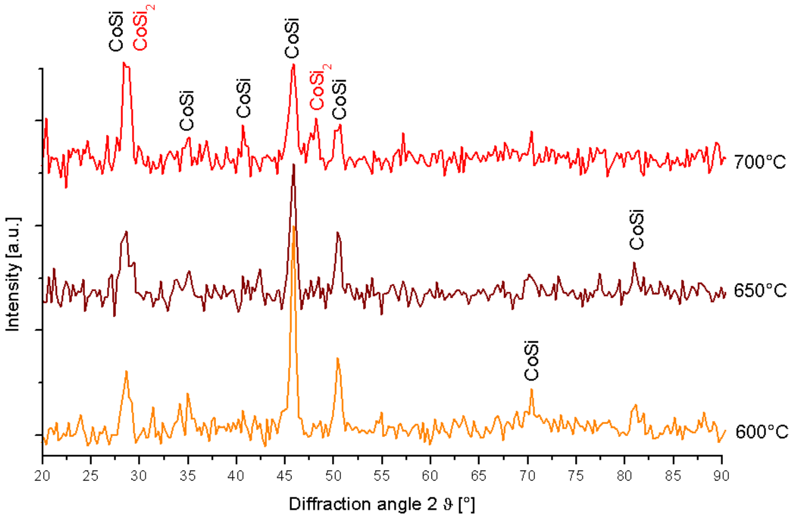

Fig. F.3: XRD results of Co-Ni|Si sample with Ti capping layer in the temperature range 600 °C–700 °C (λ=1.5414 Å).

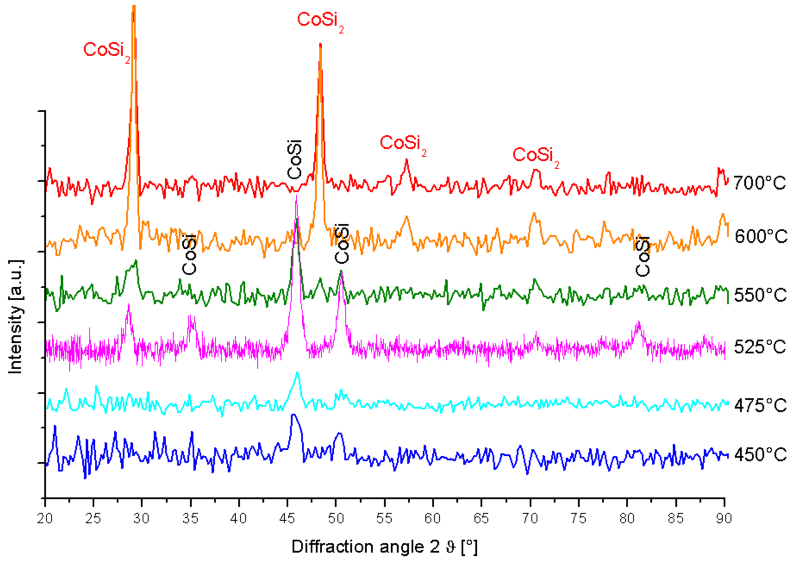

Fig. F.4: XRD results of Co-Ni|Si sample without Ti capping layer in the temperature range 600 °C–700 °C (λ=1.5414 Å).

Appendix G

XRR results

G.1 Samples with single crystal silicon substrate

G.1.1 XRR results of Ni|Si samples without capping layer

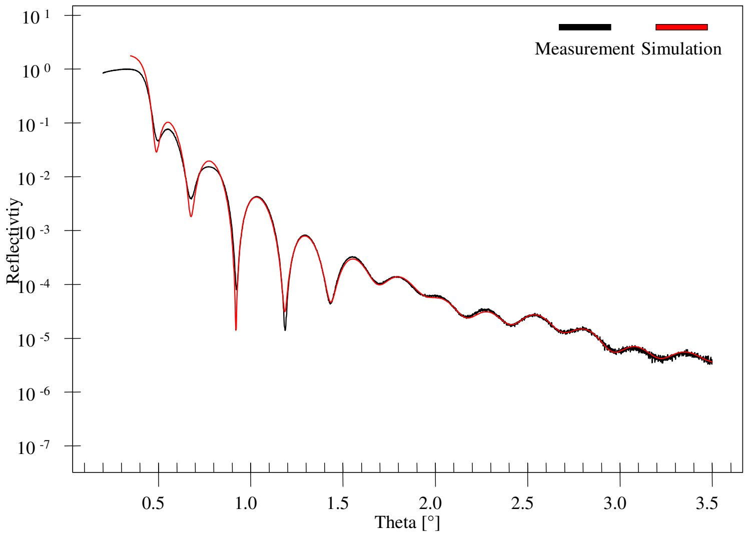

Fig. G.1: XRR result of undoped 15 nm Ni|Si sample without capping layer (λ=1.5414 Å). XRR results: 15.35 nm Ni with 1.1 nm Ni oxide on top.

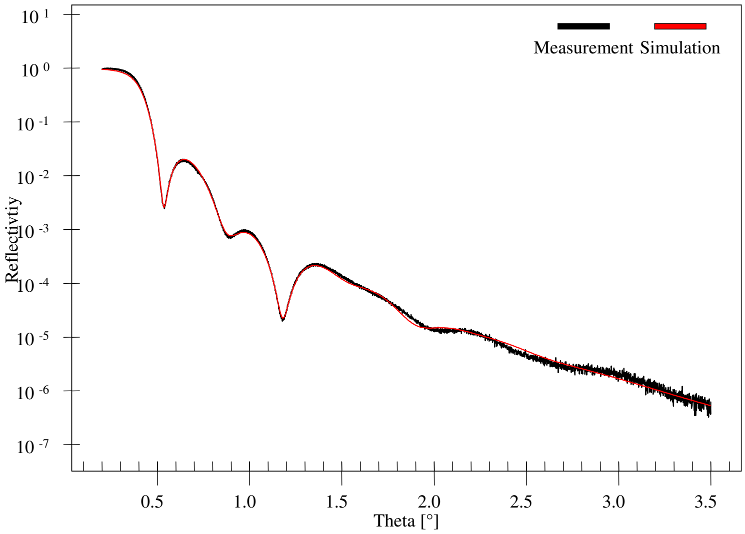

Fig. G.2: XRR result of B^+ doped 8 nm Ni|Si sample without capping layer (λ=1.5414 Å). XRR results: 10.4 nm Ni with 1.3 nm Ni oxide on top.

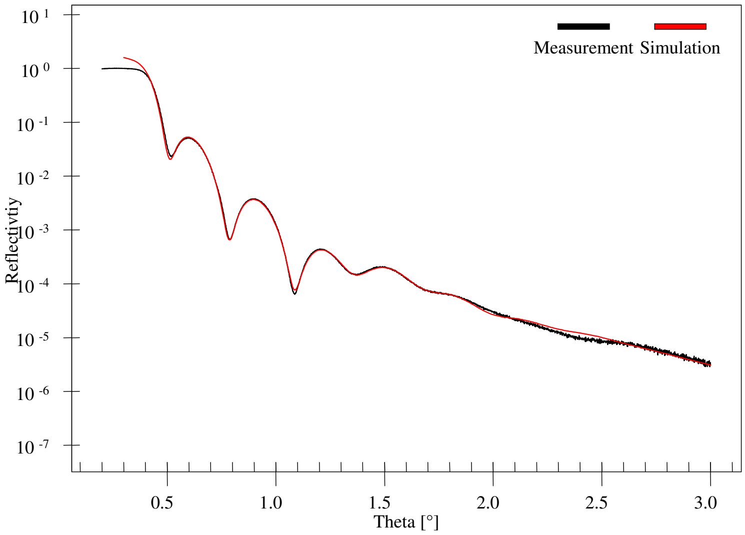

Fig. G.3: XRR result of B^+ doped 10 nm Ni|Si sample without capping layer (λ=1.5414 Å). XRR results: 12.48 nm Ni with 0.98 nm Ni oxide on top.

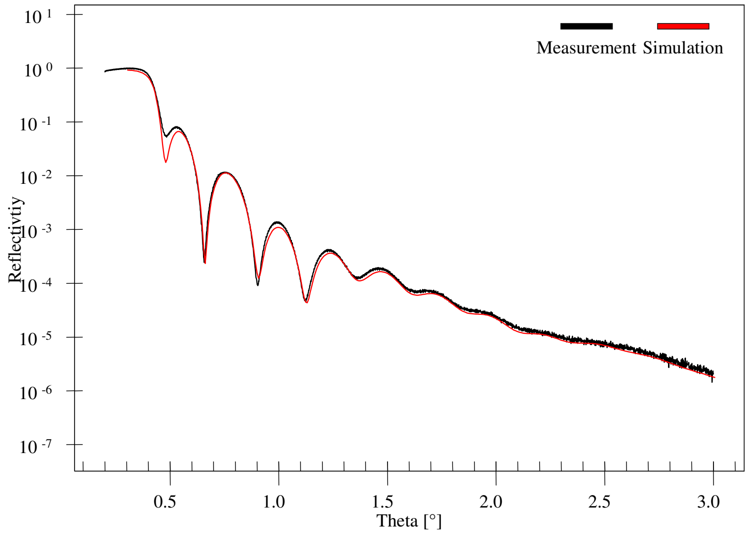

Fig. G.4: XRR result of B^+ doped 15 nm Ni|Si sample without capping layer (λ=1.5414 Å). XRR results: 16.17 nm Ni with 0.96 nm Ni oxide on top.

G.1.2 XRR results of Ni|Si samples with capping layer

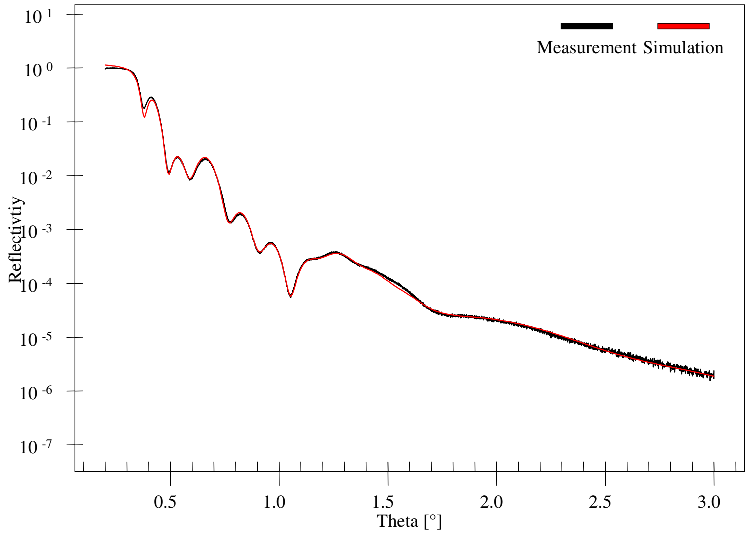

Fig. G.5: XRR result of B^+ doped 10 nm Ni|Si sample with TiN capping layer (λ=1.5414 Å). XRR results: 12.75 nm Ni with 13.77 nm TiN on top.

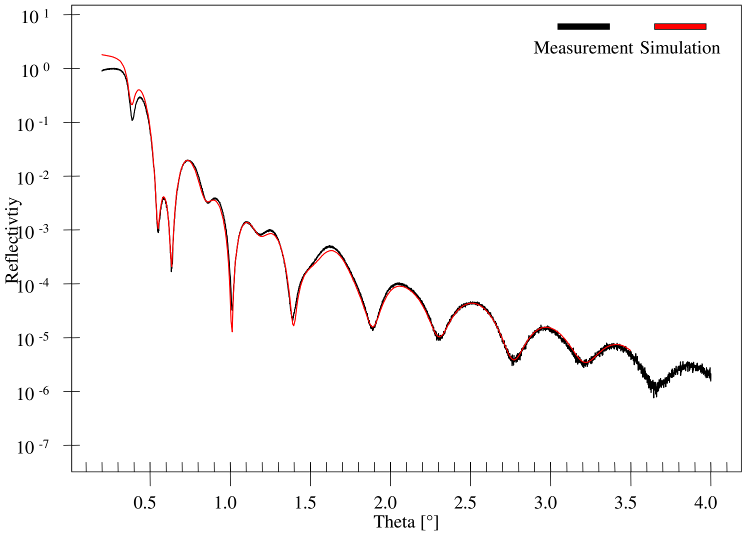

Fig. G.6: XRR result of undoped 8 nm Ni|Si sample with TiN capping layer (λ=1.5414 Å). XRR results: 9.70 nm Ni with 13.34 nm TiN on top.

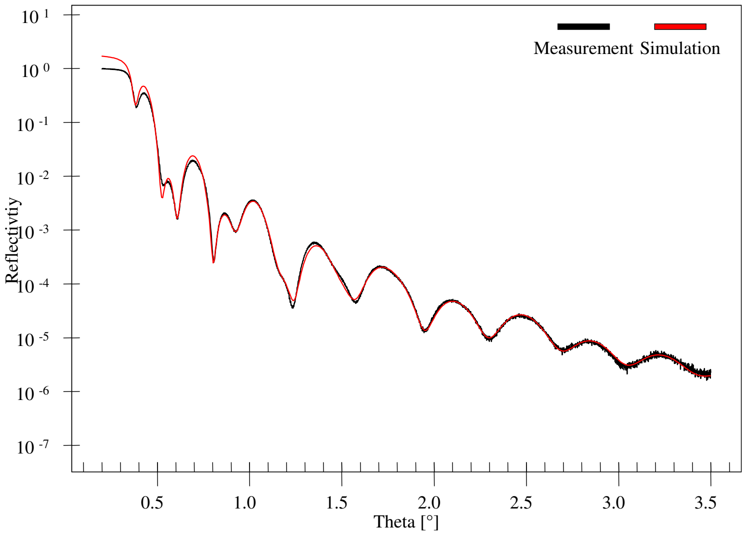

Fig. G.7: XRR result of undoped 10 nm Ni|Si sample with TiN capping layer (λ=1.5414 Å). XRR results: 13.51 nm Ni with 11.95 nm TiN on top.

G.2 Samples with polycrystalline Si substrate

G.2.1 XRR results of Ni|Si samples without capping layer

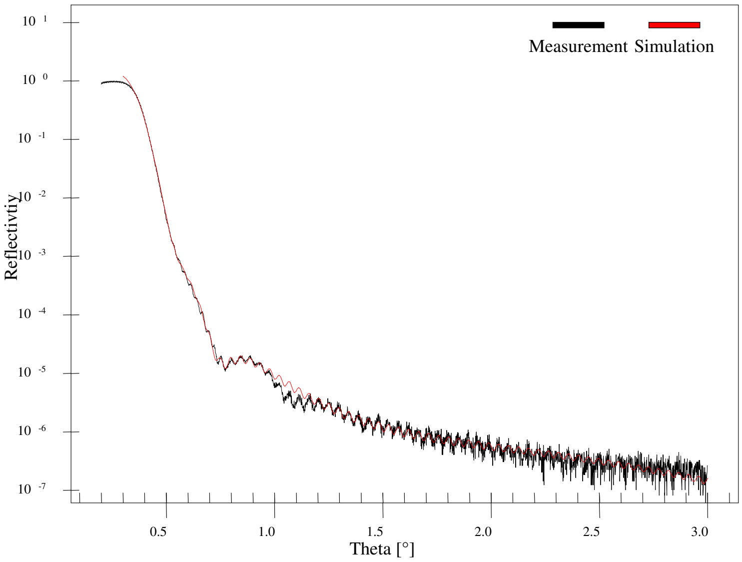

Fig. G.8: XRR result of B^+ doped 8 nm Ni|Si sample without capping layer (λ=1.5414 Å). XRR results: 9.70 nm Ni with 1.22 nm Ni oxide on top.

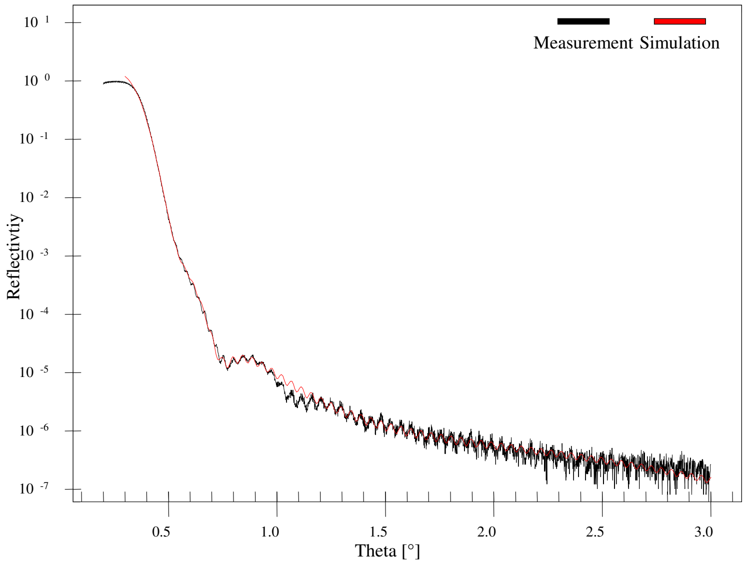

Fig. G.9: XRR result of B^+ doped 10 nm Ni|Si sample without capping layer (λ=1.5414 Å). XRR results: 10.81 nm Ni with 1.36 nm Ni oxide on top.

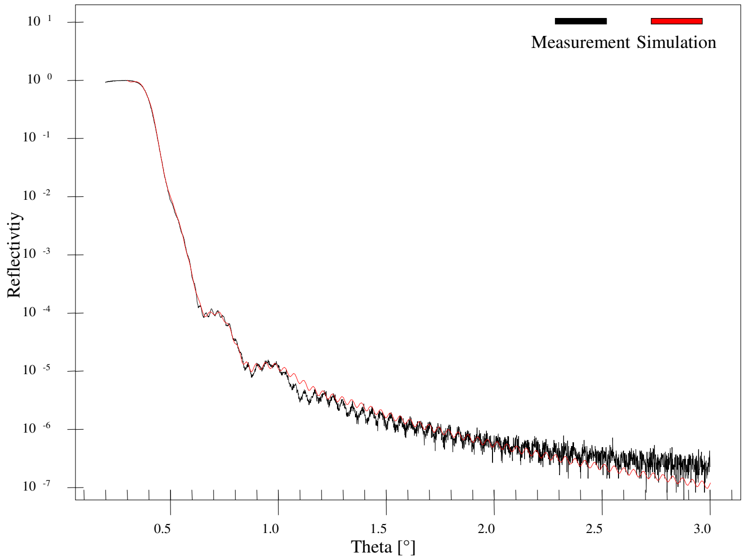

Fig. G.10: XRR result of B^+ doped 15 nm Ni|Si sample without capping layer (λ=1.5414 Å). XRR results: 15.26 nm Ni with 0.7 nm Ni oxide on top.

G.2.2 XRR results of Ni|Si samples with TiN capping layer

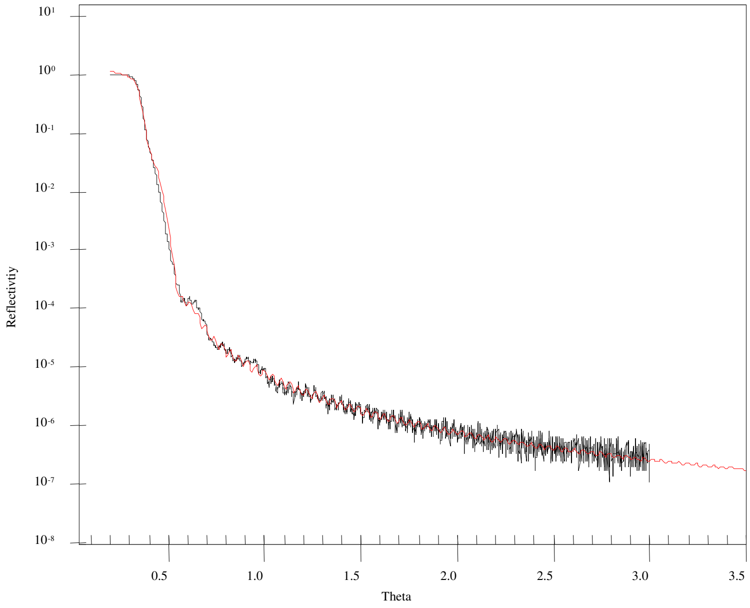

Fig. G.11: XRR result of B^+ doped 10 nm Ni|Si sample with TiN capping layer (λ=1.5414 Å). XRR results: 9.73 nm Ni with 10.22 nm TiN on top.

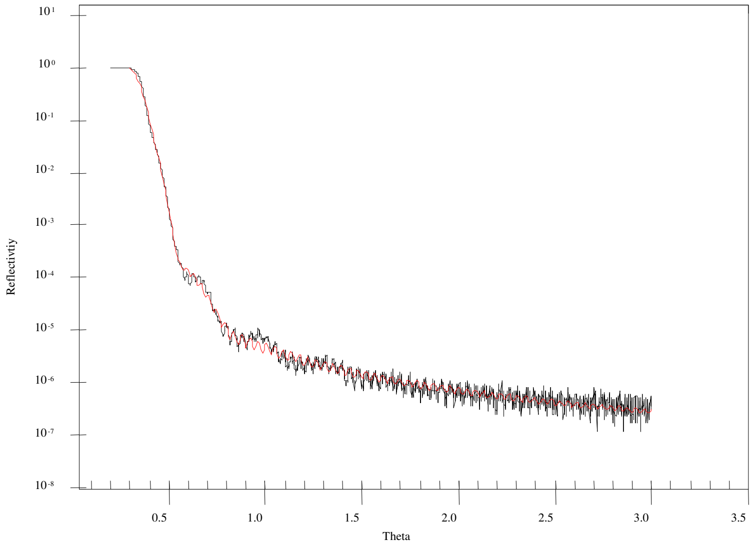

Fig. G.12: XRR result of undoped 10 nm Ni|Si sample with TiN capping layer (λ=1.5414 Å). XRR results: 9.25 nm Ni with 17.99 nm TiN on top.